WATER WAVES GENERATED BY UNDERWATER LANDSLIDES

Thesis by

Philip Watts

In Partial Fulfillment of the Requirements

for the Degree of

Doctor of Philosophy

California Institute of Technology

Pasadena, California

1997

(Submitted May 16, 1997)

For Hilary Norcliffe

The Islet

Emerald lagoons
Fed by trickles of sweat
Site of soothing baptisms
From the daily fire

Spires of rock
Beacons to the stranger
Distant icons to the flock
That needs fertile soil

Acknowledgments

The work presented in this thesis was funded by the National Science Foundation. A significant part of my salary over three years was paid by the Province of Québec through the FCAR scholarship program. *Merci bien.*

I would like to thank my advisor Dr. Fredric Raichlen for being an outstanding promoter of experimental wave measurements. I also wish to acknowledge the essential and cheerful guidance of Dr. Norman Brooks. I benefited from the insightful observations offered by Dr. E. John List. Profs. Chris Brennen and Ron Scott have guided my research through very helpful discussions of theoretical and experimental results. Dr. Channing Ahn and Hilary Norcliffe both helped process material landslide profiles in very different but important manners. Caltech undergrad Donna Ebenstein analyzed material particle sizes and motions. Fellow graduate student Selena Forman provided the analyses of garnet sand included in Chapter 4. Special assistance was provided by Dr. John Brady and Mike Vicic regarding suspensions rheology and by Dr. Stuart Savage regarding granular media. Various parts of this work have benefited from discussions with Prof. Stewart Turner, the late Dr. Ed Zukoski, and Dr. Tony Leonard. An e-mail exchange with Dr. Joe Hammack was much appreciated. Dr. Julian Lee first spotted the multiple wave events in glass bead gravity currents.

A brief but intense visit with Dr. Stéphan Grilli was instrumental in performing the simulations contained in this work and I am deeply grateful for his guidance and his BEM code. The assistance of Mr. Juan Horrillo at the University of Rhode Island was much appreciated in getting simulations of underwater landslides started and processed. Discussions with Dr. George Carrier and Prof. Howell Peregrine were instrumental in recognizing and formulating theoretical wave generation problems that could be solved. Their ideas deserve more attention than given herein.

Many people in the Keck Hydraulics Laboratory and Environmental Engineering Sciences option have contributed to the completion of my doctoral research. Carmen Lopez, Fran Matzen, Linda Scott and Andrea Wilson have all been helpful and supportive during the daily grind. Rayma Harrison and Susan Leising ran a fabulous "satellite" library while it lasted. Rich Eastvedt, Russ Green, Hai Vu, and Joe Montana were indispensable and I am deeply indebted for their skillful work and frequent mentoring.

Cecelia Lin cheerfully drew a number of the figures while the folk at Graphic Arts always came through for me. "You must be one of Dr. Raichlen's students."

Lifestyle is an often neglected component of Ph.D. work and thanks are due to Sandy Watson for a fabulous apartment at affordable cost. Harry and Levon at Burger Continental offered amazing deals to a very hungry student. Naoko Takarabe and Clint Dodd went beyond the call of duty in the Caltech pool and elsewhere. Tom Lloyd and Marc Kuchner deserve thanks for something that was also inspired in part by Prof. Jim Morgan. Lara Hughes and Neil Fernandes were reliable band members. Don Caldwell and the Caltech Men's Glee Club were inspirational. Hilary Norcliffe has enhanced my life in too many ways to mention.

While numerous people have contributed to this work in some manner or another, any remaining errors, omissions or shortcomings are my sole responsibility.

Abstract

Water waves generated by underwater landslides threaten coastal communities near heads of fjords, near heads of underwater canyons, near river deltas, and on volcanic islands. This work provides a thorough analysis of water waves generated by two-dimensional underwater landslides using experimental, theoretical, and computational means. Water wave amplitudes generated by an underwater landslide are a function of the landslide length, the initial landslide submergence, the incline angle measured from horizontal, the characteristic distance of landslide motion, the characteristic duration of landslide motion, and the landslide rate of deformation. Nondimensional wavemaker curves constructed from the aforementioned parameters allow water wave amplitudes to be predicted. These wavemaker curves apply broadly to water waves generated by unsteady motion of a submerged object provided the motion is governed by only one characteristic distance scale and one characteristic time scale. Water wave amplitude predictions can be used for hazard mitigation studies.

An analytical solution of underwater landslide center of mass position in time provides the characteristic distance and time scales of landslide motion. Two-dimensional experimental results on a 45 degree incline confirm the existence of wavemaker curves for solid block landslides as a function of nondimensional geometrical quantities and what is called the Hammack number. The Hammack number is the correct nondimensional time for water wave generation problems. Water wave amplitudes generated by solid block landslides can be predicted from the wavemaker curves if the center of mass motion is known. The analytical solution reproduces the center of mass motion of solid block and granular material landslides. Experimental results of granular material landslides on a 45 degree incline show that landslide deformation reduces water wave amplitudes. Therefore, water waves generated by solid block landslides provide an upper bound on water waves generated by geometrically and kinematically similar deforming landslides. A criterion for the generation of linear water waves is given along with criteria for deep (or long) wave propagation down a constant depth channel. Simulations of water waves generated by underwater landslides were conducted with an inviscid fluid dynamics code. The waves simulated by the code agree reasonably well with experimental results.

Table of Contents

List of Tables

Nomenclature

Roman Symbols

A	Area of two-dimensional landslide; solid block velocity
Ai	Airy function
a	Acceleration
a_o	Initial landslide acceleration
B	Solid block velocity
b	Initial length of top face of landslide
C_d	Drag coefficient
C_f	Lubrication coefficient
C_m	Added mass coefficient
C_n	Coulombic friction coefficient ($C_n=\tan\psi$)
c	Initial length of front face of landslide
D	Nominal diameter of particles; displacement; denominator
d	Initial landslide submergence; differential; distance
E	Wave energy per wavelength per unit width
E_p	Integral of wave amplitude squared over all time at some fixed position
e	Coefficient of restitution of particle collisions; energy conversion
F	Force; conversion factor
f	Function; frequency
g	Mean gravitational acceleration on earth surface; function
H	Wave height; Heaviside function
h	Constant channel depth; lubrication gap height
h_o	Characteristic lubrication gap height
h_L	Left side lubrication gap height
h_R	Right side lubrication gap height
I	Integral
I_n	Integral dependent on the integer value of n
Im	Imaginary part of a complex argument
i	Square root of minus one; integer
j	Integer
K	Nondimensional pressure
k	Constant coefficient

L	Geometric packing factor
ℓ	Length of landslide along the incline
m	Mass; integration change of variable; slope
m_b	Solid block mass
m_o	Mass of displaced water
N	Normal force; sample number; numerator
n	Integer; coordinate normal to s; exponent
P	Static pressure at a point; polynomial
p	Perimeter
Q	Physical quantity in dimensional analysis; volumetric source strength
q	Laplace analog of t
R	Transformed coordinate
r	Radial distance coordinate; radius; correlation coefficient
S	Stroke of wavemaker; transformed coordinate
s	Position coordinate along boundary or incline
$s*$	Particular distance along the incline at $t*$
s_o	Characteristic length scale of motion
T	Wave period; landslide thickness
t	Time coordinate of landslide motion along incline
t_c	Characteristic time scale of motion used by Hammack (1972)
t_o	Characteristic time scale of motion
$t*$	Particular value of time
u	Horizontal water velocity at a point; instantaneous block velocity
u_p	Terminal velocity of single material particle
u_t	Landslide terminal velocity
$u*$	Particular velocity at $t*$
V	Voltage; volume
V_o	Total volume
V_m	Material volume
v	Vertical water velocity at a point
w	Width of two-dimensional landslide
x	Horizontal position coordinate
y	Nondimensional coordinate of integration
z	Vertical position coordinate
z_c	Perpendicular distance from incline to landslide centroid

Greek Symbols

α	Angle of top face of landslide with incline
β	Aspect ratio b/2d
χ	Chi squared function from statistics
Δ	Finite difference
∂	Partial differential
ε	Small number
ϕ	Material internal friction angle; phase function; velocity potential
Γ	Rate of deformation $d\alpha/dt$; fluid circulation
γ	Specific Density
η	Free surface amplitude
η_{max}	Maximum amplitude above middle of initial landslide position
κ	Wavenumber; Fourier analog of x
λ	Wavelength
μ	Sample mean
μ_o	Dynamic viscosity of pure water at 20°C
μ_g	Geometric mean
ν_o	Kinematic viscosity of pure water at 20°C
ν_s	Local solid volume fraction of material
Π	Generic nondimensional grouping in dimensional analysis
π	Irrational number pi
θ	Angle of the incline from horizontal
ρ	Density
ρ_b	Average density of solid block
ρ_m	Density of material
ρ_o	Density of pure water at 20°C
ρ_s	Bulk density of material suspension
σ	Sample standard deviation
σ_g	Geometric standard deviation
τ	Shear stress
ω	Dispersion relation of water waves; circular frequency
ψ	Critical incline angle for block or material sliding on incline
ζ	Motion of wave generating section of channel bottom

Nondimensional Numbers

a_{nd}	Nondimensional acceleration: initial over characteristic acceleration, (3.54)
Ba	Bagnold number: ratio of two shear stress scalings, (5.15)
Co	Courant number: time step over time of wave propagation, (3.118)
Fr	Froude number: square root of inertial force over gravitational force, (3.25)
Ha	Hammack number: time over wave propagation time scale, (3.31)
Ha_o	Hammack number evaluated at time t_O, (3.20)
Re	Reynolds number: ratio of inertial force over viscous force, (3.26)
SF	Shape Factor, (4.18)
Sg	Submergence number: acceleration length scale over initial submergence, (3.20)
u_{nd}	Nondimensional velocity: terminal over characteristic velocity, (3.53)

Subscripts

.	Separates different subscripts
A	Added mass
a	Solid block ballast; solid block corner
airy	Airy wave
B	Basset
b	Solid block; solid block ballast; buoyancy; solid block corner
C	Centroid
c	Solid block ballast; center of mass; characteristic
d	Drag; solid block ballast
e	Solid block ballast; external
eff	Effective
f	Lubrication; final
g	Geometric; gravitational
I	Intersection
i	Integer
j	Integer
L	Left
l	Lead solid block ballast
m	Added mass; material
max	Maximum or upper bound
min	Minimum

n	Dynamic Coulombic friction; normal block ballast; integer
nd	Nondimensional
o	Ambient water; initial; characteristic; no solid block ballast; total
p	Particle
R	Right
s	Suspension; solid phase
t	Terminal
v	Vortex
x	Crossing
1	Index
2	Index
3	Index
*	Special or particular value
∞	Infinity

Superscripts

'	Nondimensional
+	Infinitesimally larger than

Chapter 1

1. Introduction

Tsunamis are water waves generated by impulsive geophysical events such as earthquakes, volcanic eruptions, or landslides that usually occur at the ocean bottom or along steep banks. Tsunamigenic underwater landslides involve the failure of a mass of sediment (or fill) that can range in length over more than six orders of magnitude, with larger landslides typically occurring less frequently. Damaging tsunamis may result from the failure of sediment along the steep bank of a fjord, near the head of a nearshore submarine canyon, at the mouth of a river, or along the coast of volcanic islands. Figure 1.1 indicates the location of large underwater canyons immediately off the California coastline. Sediment failure may occur spontaneously during extremely low tides or sediment laden flooding; or, failure may be triggered by an earthquake, storm waves, or by external loading of the sediment (or fill). A number of damaging underwater landslides that were on the order of a few hundred meters in length appears to have been induced by nearshore human construction over the last century. Evidence of tsunamigenic landslides tens to hundreds of kilometers in length have been documented at underwater alluvial deposits with typical slopes smaller than several degrees. When underwater landslides of this magnitude occur, sediment failure is either presumed or known to be seismic in origin and may involve liquefaction (or translational motion) of an enormous volume of sediment. Modern sonar soundings and records of underwater cables sheared apart by sediment failure often form the only quantitative evidence of tsunamigenic underwater landslides. Some form of wave run-up observation or evidence is often the only indication of wave heights.

1.1 Qualitative Laboratory Scale Results

A qualitative introduction to the experiments conducted for this work will orient the reader in the following chapters. It is also important at this time to describe some of the constraints that have shaped the experimental work. The height of a tsunami is often its most important feature when conducting hazard mitigation studies or when attempting to explain existing wave damage. An experimental study of water waves generated by underwater landslides should enable prediction of wave heights near the wave generation region. In general, wave heights can be predicted based on the initial landslide geometry, the landslide center of mass motion, and the landslide rate of deformation about the center of mass. The height of a tsunami helps determine if it should be considered as a linear or a nonlinear wave. One expects underwater landslides to generate linear water waves if the nondimensional initial submergence is large or the slope of the incline is small. Since these conditions are met by most underwater landslides, some authors have doubted the ability of an underwater landslide to generate significant water waves, including LeBlond and Jones (1995). An important exception is landslides induced by nearshore human activity which are often partially aerial and exhibit nonlinear wave phenomena such as bores. At laboratory scales, breaking waves are subject to surface tension, viscous, and air entrainment scale effects and are therefore not studied in this work. Almost all of the water waves generated by underwater landslides in this work will be shown to have been linear waves.

In the context of this experimental work, a landslide is understood to be any submerged body (or mass of granular material) sliding down the surface of an underwater incline. When a solid block is used to simulate an underwater landslide, the results can be scaled up to any size provided that scale effects do not significantly alter the laboratory solid block motion or wave propagation. For the size and density of solid blocks used herein, there are no relevant scale effects. Hence, all that is required to study the water waves generated by solid block landslides is that the solid block material be able to slide along the incline material (which occurs at an incline angle $\theta>20^{\circ}$ for the materials used herein). The situation is not so simple for deformable material landslides. While underwater landslides can be triggered along oceanic slopes of less than 1°, these events typically cover many square kilometers and are usually initiated through liquefaction of a sediment layer by an earthquake. The sediment gravitational force manages to overcome the shear stress along some shear plane only because an external action has raised pore water pressures and reduced effective sediment strength in a shorter period of time than

diffusion of pore water pressure away from the shear plane. Moreover, the sediment shearing produced by underwater landslide motion is often sufficient to keep landslides moving over distances of many kilometers.

Water waves generated by an underwater landslide at laboratory scale can have wave heights that are only a fraction of a centimeter above or below the still water level. So, although Scott (1989) describes how to scale landslide failure (with corresponding pore water pressures and effective stresses) to laboratory scale with natural sediment inside a centrifuge, it would be difficult to measure accurate wave heights in such an experimental system. Inducing positive pore water pressures on sediment landslides under ordinary gravitational conditions would also impair the accuracy of wave measurements. For example, injecting pressurized water into the sediment raises the still water level measurably, and shaking the sediment induces additional surface waves. On the other hand, a dense sediment with equilibrium pore water pressures prior to failure can experience negative pore water pressures during failure. Negative pore water pressures hold sediment particles together and inhibit realistic sediment failure. Consequently, the solution used to ensure material landslide failure herein involves two separate measures: i) granular materials with large particle sizes (about 1 mm in diameter) and correspondingly large hydraulic diffusivities were used in order to ensure that pore water pressures remained near equilibrium; and, ii) the incline angle was steep enough for the granular materials to fail in the absence of external stimuli (which translated into an incline angle $\theta>30^\circ$ for the granular materials used herein). Hence, material failure and landslide motion were assured *a priori* for material landslides, as was the generation of water waves.

Figure 1.2 shows that a cross-section of the southwest face of La Jolla canyon can attain slopes approaching 22°. Fjord banks can achieve even higher slopes of around 30°. For all experiments reported herein, a sediment mass accumulated along a steep underwater canyon or fjord bank was modeled as a right triangle initially at rest on a straight incline $\theta=45^\circ$ from horizontal. The right triangle geometry results in a convenient separation of wavemaker physics as the solid block slides down the incline: the motion of the horizontal top face creates a trough above the block while the motion of the vertical front face creates a crest ahead of the block. The combined water movement acts like a submerged flow doublet when landslide motion first begins. All underwater landslides studied in this work will initially have a top face parallel to the undisturbed free surface and a front face perpendicular to the free surface. The use of a single initial landslide

geometry for all experiments allows for geometrical similarity between experiments. In addition, the dynamical coefficients for both added mass and drag forces can be determined empirically as a function of this geometry for all landslides studied. The combination of incline length and initial block submergence used herein allows most solid blocks to reach velocities within a few per cent of the terminal velocity near the bottom of the incline. While the experimental geometry is not natural, it is also not too far away from real wave generation scenarios.

Figure 1.3 shows four frames of a solid block sliding down and coming to rest at the bottom of the incline. Dye had been deposited on the block surface just before motion began in order to visualize the water flow near the block. The first frame (a) shows the vortex formed behind the sharp edge of the accelerating block, the only large scale feature of the fluid dynamics that is controlled by viscosity. A dip in the free surface is formed immediately above the accelerating block whereas the front face of the moving block has created a positive wave further to the right. The exposure time was long enough to demonstrate block motion while the framing rate of 5 frames per second provided a few frames per trial. The second frame (b) shows the formation of a recirculation region behind the block just prior to coming to rest. The dip in the free surface seems to be following the top of the solid block. The shoreward side of the free surface dip is steep enough for significant nonlinear piling up of water and potentially wave breaking (while propagating to the right away from the shoreline). The last two frames (c) and (d) show the evolution of the shed vortex and the free surface after the block has come impulsively to rest. The vortex core consists of small bubbles swept from the block surface and trapped in a (virtual) line connecting one wall to the other.

Figure 1.4 documents the deformation of a mass of crushed calcite initially the same shape as the solid block in Figure 1.3 into a gravity current near the bottom of the incline. The first frame (a) shows the landslide material initially impounded behind a gate that retracted into the incline in about 40 ms. The shearing of the material by the retracting gate energized the adjacent layer of particles that then moved about one particle diameter to the right in the time it took to fully retract the gate. For early times around that of frame (b), the initially solid mass of material failed and underwent large strains mostly in the direction parallel to the incline. Particle blurring indicates that the particles further down the incline are moving faster. In frames (c) and (d), surface shearing by the water stripped material from the landslide surface to form a gravity current with significant internal circulation. Particles near the gravity current surface are seen to be nearly

immobile relative to the main body of particles. The two wave generation mechanisms described above were also acting to form a leading positive wave followed by a negative wave above the material. The waves propagated down the constant depth channel as a dispersive wave train. Figure 1.5 shows detailed traces obtained from a high speed movie of a similar mass of crushed calcite moving down the incline. The lines on the right of each landslide delineate the front face of the landslide from the side and help eliminate changes in camera perspective. The transition from strained landslide material to flowing gravity current is perhaps more evident in Figure 1.5 than Figure 1.4.

Figure 1.6 provides a qualitative comparison of landslide failure for three different landslide materials. Each cross-sectional profile was drawn 0.30 s after the material landslide began. Results in Section 5.1 demonstrate that elapsed time (as opposed to distance traveled) is the correct way to compare these three material landslides. There is one large friction angle material (crushed calcite) and one large density material (lead shot). All particle sizes are roughly identical at about 3 mm in nominal diameter. The masses of spheres had an internal friction angles of nearly 30° in water whereas the crushed calcite had an internal friction angle of 47° in water. All materials can be considered noncohesive. For each material, the center of mass motion, the rate of strain, the mode of failure, and the relative strength of water shearing to gravitational forcing are all different. The crushed calcite landslide apparently retains some memory of its original shape while the lead shot landslide has significantly collapsed. The glass bead landslide shows some intermediate behavior. At 0.30 s after release, the lead shot landslide exhibits a center of mass displacement along the incline of nearly twice the other two landslides. Indeed, each material shown in Figure 1.6 can be said to be in a different constitutive regime at early times. The crushed calcite behaves as a strained soil that is deformed largely by surface shearing; the lead shot behaves like a granular medium in air; and, the glass beads behave as an immiscible Newtonian fluid mass that is molded by boundary shearing.

1.2 Novel Contributions

Two-dimensional water waves generated by underwater landslides have been studied experimentally using solid blocks in the past. The work done to date provides a qualitative understanding of the water waves generated by underwater landslides but does not allow for prediction of the wave heights that may result from an arbitrary underwater landslide. A few underwater landslides have also been simulated numerically without

gaining much insight into the landslide parameters that control wave amplitude. In this work, the theoretical wavemaker formalism of Hammack (1972) is applied to underwater landslides for the first time. Solid blocks of one chosen geometry are then used to construct the first experimental wavemaker plot for underwater landslides on a 45° incline. The characteristic wave amplitude obtained from the wavemaker plot are used to scale other wave characteristics such as the conversion of solid block kinetic energy into wave energy. Conditions for the generation of linear water waves by an underwater landslide are given for the first time along with conditions that determine whether far-field waves in a constant depth channel propagate as deep water waves or as long waves. The wavemaker formalism is also extended to describe the water waves generated by deformable material landslides. This marks the first parametric study relating the observed landslide rate of deformation to changes in the nondimensional wave amplitudes. This work provides the theoretical foundations and experimental methods to study the water waves generated by arbitrary underwater landslides. That is, the general form of the wavemaker plot can be applied to different landslide geometries, different landslide kinematics, and new far-field bathymetries. As a case in point, simulations of water waves generated by underwater landslides yield wavemaker curves for a variety of initial landslide geometries.

1.3 Thesis Outline

This chapter has introduced general features of underwater landslides, described some of the constraints of laboratory scale studies of underwater landslides, and outlined the novel contributions contained within this thesis. Chapter 2 summarizes the literature of water waves generated by underwater landslides, including field observations, experimental work, and numerical simulations. Some soil mechanics and gravity current literature are also discussed. Chapter 3 derives the theoretical form of the nondimensional wavemaker plot. The analysis shows that the landslide kinematics must be known in order to predict wave amplitudes. Therefore, solid block motion is studied theoretically in Chapter 3 in order to understand the influence of landslide properties on landslide kinematics and wave generation. Analytical tools are also developed that are able to predict water wave amplitudes generated by underwater landslides given landslide kinematics. Chapter 4 discusses the experimental apparatus and procedures used to obtain and interpret the experimental results presented in the following chapter. Chapter 5 begins with the results of landslide kinematic observations to be used in the wavemaker formalism. Next, the wavemaker plots for solid block and deforming landslides are presented along with

general features of the water waves generated by underwater landslides. For many wave characteristics, the experimental results are compared with the literature cited in Chapter 2 and the theoretical results of Chapter 3. Chapter 5 also features some numerical simulations of underwater landslides. Chapter 6 summarizes the thesis and restates the main conclusions to be drawn from this work. Appendix A compares all wave records of repeated trials including numerical simulations. Appendix B provides the error analyses of experimental and simulation results. Appendix C summarizes the raw experimental, theoretical and simulation data.

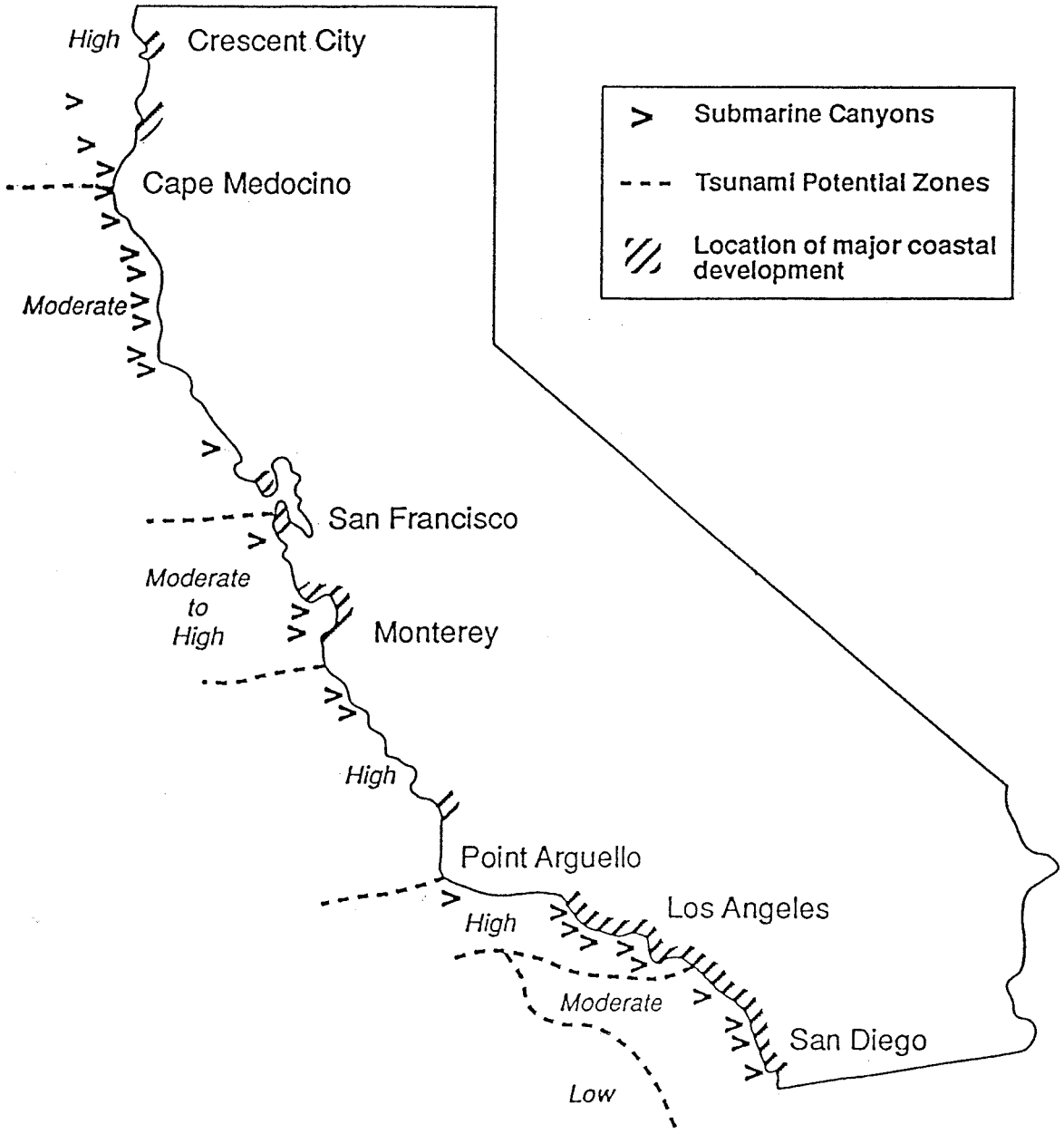

Figure 1.1: Location and tsunami hazard of submarine canyons off of the coast of California taken from McCarthy *et al.* (1993). Major coastal development may be at risk due to water waves generated by earthquake triggered underwater landslides. High, moderate, and low are designations given by McCarthy *et al.* (1993) for tsunami hazard.

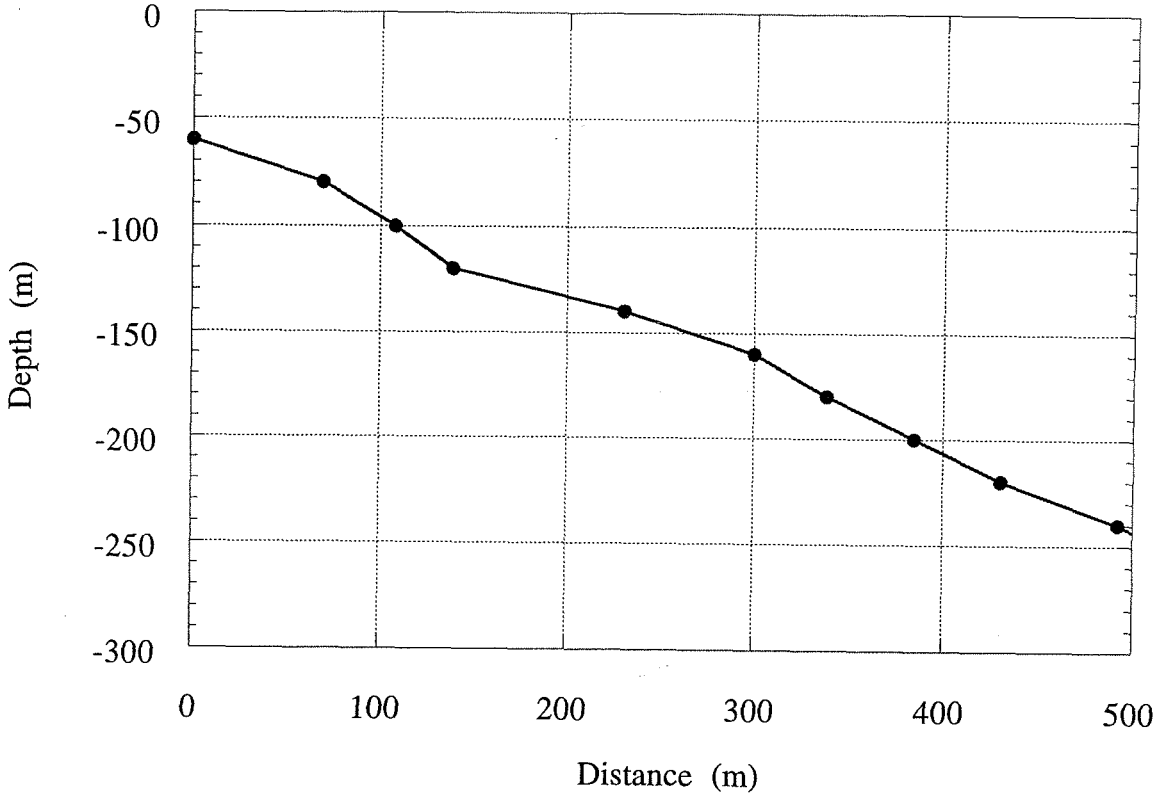

Figure 1.2: Bathymetry near the head of La Jolla submarine canyon taken from Shepard and Dill (1966). The southwest face of La Jolla canyon has a mean slope of 22° that faces the shoreline. An earthquake could initiate an underwater landslide if sufficient sediment were to accumulate on such a slope.

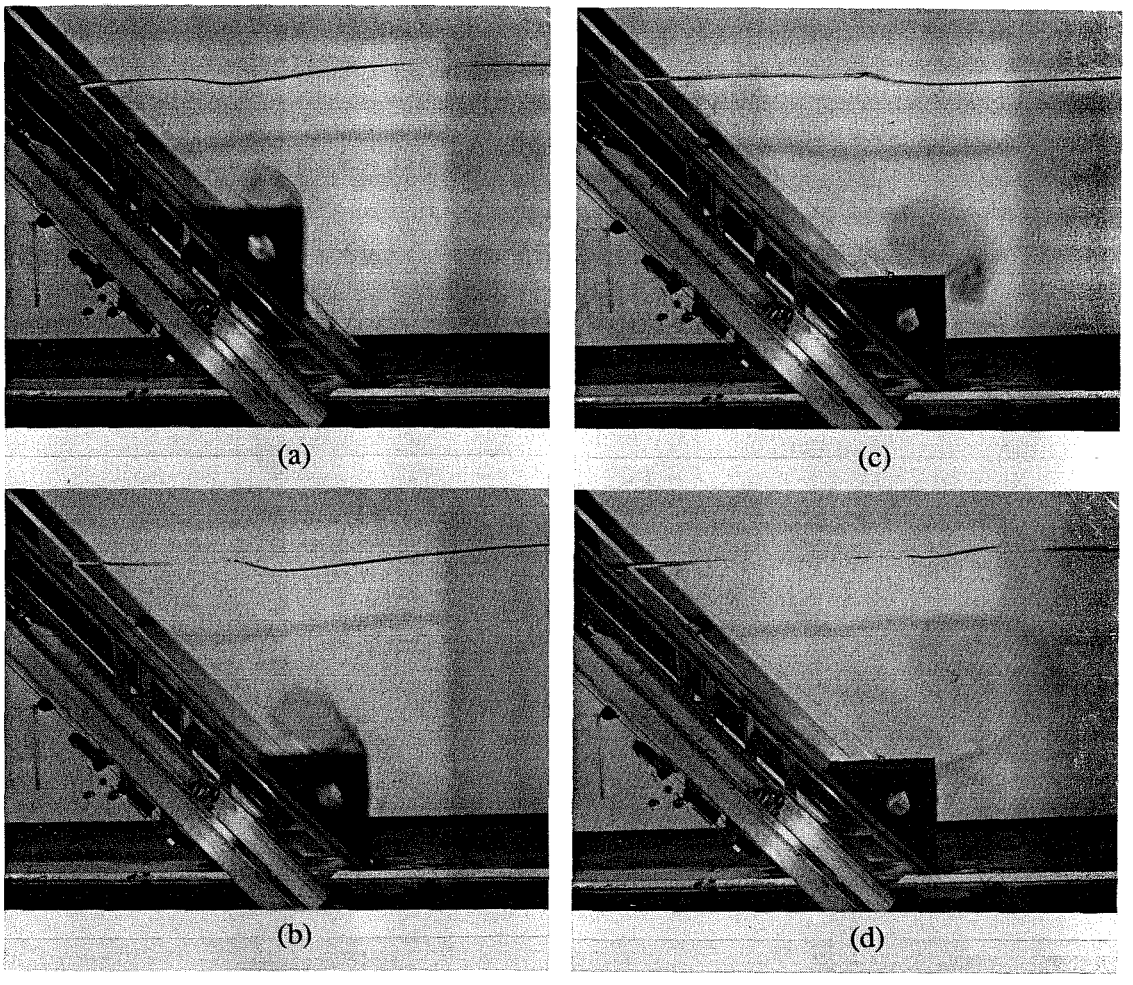

Figure 1.3: Four frames from a solid block landslide with dye initially deposited on the block surface. A starting vortex is formed in the wake of the block. The vortex is shed when the block comes to rest at the bottom of the incline. A negative wave is clearly visible above the solid block while it is still in motion.

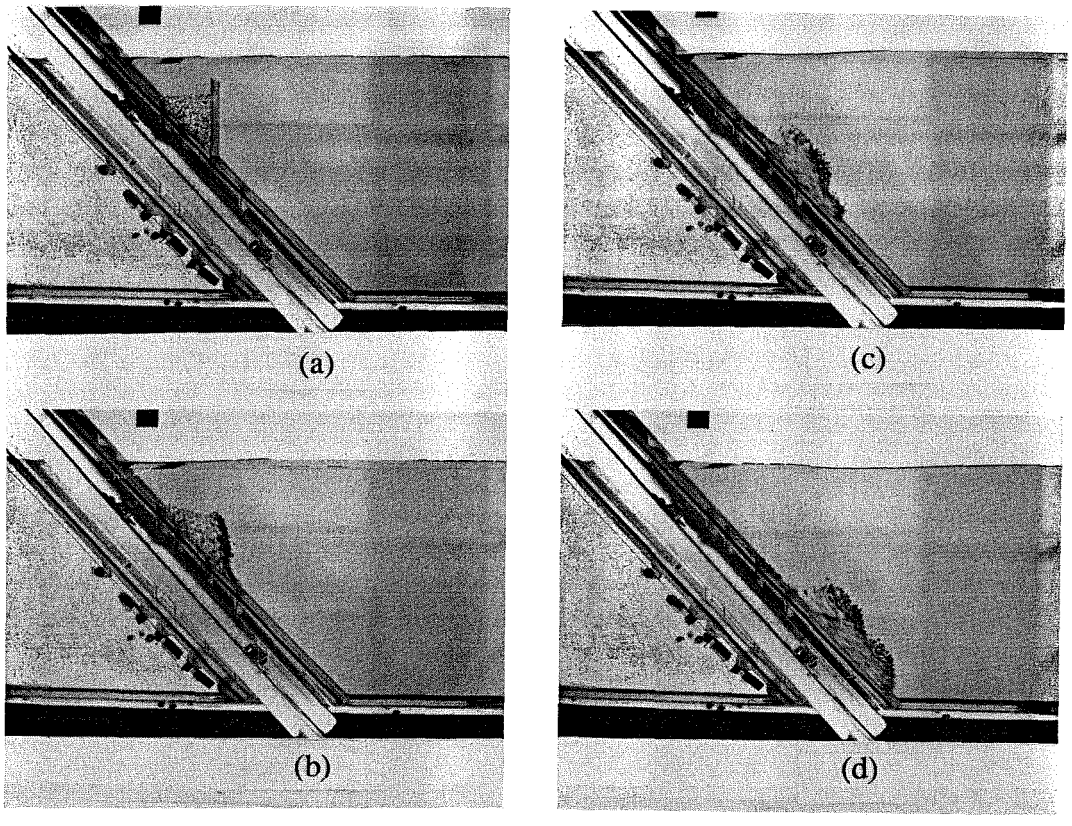

Figure 1.4: Four frames from a material landslide of crushed calcite on a 45° incline. The initial deformation of the material consists of lateral spreading before a gravity current is formed by shearing the surface of the landslide. A negative wave is visible above the material when it is in motion.

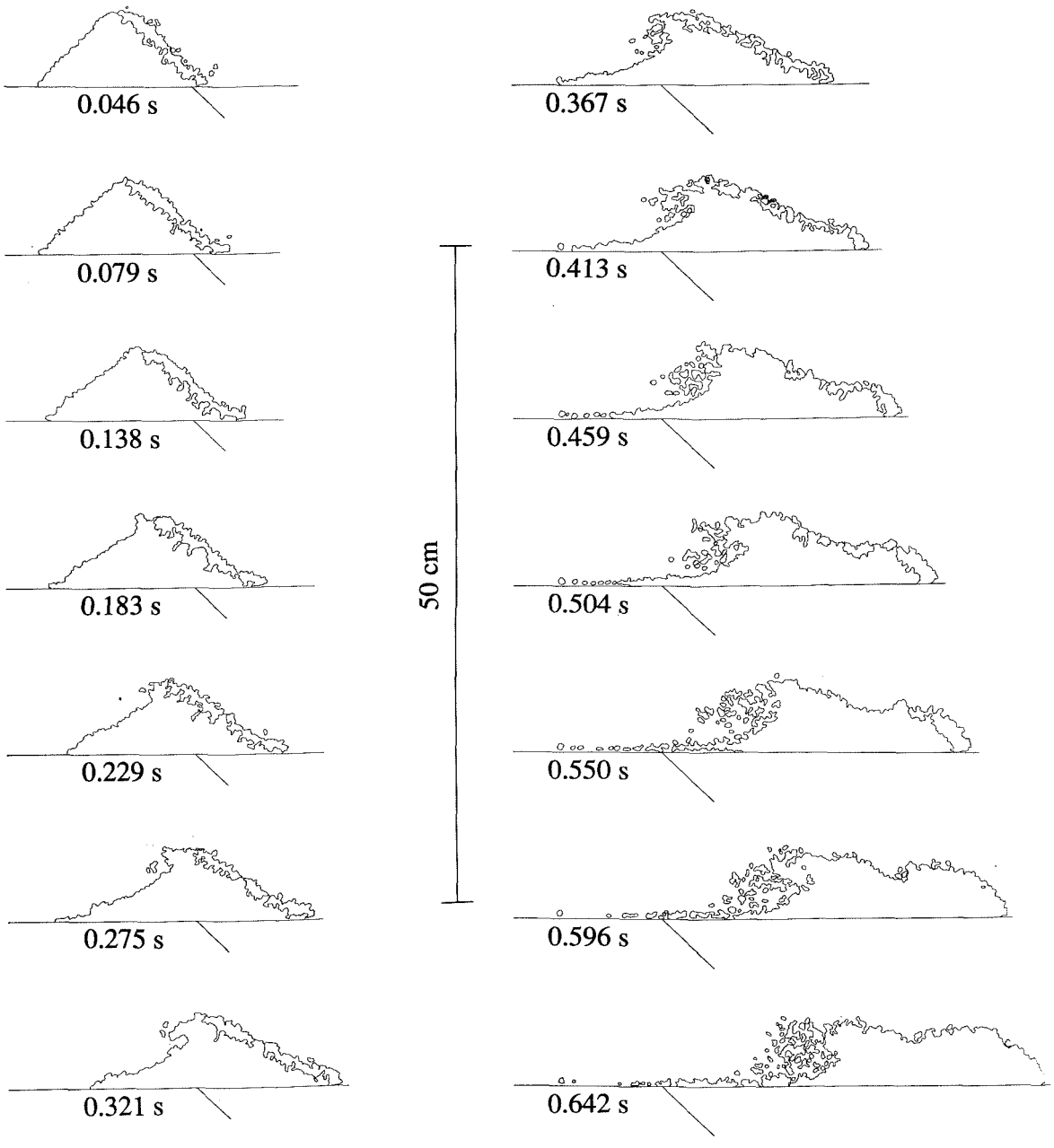

Figure 1.5: Profile traces of a crushed calcite material landslide showing material deformation and development of a gravity current with more temporal resolution than Figure 1.4. The lines appearing on the front face of the landslide resulted from a combination of perspective and lighting.

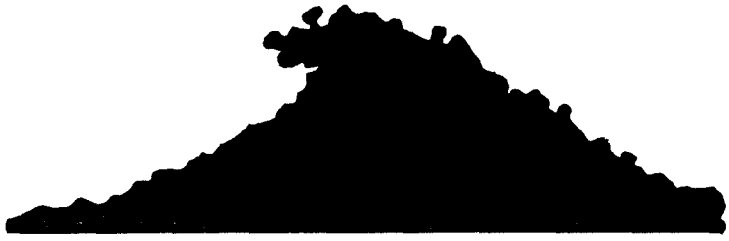

Crushed calcite with nominal diameter 3.33 mm, suspension density 1950 kg/m^3, and internal friction angle 47°. Profile from Trial 32 with center of mass 164 mm down incline.

Glass beads with nominal diameter 2.96 mm, suspension density 1935 kg/m^3, and internal friction angle 29°. Profile from Trial 82 with center of mass 183 mm down incline.

Lead shot with nominal diameter 3.11 mm, suspension density 7320 kg/m^3, and internal friction angle 34°. Profile from Trial 86 with center of mass 321 mm down incline.

Figure 1.6: Comparison top to bottom of crushed calcite, glass bead, and lead shot material landslides at 0.30 s. The cross-sectional profiles were traced from high speed movies of landslide motion and are shown to size. All materials have similar particle nominal diameters and initial landslide volumes. Landslides are moving to the right.

Chapter 2

2. Literature Review

English language literature pertaining to water waves generated by underwater landslides is reviewed in this chapter. Observations of underwater landslide-generated water waves are taken from the open literature. Significant variations exist in landslide scale, regional geology, and wave amplitudes associated with the observations. Experimental studies of water waves generated by solid block landslides and similar analogs are reviewed, followed by a summary of attempts to simulate water waves generated by underwater landslides. Soil mechanics related to undrained soil failure are briefly discussed as they are crucial to understanding landslide initiation. The precise moment of landslide initiation and the exact extent of metastable sediment failure are fundamentally unpredictable as shown in a discussion of sand pile dynamics. The chapter closes with a brief review of gravity current characteristics that may be relevant for landslide kinematics. General reviews of tsunamis affecting the United States including Alaska can be found in Lander and Lockridge (1989), Lander *et al.* (1993), and Lander (1996).

2.1 Observations of Underwater Landslide-Generated Waves

Underwater landslides can often be related to an increase in pore water pressure along (at least) the initial failure plane of the landslide. This can be inferred for many loose sediment banks in nature or measured *post facto* from nearby sediment samples. Terzaghi (1956) points out the role that positive pore water pressure plays in inducing underwater landslides in actively consolidating sediments such as at river deltas. In general, excess pore water pressure can be induced in sediment by extreme low tides,

application of an external load (including a new layer of sediment), earthquake ground motion, wave action, or any combination of these or similar factors. Most large underwater landslides appear to have been initiated by either an extreme low tide or an earthquake.

2.1.1 Tidal and External Load Induced Landslides

Bjerrum (1971) describes six documented underwater landslides in Norwegian Fjords spanning a full century of observation. All six landslides are known to have occurred at fjord heads near postglacial deltas that delivered cohesionless fine sand and weakly cohesive silt onto loosely consolidated sediment forming steep underwater banks. Typical underwater slopes along the edges of the fjords were greater than or equal to 5 per cent (or about 3°). All of the landslides occurred spontaneously at (or immediately following) an exceptionally low Spring tide. In several instances, construction work on or near the landslide contributed to the load and/or perturbation of a metastable sediment, which often destroyed buildings near the construction site and sometimes killed construction workers upon failure. The sediment motion generated waves ranging from 1-7 m in amplitude observed in the fjords up to several minutes following the slides. Terzaghi (1956) describes an underwater landslide along Howe Sound in British Columbia, Canada that closely resembles the slides described by Bjerrum (1971). A pulp mill was constructed on coarse sand with uniform slopes of 26-28° down to a depth of 230 m. The landslide occurred during an extremely low tide and had a maximum thickness of 12 m. A wharf and warehouse located on top of the unstable sediment were destroyed. Terzaghi (1956) makes no mention of wave heights.

Murty (1979) summarizes the history of known underwater landslides in the northern Kitimat Arm of the Douglas Channel, which is a system of fjords in British Columbia, Canada. One underwater landslide in 1974 generated a 2.8 m amplitude wave although the location of the slide remains unknown. Another underwater landslide in 1975 involved an estimated 30 million cubic meters of sediment; the head of the fjord experienced a depth increase of about 30 m as a result of the landslide carrying sediment seaward. The landslide occurred 53 minutes following a low tide and in the absence of seismic activity. Severe damage to the local coastline resulted from several water waves generated by the underwater landslide with one observed wave crest 4.6 m in amplitude along with a trough of 3.6 m. Water wave activity lasted for about an hour within Kitimat Inlet. Using the estimated landslide geometry, Murty (1979) calculated a

characteristic wave height of H≈6.3 m based on an approximate analysis given by Striem and Miloh (1976). Using the theoretical wave predictions of Das and Wiegel (1971) for a moving vertical wall, Murty (1979) also calculated a wave amplitude of $\eta \approx 4.3$ m at a distance of 300 m seaward from the landslide. While neither prediction strictly applies to water waves generated by underwater landslides, it nevertheless appears possible to predict a characteristic wave amplitude from approximate theoretical considerations.

On November 3, 1994, a partially aerial landslide in Skagway, Alaska, destroyed the southern 300 m of the White Pass Co. railway dock and claimed the life of one construction worker. The railway dock was under construction that involved depositing a large external load of rip-rap and fill along the shoreline. About 30 minutes following a predicted -1.22 m MLLW tide, an estimated 3-10 million cubic meters of loose alluvial sediment (at an average initial angle of about 25° near the construction site) slid west into the harbor creating large waves and inducing a strong 3 minute period harbor resonance near the tide gauge that took over an hour to decay. No seismic activity was recorded in the Skagway region immediately prior to the landslide. Estimates of observed wave heights range from 3-11 m at different locations in the harbor. Cornforth (1995) provides the soil mechanical properties of the sediment while Campbell and Associates (1995) provide the detailed harbor bathymetry after the landslide. The Skagway tide gauge record and harbor resonance characteristics have been studied by Kulikov *et al.* (1996) and Raichlen *et al.* (1996). According to Yehle and Lemke (1972), who studied the geological hazards in the Skagway region, a similar landslide occurred at the end of the railway dock in 1966.

River deltas are active sedimentary systems that are generally prone to underwater landslides. Bornhold *et al.* (1994) recorded underwater landslide events at river deltas but do not mention water waves generated by these events. Hamilton and Wigen (1987) discuss evidence of historical underwater landslides at the Fraser river delta in British Columbia, Canada. Terzaghi (1956) shows that underwater landslides at the Mississippi river delta occur because sediment accumulation is sometimes faster than sediment consolidation. Sediment pore water unable to drain from deeper sediment layers can build pore water pressures to the point of sediment failure. A relatively recent underwater landslide near the Var river delta at Nice, France is described by Hamilton and Wigen (1987) as well as Sabatier (1983). On October 16, 1979, a tsunami of height around 3 m was observed in Baie des Anges following an underwater landslide that involved part of a construction site in the port of Nice. Failure may have been induced by

recent loading of the subtidal platform by a 300 m long bank of dredge spoils. The initial volume of sediment in the landslide was estimated to range from 1-10 million cubic meters located along an underwater slope of 4° with significant downstream erosion or secondary landslides involving up to 100 million cubic meters of sediment. Hamilton and Wigen (1987) estimate that landslide material was carried at least 90 km down an adjoining submarine canyon and onto the abyssal plain. At least two submarine cables were broken by the gravity current.

2.1.2 Earthquake Induced Landslides

Earthquakes provide a ready trigger of underwater landslides with considerable tsunami generation capability. Waves are typically generated when a large mass of accumulated loose, fine sand or silt is (partially) liquefied along an incline (or failure plane) by strong ground motion. Water waves generated by underwater landslides are a geological hazard along the entire Pacific coastline of North America due to the presence of either fjords or underwater canyons combined with intense seismic activity from Baja California all the way up to Cook Inlet. McCarthy *et al.* (1993) have examined the potential for tsunami generation along the California coastline, pointing out the rapid arrival and potentially long duration of tsunami activity when waves are generated nearshore. More importantly, McCarthy *et al.* (1993) focus on the possibility that 21 large underwater canyons along the Californian coast have been and will continue to be future sources of tsunamis due to underwater landslides. Underwater canyons along the California coastline and elsewhere in the world have been studied and mapped by Shepard and Dill (1966).

A case in point is the October 17, 1989 Loma Prieta earthquake that significantly damaged San Francisco and caused underwater landslides at Moss Landing. Moss Landing is halfway between the cities of Santa Cruz and Monterey and located at the head of Monterey canyon, an underwater canyon that Shepard and Dill (1966) show is as immense as the Grand Canyon. A computer analysis of seismic motion and tsunami generation by Ma *et al.* (1991) shows that the tide gauge record at Monterey consists of two superposed signals: a 0.5 m high tsunami generated by seismic uplift in the northern portion of Monterey Bay as well as a shorter wavelength 0.7 m high tsunami consistent with underwater landslides along the southern edge of Monterey canyon. Gardner-Taggart and Barminski (1991) reveal at least three underwater landslides into Monterey Canyon totaling about 2 million cubic meters of sediment. These landslides occurred

along the southern face of the canyon within about 500 m from the harbor entrance with one slump scarp measuring 3-6 m deep over a length of 100 m. The landslide sediment may have consisted of fresh deltaic deposits from the Salinas river just south of Moss Landing. Coincidentally, approximately two minutes after the earthquake, a video camera facing the harbor entrance documented waves with T=2 s period entering the harbor. Greene *et al.* (1991) report that the waves entering the harbor were 0.5 m high. Gardner-Taggart and Barminski (1991) estimate the wave arrival time to be consistent with landslide-generated water waves.

An excellent case study of the potential damage due to earthquake triggered underwater landslides is afforded by the Alaskan Good Friday earthquake of 1964 described by Grantz *et al.* (1964). The harbors of Whittier, Seward and Valdez were all situated on saturated, loosely consolidated sands and silts accumulated roughly 100 m thick on bedrock and forming slopes between 20-35° heading into the fjord. Submarine landslides destroyed the shoreline of each of these harbors, and occurred at Thumb Cove as well as other sites within Prince William Sound, often increasing water depth locally by 20 m or more. Wave action induced by the landslides was often described as water withdrawal followed by a large positive wave, where Grantz *et al.* (1964) attribute the positive wave generation to the curious mechanism of muddy boils from the landslide. Unexplained wave action at at least eight other locations in and around Prince William Sound accounted for more than 43 deaths. A group of waves was described at a number of locations as a small positive wave, followed by a large negative wave, and a large positive wave reaching up to 10 m in amplitude and running up the coast to heights of more than 25 m. Such wave groups are consistent with experimental results of water waves generated by underwater landslides. The observations noted by Grantz *et al.* (1964) suggest that tsunamis generated locally by a landslide can be differentiated from tsunamis generated in the open ocean by bottom motion during a large earthquake. Tsunamis generated by an underwater landslide often strike within less than a couple of minutes after an earthquake is felt, involve rapid rising and falling of relatively short period waves, and run-up of the waves is often not associated with large, persistent inland water flows.

Heezen and Ewing (1952) provide considerable evidence of underwater cables being broken by oceanic gravity currents, most often within submarine canyons but sometimes along continental slopes. Evidence of an underwater landslide resulting from the 1929 Grand Banks earthquake is summarized by Heezen and Ewing (1952). Twelve

underwater cables were broken in 28 places for up to 13 hours following the earthquake. The breaks occurred in a successive pattern of increasing depth over a distance of 570 km and across a fan up to 340 km wide. The average underwater slope was about 2° with half of the cable breaks occurring along slopes less than 1°. Kuenen (1952) estimated that the Grand Banks underwater landslide was around 50 m thick, contained 760 cubic kilometers of sediment, and eroded a layer of bed sediment 11 m thick. A tsunami on the order of 30 cm in height with a period of one to two hours caused loss of life and damage to fishing boats along the southern coast of Newfoundland, particularly at Placentia Bay. Heezen and Ewing (1952) mention the possibility that the wave may have been generated by the underwater landslide.

Striem and Miloh (1976) attribute several ancient drawdowns of sea level along the coast of Israel to underwater landslides triggered by earthquakes. These events are characterized by a recession of the sea because the landslide would head away from the coastline. Striem and Miloh (1976) extrapolated the results of Wiegel (1955) to estimate a drawdown of 10 m that would lay bare 1 km of sea floor for about one hour. A single solitary wave was assumed to have been created by the underwater landslide. A characteristic wave height was estimated by assuming that 1% of the landslide potential energy was converted into water wave energy. Striem and Miloh (1976) describe at least four historical events with such characteristics.

2.1.3 Wave Induced Landslides

Storm waves may also trigger underwater landslides, although the available evidence indicates that these events are typically smaller than those described above. The rate of sediment transport down Scripps Canyon, La Jolla, California, has been studied by Inman (1953), who documented losses of up to 9000 cubic meters of fine sand accumulated at the canyon head following a single storm event. Transport of the sediment may have been gradual or it may have involved a sequence of underwater landslide events. Even if the transport occurred mainly as a single underwater landslide, it may have been impossible to discern the waves generated by the underwater landslide from the storm waves. Regardless, the head of Scripps canyon is located a mere 300 m from the shoreline and sediment transport rates down the canyon can be quite large; the canyon walls form 20-30 degree slopes, parts of which face the shoreline. Figure 1.2 shows that the canyon walls are able to accumulate sediment that could be dislodged during an earthquake or storm.

Shepard and Dill (1966) correlate massive transport of underwater sediment with large storm swells. Greene *et al.* (1991) report that divers returning to the site of slump scarps at the head of Monterey canyon after two stormy months could no longer locate any remaining evidence of the scarps. On the other hand, Bornhold *et al.* (1994) did not discover any correlation between turbidity currents in a British Columbia fjord and storm activity.

2.2 Water Wave Generation Experiments

Almost all of the experimental work on water waves generated by underwater landslides reported to date in the literature was performed by Wiegel (1955). Exploratory work on water waves generated by slumping gravel piles and sand impounded behind a vertical gate was described by Wiegel (1955) but was discontinued in favor of solid block landslides. Wiegel (1955) generated water waves in a constant depth channel by releasing solid blocks of different sizes, shapes, and densities with some initial submergence along an incline 22°-54° from horizontal. Resistance wave gauges recorded the surface time histories at given distances down the horizontal channel. The leading wave in the far-field wave train was always found to be a positive, long wave traveling at the theoretical long wave celerity. Wiegel (1955) found that the leading wave amplitude increased with increasing block density, decreasing initial block submergence, and increasing incline angle. The typical wave period was found to increase with increasing length of the submerged block and decreasing incline angle. Immediately above the solid block landslides, a trough was measured in the free surface followed by a free surface rebound of similar magnitude. Wiegel (1955) calculated that around 1-2 per cent of the block potential energy went into wave energy. Energy conversion increased with decreasing initial submergence and decreasing channel depth.

Tsunami generation by the vertical motion of a piston initially flush with a channel of constant depth was studied experimentally and theoretically by Hammack (1972). Piston motion was controlled hydraulically and given either an exponential or a sinusoidal position *versus* time profile. Hammack (1972) found that if the piston motion was much slower than the wave propagation out of the generation region, then the wave heights measured were independent of the aspect ratio (depth to width) of the two-dimensional generation region. Nondimensional wave heights were found to depend on the inverse power of the nondimensional time of wave generation. This constituted a single

wavemaker curve for all bed motions slower than wave propagation. Since the wave amplitude was made nondimensional by the characteristic distance of bed displacement while the nondimensional time involved the characteristic time of bed motion, the wave amplitude was directly related to bed motion. Kajiura (1970) studied the same wavemaker geometry theoretically using the long wave approximation.

Prins (1958) studied experimental water waves generated by an initial rectangular elevation or depression over a region of the free surface propagating down a constant depth channel. Hammack (1971) pointed out that the initial wave profile studied by Prins (1958) would arise only through very fast vertical motion of a wavemaker body over a finite vertical distance. This implies that the time scale of wave generation would need to be much faster than the time scale of wave propagation out of the generation region for the results of Prins (1958) to apply to underwater landslides. However, water waves generated by underwater landslides are most often situated in the opposite asymptotic regime whereby water waves leave the generation region much faster than the wavemaker body moves. Since Prins (1958) studied water waves generated by a net volumetric displacement of water, solitary waves were observed to emerge from the wave train during some of the experiments. These observations apparently caused Striem and Miloh (1976) as well as Murty (1979) to confuse the leading wave in a group of linear waves (called an Airy wave herein) with a solitary wave. For a fully submerged landslide, there is no net displacement of volume.

Heinrich (1992) conducted one underwater landslide experiment with a weighted block that slid on rollers down a 45° incline. The solid block comprised a right triangle 0.5 m long on the front and top with a mass of 140 kg and a mean density of 2040 kg/m^3. The water depth in a constant depth channel was 1 m and the top of the block was initially 1 cm below the free surface when the block was released from rest. The experiment was conducted in order to validate numerical simulations.

Iwasaki (1982) measured water wave heights resulting from the transient horizontal motion of a sloping incline in a constant depth channel. The measured nondimensional maximum wave amplitudes were related to the nondimensional time of wave generation and the slope of the moving incline in the form of wavemaker curves.

2.3 Numerical Simulations of Landslide-Generated Waves

Heinrich (1992) simulated water waves generated by a solid block sliding down an incline at one end of a long, horizontal channel. The two-dimensional Navier-Stokes equations for incompressible water were approximated by a standard finite difference method incorporating a marker and cell scheme for the free surface as well as the moving solid boundaries. The code was validated by simulating a propagating solitary wave as well as the theoretical predictions of Hammack (1973) for tsunami generation. The motion of the block was simulated at each time step within the code by integrating the surface force (obtained using the free-slip boundary condition) and solving a separate equation of motion. Agreement between the experimental and simulated results is exceptional in both the near-field and for the dispersive wave train in the far-field. Heinrich (1992) also studied water waves generated by aerial landslides.

The coupling between surface waves and a deformable gravity current has been studied by Jiang and LeBlond (1992). The two-dimensional gravity current was modeled as a dense, viscous, homogeneous fluid that was immiscible with the surrounding water. No entrainment of water into the gravity current (dilution) and no deposition of suspension (sedimentation) were allowed to occur. Jiang and LeBlond (1992) assumed that a given volume of landslide fluid deformed as it slid down an inclined slope between 2-12° and onto a horizontal surface. The initial distribution of the landslide fluid on the incline was parabolic in height with the length of the parabola along the incline much larger than the water depth. The density current was assumed to be laminar despite being initially 690 m long, 24 m high, and traveling for over 4 km. The shallow water (or long wave) approximation was employed so that the vertical pressure distribution was assumed to be hydrostatic and the vertical component of the fluid velocities was assumed to vanish. This means that the surface waves generated by the landslide would not be dispersive and the triangle waves described by Whitham (1973) can be expected as an asymptotic wave form. The vertical velocity profile within the landslide fluid was assumed to be parabolic for all times and positions along the incline (with no slip along the incline and no shear between the two fluids). Based on these assumptions, an elegant finite difference scheme was developed for the shallow water wave equations coupled to conservation of landslide mass and momentum expressed by landslide height and maximum velocity. The effects of landslide density, viscosity, size, initial depth, and coupling with the surface waves were investigated. A leading positive long wave and subsequent trough above the landslide were found to have amplitudes up to 5 m on a 4° incline. A smaller trough

traveled shoreward. The energy transfer ratio from landslide potential energy into wave energy for these shallow water waves could reach instantaneous values between 5-15 per cent. More recent work by Jiang and LeBlond (1993) has incorporated a Bingham plastic constitutive relation to simulate an underwater mudslide that can solidify. Interestingly, LeBlond and Jones (1995) seem to use the previous results to discount tsunami generation by underwater landslides.

Harbitz (1992) has simulated the two-dimensional tsunamis generated by two of the three Storegga slides off of the coast of Norway. Geological evidence indicates that all three slides transported 5600 cubic kilometers of sediment along 300 km of Norwegian coastline roughly 500 km into the Norwegian sea. The average slope in the direction of the slides is currently 0.5°; the slides were probably triggered by earthquakes. All three slides occurred between 50,000 and 6,000 years ago, leaving marine sediments and taxa 4-6 m above sea level along the coasts of Scotland, Iceland, and Norway. Based on criteria given by Hammack (1973), Harbitz (1992) established that a linear, long wave momentum equation with linear, depth averaged continuity equation could describe the tsunami generation and propagation. The finite difference scheme included a recursively calculated bottom shear stress for the waves and depicted the current North sea bathymetry with a resolution of 12.5 km squares. Landslide motion along the sea bottom was prescribed by a cosine function in time, similar to the piston motion employed by Hammack (1973). The landslide was assumed to remain laminar because of the large viscosity of the dense sediment suspension comprising the gravity current. The initial acceleration of the landslide was found to strongly influence simulated wave heights. A single initial acceleration a_0=0.016 m/s^2 was chosen based on separate simulations of landslide motion *versus* time. Estimated water wave run-up values were between 5-10 m along Scotland, Iceland, and Norway. For the parameters used in the simulation, bottom shear stress between the gravity current and the water accounted for 40% of the shallow water wave generation.

Villeneuve and Savage (1993) derive a wave equation governing long wave propagation in shallow water that includes nonlinear and dispersive effects to the same perturbative order. The wave equation was then used to study water waves generated by moving beds. Five wavemaker geometries were simulated by Villeneuve and Savage (1993): a conventional piston wavemaker, horizontal motion of a submerged wedge, horizontal motion of a submerged shelf, horizontal motion of an incline, and rotation of a submerged plate. All five wavemaker geometries involved a net displacement of mass

and the appearance of solitary waves. Wave amplitudes were not studied as a function of boundary motion.

Iwasaki (1987) studied the water waves generated by an initially submerged rectangular block falling vertically in a constant depth channel. Block motion began at t=0 and proceeded at constant velocity until the block rested on the channel bottom. Water wave generation was simulated by an inviscid boundary element method code.

2.4 Soil Mechanics, Sand Piles and Natural Sediment

Underwater landslides can often be related to an increase in the sediment pore water pressure. External construction loads imposed on a sediment are initially supported by a pore water pressure increase until normally consolidated; storm waves and earthquakes can cyclically load or shear loose sediment such that grain contact can be lost and pore water pressure increased; low tides lower the sediment retaining force causing mean pore pressures deep in the sediment to become temporarily excessive. Scott (1963) describes the mechanics of soil consolidation. Terzaghi (1956) provides the basic soil stability analyses that apply to underwater landslides. Soil stability analysis is often based on a single critical friction angle beyond which failure must occur. The actual occurrence of a landslide cannot be predicted. Terzaghi (1956) observes that a metastable bank of sediment may initiate an underwater landslide through small perturbations such as mild earthquakes, local blasting operations, artesian water flow, or pile driving operations that would otherwise be incapable of causing large scale soil failure in a stable bank.

However, experiments conducted on sand pile landslides indicate that a single angle of repose may be too simplistic for geologically active regions where sediment is constantly in flux through the system. Bak (1993) considered the evolution of a sand pile as grains were continuously added at the top of the pile. By adding grains to the sand pile, local landslides occurred as the pile grew but the fundamental shape of the whole sand pile remained the same. The role of the landslides was to redistribute the sand grains in such a manner as to keep the angle of repose nearly constant. A critical state was reached whereby a lesser sand pile angle would allow the pile to become steeper while a greater angle would be subject to frequent landslides that would broaden the sand pile. According to Bak (1993), landslides have no overall scale since there is theoretically no typical landslide size for a given sand pile size. Consequently, nondimensional landslide size was related to the probability of occurrence by a simple power law relationship.

The results of Nagel (1992) and indicate that there are actually two angles of repose for a sand pile: one angle that is stable to small perturbations and another a few degrees larger that is the maximum possible angle of repose of the sand pile and leads to catastrophic landslides. The catastrophic landslide almost always spans the whole sand pile and reduces the angle of repose to near its equilibrium value. Angles in between the two critical values give rise to metastable sand piles subject to failure for sufficiently large perturbations. Hence, by steadily tilting a sand pile, Nagel (1992) obtained quasi-periodic landslides of roughly similar volume, evidence that refutes the observations of Bak (1993). The stability of a sand slope was examined using a simple heuristic model by Jaeger *et al.* (1990) in a manner that captures the two angles of repose just described. Meakin and Skjeltorp (1993) review the sand pile literature.

2.4.1 Natural Sediment Observations

Underwater canyons play an important role in redistributing natural sediment. The budget of littoral sediments off the coast of California is discussed by Komar (1976) who notes that submarine canyons are an important factor in funneling sand and sediments from near shore to deep water. Inman (1953) has performed repeated sediment surveys at the head of La Jolla canyon and provides the mean size of the fine quartz sand to be around 0.13 mm in diameter at the canyon head. Natural sorting of sediment into nearly uniform grain size appears to be a common feature of geological regions prone to underwater landslides. Shepard and Dill (1966) provide detailed qualitative descriptions of La Jolla and Scripps canyons as well as the bathymetry of these and other canyons. Shepard and Dill (1966) provide an appendix listing the physical dimensions of many submarine canyons around the world. Quadfasel *et al.* (1990) discuss underwater landslides as a means of deep-water renewal in the Sulu sea.

Side-scan sonar imagery of Kitimat Inlet, British Columbia by Prior *et al.* (1982) revealed evidence of subaqueous slides varying over several orders of magnitude in size as well as a multitude of transverse cracks and scallops in sediments along steep underwater banks with slopes of 4-10°. Sediment was estimated to accumulate at rates of between 2-5 mm/year with smaller sized sediment settling farther out in the fjord. Further evidence that underwater landslides are rather common on the banks of fjord deltas is provided by Yehle and Lemke (1972) as well as Prior *et al.* (1981), although most landslides are apparently too small, too slow or too deep to produce noticeable waves. Typically,

chutes or scallops in fjord deltas are 2-5 m deep, 10-30 m wide, and found on the front slope of the delta in 5-30 m of water along slopes inclined 11-16°. Bornhold *et al.* (1994) have studied the frequency of turbidity currents in British Columbia fjords and found roughly twenty significant events per year with no correspondence between the time of events and extreme tidal ranges. In fact, the majority of events correlated with periods of elevated river discharge although not necessarily with individual discharge peaks. In one instance, the failure of a causeway under construction at the head of an inlet a few kilometers from the detection device was not detected as a turbidity current. This shows that turbidity currents resulting from an underwater landslide do not necessarily travel many kilometers down a fjord.

Greene *et al.* (1991) document the liquefaction of an 8 km^2 layer of sediment 9-15 m under Moss Landing spit as well as the 0.3-0.65 m subsidence and 1.3 m lateral spreading of the sand spit that destroyed the Moss Landing Marine Laboratories during the Loma Prieta earthquake. The canyon head is a mere 100 m from the sand spit. Moss Landing spit had undergone liquefaction during the 1906 San Francisco earthquake and parts of Moss Landing pier have apparently been disappearing into the canyon at regular intervals in the past century.

An important conclusion drawn by Bjerrum (1971) is that an initial underwater landslide often formed a gravity current, entrained sediment, and undercut the base of a much larger underwater landslide. Hence, a relatively benign initial underwater landslide can amplify its effects to ultimately generate large water waves through secondary landslides. Terzaghi (1956) disputes this claim and proposes the slow and successive slumping of landslides observed in the Province of Zeeland of the Netherlands as a model of sediment mobility. It is quite probable that both authors are correct for different geological settings and geometrical configurations of sediment.

2.5 Underwater Landslides and Gravity Currents

Natural and experimental gravity currents are extensively reviewed by Simpson (1987). Turner (1973) proposes that two-dimensional gravity currents should spread linearly with distance and have the density fall off inversely with distance. However, Harbitz (1992) models the enormous Storrega underwater landslides as a sliding solid block while Prior *et al.* (1982) provide sonar scanning evidence that certain large portions of a landslide remain intact when sliding down a slope of 1° or less. Prior *et al.* (1982) point out that

this behavior is also observed in terrestrial landslides of weak mudflows and quick clay flowslides. Shaller (1991) describes the appearance of geological records of large landslides on earth and Mars.

2.5.1 Gravity Current Velocities

Underwater landslides in Norwegian fjords apparently resulted in gravity currents. In three cases, Bjerrum (1971) estimates that mean gravity current speeds reached 10-25 km/hr (or about 3-7 m/s) based on a succession of broken underwater cables and an anchor dragging a barge. Broken underwater cables allowed Hamilton and Wigen (1987) to calculate a gravity current velocity of 22 km/hr (or 6 m/s) along a 0.5° slope far from the original underwater landslide at the Var river delta. Based on the timing of underwater cable breakage during the 1929 Grand Banks event, Kuenen (1952) estimates that the gravity current had velocities varying between 18-108 km/hr (or 5-30 m/s). The Grand Banks underwater landslide achieved maximum speeds of around 72-108 km/hr (or 20-30 m/s) early on in the motion down steeper slopes of about 2°. Based on numerous terrestrial observations, Terzaghi (1956) proposes a maximum underwater landslide velocity of around 5-15 km/hour (or 1-5 m/s). Mechanistic interpretations of landslide run-out still involve open questions for both terrestrial and underwater landslides. There is no doubt however from observations of terrestrial landslide motion and deposition, as well as sonar observations of underwater landslide deposits, that landslide run-out can occur considerably faster and extend further than Terzaghi (1956) was willing to accept. Shaller (1991) provides a detailed review of these issues and summarizes known landslide evidence and observations.

While the existence of gravity current terminal velocity in nature has not been proven to exist, Harbitz (1992) notes that the terminal velocity of a finite mass gravity current is often scaled as

$$u_t \approx \sqrt{\frac{(\rho_s - \rho_o)\, T\, g \sin\theta}{C_d\, \rho_o}} \qquad (2.1)$$

where ρ_s is a typical suspension density and T is the landslide thickness. Harbitz (1992) suggested using a drag coefficient $C_d \approx 0.002$ for underwater landslides. With typical values for the landslide density $\rho_s \approx 1700$ kg/m^3 and slide thickness $T \approx 120$ m, the maximum velocity of the first Storegga slide was estimated to be about 35 m/s. Harbitz

(1992) treated the landslide as a solid body without entrainment. Jiang and LeBlond (1992) simulated underwater landslide velocities between 20-45 m/s on inclines from 2-12° along with typically little coupling between the landslide motion and the water waves. However, the rheology employed by Jiang and LeBlond (1992) was simplistic compared to the rheology of fine suspensions developed by Brady (1993). Moreover, the gravity current dynamics explored by Parker *et al.* (1986) were neglected. Britter and Linden (1980) have shown that a typical value of the drag coefficient in equation (2.1) is $C_d \approx 0.004$. For Reynolds numbers larger than 10^3 and for incline angles $5° < \theta < 90°$, Britter and Linden (1980) found that the front velocity of a steady turbulent gravity current was essentially independent of both the Reynolds number and the incline angle. Britter and Linden (1980) attribute the invariant front velocity to increased entrainment at steeper angles which retards the advance of the gravity current.

Chapter 3

3. Theoretical Analyses

The first goal of this chapter is to establish that a wavemaker curve exists for water waves generated by underwater landslides. The correct nondimensional construction of a wavemaker curve (yielding a characteristic wave amplitude) is found from a scaling analysis of the governing differential equations. The development assumes that the landslide center of mass motion is governed by a single characteristic length scale s_o and a single characteristic time scale t_o. An analysis of solid block motion validates this assumption and provides analytical expressions for the characteristic length scale s_o and time scale t_o. Material landslide motion is observed empirically along with rates of deformation about the center of mass motion. A linear water wave generation analysis provides approximate near-field wave amplitudes above an underwater landslide. A more involved and elaborate analysis of near-field wave generation is achieved using fully nonlinear simulations of water waves generated by underwater landslides.

3.1 Dimensional Analysis and Scaling Considerations

This section begins by assuming that underwater landslide motion can be described by only one characteristic distance s_o and one characteristic time t_o. It is therefore assumed that all other distance and time scales associated with landslide motion are either negligibly small or too large to matter. Given this assumption, the characteristic distance s_o and time t_o are then defined by the canonical equation of motion

$$\frac{s}{s_o} = f\left(\frac{t}{t_o}\right) \tag{3.1}$$

provided an explicit function $f(t/t_o)$ exists. Hammack (1972) used two bed time-displacement histories in the form of equation (3.1) in his study of tsunami generation although he defined characteristic times of motion $t_c \propto t_o$ rather than $t_c = t_o$. Given landslide motion in the form of equation (3.1) with corresponding expressions for s_o and t_o, considerable information can now be obtained from dimensional and scaling analyses of the landslide and wavemaker problems. For example, a scaling analysis of the governing differential equations yields the form of the wavemaker plot in Section 3.1.3. However, the form of equation (3.1) is valid only for landslide center of mass motion whereas landslide deformation about the center of mass introduces another (albeit larger) time scale into the problem. Even though the initial assumption strictly holds only for solid block landslides, the results of this section will guide the rest of the theoretical work in this chapter as well as the data presentation of the experimental results in Chapter 5. This section begins with the dimensional analysis of solid block landslide motion down an incline as well as near-field water wave generation. A similar analysis is applied to material landslides with the appearance of many more independent variables than for the solid block analysis. This section closes with a general scaling analysis of the governing partial differential equations.

A more precise meaning of dimensional analysis will now be given. The most commonly encountered dimensions in this work are mass, length, and time. Buckingham (1914) showed that for a dependent physical quantity Q_1 that is a function of n-1 independent physical quantities $Q_2, \ldots, Q_n$ comprising a total of j physical dimensions, the functional relation

$$Q_1 = f(Q_2, \ldots, Q_n) \tag{3.2}$$

may be substituted by an equivalent but different functional relation

$$\Pi_1 = g(\Pi_2, \ldots, \Pi_{n-j}) \tag{3.3}$$

where the n-j quantities Π_i represent independent, nondimensional groupings of the Q_i. Physical intuition and experience are important guides when choosing a list of physical quantities Q_i for dimensional analysis that is neither redundant nor missing important

physical quantities. The nondimensional numbers Π_i may represent simple geometric length ratios or well established nondimensional numbers named after famous scientists. Regardless, the end result of dimensional analysis is to reduce n dimensional parameters to n-j nondimensional numbers and thereby simplify a parametric analysis of the dependent quantity Q_1.

Scaling analysis is to be understood as something completely different from dimensional analysis, although the conclusions often appear similar. The simplest form of scaling analysis amounts to writing approximate expressions for each force relevant in a physical problem and normalizing by the dominant force to find the relative importance of the remaining forces. A list of n forces therefore results in n-1 nondimensional force ratios that are often recognized as common dimensionless numbers. A related scaling analysis can be based on other quantities such as length scales or time scales. However, a more rigorous scaling analysis involves providing a typical scale for each dependent and independent variable in a differential equation along with its initial conditions and boundary conditions. After some suitable division, one obtains a nondimensional differential equation with nondimensional initial and boundary conditions. In front of each differential term one finds nondimensional numbers that render the differential equation scale invariant when all of these numbers have identical values. Since many differential equations involve a local force balance, the two types of scaling analyses described above often produce identical nondimensional numbers and both methods will be used herein. The art in scaling analysis rests in choosing force expressions or variable scales that are representative of the particular physical problem at hand.

3.1.1 Dimensional Analysis of Solid Block Landslides

Consider a solid block landslide of size b and density ρ_b initially submerged a depth d in water along an incline of nondimensional angle θ to horizontal as shown in Figure 3.1. The solid block has a critical friction angle ψ with the incline material and therefore a nondimensional Coulombic friction coefficient $C_n=\tan\psi$. Coulombic friction can be considered to represent the choice of landslide and incline materials. A rigorous application of Buckingham's Pi theorem requires a choice of dependent variable. There are three interesting choices of dependent variable that can be made as of now: i) the characteristic length scale of landslide motion s_o, ii) the characteristic time scale of landslide motion t_o, and iii) a characteristic wave amplitude η chosen within the near-field wave generation region. The solid block landslide experiment involves up to seven

independent quantities g, d, b, ρ_b, ρ_o, θ, and ψ for each chosen dependent variable. It follows from the Pi theorem that the dependent variables can be written as unknown functions f_i

$$\frac{s_o}{b} = f_1\left(\frac{d}{b}, \frac{\rho_b}{\rho_o}, \theta, \psi\right) \tag{3.4}$$

$$t_o\sqrt{\frac{g}{b}} = f_2\left(\frac{d}{b}, \frac{\rho_b}{\rho_o}, \theta, \psi\right) \tag{3.5}$$

$$\frac{\eta}{b} = f_3\left(\frac{d}{b}, \frac{\rho_b}{\rho_o}, \theta, \psi\right) \tag{3.6}$$

of four independent nondimensional numbers, where the gravitational acceleration g enters only in equation (3.5). A five-dimensional space is needed to represent solid block trial results if these independent nondimensional numbers are utilized to characterize the trials. In general, there are too many nondimensional numbers to be presented on a single two-dimensional wavemaker plot. One is therefore motivated to consider even more powerful ways of organizing experimental results.

3.1.2 Dimensional Analysis of Granular Material Landslides

Dimensional analysis of the chosen near-field wave amplitude for a granular material landslide involves many more quantities than the previous analysis for a solid block. Even for materials with a uniform particle size, granular material landslides introduce new quantities that describe particle size, particle shape, and particle interactions. Nevertheless, the Pi theorem guarantees the existence of an unknown function giving a nondimensional wave amplitude

$$\frac{\eta}{b} = f_4\left(\frac{d}{b}, \frac{D}{b}, \frac{\rho_m}{\rho_o}, e, SF, \nu_s, \theta, \phi, \psi\right) \tag{3.7}$$

where D is the particle nominal diameter, ρ_m is the material density, e is the particle coefficient of restitution during collisions, SF is the particle shape factor, ν_s is the characteristic solid volume fraction, and ϕ is the internal friction angle of the material. In general, fluctuational quantities (such as granular temperature or slip velocities) and

additional wall properties (such as a wall coefficient of restitution) were left out of the list of quantities governing the granular material wavemaker. A more comprehensive dimensional analysis of granular material flows can be found in Savage (1992). A similar dimensional analysis of a characteristic rate of landslide deformation provides

$$\Gamma\sqrt{\frac{b}{g}} = f_5\left(\frac{d}{b}, \frac{D}{b}, \frac{\rho_m}{\rho_o}, e, SF, \nu_s, \theta, \phi, \psi\right) \tag{3.8}$$

where the rate of deformation Γ is expressed in radians per second. Due to the large number of independent nondimensional numbers, a manner of consolidating the numbers into physically relevant compound quantities is sought. Examples of useful compound quantities are provided by equations (3.4) and (3.5) above that will in turn be used in a scaling analysis of wave generation. Theoretical predictions of landslide motion down an incline and of landslide rates of deformation further legitimizes such an organizational framework.

3.1.3 Scaling Analysis of Wave Generation

In this section, the independent nondimensional numbers needed to prescribe similarity of the inviscid wave generation problem are considered. A near-field wave amplitude is chosen as dependent variable of interest. In this work, the maximum near-field wave amplitude η_{max} serves as a characteristic wave amplitude of the entire wave generation process. Other choices for a characteristic wave amplitude, such as a suitably averaged mean wave amplitude further removed from the generation region, are also possible but are not considered herein. Therefore, the scaling analysis is very general in its implications for water waves generated by submerged, unsteady objects. Water waves generated by underwater landslides are governed by the conservation of mass and momentum. In two dimensions, these conservation equations can be expressed as three partial differential equations subject to well-posed boundary conditions. The free surface is subject to the kinematic and dynamical boundary conditions. The surface of the landslide is subject to kinematic boundary conditions. For an inviscid fluid, the remaining surfaces are governed by no-flux boundary conditions. Since the dynamical free surface boundary condition is derived from the conservation of momentum, the boundary condition contributes no new information to a scaling analysis. Likewise, the landslide kinematic boundary conditions contribute no new information since the landslide motion is part of the scaling analysis.

The scaling analysis involves four differential equations. The x spatial coordinate is taken as horizontal and increasing to the right while the z spatial coordinate is taken as vertical and increasing upwards. For an incompressible liquid of uniform density, conservation of mass can be written

$$\frac{\partial u}{\partial x} + \frac{\partial v}{\partial z} = 0 \tag{3.9}$$

where u is the horizontal velocity and v is the vertical velocity. The inviscid equations of motion are given by Euler's partial differential equations

$$\frac{\partial u}{\partial t} + u\frac{\partial u}{\partial x} + v\frac{\partial u}{\partial z} + \frac{1}{\rho_o}\frac{\partial P}{\partial x} = 0 \tag{3.10}$$

$$\frac{\partial v}{\partial t} + u\frac{\partial v}{\partial x} + v\frac{\partial v}{\partial z} + \frac{1}{\rho_o}\frac{\partial P}{\partial z} + g = 0 \tag{3.11}$$

where ρ_o is the water density, g is gravitational acceleration, and P=P(x,z,t) is the static pressure field in the water. The kinematic boundary condition on the free surface $z=\eta(x,t)$ can be written

$$v = \frac{\partial \eta}{\partial t} + u\frac{\partial \eta}{\partial x} \tag{3.12}$$

which ensures that the free surface motion follows that of the water at $z=\eta(x,t)$. In order to proceed, all field variables and position coordinates need to be associated with a scale that is relevant to the wave generation process.

The scaling analysis is carried out for a solid block landslide with the initial geometry depicted in Figure 3.1. Measures of landslide size and submergence can be generalized to other geometries of interest if the need arises. The scaling relations provided immediately below apply to the motion of any submerged body that undergoes unsteady motion according to equation (3.1) and has a component of that motion in the vertical direction. The focus of the wave generation scaling is on the region immediately above the landslide and involves characteristics of the landslide motion in equations (3.4) and (3.5). The time scale of solid block motion is anticipated to be much longer than the time

scale of wave propagation out of the generation region above the block. Therefore, the equations of motion are scaled in the same manner as the "creeping" analysis of Hammack (1972). This choice in scaling analysis must be verified *a posteriori*. Nondimensional quantities are denoted by primes.

The pressure $P=\rho_o g d P'$ scales with the hydrostatic pressure at the surface of the solid block. The horizontal velocity $u=\sqrt{gd}\,u'$ scales with the initial long wave celerity $\sqrt{gd}$ above the solid block. All related wave problems scale the pressure and horizontal velocity in this manner. The time

$$t = \frac{b}{\sqrt{g\,d}}\,t' \tag{3.13}$$

scales with the characteristic time of long wave propagation over the surface of the solid block. This time scale governs wave propagation out of the generation region and is expected to be smaller than the characteristic time of solid block motion t_o. The horizontal position $x=t_o\sqrt{gd}\,x'$ scales with distance traveled by a long wave over the block during the characteristic time t_o of solid block motion. The horizontal length scale $\lambda=t_o\sqrt{gd}$ can also be considered a characteristic wavelength of the wave generation process since the leading waves leave the generation region at the local long wave celerity. The vertical position $z=dz'$ scales with the initial submergence d of the solid block. The scale of the free surface amplitude is found from conservation of volume. The top face of the solid block spans a characteristic volume $bs_o\sin\theta$ per unit width. The corresponding trough in the free surface above the solid block should have an equal volume given roughly by $\lambda H/2$ per unit width, where H is the wave height and λ is the characteristic wavelength. Solving for the characteristic wave amplitude H/2 yields

$$\eta = \frac{H}{2}\,\eta' = \frac{b\,s_o \sin\theta}{t_o\sqrt{g\,d}}\,\eta' \tag{3.14}$$

which scales with the component of the characteristic distance s_o in the vertical direction. It is important that the wave amplitude depend on the motion of the solid block since this is the source of wave generation. Last of all, the vertical velocity $v=s_o\sin\theta v'/t_o$ scales with the vertical component of the characteristic solid block velocity s_o/t_o. Note that the x and z directions must scale differently for the scaling analysis to capture the wave

generation properly: the x-direction always scales with water wave features while the z-direction always scales with underwater landslide features.

Having proposed scales for each field variable and the position coordinates, these need to be inserted into the four partial differential equations (3.9) to (3.12). Upon insertion of the scaled variables, the conservation of mass gives

$$\frac{\partial u'}{\partial x'} + \frac{s_o \sin\theta}{d} \frac{\partial v'}{\partial z'} = 0 \tag{3.15}$$

while the nondimensional Euler equations become

$$\frac{\partial u'}{\partial t'} + \frac{b}{t_o \sqrt{g\,d}}\, u' \frac{\partial u'}{\partial x'} + \frac{b\, s_o \sin\theta}{t_o\, d \sqrt{g\,d}}\, v' \frac{\partial u'}{\partial z'} + \\ + \frac{b}{t_o \sqrt{g\,d}} \frac{\partial P'}{\partial x'} = 0 \tag{3.16}$$

$$\frac{\partial v'}{\partial t'} + \frac{b}{t_o \sqrt{g\,d}}\, u' \frac{\partial v'}{\partial x'} + \frac{b\, s_o \sin\theta}{t_o\, d \sqrt{g\,d}}\, v' \frac{\partial v'}{\partial z'} + \\ + \frac{g\, b\, t_o}{s_o \sin\theta \sqrt{g\,d}} \left[\frac{\partial P'}{\partial z'} + 1 \right] = 0 \tag{3.17}$$

and the nondimensional kinematic surface boundary condition yields

$$v' = \frac{\partial \eta'}{\partial t'} + \frac{b}{t_o \sqrt{g\,d}}\, u' \frac{\partial \eta'}{\partial x'} \,. \tag{3.18}$$

In the limit as $\theta \to 0$, the long wave equations are recovered. This is another reason for including the sine of the incline angle. Following Hammack (1972), the nondimensional coefficients in front of the differentials can be broken into four basic nondimensional groups

$$\Pi_1 = \frac{b}{d} \,,\ \Pi_2 = \theta \,,\ \Pi_3 = t_o \sqrt{\frac{g}{d}} \,,\ \Pi_4 = \frac{s_o}{d} \tag{3.19}$$

where Π_1 is a geometric length ratio, Π_2 is the geometric angle of the incline, Π_3 is a typical expression of nondimensional time for wave problems, and Π_4 scales the characteristic distance of landslide motion with the other two length scales. For the chosen landslide configuration, there are two nondimensional numbers governing geometric similarity and two nondimensional numbers governing dynamic similitude. Wave generation problems are similar when all four nondimensional numbers Π_i are identical. Equations (3.19) form the essential components of Hammack's (1972) wavemaker formalism arrived at through scaling of the governing differential equations and boundary conditions.

It is advantageous to consider aggregates of the basic nondimensional groupings in equations (3.19) in order to arrive at simpler physical interpretations of the connections between landslide motion and wave generation. Dynamic similitude of the wave generation problem also results if the two nondimensional numbers

$$Sg \equiv \Pi_4 \sin \Pi_2 = \frac{s_o \sin \theta}{d} \quad , \quad Ha_o \equiv \frac{\Pi_3}{\Pi_1} = \frac{t_o \sqrt{g\, d}}{b} \tag{3.20}$$

are identical. Geometric similarity still requires identical values of Π_1 and Π_2. The Submergence number Sg is the ratio of the vertical length scale of wave generation to the initial landslide submergence. When scaling an underwater landslide, the characteristic length of the landslide motion s_o must therefore scale with all other length scales. The Hammack number Ha_o is the ratio of the time scale of wave generation to the time it takes waves to leave the generation region. The subscript for Ha_o denotes the characteristic time $t=t_o$ since the Hammack number also serves as a nondimensional wavemaker time as shown in equations (3.31) and (3.97) below and in Section 5.2.1. The two nondimensional numbers Sg and Ha_o can substitute for the two nondimensional quantities Π_3 and Π_4. A characteristic near-field wave amplitude can therefore be considered as a function of the four nondimensional numbers

$$\frac{\eta}{s_o \sin \theta} = \frac{1}{Ha_o} f\left(\frac{b}{d}, \theta, Sg, Ha_o\right) \tag{3.21}$$

where there is no Reynolds number because viscosity has been neglected. Equation (3.21) is clearly analogous to equation (3.6) despite the superficial differences. The importance of the landslide dynamics in the wave generation problem are highlighted by

the use of t_o and s_o in the scaling analysis since the characteristics of wave generation must depend on the solid block motion. Values for t_o and s_o are found in Section 3.2.1 below when analyzing solid block dynamics.

The inverse of the Hammack number Ha_o appears in front of the nonlinear terms in equations (3.16) to (3.18). Hence, in the limit

$$Ha_o \rightarrow \infty \tag{3.22}$$

the governing differential equations and boundary conditions all become linear in the first approximation. The additional condition

$$\frac{Sg}{Ha_o} \rightarrow 0 \tag{3.23}$$

must be made in order to ensure that the Submergence number Sg remains bounded. Only when $Ha_o \gg Sg$ are all nonlinear terms guaranteed to vanish. If it is established that a given underwater landslide generates linear water waves, then the generic water wave integral solution

$$\eta(x,t) = \frac{H}{2\pi} \int_{-\infty}^{\infty} f(\kappa) \exp(i \kappa x - i \omega(\kappa) t)\, d\kappa \tag{3.24}$$

can describe wave propagation, where the dimensionless expression $f(\kappa)d\kappa$ implicitly contains all of the necessary geometrical information about the waves. Therefore, any characteristic wave amplitude in the wave basin is linearly related to all other characteristic wave amplitudes through the wave height H.

The Froude number Fr is a familiar nondimensional number where Fr^2 is proportional to the ratio of inertial to gravitational forces. Since this nondimensional number is usually associated with the gravitational term in Euler's equations, it follows that

$$\frac{1}{Fr^2} = \frac{g\, b\, t_o}{s_o \sin\theta \sqrt{g\, d}} \tag{3.25}$$

where one finds after multiplying by the Hammack number Ha_o a new nondimensional group $gt_o^2/s_o\sin\theta$. Hence, given geometric similarity, underwater landslides are similar only if their initial accelerations are identical. The usual Froude scaling of water waves is recovered such that all lengths change by the same scale factor while the time changes by the square root of the scale factor. Hughes (1993) shows that this must be the case for Euler's equations on dimensional grounds even if the scaling analysis fails to recover the usual forms of the nondimensional numbers.

A short digression into the viscous effects experienced by underwater landslides is in order here. In Figure 1.3, a starting vortex was shown to exist behind solid block landslides. Separation of the flow near the landslide vertex would not occur in an inviscid fluid. The forces associated with the vortex is examined in section 3.2.1.1 below. The underwater landslides studied in this work rapidly achieved Reynolds numbers based on instantaneous landslide velocity u(t) and landslide size b on the order of Re≈50,000. Therefore, a boundary layer rapidly forms around landslides and contributes to drag. Skin friction contributions to landslide drag is shown to be negligible in section 3.2.1.3 below. There remains the question of what Reynolds number one obtains from performing the scaling analysis on the Navier-Stokes equations rather than Euler's equations. One new nondimensional grouping is found

$$\mathrm{Re} = \frac{b\sqrt{g\,d}}{\nu_o} \tag{3.26}$$

where the long wave celerity $\sqrt{gd}$ plays the customary role of a velocity. For most underwater landslides studied herein, the Reynolds number given by equation (3.26) is on the order of $\mathrm{Re}\approx 10^5$.

Some significant simplifications can be expected in equation (3.21) based on wavemaker theory and previous experimental results. Hammack (1972) considered the generation and propagation of linear and nonlinear water waves by the vertical motion of a horizontal piston initially flush with a constant depth channel. Hammack (1972) showed that Ha_o is the only dynamical number relevant for linear wavemaker problems. That is, the Submergence number Sg does not appear in a linear wave solution analogous to equation (3.24). A linear wavemaker analysis in Section 3.3 also shows that Ha_o is the only dynamical number relevant to wave generation. Hence, linear wave amplitudes near the underwater landslide have the general functional form

$$\frac{\eta}{s_o \sin\theta} = \frac{1}{Ha_o} f\left(\frac{b}{d}, \theta, Ha_o\right) . \tag{3.27}$$

When the angle θ=45° is fixed, only two independent nondimensional numbers remain in the wavemaker problem. The condition $Ha_o \gg 1$ given by equation (3.22) will be met whenever the nondimensional initial submergence d/b is much larger than

$$\frac{d}{b} \gg \frac{b}{g t_o^2} \tag{3.28}$$

where $b/gt_o^2 \approx 0.1$ for most landslides studied herein. Smaller Hammack numbers are therefore associated with smaller initial submergences. If equation (3.28) is satisfied, then strongly nonlinear phenomena such as bores and wave breaking should be absent from wave generation and propagation. As the initial solid block submergence approaches zero, $Ha_o < 1$ and surface waves are unable to escape the wave generation region faster than the solid block motion. The result is a dramatic change in wave generation above the solid block: a water bore propagates shoreward over the block and is sometimes followed by a reflected wave that becomes a plunging breaker. At laboratory scales, these nonlinear phenomena are subject to surface tension, viscous, and air entrainment scale effects. Therefore, breaking waves were not studied in this work. This experimental study has been limited to cases where $Ha_o > 2$.

There are two general features of the wavemaker curves found by Hammack (1972) that appear in this work too. For a given wavemaker geometry, Hammack (1972) found a power law relation for the characteristic wave amplitude as a function of the Hammack number Ha_o. This first feature of the wavemaker curve is valid in the region $Ha_o \gg 1$ that in general corresponds to linear wave generation. In this work, the power law relation

$$\frac{\eta}{s_o \sin\theta} = \frac{k}{Ha_o^n} \tag{3.29}$$

is fit to experimental data, where the constant coefficient k and the exponent n depend on the nondimensional geometric quantities the initial submergence d/b and the incline angle θ. As the Hammack number decreases, the time scale for waves to leave the generation region approaches the time scale of landslide motion. Therefore, the second general

feature of the wavemaker curve is that the power law relation in equation (3.29) can be expected to break down near some minimum Hammack number $Ha_{o.min}$ on the order of unity. The wave amplitude data still constitute a wavemaker curve although the power law description of the curve in equation (3.29) ceases to be valid below $Ha_{o.min}$.

Hammack (1996) has noted the implicit use of the Hammack number in certain long wave generation problems. Following Hammack (1996), consider a piston wavemaker oscillating with stroke s_o=S and period t_o=T in shallow water of depth h. The wave height H can be written in nondimensional form as

$$\frac{H}{S} \approx \kappa h \tag{3.30}$$

where the wavenumber is $\kappa=2\pi/\lambda$ and the wavelength is $\lambda=T\sqrt{gh}$. It follows immediately that

$$\frac{H}{S} \approx \frac{2\pi h}{T\sqrt{g h}} = \frac{2\pi}{Ha} \tag{3.31}$$

where the vertical water depth h plays the same role as the horizontal extent of the wavemaker b above. Hence, the Hammack number, as opposed to the Froude number, governs other wavemaker problems as well. Moreover, equation (3.31) reveals that, in this simple horizontal wavemaker example, the Hammack number becomes the customary nondimensional time $T\sqrt{g/h}$ since the water depth and the extent of the wavemaker are identical. The Hammack number in equation (3.31) therefore reduces to a conventional expression of nondimensional time solely because of the simple wavemaker geometry. This very fact has been noted by Iwasaki (1982), who considers the correct nondimensional time scales for three related wavemaker problems, including a piston wavemaker. It therefore appears that the Hammack number is a general expression of nondimensional time for wavemaker problems.

The Hammack number is an important nondimensional quantity that governs wave generation processes. The name is given to the nondimensional number for the first time in this thesis. The Hammack number first appeared in its present form in Kajiura (1970) from a long wave analysis of water waves generated by vertical piston motion in a constant depth channel. The relevance of Ha_o to water waves generated by underwater landslides was pointed out by Hammack (1971) in a discussion of Wiegel *et al.* (1970).

A complete scaling analysis was then developed in Hammack (1972) and published in Hammack (1973) for the case of tsunamis generated by vertical piston motion in a constant depth channel. Three Hammack numbers appear explicitly for the three wavemaker problems considered by Iwasaki (1982): vertical motion of a piston in a constant depth channel, horizontal motion of a piston wavemaker, and horizontal motion of a sloping wall. Iwasaki (1982) shows that long wave generation for all three wavemaker problems can be reduced to a single equation with different but related definitions of characteristic quantities.

3.2 Theoretical Landslide Dynamics and Kinematics

The characteristic time t_o and distance s_o of the solid block motion have already been shown to be useful for scaling water waves generated by underwater landslides. However, the theoretical waves community has traditionally considered wave generation and wave propagation separately. For most theoretical wave propagation problems, either an initial wave amplitude or wave impulse profile is used as the input for an analytical solution. Here, the wave amplitude profile needed to consider wave propagation is derived from the solid block motion during wave generation and therefore the two aspects of the water waves cannot be separated in the near-field. Many authors studying wave propagation assume that one or the other profile is known and proceed with the analysis. A rather forthright paper is that of Noda (1970), who comments that "the dynamics of the landslide motion are not considered" and are assumed to be known. In order to study the motion of the solid blocks, straightforward analytical solutions of a plausible equation of motion are sought. The characteristic time t_o and distance s_o emerge from the final model of solid block motion. A model of material landslide deformation is then proposed at the end of this section.

3.2.1 Solid Block Landslide Theory

Consider a solid block of known dimensions and mass instantaneously released from rest along a straight underwater incline. The solid block inertia is acted upon by a sum of at least six distinct external forces with components parallel to the incline. One can write

$$m_b \frac{d^2 s}{dt^2} = F_A + F_g + F_b + F_n + F_d + F_f \tag{3.32}$$

where F_A is the added mass force, F_g is the component of the gravitational force acting along the incline, F_b is the buoyancy force acting along the incline, F_n is the dynamic friction force between the block and the incline, F_d is the drag force induced by the water, F_f is the force associated with lubrication drag. Dynamic friction and lubrication forces can exist simultaneously because of imperfections in the solid block bottom.

The inertial and added mass forces both depend on the instantaneous solid block acceleration a(t). A known added mass coefficient C_m is assumed to characterize the added mass force. The gravitational, buoyancy, and Coulombic friction forces are assumed to be constant in time. The Coulombic friction coefficient C_n between solid block and incline materials is assumed to be a known constant independent of block position or velocity. The drag force can be separated conceptually into three distinct forces: i) the steady state form drag F_d resulting from the skin friction and the pressure distribution on the surface of the solid block long after reaching terminal velocity, ii) the unsteady drag force F_v induced by the starting vortex, and iii) the unsteady Basset drag F_B induced by diffusion of the viscous boundary layers during solid block acceleration. Form drag depends on the instantaneous block velocity u(t) squared and be characterized by a drag coefficient C_d. Lubrication along the bottom of the solid block retards motion according to the first power of the solid block velocity u(t), a lubrication coefficient C_f, and a mean gap height h_o between the incline and the bottom of the block. The motion of the solid block is assumed to be well characterized by four constant dynamical coefficients C_m, C_n, C_d, and C_f. Of these four coefficients, the lubrication coefficient C_f and the mean gap height h_o are not known *a priori*, so the importance of the lubrication force cannot be gauged in advance. However, the starting vortex and Basset forces are easily shown to be negligible.

3.2.1.1 Scaling Analyses of Two Unsteady Drag Forces

Equation (3.32) contains two drag forces that arise due to unsteady fluid dynamics. Scaling analyses show that the starting vortex induced by the motion of the solid block can be neglected in a force balance and that the diffusion of vorticity leads to a negligible Basset or "history" drag term. The strength of the vorticity sheet separated from the block apex can be approximated as

$$\frac{d\Gamma}{dt} \approx \frac{u^2}{2} = \frac{a_o^2 t^2}{2} \tag{3.33}$$

where the instantaneous velocity is $u \approx a_o t$ for short times $t \approx 0^+$ and Γ is the circulation shed by the solid block apex. Integrating equation (3.33) provides an estimate of the vortex strength in time by assuming that all circulation is immediately fed into the vortex core located near the initial position of the solid block apex s=0. The velocity induced by this vortex and its image on the surface of the solid block is roughly

$$u_V \approx \frac{\Gamma}{\pi r} = \frac{a_o^2 t^3}{6 \pi r} = \frac{\sqrt{2}}{3 \pi} u \tag{3.34}$$

where $r=s/\sqrt{2}$ is the shortest distance from the vortex to the solid block for an incline at $\theta=45^\circ$ and $s \approx a_o t^2/2$ for short times. The dynamic pressure associated with the velocity scale u_V acts over the downstream surface area A=bw and induces an additional drag force on the solid block. The component of the vortex drag force opposing motion down the incline is approximately

$$F_V \approx \frac{\rho_o u_V^2}{2} \frac{b w}{\sqrt{2}} = \frac{2}{9 \pi^2} \frac{\rho_o u^2}{2} \frac{b w}{\sqrt{2}} \tag{3.35}$$

which acts like an additional drag force with drag coefficient $C_d=2/9\pi^2 \approx 0.023$. Clearly, this drag coefficient is negligible when compared to the drag coefficient on the order of unity ordinarily experienced by the solid block because of form drag. For short times, the Basset force scales like

$$F_B \approx m_o a_o \sqrt{\frac{\nu_o t}{2 A}} \tag{3.36}$$

where $\nu_o \approx 10^{-6}$ m^2/s is the kinematic viscosity of water, m_o is the mass of displaced water, and A=bw as before. Even after one full second, $F_B \approx 5 \times 10^{-3}$ N which can be neglected given that gravitational forcing is constant and on the order of 1 N in magnitude for all solid blocks studied herein.

3.2.1.2 General Analysis of Solid Block Motion

Equation (3.32) is an ordinary differential equation that governs solid block motion. Given the information regarding each force in Section 3.2.1, it is possible to solve the differential equation in a compact form prior to modeling the remaining six forces on the

right hand side of equation (3.32). One must assume for now that the dynamical coefficients are constant and divide through the differential equation by the parameters in front of the solid block acceleration. The equation of motion expressed in the coordinate s along the incline can be approximated with three positive, constant coefficients k_1, k_2, and k_3 in the form

$$\frac{d^2s}{dt^2} \equiv \frac{du}{dt} = k_1 - k_2\, u - k_3\, u^2 \equiv$$

$$\equiv -k_3\,(u - A)\,(u + B) = P(u) \tag{3.37}$$

with initial conditions s=0 and u=0 at t=0, and where A, B are known roots of the quadratic right hand side with B>A>0. Note that A is not used to represent area in this section. Three cases are considered in this section: the case where $k_2 \neq 0$ and $k_3 \neq 0$, the case where $k_3=0$, and the case where $k_2=0$. These three cases correspond to i) all of the forces remaining in equation (3.37) being significant, ii) negligible form drag, and iii) negligible lubrication, respectively. The point of the exercise is to show that the polynomial in velocity P(u) on the right hand side of equation (3.37) yields solutions with very similar properties. Once the importance of lubrication is ascertained, then a particular case can be chosen to study actual block motion. The constant coefficient k_3 is given by

$$k_3 = \frac{C_d\, \rho_o\, \ell\, w \cos\theta \sin\theta}{2\,(m_b + C_m\, m_o)} \tag{3.38}$$

where k_3 represents the constant quantities of the drag force divided by the constant quantities from the inertial and added mass forces. The values of the characteristic velocities A and B are readily found from the following two expressions

$$k_1 \equiv k_3\, A\, B = \frac{(m_b - m_o)\, g\, (\sin\theta - C_n \cos\theta)}{m_b + C_m\, m_o} \tag{3.39}$$

$$k_2 \equiv k_3\,(B - A) = \frac{C_f\, \mu_o\, \ell\, w}{h_o\,(m_b + C_m\, m_o)} \tag{3.40}$$

where k_1 represents the constant gravitational, buoyancy and dynamic friction forces while k_2 represents the constant quantities of the lubrication force both divided by the

constant quantities from the inertial and added mass forces. Equations (3.39) and (3.40) can be inverted to obtain the quadratic expressions for the velocities A and B

$$A^2 + \frac{2\,C_f\,\mu_o}{h_o\,C_d\,\rho_o\cos\theta\sin\theta}\,A - \frac{2\,(m_b - m_o)\,g\,(\sin\theta - C_n\cos\theta)}{C_d\,\rho_o\,\ell\,w\cos\theta\sin\theta} = 0 \qquad (3.41)$$

$$B^2 - \frac{2\,C_f\,\mu_o}{h_o\,C_d\,\rho_o\cos\theta\sin\theta}\,B - \frac{2\,(m_b - m_o)\,g\,(\sin\theta - C_n\cos\theta)}{C_d\,\rho_o\,\ell\,w\cos\theta\sin\theta} = 0 \qquad (3.42)$$

where the positive root is understood otherwise.

It is most efficient to consider first the general nonlinear, autonomous, ordinary differential equation and then study specific cases. For example, the initial acceleration of the block will always be $a_o=k_1$ since the block starts from rest with u=0. The initial acceleration of the block will always be positive ($k_1>0$) provided that the density of the block is greater than that of the surrounding medium (tap water herein). This definition of a positive acceleration implies that s increases going down the incline as shown in Figure 3.1. Solving equation (3.37) with a regular Taylor series about t=0 shows that the three cases all have solutions of the form

$$s(t) = \frac{k_1}{2}\,t^2 + \frac{k_1\,k_2}{6}\,t^3 + \frac{k_1\,k_2^2 + 2\,k_3\,k_1^2}{24}\,t^4 + \ldots \qquad (3.43)$$

where $k_1\neq0$ since u=0 would become a stationary point of the differential equation and no motion would occur given the initial conditions. If $k_2\neq0$, then the time at which the second term becomes important in the Taylor series is

$$t \approx \frac{3}{k_2} \qquad (3.44)$$

whereas, if $k_2=0$, then the series consists of powers in t^2 and the second term becomes important around

$$t \approx \sqrt{\frac{6}{k_1\,k_3}}\,. \qquad (3.45)$$

The time scales provided by equations (3.44) and (3.45) indicate the approximate duration of quadratic acceleration for the purpose of curve fitting the early motion of the

solid block with a parabola. These time scales are also proportional to the characteristic time scale of motion t_o as will be seen in the following three sections. Another general fact that follows from the differential equation is that a terminal velocity $u_t=A$ is approached exponentially as $t->\infty$ since $u=A$ is the only stable stationary solution of the differential equation (with $u>0$). Solid block position as a function of time is depicted in Figure 3.2.

3.2.1.2.1 Case One of Solid Block Motion

The first case is a general solution of the differential equation (3.37) with the specification that $k_2 \neq 0$ and $k_3 \neq 0$. The differential equation is separable and is readily integrated using the method of partial fractions. The first integration (that satisfies the initial condition $u=0$ at $t=0$) yields

$$u(t) = \frac{ds(t)}{dt} = \frac{A\,B\left[1 - \exp(-k_2\,t)\right]}{B + A\exp(-k_2\,t)} \tag{3.46}$$

where the approach to the terminal velocity $u_t=A$ is seen to be exponential in time. Defining a new independent variable

$$m \equiv \exp(-k_2\,t) \tag{3.47}$$

allows the second integration to be performed, once again using the method of partial fractions. Requiring $s=0$ at $t=0$, the position *versus* time curve of solid block motion is

$$s(t) = A\,t - \frac{A+B}{k_2}\ln(A+B) + \frac{A+B}{k_2}\ln\left[A\exp(-k_2\,t) + B\right] \tag{3.48}$$

which for $t \approx 0^+$ does indeed behave as an initial acceleration $a_o=k_1$ of the solid block. The characteristic distance of solid block motion

$$s_o = \frac{A+B}{k_2} \tag{3.49}$$

is the distance used to render $s(t)$ nondimensional. The characteristic time of solid block motion $t_o=1/k_2$ resides in the exponential function and at $t \approx 4t_o$ the instantaneous block velocity $u(t)$ has reached approximately 99% of its terminal velocity. As the exponential

function vanishes for $t>4t_o$, the asymptotic position *versus* time of the block becomes linear

$$s(t: t>4t_o) \approx u_t\, t + s* \tag{3.50}$$

where this line misses the origin s=0 at t=0 as indicated in Figure 3.2. According to the linear asymptotic motion $s(t: t>4t_o)$, the false origin of the linear motion at t=0 was the negative position

$$s* = -\frac{A+B}{k_2} \ln\left(\frac{A+B}{B}\right) = -s_o \ln\left(\frac{A+B}{B}\right) \tag{3.51}$$

which is always proportional to the characteristic distance of motion s_o. The asymptote reaches s=0 at a time

$$t* \equiv -\frac{s*}{u_t} = \frac{A+B}{A\,k_2} \ln\left(\frac{A+B}{B}\right) = t_o \frac{A+B}{A} \ln\left(\frac{A+B}{B}\right) \tag{3.52}$$

which is always proportional to the characteristic time of motion t_o. By definition, the terminal velocity is $u_t \equiv s*/t*$ so that it is always be proportional to s_o/t_o. Therefore, it seems logical to define a nondimensional terminal velocity

$$u_{nd} \equiv \frac{u_t\, t_o}{s_o} = \frac{A}{A+B} \tag{3.53}$$

as well as a nondimensional initial acceleration

$$a_{nd} \equiv \frac{a_o\, t_o^2}{s_o} = \frac{A\,B}{B^2 - A^2} \tag{3.54}$$

which are naturally constant for a given solid block.

3.2.1.2.2 Case Two of Solid Block Motion

The second case involves solid block motion with negligible form drag when compared with lubrication. It is interesting to observe that the general scaling relations found immediately above also hold true here. In this case $k_3 \approx 0$ and equation (3.37) is easily integrated to obtain

$$u(t) = \frac{ds(t)}{dt} = \frac{k_1}{k_2}\left[1 - \exp(-k_2\, t)\right] \tag{3.55}$$

which obviously approaches the terminal velocity $u_t=k_1/k_2$ exponentially with a characteristic time $t_o=1/k_2$. The position of the solid block *versus* time is

$$s(t) = \frac{k_1}{k_2}\, t + \frac{k_1}{k_2^2}\left[\exp(-k_2\, t) - 1\right] \tag{3.56}$$

which has a characteristic distance $s_o=k_1/k_2^2$. For large times, the solid block motion can be considered a straight line that passed through $s*=-k_1/k_2^2=-s_o$ at $t=0$. Alternatively, the asymptote of the large time motion passes through $s=0$ at $t*=-s*/u_t=s_o/u_t=1/k_2=t_o$ which is coincidentally the characteristic time of motion. As a result, the nondimensional terminal velocity is always $u_{nd}=1$ and the nondimensional initial acceleration is always $a_{nd}=1$ regardless of the dynamical coefficients and of the particular solid block.

3.2.1.2.3 Case Three of Solid Block Motion

For the third case, if lubrication forces are in turn negligible, then $k_2\approx 0$ and it follows that $A=B$ and $k_1=A^2k_3$. The terminal velocity in this case must be written

$$u_t = A = \sqrt{\frac{k_1}{k_3}}\ . \tag{3.57}$$

Instead of using partial fractions here, it is advantageous to recognize the differential of the inverse hyperbolic tangent function. The solution for the velocity is

$$u(t) = \frac{ds(t)}{dt} = A \tanh(A\, k_3\, t) \tag{3.58}$$

which approaches the terminal velocity exponentially as $t->\infty$ based on the definition of the hyperbolic tangent and geometric series. The characteristic time of motion is $t_o=1/Ak_3$ for this case. The position *versus* time curve satisfying the initial conditions is

$$s(t) = \frac{1}{k_3}\ln\left[\cosh(A\, k_3\, t)\right] \tag{3.59}$$

which represents the natural logarithm of the hyperbolic cosine. Clearly, the characteristic distance is given by $s_o=1/k_3$. By eliminating the exponentially small term in the hyperbolic cosine, the virtual origin of the asymptotic motion is found to be

$$s* = -\frac{\ln 2}{k_3} = -s_o \ln 2 \tag{3.60}$$

and the axis s=0 is crossed at time

$$t* \equiv -\frac{s*}{u_t} = \frac{\ln 2}{A\,k_3} = t_o \ln 2 \ . \tag{3.61}$$

The nondimensional terminal velocity is $u_{nd}=1$ while the nondimensional initial acceleration is $a_{nd}=1$ which are once again both independent of the dynamical coefficients and of the particular solid block. Apparently, the nondimensional quantities u_{nd} and a_{nd} become complicated only when there are two competing retarding forces. This completes the study of the three cases.

3.2.1.3 Lubrication and Solid Block Motion

A scaling analysis is now performed that compares the magnitude of the lubrication force to that of the form drag force for a solid block sliding down an incline. The roughness and irregularities on the bottom of all four blocks are approximately $h\approx0.1$ mm in height. Imperfections on the solid block bottom enable both Coulombic friction and lubrication forces to exist simultaneously although the usual normal force of the block on the incline may be reduced or increased. In addition, construction of the incline left regions that are a fraction of a millimeter above or below a mean straight line in waves of wavelength $\lambda\approx\ell$. The combination of block imperfections and incline waviness enables some degree of lubrication between block and incline to occur. Consider a solid block with a typical length $\ell\approx0.1$ m along the bottom and a typical terminal velocity $u_t\approx0.5$ m/s. Inertial terms may be neglected during lubrication if

$$\frac{\rho_o\, u_t\, \ell}{\mu_o}\,\frac{h^2}{\ell^2} \approx 0.05 \ll 1 \tag{3.62}$$

where $\rho_o\approx1000$ kg/m^3 is the density and $\mu_o\approx10^{-3}$ kg/m·s is the dynamic viscosity of water used in this section. In Section 3.2.1.2 it was shown that $u_t=A$ while equation (3.57)

shows that the terminal velocity A scales with the square root of the solid block length $\ell^{1/2}$. Therefore, equation (3.62) scales with $\ell^{-1/2}$ and larger landslides have increasingly negligible inertial terms. The fluid flow can be considered quasi-steady if

$$\frac{\rho_o a_o h^2}{\mu_o u_t} \approx 0.04 \ll 1 \tag{3.63}$$

where $a_o \approx 2$ m/s^2. The initial acceleration is size invariant and depends primarily on the landslide density. Therefore, equation (3.63) also scales with $\ell^{-1/2}$ so that larger landslides have increasingly quasi-steady flows. Under these conditions, consider the flow in the gap as a general Couette-Poiseuille flow with the top wall traveling to the left at the instantaneous block velocity u(t). This is the reverse of the usual perspective where the solid block is sliding down to the right and is obtained from the simple transformation u(t)->-u(t). The gap height between the solid block and the incline can be approximated as a straight line in a local coordinate system traveling with the block

$$h(x) \approx h_L + (h_R - h_L)\frac{x}{\ell} \tag{3.64}$$

where h_L is the gap on the left (or front) of the block, h_R is the gap on the right (or rear) of the block, and the case $h_L > h_R$ is considered -- the flow is reversible so that the pressure merely changes sign if $h_R > h_L$. For a linear gap height, White (1991) provides the nondimensional pressure supporting the solid block and driving the Poiseuille flow as

$$K\left(\frac{x}{\ell}\right) \equiv \frac{\Delta P\, h_L^2}{\mu_o\, u\, \ell} = \frac{6\,\frac{x}{\ell}\left(1-\frac{x}{\ell}\right)\left(1-\frac{h_L}{h_R}\right)}{\left(1+\frac{h_L}{h_R}\right)\left[1-\left(1-\frac{h_L}{h_R}\right)\frac{x}{\ell}\right]^2} \tag{3.65}$$

where $\Delta P = P(x) - P_\infty$ is the local pressure difference. The pressure difference is assumed to vanish at both ends of the solid block whereas it vanishes identically when $h_L = h_R$. In reality, there may persist a pressure difference in the wake of the solid block on the order of 100 Pa due to the separation of a streaming flow with $u_t \approx 0.5$ m/s. A typical value of $\Delta h \equiv h_L - h_R$ for a solid block on the incline is $\Delta h \approx h_R \approx 0.1$ mm from imperfections in the PVC laminates so that $h_R/h_L \approx 0.5$. For $h_R/h_L \approx 0.5$, the maximum nondimensional pressure $K_{max} \approx 1$ occurs close to $x/\ell = 0.7$. For $h_R/h_L \approx 0.9$, the pressure difference is almost parabolic with the maximum nondimensional pressure $K_{max} \approx 0.1$ occurring near

$x/\ell=0.5$ and little lubrication actually occurs. White (1991) provides further plots of K(x) as a function of h_R/h_L.

The nondimensional pressure difference K(x) can be used to estimate the mean gap height needed to support the solid block, or to calculate the shear force incurred by lubrication. The normal force exerted by a typical buoyant solid block on the incline is about N≈2.5 N in water. If the pressure rise within the gap is assumed to be purely parabolic, then the maximum pressure difference needed to support the solid block is

$$\Delta P_{max} \approx \frac{3\,N}{\ell\,w} = 750\ Pa \tag{3.66}$$

where $A=\ell w$ is the bottom area of the block. Equation (3.66) scales with length of the landslide since the submerged weight depends on the landslide volume for a given solid block density. One can use the condition N=0 to calculate the maximum possible lubrication force acting on the solid block. When N=0, there is also no dynamic friction force acting on the solid block. Using a typical value of $K_{max}\approx 1$ that follows from $h_R/h_L\approx 0.5$, the value of h_L needed to support the solid block at terminal velocity is

$$h_L \approx \sqrt{\frac{K_{max}\,\mu_o\,u_t\,\ell}{\Delta P_{max}}} = 0.26\ mm \tag{3.67}$$

whereby $h_R\approx 0.13$ mm, which is in close agreement with the roughness and irregularities of the solid block surface. Therefore, the gap height described by equation (3.64) is plausible and a block may indeed experience no normal force to the incline. Equation (3.67) shows that the lubrication gap height must grow proportional to $\ell^{1/4}$ in order to support larger landslides.

The shear stress incurred by lubrication is comprised of a Couette shear stress superposed with a Poiseuille shear stress induced by the pressure difference ΔP. The contribution of the Poiseuille flow to the rate of strain vanishes identically when averaged over the length of the solid block. Define $h_o\equiv(h_L+h_R)/2$ as a mean gap height and a characteristic height of the block above the incline, where $h_o=3h_R/2$ when $h_L=2h_R$. Averaging the Couette flow rate of strain over the block length (using equation (3.64) for the linear gap height) yields

$$\frac{\partial u}{\partial n} = \frac{u}{\Delta h} \ln\left(\frac{h_L}{h_R}\right) = \frac{u \ln 2}{\Delta h} \approx \frac{u}{h_o} \tag{3.68}$$

for $h_R/h_L \approx 0.5$ and where $\Delta h/\ln(2) \approx 3h_R/2 = h_o$ are numerically similar expressions of a mean gap height given that $\Delta h \equiv h_L - h_R \approx h_R \approx 0.1$ mm. The maximum possible lubrication force is therefore

$$F_{f.max} \approx \frac{C_f \mu_o u w \ell}{h_o} \tag{3.69}$$

where $C_f \approx 1$ for $\Delta h \equiv h_L - h_R \approx h_R \approx 0.1$ mm from equation (3.68). For a 0.1 m long solid block sliding at its terminal velocity on an incline at $\theta = 45°$, the minimum ratio of form drag force to lubrication force is

$$\frac{F_d}{F_{f.max}} \equiv \frac{\rho_o u_t h_o}{\mu_o} \frac{C_d}{4} \approx 30 \tag{3.70}$$

which is a modified Reynolds number and whereby the lubrication force is seen to be negligible -- a drag coefficient of $C_d = 1.6$ was used in the calculation. Equation (3.70) is proportional to $\ell^{1/2}$ which shows that the drag force increases more rapidly with landslide size than the lubrication force. One can estimate that the two forces would have similar magnitudes for solid blocks of length $\ell \approx 0.1$ mm. Since the lubrication force is proportional to the solid block velocity whereas the drag force is proportional to the block velocity squared, there must exist a velocity $u*$ at which the two forces are hypothetically equal and lubrication could still support the block weight. That special velocity is

$$u* = \left[\frac{256 \mu_o N}{9 C_d^2 \rho_o^2 \ell^2 w}\right]^{1/3} \approx 0.03 \text{ m/s} \tag{3.71}$$

and corresponds to a gap height of about $h_L \approx 64$ μm. While this scenario is plausible, it would typically last less than $t* \approx 20$ ms given $u(t) \approx a_o t$ for small times and $a_o \approx 2$ m/s^2. Even more important, equation (3.71) and the time $t* = u*/a_o$ are both independent of the solid block length whereas the characteristic time of motion t_o is proportional to $\ell^{1/2}$. Therefore, the lubrication force can safely be neglected over the entire block motion for the solid blocks studied in this work.

3.2.1.4 Summary of the Equations of Motion

Based on the foregoing analyses, the best description of submerged solid block motion down an incline appears to result from the third case considered in Section 3.2.1.2.3. For this case, the force balance of a solid block on an incline can be approximated by the equation of motion

$$(m_b + C_m m_o)\frac{d^2s}{dt^2} \approx (m_b - m_o)\, g\, (\sin\theta - C_n \cos\theta) -$$

$$- 0.5\, C_d\, \rho_o\, w\, \ell \cos\theta \sin\theta \left(\frac{ds}{dt}\right)^2 \qquad (3.72)$$

with an added mass coefficient C_m, a Coulombic friction coefficient C_n, and a drag coefficient C_d. The lubrication force in neglected in equation (3.72). Experimental values and functional dependencies of the dynamical coefficients are examined in Chapter 5. The theoretical initial acceleration of a solid block follows directly from u=ds/dt=0 in equation (3.72) and is given by the remaining two terms as

$$\frac{d^2s(0)}{dt^2} = a_o = \frac{(m_b - m_o)\, g\, (\sin\theta - C_n \cos\theta)}{m_b + C_m m_o} \qquad (3.73)$$

where C_m is evaluated at the initial submergence d/b of the solid block for a given incline angle θ. The terminal velocity of a solid block is obtained from equation (3.72) when $d^2s/dt^2=0$ so that

$$\frac{ds(\infty)}{dt} = u_t = \sqrt{\frac{2\,(m_b - m_o)\, g\, (\sin\theta - C_n \cos\theta)}{C_d\, \rho_o\, w\, \ell \cos\theta \sin\theta}} \qquad (3.74)$$

where the numerator is once again seen to be the motive force behind solid block motion. Based on the analysis in Section 3.2.1.2.3, it is readily shown that

$$s_o = \frac{u_t^2}{a_o}\,,\quad t_o = \frac{u_t}{a_o} \qquad (3.75)$$

for this equation of motion. Hence, only one characteristic length scale s_o and one characteristic time scale t_o govern the motion of a solid block wavemaker. Moreover, the

equations (3.75) provide analytical expressions for the characteristics of motion based on observable quantities, namely the initial acceleration and the terminal velocity. The equation of motion can be put in the canonical form of equation (3.1) by introducing nondimensional distance, time and velocity quantities

$$s = s_o\, s' \;,\; t = t_o\, t' \;,\; u = \frac{s_o}{t_o} u' \tag{3.76}$$

so that the differential equation governing the motion of the solid block can be written nondimensionally as

$$\frac{d^2 s'}{dt'^2} = 1 - u'^2 \;. \tag{3.77}$$

Assuming constant dynamical coefficients, the theoretical solution of the solid block motion down the incline as a function of time is

$$s(t) = \frac{u_t^2}{a_o} \ln\left[\cosh\left(\frac{a_o\, t}{u_t}\right)\right] = s_o \ln\left[\cosh\left(\frac{t}{t_o}\right)\right] . \tag{3.78}$$

Solving equation (3.78) for the time $t*$ to reach a given distance $s*$ provides

$$\frac{t*}{t_o} = \ln\left[\exp\left(\frac{s*}{s_o}\right) + \sqrt{\exp\left(\frac{2s*}{s_o}\right) - 1}\;\right] \tag{3.79}$$

which is a useful analytical expression for judging the extent of an underwater incline relative to the characteristic time of landslide motion and wave generation. By integrating equation (3.77) once or differentiating equation (3.78) once with respect to time, the velocity of the solid block at any instant of time is given by

$$u(t) = u_t \tanh\left(\frac{t}{t_o}\right) = \frac{s_o}{t_o} \tanh\left(\frac{t}{t_o}\right) . \tag{3.80}$$

By introducing equation (3.80) into equation (3.77) or differentiating equation (3.78) twice with respect to time, the acceleration of the solid block at any instant of time is given by

$$a(t) = a_o \operatorname{sech}^2\left(\frac{t}{t_o}\right) = \frac{s_o}{t_o^2} \operatorname{sech}^2\left(\frac{t}{t_o}\right) . \tag{3.81}$$

It should be emphasized once again that the solid block motion depends on only two observable quantities a_o and u_t. However, it is also clear that the initial acceleration and the terminal velocity (and by extension s_o and t_o) are functions of only d/b, ρ_b/ρ_o, θ, and ψ so that equations (3.4) and (3.5) are also satisfied and can now be replaced with known functional relationships. Therefore, the desirable contraction of landslide motion from four nondimensional quantities into two observable quantities has taken place. Also, the original assumption that landslide motion depends on only one characteristic distance s_o and one characteristic time t_o has been shown to be true for the case of solid block landslides.

3.2.2 Material Landslide Theory

Material landslides differ from solid block landslides because landslide form changes as it moves (oftentimes because of motion itself). Several attempts have been made by the author to model the center of mass motion of a material landslide in the same manner as a solid block landslide. For example, one can make the dynamical coefficients functions of distance traveled or of time elapsed and seek (in the very least) series solutions of the center of mass motion. These series solutions do not differ in any essential way from the Taylor series expansion of equation (3.78) about $t=0^+$. In particular, the first term in each series solution must be identical to the quadratic term that initiates solid block motion. In addition, the higher order effects introduced by variations in dynamical coefficients may not be detectable for material landslides conducted for this work since equation (3.45) shows that the quadratic term can dominate motion up to $t \approx \sqrt{6}\, t_o$. For specific materials, the deformation of the material landslide into a gravity current may be too slow to detect any change in center of mass motion for the relatively short incline used herein. Regardless, the single most difficult problem with these models is that they introduce unknown coefficients into the description of landslide motion. However, if the difference in center of mass motion between solid block and material landslides is small, then it is nearly impossible to accurately determine these coefficients through curve fitting of the landslide motion. It is shown in Chapter 5 that the center of mass motion of material landslides closely resembles that of solid block landslides. Therefore, the pragmatic approach of using equation (3.78) to describe the center of mass motion of material landslides is employed from now on. In addition, material landslide position data can be curve fit to yield the important scaling quantities s_o and t_o. The accuracy of these curve fits is surprisingly high for many material landslides.

3.2.2.1 Model of Deforming Landslides

The objective of this section is to characterize material landslide rates of deformation based on observed landslide cross-sectional area and center of mass height above the incline. Close examination of Figure 1.5 reveals that the cross-sectional area of the crushed calcite landslide increases with time while the center of mass height above the incline decreases at first. At early times, the material landslide appears to deform while keeping the approximate shape of an isosceles triangle. Therefore, a self-similar model of landslide deformation is developed for an incline at an angle $\theta=45^\circ$ to horizontal. The analysis assumes that all material landslides conducted for this work deform while remaining isosceles triangles (at least for early times). Material landslide cross-sectional area and center of mass height above the incline are the only two observations available to describe the geometry of the isosceles triangle in time. Two rates of strain are obtained from these observations of material landslides and converted into rates of deformation using simple geometry.

Consider an isosceles triangle of material resting on an incline with both edges of the triangle making an angle $\alpha(t)$ with the incline. The initial value of the angle is $\alpha(0)\approx\theta=45^\circ$ and the rate of change of the angle $\alpha(t)$ in time is sought as a measure of the macroscopic landslide rate of deformation. The landslide cross-sectional area A and the height of the center of mass above the incline z_c constitute the two measured independent variables. The height of the center of mass above the incline z_c is defined in Figure 3.1. The length of the triangle base ℓ is defined in Figure 3.6. The area of the triangle is

$$A = \frac{3\, z_c\, \ell}{2} \tag{3.82}$$

which can be used to solve for the length of the triangle base along the incline ℓ. Taking the derivative of both sides of equation (3.82) with respect to time and dividing by the instantaneous cross-sectional area yields

$$\frac{1}{A}\frac{dA}{dt} = \frac{3}{2\, z_c}\frac{dz_c}{dt} + \frac{3}{2\,\ell}\frac{d\ell}{dt} \tag{3.83}$$

which shows that the rate of change of area with respect to time is the sum of two orthogonal rates of strain. For a uniformly deforming isosceles triangle, the two orthogonal rates of strain are constant throughout the material. Therefore, the rate of

change of area in time is proportional to the trace of the rate of strain tensor and is simultaneously a local and a global measure of the total rate of strain.

It follows directly from the definition of the tangent function and equation (3.82) that the internal angle α between the triangle edge and the incline is given implicitly by

$$\tan \alpha(t) = \frac{9\, z_c^2}{A} \tag{3.84}$$

where $\alpha(0) \approx \theta = 45°$. The two angles $\alpha(0)$ and θ are not necessarily equal since the top face of the material landslide was not exactly horizontal. Taking the implicit derivative of equation (3.84) with respect to time and solving for the rate of deformation $d\alpha/dt$ gives

$$\Gamma(t) \equiv \frac{d\alpha}{dt} = \frac{1}{\frac{A}{9\, z_c^2} + \frac{9\, z_c^2}{A}} \left[\frac{2}{z_c} \frac{dz_c}{dt} - \frac{1}{A} \frac{dA}{dt} \right] \tag{3.85}$$

where the definition of $\cos(\alpha)$ has been used along with equation (3.82). Equation (3.85) provides the triangle rate of deformation and is readily evaluated based on experimental observations, provided of course that the experimental landslide cross-sectional profiles appear like isosceles triangles at short times. In the ideal initial case where $\alpha = \theta = 45°$, equation (3.85) reduces to the more simple form

$$\Gamma(t) = \frac{1}{z_c} \frac{dz_c}{dt} - \frac{1}{2\, A} \frac{dA}{dt} \tag{3.86}$$

since $A/9z_c^2$ is identically unity. For all materials studied, the initial values of $A_o/9z_{c.o}^2$ in Table C.12 were between 0.80 and 0.98 (with an arithmetic mean of 0.89) so that the simpler equation (3.86) is an excellent approximation of equation (3.85). A mean value $A_o/9z_{c.o}^2 \approx 0.89$ corresponds to a mean initial angle $\alpha(0) \approx 48°$ from equation (3.84).

The initial value of the rate of deformation evaluated at time $t=0^+$ is used to scale wave amplitudes in chapter 5. As noted in the introduction to Section 3.1, the landslide rate of deformation introduces another time scale into the wave generation problem. This time scale was neglected when developing the wavemaker formalism in Section 3.1.3. In general, it is found in Section 5.1 below that $1/\Gamma \geq t_o$ which provides the nondimensional rate of deformation $\Gamma t_o \leq 1$. If the nondimensional landslide deformation $|\Gamma t_o|$ is small

enough, then it can be considered as a perturbation to the solid block analysis given in Section 3.1.3. This idea is developed in Section 5.1.6 as well as Section 5.3.

3.3 Theoretical Linear Wavemaker Analyses

Water waves generated by solid block landslides are often linear waves if the initial block submergence is sufficiently deep. Wave generation can therefore be studied with linear transform techniques provided the wavemaker geometry corresponds to a particular transform geometry. Two usual choices are Fourier transforms for an infinite constant depth channel and Hankel transforms for an infinite straight incline. Small motions along the solid boundary in either geometry can be treated by perturbation methods in combination with linear transforms. For two-dimensional wavemaker studies, conformal mappings in the complex plane can also be used to transform an underwater landslide into one of the standard transform geometries. For a two-dimensional solid block and incline geometry composed of straight lines, a Schwartz-Christoffel transformation maps the entire fluid boundary onto the edge of a half plane using a complex integral. If the underwater landslide is allowed to move a finite distance in real space, then a convolution integral in time is introduced and the linear solution requires yet another integral. These are admittedly simple descriptions of some mathematically involved techniques. Examples of such calculations can be found in Stoker (1957), Wehausen and Laitone (1960), and Mei (1983).

Noda (1969) modeled linear water waves generated by a horizontal piston wavemaker in a constant depth channel. This two-dimensional wavemaker geometry is readily analyzed using Fourier and Laplace transforms. Noda (1971) also modeled the experimental results of Prins (1958) using an initial free surface profile and linear wave propagation. The fact that the initial free surface profile is only known when the wavemaker moves rapidly compared to the speed of wave propagation was discussed in Section 2.2. Iwasaki (1982) has studied long waves generated by the horizontal motion of a sloping bottom. Tuck and Hwang (1972) have shown how to analyze this wavemaker geometry using Hankel transforms. Iwasaki (1987) has calculated the linear water waves generated by a submerged two-dimensional box falling vertically at constant velocity. Iwasaki (1990) has also calculated the linear water waves generated by a two-dimensional box sliding horizontally at constant velocity along the bottom of a constant depth channel. None of these linear water wave models contains transient wave generation using realistic

underwater landslide motion. Therefore, wave generation in these models cannot be properly related to the landslide kinematics.

Before committing to any specific mathematical analysis, one should clearly state the desired outcome. For this work, the most useful purpose of a linear wavemaker theory is to predict a characteristic near-field wave amplitude for a sufficiently submerged underwater landslide. The chosen characteristic near-field wave record is that above the middle of the initial landslide position. This position is designated mathematically by x=0 and can be considered an approximate plane of symmetry with respect to the top face of the solid block. The symmetry is evident from the free surface profiles in frames (a) and (b) in Figure 1.3. The maximum absolute wave amplitude recorded at x=0 is the chosen characteristic wave amplitude of the entire wave generation problem. Given the complicated geometry of solid block landslides depicted in Figure 3.1, either a Schwartz-Christoffel transformation needs to be applied to the geometry or some geometrical simplifications need to be made. For example, the region immediately above a solid block landslide has the geometric appearance of a constant depth channel. For short times, the solid block has not advanced very far down the incline and the position x=0 is still located above the top of the block. Therefore, at early times, an observer at x=0 looking down onto the block sees vertical motion but does not yet know that the solid block is also moving forward. Choosing an analysis with this approximate geometry has the additional advantage of being very similar to that performed by Hammack (1972), who considered the vertical motion of a piston initially flush with a constant depth channel. Kajiura (1970) studied the same wavemaker geometry by assuming that long waves were generated by a slightly different piston motion. By choosing to study water waves generated by an approximate geometry, the linear wavemaker theory results must be interpreted as being proportional to the experimental results and not as being equal to them.

3.3.1 Near-field Wavemaker Analysis

The motion of a solid block landslide has been studied theoretically in Section 3.2. The solid block is now considered as a wavemaker with a characteristic wave amplitude depending directly on solid block motion. An approximate linear theory is developed in this section to predict the maximum near-field wave amplitude at x=0 above the initial solid block position. The theory is approximate for two very different reasons: i) the maximum near-field wave amplitude occurs at a relatively small time so that a Taylor

series expansion about $t=0^+$ can be used to describe vertical solid block motion, and ii) the theory employs an approximate geometry in order to find a simple yet practical linear wavemaker solution. The theoretical wave amplitudes are compared with experimental wave results in Section 5.2.3 below. The linear wavemaker theory can also be used to predict wave amplitudes for hypothetical solid block landslides provided a linearity criterion developed in Section 5.3.2 is met. The model requires five inputs: the landslide size b, the initial landslide submergence d, the incline angle θ, the landslide initial acceleration a_o, and the landslide terminal velocity u_t. There are three geometric and two dynamical quantities.

The maximum near-field wave amplitude occurs at a relatively small time $t \approx t_o$ in the solid block motion. Therefore, the full analytical form of equation (3.78) is not needed to accurately describe solid block motion. The nondimensional solid block motion along the incline can be expanded into a Taylor series given by

$$\frac{s(t)}{s_o} = \ln\left[\cosh\left(\frac{t}{t_o}\right)\right] = \frac{1}{2}\frac{t^2}{t_o^2} - \frac{1}{12}\frac{t^4}{t_o^4} + \frac{1}{D_3}\frac{t^6}{t_o^6} - \frac{N_4}{D_4}\frac{t^8}{t_o^8} +$$

$$+ \frac{N_5}{D_5}\frac{t^{10}}{t_o^{10}} - \frac{N_6}{D_6}\frac{t^{12}}{t_o^{12}} + \frac{N_7}{D_7}\frac{t^{14}}{t_o^{14}} - \frac{N_8}{D_8}\frac{t^{16}}{t_o^{16}} + \ldots \qquad (3.87)$$

where the numerators and denominators are provided in Table 3.1, and s_o and t_o are defined by equations (3.75) above. Equation (3.87) describes solid block motion along the incline and accounts for the need to input the initial acceleration a_o and the terminal velocity u_t. The vertical component of solid block motion is $s(t)\sin\theta$ which marks the only use of the incline angle in this theoretical development. The vertical motion of the solid block is analogous to the vertical motion of the piston in Hammack's (1972) work. Equation (3.87) converges uniformly to $s(t)/s_o$ provided $t/t_o < \ln(2+\sqrt{3}) \approx 1.32$ according to the Taylor series expansion of $\ln(1+x)$. Since only the first few terms of the infinite series is used, the finite sequence becomes asymptotic outside of its radius of convergence. The asymptotic series can be used to describe solid block motion to within the error implied by the next term of the alternating series. The first four terms of equation (3.87) are compared with the exact solution given by equation (3.78) in Figure 3.3. Two terms from the Taylor series describe most of the solid block motion up to around $t/t_o \approx 1$.

Table 3.1: Numerators and Denominators in the Taylor Series Expansion of Theoretical Solid Block Motion

Term, i	Numerator, N_i	Denominator, D_i
3	1	45
4	17	2 520
5	31	14 175
6	691	935 550
7	10 922	42 567 525
8	929 569	10 216 206 000

When the solid block motion is input into a wavemaker theory, the generation and propagation of waves can be described in terms of s_o and t_o. The linear wave generation theory of Hammack (1972) is used as an approximation of the wavemaker geometry immediately above the solid block. This means that wave generation is assumed to occur in a constant depth channel of depth d corresponding to the initial submergence of the solid block. Consider the initial solid block position in Figure 3.1. The fact that the incline rises at 45° to the left of the solid block and can reflect waves back over the block is ignored in the wavemaker theory. It is likely that water waves generated by the solid block will not have time to propagate up the incline and back before the maximum near-field wave amplitude occurs. If the leading disturbance travels at the long wave celerity up the 45° incline and back, then the minimum time needed for the return trip is

$$2 \int_0^d \frac{dx}{\sqrt{g\,x}} = 4 \sqrt{\frac{d}{g}} \tag{3.88}$$

which for a typical initial submergence d≈75 mm found in this work takes t≈0.35 s. This is almost exactly the time at which the maximum near-field wave amplitude occurs for most underwater landslides conducted herein. The fact that there is no constant depth channel to the right of the solid block is also ignored in the wavemaker theory. This geometrical approximation actually slows wave propagation away from the solid block towards the constant depth channel and should not seriously affect the prediction of near-field wave amplitudes. Therefore, the approximate linear theory will correctly model wave generation up to at least the occurrence of the maximum near-field wave amplitude.

The approximate linear theory only captures the near-field wave generation due to vertical block motion. According to the approximate geometry considered in this section, a piston spanning $x=\pm b/2$ and initially flush with a constant depth channel of depth d is allowed to accelerate vertically downward. This description of the geometry accounts for the last two model inputs. The chosen characteristic wave amplitude is located at $x=0$ above the middle of the piston. This description of wave generation neglects forward motion of the block. The maximum near-field wave amplitude occurs at around $t \approx t_o$. It follows from equation (3.78) that

$$s(t_o) \approx 0.43\, s_o \tag{3.89}$$

where a typical value is $s_o \approx 0.2$ m in this work. Therefore, a typical solid block with $b \approx 0.09$ m will have advanced horizontally $s(t_o)\cos\theta \approx 0.06$ m along an incline at $\theta = 45°$. The solid block will have advanced less than the length of the top face of the block. The approximate nature of the geometry is evident although the approximation itself is justifiable. The mathematical simplifications that arise from the approximate geometry are considerable.

In the work of Hammack (1972), the overall extent of vertical piston motion was typically small compared to the channel depth. Therefore, linearization of the piston motion about the channel depth represented a reasonably accurate and justifiable first order perturbation. A further approximation arises in the linear theory developed here from the linearization of the piston boundary condition. The kinematic boundary condition of the piston is linearized about its initial depth d despite the large amplitude of piston motion. Since the motion of the incompressible water in the section spanning $x=\pm b/2$ must follow the motion of the piston, the linearized boundary condition properly captures the water kinematics at the depth d. After all, incompressible water has a uniform velocity within the piston bore from the surface of the piston up to depth d. However, the linearized boundary condition does not capture the correct wave celerity immediately above the solid block. All waves generated above the piston propagate as if the piston surface were still at depth d even if the piston is significantly deeper.

The wavemaker geometry considered here is that of a constant depth channel in which a piston initially flush with the channel bottom moves vertically down. Let the function

$\zeta(x,t)$ represent the difference between the piston and the channel bottom at z=-d as a function of time. The mathematical expression of the vertical piston motion is

$$\zeta(x,t) = - s(t) \sin\theta \; H(b^2/4 - x^2) \tag{3.90}$$

where s(t) is the solid block motion along the incline given by equation (3.87) and H is the Heaviside function. The Heaviside function is defined as H≡1 when the argument is positive and H≡0 when the argument is negative. The Heaviside function is used to represent the fact that the piston between x=±b/2 is the only part of the channel bottom that is moving vertically.

The resulting linear water wave problem is given in terms of a velocity potential by Hammack (1972). By taking a Fourier transform of the spatial coordinate x and a Laplace transform of time, an ordinary differential equation for the velocity potential in the vertical coordinate z arises that is readily solved. Let the function $\eta(t,x)$ represent the difference between the free surface and the still water level at z=0 as a function of time. The linear free surface amplitude $\eta(t,x)$ is a function of the velocity potential solution found for this wavemaker geometry. In terms of the transformed Fourier and Laplace coordinates κ and q, respectively, the linear wavemaker solution of the free surface amplitude is given by Hammack (1972) as

$$\eta(q,\kappa) = \frac{q^2 \, \zeta(\kappa,q)}{(q^2 + \omega^2) \cosh \kappa d} \tag{3.91}$$

where $\zeta(\kappa,q)$ is the transformed piston motion and $\omega(\kappa,d)=\sqrt{\kappa g \tanh(\kappa d)}$ is the familiar water wave dispersion relation for a depth d. The transformed piston motion is given by

$$\zeta(\kappa,q) = -\frac{2 s_o \sin\theta \, P(1/q)}{\kappa} \sin\frac{\kappa b}{2} \tag{3.92}$$

where the polynomial in the transformed time coordinate 1/q is

$$P(1/q) = \frac{1}{q^3 t_o^2} - \frac{2}{q^5 t_o^4} + \frac{16}{q^7 t_o^6} - \frac{272}{q^9 t_o^8} + \frac{7\,936}{q^{11} t_o^{10}} -$$

$$- \frac{353\,792}{q^{13} t_o^{12}} + \frac{22\,368\,256}{q^{15} t_o^{14}} - \frac{1\,903\,757\,312}{q^{17} t_o^{16}} + \ldots \tag{3.93}$$

from the Laplace transform of equation (3.87). Using equation (3.87), the Taylor series expansion of the solid block motion, prior to taking the Laplace transform amounts to taking the Laplace transform of equation (3.78) and then considering the asymptotic inversion for large q of equation (3.91). This fact is related to the asymptotic analysis known as the method of Laplace. The connection between small time and large q is readily seen by comparing successive terms from equation (3.87) with equation (3.93).

The Laplace inversion of equation (3.91) is straightforward. Inserting equation (3.93) into equation (3.91) shows that there are three poles in the complex q-plane at q=0, q=iω, and q=-iω. The pole at q=0 is of first order for the first term in equation (3.93) and increases in order by two for each successive term. The other two simple poles yield the function cos(ωt) in the integrand of the Fourier inversion integral. The fact that only the wave amplitude at x=0 is sought simplifies the Fourier inversion integral: the factor exp(-ikx) becomes unity. Each term in equation (3.93) has a separate Fourier inversion integral

$$\frac{\eta(t,0)}{s_o \sin\theta} = \frac{2}{\pi t_o^2} \int_0^\infty \frac{\sin(\kappa b/2)}{\kappa \cosh(\kappa d)} \frac{[\cos(\omega t) - 1]}{\omega^2} d\kappa +$$

$$+ \frac{4}{\pi t_o^4} \int_0^\infty \frac{\sin(\kappa b/2)}{\kappa \cosh(\kappa d)} \frac{[\cos(\omega t) - 1 + \frac{t^2\omega^2}{2}]}{\omega^4} d\kappa +$$

$$+ \frac{32}{\pi t_o^6} \int_0^\infty \frac{\sin(\kappa b/2)}{\kappa \cosh(\kappa d)} \frac{[\cos(\omega t) - 1 + \frac{t^2\omega^2}{2} - \frac{t^4\omega^4}{24}]}{\omega^6} d\kappa + \ldots \qquad (3.94)$$

where each integrand is even in the wavenumber κ allowing the integration to be taken over only the positive real κ-axis. Therefore, each numerical coefficient in equation (3.94) is simply two times the corresponding numerical coefficient in equation (3.93).

An example of a water wave generated above the initial solid block position can be seen in frames (a) and (b) of Figure 1.3. A trough in the free surface about the same length as the solid block $\lambda \approx b$ was generated above the block. For a solid block landslide with a nondimensional initial submergence of $d/b \approx 0.9$, it follows that

$$\kappa d \approx \frac{2\pi d}{b} \approx 6 > \pi \tag{3.95}$$

which indicates that a deep water wave was formed above the block. For deep water waves, an approximate form of the dispersion relation

$$\omega^2(\kappa,d) = \kappa g \tanh(\kappa d) \approx |\kappa| g \tag{3.96}$$

can be used to simplify the mathematical analysis. Equation (3.96) was used in equation (3.94) in order to evaluate the approximate linear wave amplitude.

Expanding the cosines in equation (3.94) using Taylor series (with infinite radius of convergence) about $t=0^+$ gives the wave amplitude at $x=0$ as a series solution in time. The first term from each integral in equation (3.94) is independent of the dispersion relation because the circular frequencies in the numerator and denominator cancel. The dispersion relation in equation (3.96) is substituted for ω^2 everywhere else. The result is a small time asymptotic solution of the free surface amplitude at $x=0$

$$\frac{\eta(t,0)\,\pi}{s_o \sin\theta} = \frac{I_1}{2}\frac{t^2}{t_o^2} - \left(\frac{I_1}{12} + \frac{I_2\, Ha_o^2\, b^2}{24\, d^2}\right)\frac{t^4}{t_o^4} +$$

$$+ \left(\frac{I_1}{45} + \frac{I_2\, Ha_o^2\, b^2}{360\, d^2} + \frac{I_3\, Ha_o^4\, b^4}{720\, d^4}\right)\frac{t^6}{t_o^6} -$$

$$- \left(\frac{17\, I_1}{2\,520} + \frac{I_2\, Ha_o^2\, b^2}{2\,520\, d^2} + \frac{I_3\, Ha_o^4\, b^4}{20\,160\, d^4} + \frac{I_4\, Ha_o^6\, b^6}{40\,320\, d^6}\right)\frac{t^8}{t_o^8} + \ldots \tag{3.97}$$

where the Fourier integrals I_n are pure numbers dependent on the nondimensional initial solid block submergence d/b. The Taylor series for the piston motion, equation (3.87) with Table 3.1, is seen to be recovered in equation (3.97) multiplied by the integral I_1. The integrals I_n are Fourier integrals along the real axis given by

$$I_n(\beta) = 2 \int_0^{\infty} \frac{\sin(\beta y)\, y^{n-2}}{\cosh y}\, dy \tag{3.98}$$

where $y \equiv \kappa d$ is the nondimensional integration variable and $\beta = b/2d$ is a measure of the aspect ratio of the wave generation region. The integral index n begins at unity. The Fourier integrals $I_n(\beta)$ are functions of only the wavemaker geometry and not functions of the solid block kinematics or of time. If an exact geometry corresponding to Figure 3.1 had been used to solve for the linear wave amplitudes, then it would be the form of the exact integrals $I_n(\beta)$ and their numerical values that would have changed. Exact integrals would also be explicit functions of the incline angle, which enters into the approximate geometrical analysis in only a basic manner.

Every other Fourier integral $I_n(\beta)$ can be evaluated analytically using complex contour integrals. The first Fourier integral

$$I_1(\beta) = 2 \int_0^{\infty} \frac{\sin(\beta y)}{y \cosh y}\, dy = 4 \tan^{-1}\left[\exp\left(\frac{\pi \beta}{2}\right)\right] - \pi \tag{3.99}$$

yields an analytical solution by differentiating the integral with respect to β and evaluating a contour integral in the complex y-plane. The contour follows the entire real axis $\mathrm{Im}(y)=0$ and then returns along the straight line $\mathrm{Im}(y)=i\pi$. There is a single pole located at $y=i\pi/2$ with a residue that is readily evaluated. The solution

$$\frac{\partial I_1(\beta)}{\partial \beta} = \int_{-\infty}^{\infty} \frac{\cos(\beta y)}{\cosh y}\, dy = \pi \,\mathrm{sech}\left(\frac{\pi \beta}{2}\right) \tag{3.100}$$

is then integrated with respect to β under the condition that $I_1(0)=0$ to obtain the right hand side of equation (3.99). All odd indexed Fourier integrals $I_n(\beta)$ give rise to contour integrals with the same contour of integration. These Fourier integrals can be found by integrating equation (3.98) n-2 times with respect to β so that the power of y in the integrand becomes zero. The integrations with respect to β are elementary and provide a basic contour integral to solve. One simple pole is located at $y=i\pi/2$ within the contour of

each contour integral. The solution of the contour integral is then differentiated n-2 times with respect to β in order to recover the desired analytical solution to $I_n(\beta)$.

Despite the elegant mathematics that allow half of the Fourier integrals $I_n(\beta)$ to be solved analytically, the integrals were in fact solved numerically within a Mathematica program that provided the approximate linear wave amplitude at x=0 given the inputs d, b, a_o, and u_t. The first eight terms of equation (3.97) were employed in the program whereas only the first four terms are given in equation (3.97) above. The Mathematica program first evaluated the magnitude of all eight terms near the maximum near-field wave amplitude. The appropriate number of terms in the asymptotic series was then chosen in order to provide the best possible accuracy. For most calculations, eight terms from equation (3.97) gave the most accurate solution; for some solid block trials, six or seven terms from equation (3.97) were more accurate since subsequent terms in the asymptotic series began diverging. Almost all calculations had errors of less than 1% based on the magnitude of the last term kept in the alternating series. The local minimum in the wave amplitude was then sought near $t \approx 0.35$ s using the Newton-Raphson algorithm "FindRoot" in Mathematica applied to the derivative of equation (3.97) in time. The algorithm found the time t_{max} corresponding to the occurrence of the maximum near-field wave amplitude. Evaluating equation (3.97) at time t_{max} gave the approximate linear theory solution for the characteristic wave amplitude η_{max}. Equation (3.97) yields the functional form of the maximum near-field wave amplitude

$$\frac{\eta_{max}}{s_o \sin\theta} = \frac{1}{\pi} f\left(\frac{d}{b} = \frac{1}{2\beta}\ ,\ Ha_o = \frac{t_o\sqrt{g\,d}}{b}\right) \tag{3.101}$$

which is the same form given in equation (3.27) provided the incline angle is held constant. The nondimensional initial submergence d/b is related to the aspect ratio β of the generation region above the piston. Ha_o is the only independent nondimensional number that contains the landslide dynamics through the characteristic time t_o.

3.3.2 Far-field Airy Waves

In a two-dimensional constant depth channel, the leading wave propagating away from a localized free surface perturbation is an Airy wave. In other words, an Airy function Ai(x,t;h) gives the correct transition from quiescent water surface to dispersive wave groups for linear water waves propagating down a channel of constant depth. The

general analysis belongs to a class of turning point problems in applied mathematics and physics. A basic example is the Airy ordinary differential equation

$$\frac{d^2f}{dy^2} - y f = 0 \tag{3.102}$$

which demonstrates exponential type growth or decay when $y<0$ and oscillatory behavior when $y>0$. The proof given here can be found in Mei (1983) or Whitham (1973). Consider a general Fourier transform solution to a linear Cauchy-Poisson water wave problem in the region $x\gg0$

$$\eta(x,t) = \frac{1}{2\pi} \int_{-\infty}^{\infty} f(\kappa) \exp(i \kappa x - i \omega(\kappa) t)\, d\kappa \tag{3.103}$$

where $\omega(\kappa)=\sqrt{\kappa g \tanh(\kappa h)}$ is the water wave dispersion relation, h is the water depth in the channel, and $f(\kappa)$ is assumed to be well behaved near $\kappa\approx0^+$. The leading waves are always the longest wavelength components of the spectrum of $f(\kappa)$ since long waves travel faster than deep water waves and the long waves separate out from shorter waves due to wave dispersion. Let $y\equiv\kappa h$ be the nondimensional variable of integration and consider the phase $\phi(x,t;\kappa)$ of the exponential function near the leading waves $\kappa\approx0^+$ (which corresponds to long waves with $\lambda\to\infty$). Using a Taylor series expansion of the dispersion relation $\omega(\kappa)$ and keeping only the first two terms of the expansion yields

$$\phi(x,t;\kappa) = y \frac{x}{h} - t \sqrt{\frac{g}{h}}\, \sqrt{y \tanh y} \approx$$

$$\approx - t \sqrt{\frac{g}{h}} \left[\left(1 - \frac{x}{t\sqrt{g h}} \right) y - \frac{y^3}{6} \right] \tag{3.104}$$

where the phase indicates that a wave front propagating at the long wave celerity exists. If the solution of the integral near the wave front is sought, then the function $f(\kappa)$ can be replaced by $f(0)$ since $\kappa\approx0^+$. The purpose of this development is not to quantify the last two approximations but rather to explain the origin of the Airy wave behavior. Defining two new variables

$$R \equiv - y \left(- \frac{t}{2} \sqrt{\frac{g}{h}} \right)^{1/3} \tag{3.105}$$

$$S \equiv -2^{1/3}\left(1-\frac{x}{t\sqrt{g\,h}}\right)\left(-t\sqrt{\frac{g}{h}}\right)^{2/3} \tag{3.106}$$

allows the integral in equation (3.103) to be put into the familiar form of the Airy integral. For the new variable of integration R, the integral can be written

$$\eta(x,t) \approx \frac{f(0)\,h}{2\pi}\left(\frac{4\,h}{t^2\,g}\right)^{1/6}\int_{-\infty}^{\infty}\exp\left(i\,\frac{R^3}{3}+i\,S\,R\right)dR \tag{3.107}$$

where the integral yields $2\pi Ai(S)$ by definition of the integral representation of the Airy function. Reorganizing the result back into the original coordinates gives the asymptotic solution

$$\frac{\eta(x,t)}{h} \approx f(0)\left(\frac{4\,h}{t^2\,g}\right)^{1/6} Ai\left[\left(\frac{2\,g}{t\,h}\right)^{1/3}\frac{x-t\sqrt{g\,h}}{\sqrt{g\,h}}\right] \tag{3.108}$$

for $x \gg 0$ and $x \approx t\sqrt{gh}$ where it is now clear that a wave front is propagating at the long wave celerity given that the Airy function has an absolute maximum near Ai(-1). The value f(0) provides a characteristic nondimensional wave amplitude near the Airy wave maximum. Equation (3.108) is strictly valid only near the absolute maximum of the Airy function, but the fundamental shape and location of the leading wave is correctly established for any linear wave propagating in a constant depth channel. However, the wavy part of the Airy function decays algebraically far from the leading wave whereas many wave problems exhibit a sequence of wave groups. Moreover, the leading wave need not be the largest wave of the first wave group as is shown in Chapter 5. A more complete analysis of the asymptotic solution in terms of a series of Airy functions can be found in Chester *et al.* (1957) that can capture the profiles of wave groups. A carefully documented application of the series expansion to water waves can be found in Noda (1969).

Two figures of experimental results are provided here to demonstrate the properties of Airy waves. A programmable wave board was used to create a repeatable two-dimensional disturbance in a wave tank filled with 35 cm of water. The water waves generated by the wave board had similar characteristics to the water waves generated by

underwater landslides studied in this work. Wave gauges were used to measure wave amplitudes at different distances from the wave board. Figure 3.4 shows that the maximum leading wave amplitude travels at the long wave celerity based on the channel water depth. Figure 3.5 demonstrates that the maximum leading wave amplitude decays with the expected -0.33 power law with distance. Similar leading wave behaviors can be expected for water waves generated by underwater landslides if the waves propagate in a two-dimensional channel of constant depth. The leading wave is referred to as an Airy wave herein. Mei (1983) shows that waves generated by a tilting body will decay more rapidly with propagation distance than the Airy waves derived in this section for a more general disturbance. This implies that far-field wave amplitudes depend primarily on the center of mass motion of a landslide since wave components generated by landslide deformation rapidly decay.

3.4 Nonlinear Wavemaker Simulations

Oftentimes, the integral solutions obtained from linear transform methods have to be solved numerically by some form of quadrature. This usually involves brute computational force since the step size of the quadrature in transform space needs to be small enough to capture the smallest wavelengths of the oscillatory integrand. The net result is that numerical integration of linear wavemaker integral solutions is often only two orders of magnitude faster than a fully nonlinear water wave simulation on the same computer. However, if convolution integrals in time and conformal mappings of a complicated boundary are also needed, then the fully nonlinear problem typically becomes faster to solve than the linear solution represented by a triple integral. In light of these basic observations, nonlinear simulations of water waves generated by underwater landslides become a necessary tool for generating accurate wavemaker curves. The only drawback is that such involved numerical simulations are still too lengthy to be used to span the entire space of nondimensional wavemaker parameters.

The development and implementation of a large (10,000 line) fluid dynamics code can often be the subject of a Ph.D. thesis in its own right. On the other hand, applications of these codes to existing fluid dynamics problems can be rewarding in practical and important ways. The goal of this section is to describe the application of an existing fluid dynamics code developed by Dr. Stephan Grilli at the University of Rhode Island to the problem of water waves generated by solid block landslides.

3.4.1 Introduction to the Numerical Simulation Model

Descriptions of the BEM code used herein can be found in Grilli *et al.* (1989) with recent modifications given in Grilli and Subramanya (1994). The summary of the BEM code provided here and in Section 3.4.3 below is taken from these papers. Water waves are often described using inviscid and irrotational fluid dynamic models since viscous effects are negligible in many wave generation and propagation problems. For the fluid dynamics code used herein, the Laplace partial differential equation of the velocity potential is first converted into a Boundary Integral Equation (BIE) using Green's third identity. Integration is then performed over discretized boundary elements using a Boundary Element Method (BEM). The influence of each boundary element on every other boundary element is calculated at each time step. A full matrix of $O(N^2)$ is inverted to solve for the velocity potential where N is the number of boundary elements. The Laplace partial differential equation is in fact solved twice: once for the velocity potential and once again for the derivative of the velocity potential with respect to time. Consequently, sufficient temporal derivatives exist to perform an accurate Lagrangian updating of the free surface using Taylor series expansions of the material derivative about the current free surface shape. Recent applications of the BEM code to shoaling and breaking of solitary waves can be found in Grilli *et al.* (1994a) and Grilli *et al.* (1994b). These simulations serve as two of many significant validations of the numerical simulation technique and of the use of potential flow to describe the generation and propagation of water waves. In Section 5.4, simulation results are first compared with experimental results and then used to calculate wavemaker data.

3.4.2 BEM Code Description

For water wave BEM codes, the velocity potential is solved subject to well-posed boundary conditions for Laplace's equation. Typical boundary conditions imposed on the domain consist of a specified potential, a specified normal flux, or more complicated mixed and free surface boundary conditions. The fully nonlinear potential flow boundary conditions for the free surface are implemented in the code used for this work. Hence, water waves can propagate over any bathymetry and undergo correct shoaling, reflection and dispersion. The BEM code becomes singular once a breaking wave strikes the free surface due to the singularity in the free space Green's function. Hence, the initial submergence and motion of an underwater landslide simulated by the BEM code must not incur wave breaking.

As with many computer simulations, accurate and efficient numerical simulations may depend more on the skillful implementation of established techniques then on errors inherent to the solution technique itself. The simulations reported herein are no exception. The Laplace partial differential equation of the velocity potential represents the conservation of volume in an inviscid fluid flow. Therefore, a useful measure of simulation accuracy is the volume of fluid contained by the boundary elements. The BEM code used for this work calculates the simulation domain volume at each time step and records changes in the volume as both an instantaneous error during a time step and an accumulated volumetric error.

An exceptional feature of these simulations is the extremely accurate $O(\Delta t^3)$ time stepping solution of the free surface motion using Taylor series expansions in local boundary coordinates. These benefits are acquired with the simultaneous loss of viscous effects such as wave energy dissipation, flow separation, and skin friction. Section 3.2 shows that some of these viscous effects play a negligible role in solid block kinematics. Fluid separation near the solid block vertex is clearly an important viscous effect that controls block motion. However, the role of fluid dynamic features such as separation on wave generation remain to be determined. Inviscid and irrotational simulations are not able to reproduce the starting vortex and flow separation depicted in Figure 1.3.

The BEM code uses the two-dimensional free space Green's function to solve a linear partial differential equation by integrating over the boundary of the simulation domain. At corners in the domain, two nodes are superposed to account for the two normal vectors. The velocity potential and normal fluxes at the two nodes are subject to continuity conditions. The BEM code used for this work was designed to have only four corner nodes placed at the four corners of a rectangular wave tank. Hence, the three corners of a solid block landslide are treated with approximate boundary conditions described immediately below and in Section 5.4.

The corners of an underwater landslide represent local singularities in an exact potential flow solution. Such singularities could be a large source of error in potential flow simulations. In reality, viscous effects and inexact geometries prevent such singularities from being fully realized. Therefore, it is both realistic and advisable to avoid such singularities in the numerical simulation too. In the BEM code, six corner elements of nondimensional size $O(10^{-3})$ were used to round out the geometry and provide accurate

potential gradients near the theoretical singularities. The boundary conditions employed on the corner elements were modeled to provide a smooth transition from the theoretically derived boundary conditions on either face of the landslide. The smoothness of the boundary condition transition around a corner mimics the smoothing behavior of the velocity potential by the Laplace partial differential equation. Hence, creating approximate boundary conditions near the singularities limits the magnitude of computational errors as well as the distance with which they can propagate into the solution domain. However, volume will no longer be conserved by the simulations.

Corners of a simulation domain can present a problem to the BEM code since the angle with which adjacent elements see one another becomes large at the same time that the rate of change of the velocity potential also becomes large. The polynomial fitting technique used to represent the velocity potential along the boundary combined with the Gaussian quadrature of the boundary integrals fail to capture these rates of change properly. Adaptive integration was employed on both sides of all four corner elements that subdivides elements into two equal parts until the angle of sight is less than 40°. A maximum of four subdivisions could be made resulting in up to 16 elements where there was once only one element. Further subdivision fails to improve the solution appreciably while significantly increasing the computational expense of checking the angle of each subdivision relative to every other one.

The time step used in a simulation involving flow or wave phenomena is often controlled by a Courant number. The Courant number is defined for this work as

$$Co = \frac{\Delta t \sqrt{g\,(d + s(t) \sin \theta)}}{\Delta r_{min}} \tag{3.118}$$

where Δt is the time step at a given time in the simulation and Δr_{min} is the smallest element length on the free surface at that time. The Courant number is a measure of how far a wave can travel along a single boundary element during a given time step. In the code, the time step is determined based on a user defined optimum Courant number that depends on the specific problem being simulated. For the BEM code used in this work, the Courant number must be $Co<0.8$ for stable wave propagation. In general, a smaller Courant number gives rise to a more accurate numerical solution of free surface waves since Taylor series expansions used to move the free surface become more accurate as the time step is reduced.

Another important simulation detail involved matching the length of the first three elements of the incline beach with the first three elements of the free surface. The incline beach was located immediately behind the landslide and was subject to highly unsteady wave action. Matching element lengths on an inclined beach allows adaptive integration to be used effectively on the last three elements. The fully nonlinear boundary conditions and Lagrangian updating of the free surface are therefore accurately exploited at the juncture of the incline and the free surface. Subsequent elements on the incline and free surface are usually far enough away from each other that such refinements are no longer needed to produce an accurate wave run-up and run-down solution. One additional detail needed attention: the predicted run-up or run-down would not quite follow the incline at each time step due to small errors in the Taylor series expansion of motion. In order not to have any compounded errors in free surface position, the horizontal coordinate of the free surface juncture with the incline was forced to lie on the incline at each time step.

3.4.3 Boundary Motion and Boundary Conditions

This section provides the geometric equations needed to describe the landslide position and motion at each time step within the BEM code. The boundary conditions on the surface of the underwater landslide are also derived in this section. These equations represent modifications that were made within BEM code subroutines that update boundary node positions and prescribe boundary conditions for the velocity potential and its derivative in time. In all, five subroutines were modified so that an underwater landslides became another wave generation option within the BEM code. A separate computer program was also written that converted the inputs of the solid block landslide problem into an initial simulation domain and separate input data for the BEM code specifically needed for the underwater landslide simulation option. This computer program will be described first.

In this work, an underwater landslide is modeled initially as a right triangle that undergoes translational motion on a straight incline with angle $\theta=45^\circ$ from horizontal. The top face of the landslide is initially horizontal with length b while the front face of the landslide is initially vertical with length c as shown in Figure 3.6. The choice of such model landslides is primarily a function of experimental expediency as explained in Section 1.1. The incline is taken as sufficiently long for landslide motion to develop over several characteristic time scales t_0 before reaching the bottom of the incline. For

underwater landslides with $Ha_o \gg 1$, this implies that almost all water waves have been generated and have left the generation region before the landslide itself is affected by any significant changes in bathymetry. This condition can be verified for an arbitrary underwater landslide using equation (3.78) or equation (3.79).

The size of the simulation domain should be as small as possible since the duration of a given simulation scales with the square of the number of boundary elements. Moreover, accuracy of the numerical solution increases with node density so that a large simulation domain can incur huge computational costs for a specified node density (or accuracy). Therefore, the simulation domain is minimized for each computation according to the specific landslide center of mass motion. One way to minimize the computational domain is to limit the duration of the simulation since the landslide will not have traveled very far down the incline. If one is only interested in the maximum near-field wave amplitude, then a simulation need not run longer than $t \approx 2t_o$. Using equation (3.78), the landslide center of mass will have traveled $s \approx 1.33 s_o$ in that time. Given the minimum length of the incline, a constant depth channel can then be introduced into the simulation domain. The channel needs to be long enough that waves reflecting off the far wall cannot return to the wave generation region before the simulation ends. Once again, a shallower channel has a slower long wave celerity and therefore can be shorter in length. These ideas are now translated into exact formulae used to calculate the size of the simulation domain.

In order to calculate landslide motion, a user must input the incline angle θ, the initial landslide size b, the initial landslide submergence d, the initial landslide density ρ_s, and the three dynamical coefficients C_n, C_d, and C_m. The incline angle is always $\theta = 45^\circ$ in this work. The initial acceleration a_o and terminal velocity u_t are readily calculated from equations (3.73) and (3.74), respectively. Likewise, the characteristic distance s_o and time t_o of the landslide motion are readily calculated from equations (3.76).

The minimum size of the simulation domain can now be calculated. The distance traveled by the landslide center of mass during $2t_o$ is roughly $1.35 s_o$. The minimum depth of the simulation domain h_{min} is therefore the initial landslide submergence d plus the height of the front face of the landslide $c = b\tan\theta$ plus the vertical component of the landslide motion along the incline or

$$h_{min} = d + c + 1.35\, s_o \sin\theta \qquad (3.109)$$

where the simulation is assumed to stop at $t=2t_o$. Since the size of the simulation domain is clearly connected to the duration of the simulation, simulations cannot be run longer than $t=2t_o$ and are therefore limited to simulating a near-field characteristic wave amplitude. The corresponding horizontal extent of the free surface above the incline is clearly $h_{min}/\tan\theta$. The horizontal extent of the constant depth channel must be $t_o\sqrt{gh}$ in order to keep long waves from reentering the generation region during a simulation time of $t=2t_o$. Dividing equation (3.109) by $\tan\theta$ and adding the constant depth channel length, the minimum horizontal extent of the entire free surface is

$$\Delta x_{min} = \frac{d}{\tan\theta} + b + 1.35\, s_o \cos\theta + t_o \sqrt{g\,h} \tag{3.110}$$

where a vertical wall is assumed to exist at the right end of the simulated wave tank. The geometry of the simulated wave tank is therefore very similar to that of the actual wave tank described in Section 4.1 and shown in Figure 4.1. The landslide vertex and two intersection points of the landslide faces with the incline are now shown to be important points in the simulation domain.

Some boundary nodes in the simulation must be redistributed at each time step in order to achieve landslide motion. The only moving boundary nodes other than the free surface are on the surface of the landslide. The incline itself does not move although the two portions of the incline exposed to the water change in size as a function of time. Therefore, boundary nodes along these two portions of the incline need to be stretched or compressed. For example, the redistribution of boundary nodes may begin at the incline bottom and place nodes along the incline up to the bottom of the landslide, more nodes up the front face of the landslide and across the top face of the landslide to the incline, and finally distribute nodes up the incline all the way to the free surface. Since the incline does not move, the landslide vertex is a useful reference point from which to describe landslide motion and locate the intersections of the landslide faces with the incline. The landslide vertex begins at a known position and follows the landslide center of mass motion. In the simulations, the intersection of the still free surface with the incline is taken as the origin. Therefore, the initial location of the landslide vertex is

$$x_o = b + \frac{d}{\tan\theta}\,, \quad z_o = -d \tag{3.111}$$

where the vertical z-axis increases upward. At any time in the landslide motion, the landslide vertex is located at

$$x_v(t) = x_o + s(t) \sin\theta \ , \ z_v(t) = z_o - s(t) \cos\theta \tag{3.112}$$

where s(t) is given by equation (3.78). It is convenient to describe the top and front faces of the landslide using radial coordinates situated at the landslide vertex and moving with the landslide center of mass.

The intersection point of the top face of the landslide with the incline is found from the vertex using the equations

$$x_a = x_v - b \tag{3.113}$$

$$z_a = z_v \tag{3.114}$$

where x_v and z_v are given by equations (3.112). The point (x_a,z_a) is needed at each time step in order to redistribute nodes along the top landslide face and the upper portion of the incline. The intersection of the bottom face of the landslide with the incline is given by

$$x_b = x_v \tag{3.115}$$

$$z_b = z_v - c \ . \tag{3.116}$$

The three points (x_v,z_v), (x_a,z_a) and (x_b,z_b) represent the three corners of solid block landslides for which approximate boundary conditions are employed. This completes the description of solid block motion within the BEM code since the redistribution of nodes is a trivial task given these three points.

The BEM code solves for the velocity potential and the derivative of the velocity potential with respect to time. Both quantities satisfy Laplace's equation and therefore need well-posed boundary conditions. The boundary conditions for the free surface are established within the BEM code and were not modified for simulations of solid block landslides. The boundary conditions for the solid walls of the simulated wave tank are trivial no-flux boundary conditions given by

$$\frac{\partial \phi}{\partial n} = 0 \ , \ \frac{\partial^2 \phi}{\partial n \, \partial t} = 0 \tag{3.117}$$

where **n** is the outward pointing normal vector. Vectors in the next two pages will be denoted by boldface type. The incline, channel bottom, and far wall of the simulated wave tank had boundary conditions prescribed by equation (3.117).

When solving for the velocity potential, the boundary condition on the solid block surface simply represents the component of center of mass velocity normal to the surface. For rigid body motion with no rotation, the general boundary condition is expressed

$$\frac{\partial \phi}{\partial n} = \mathbf{v} \cdot \mathbf{n} \tag{3.118}$$

where **v** is the center of mass velocity vector and **n** is the outward pointing normal vector. For the top face of the solid block, the boundary condition becomes

$$\frac{\partial \phi}{\partial n} = \frac{ds}{dt} \sin \theta \tag{3.119}$$

while, for the front face of the solid block, the boundary condition is

$$\frac{\partial \phi}{\partial n} = - \frac{ds}{dt} \sin \theta \ . \tag{3.120}$$

The inviscid fluid is of course free to flow tangentially along the solid block surface. Equations (3.118) and (3.119) are intuitively straightforward boundary conditions.

The boundary conditions for the derivative of the velocity potential with respect to time on the solid block surface need to be carefully derived. Clearly, the component of the center of mass acceleration normal to the surface will be part of the boundary conditions. In addition, second derivatives of the velocity potential along the solid block surface can be expected. For rigid body motion with no rotation, the general boundary condition is

$$\frac{\partial^2 \phi}{\partial n \, \partial t} = \mathbf{a} \cdot \mathbf{n} - \mathbf{v} \cdot \mathbf{s} \, \frac{\partial^2 \phi}{\partial n \, \partial s} + \mathbf{v} \cdot \mathbf{n} \, \frac{\partial^2 \phi}{\partial s^2} \tag{3.121}$$

where **a** is the center of mass acceleration vector and **v** is the center of mass velocity vector. Along the top face of the solid block, the boundary condition is

$$\frac{\partial^2\phi}{\partial n\,\partial t} = \frac{d^2s}{dt^2}\sin\theta + \frac{ds}{dt}\cos\theta\,\frac{\partial^2\phi}{\partial n\,\partial s} + \frac{ds}{dt}\sin\theta\,\frac{\partial^2\phi}{\partial s^2} \tag{3.122}$$

while, along the front face of the solid block, the boundary condition becomes

$$\frac{\partial^2\phi}{\partial n\,\partial t} = -\frac{d^2s}{dt^2}\sin\theta + \frac{ds}{dt}\cos\theta\,\frac{\partial^2\phi}{\partial n\,\partial s} - \frac{ds}{dt}\sin\theta\,\frac{\partial^2\phi}{\partial s^2}\,. \tag{3.123}$$

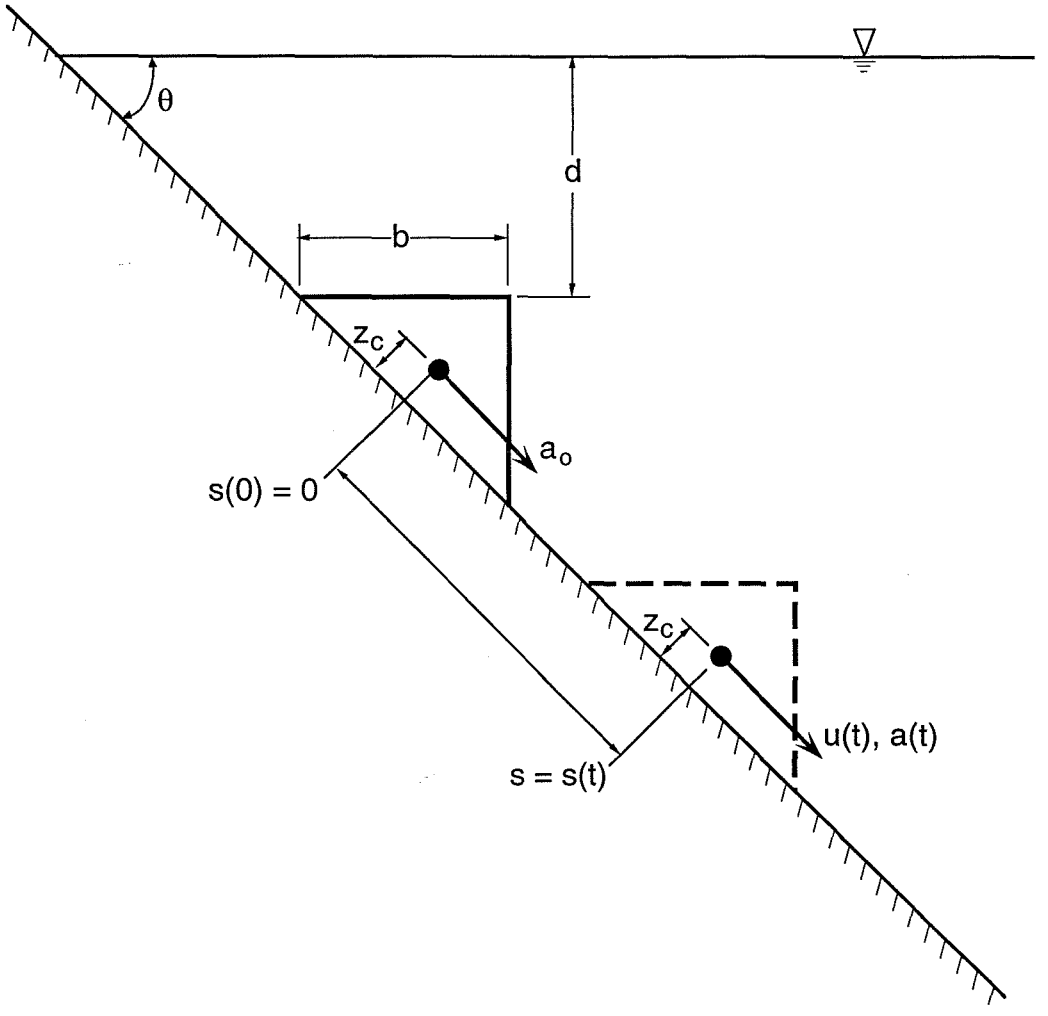

Figure 3.1: Schematic diagram of the initial conditions of a solid block landslide on a straight incline at an angle θ from horizontal. The solid block has a size b and an initial submergence d. At some later time, the center of mass position is given by s(t), the center of mass velocity by u(t), and the center of mass acceleration by a(t).

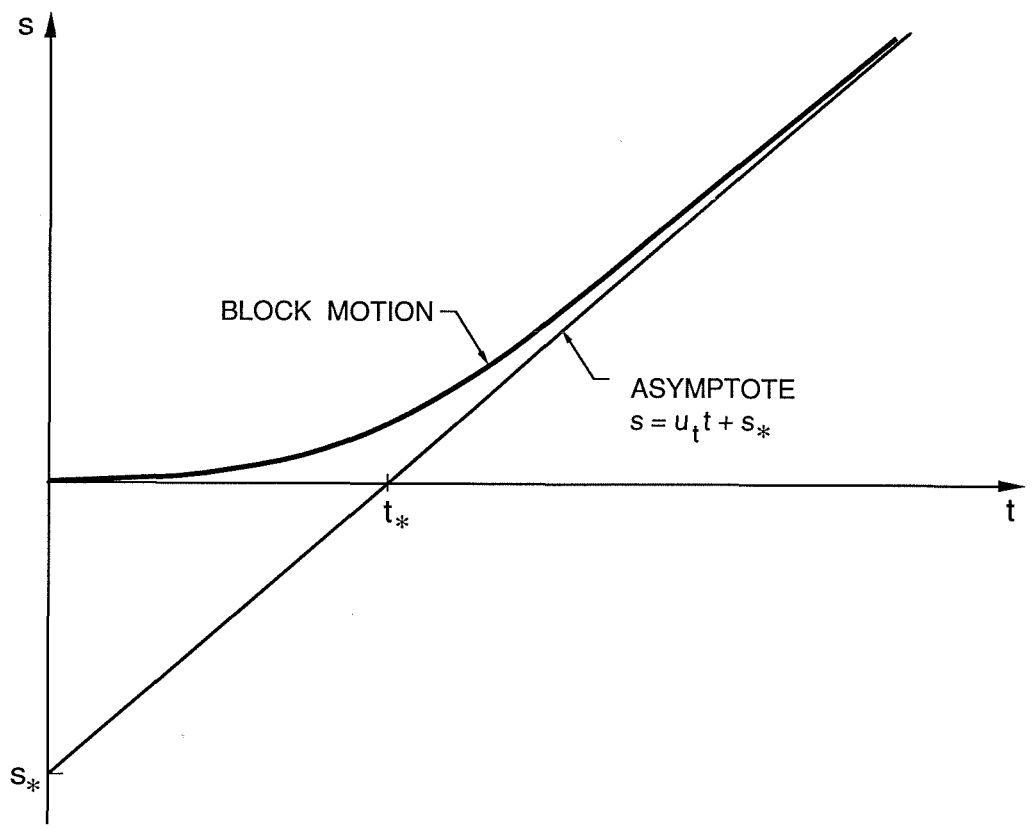

Figure 3.2: General form of solid block position as a function of time. All three cases begin at rest with an initial acceleration. All three cases also approach the asymptote exponentially. The asymptote is a straight line defined by the position s_* and the time t_* shown on the axes and given by equations (3.60) and (3.61), respectively.

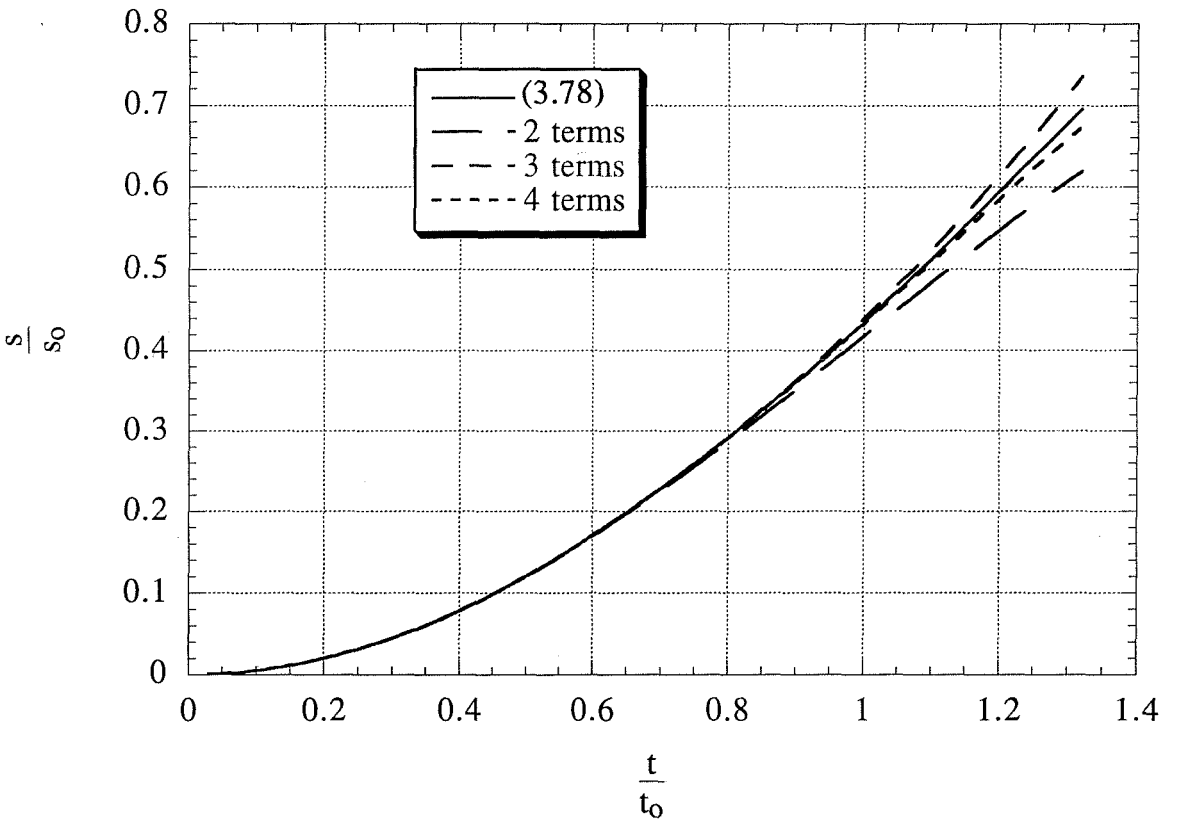

Figure 3.3: Comparison of theoretical solid block motion with the 2, 3, and 4 term Taylor series approximations of the exact motion. Differences are noticeable for 2 terms after $t/t_o \approx 0.9$, for 3 terms after $t/t_o \approx 1.1$, and for 4 terms after $t/t_o \approx 1.3$. The maximum near-field wave amplitude is usually reached around $t/t_o \approx 1$.

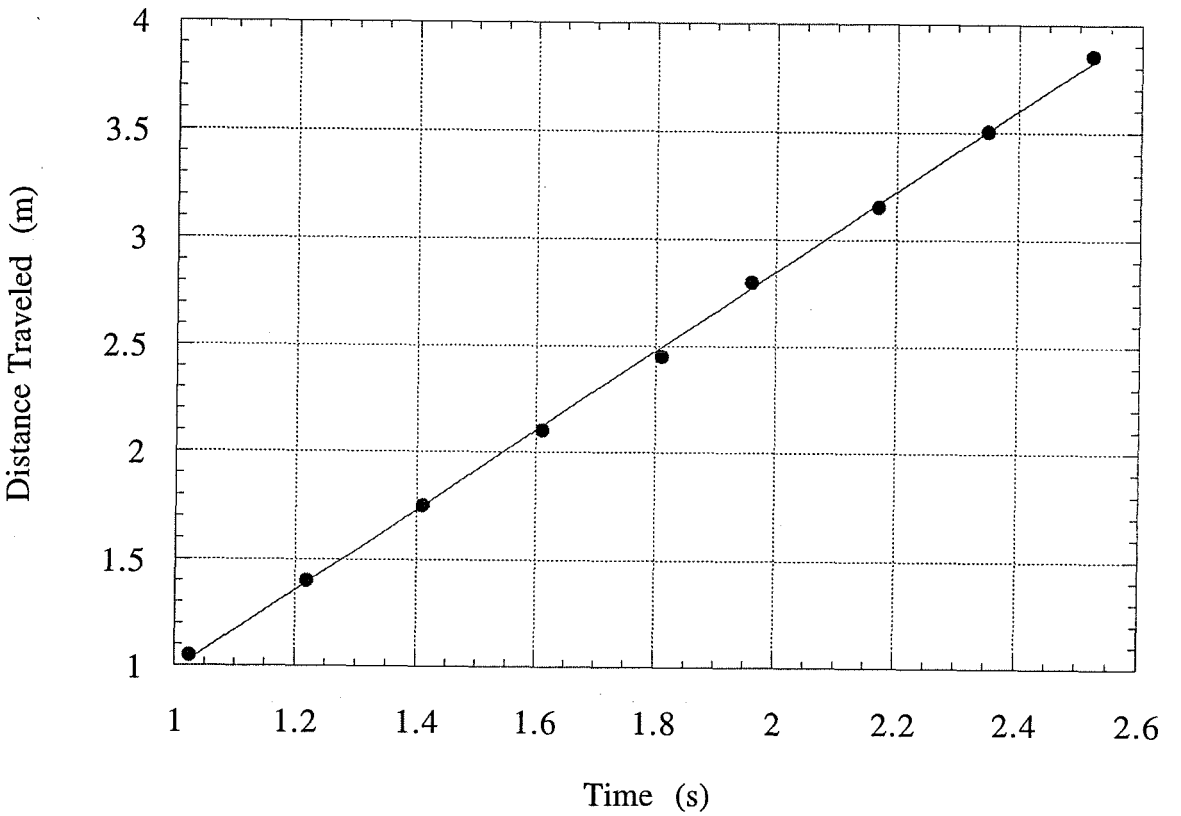

Figure 3.4: Distance that the Airy wave maximum has traveled from the piston wavemaker as a function of time. The linear least-squares curve fit of the experimental data yields a celerity c=1.87 m/s that is almost exactly the long wave celerity $c_o=\sqrt{gh}$ =1.85 m/s for the water depth h=0.35 m of the constant depth channel.

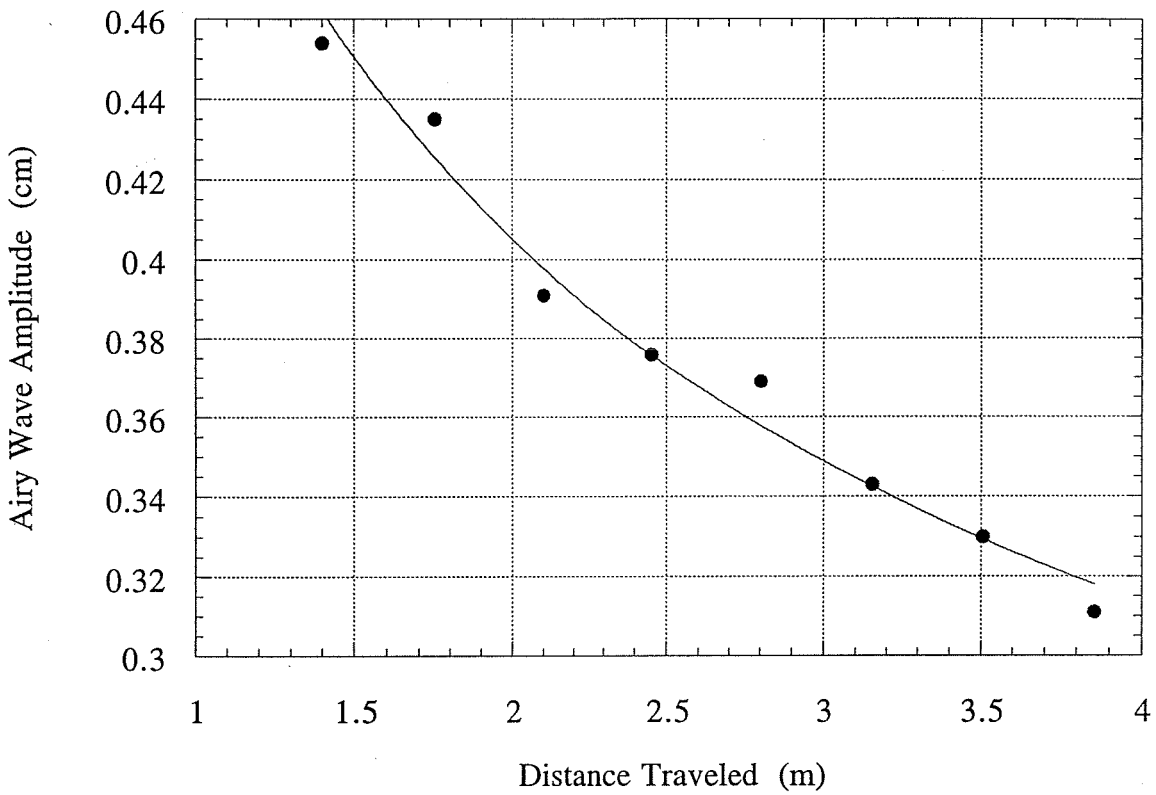

Figure 3.5: Amplitude of the Airy wave maximum as a function of the distance traveled. The power law least-squares curve fit of the experimental amplitudes yields a -0.37 power law decay whereas linear wave theory predicts a -0.33 power law decay of wave amplitude with distance.

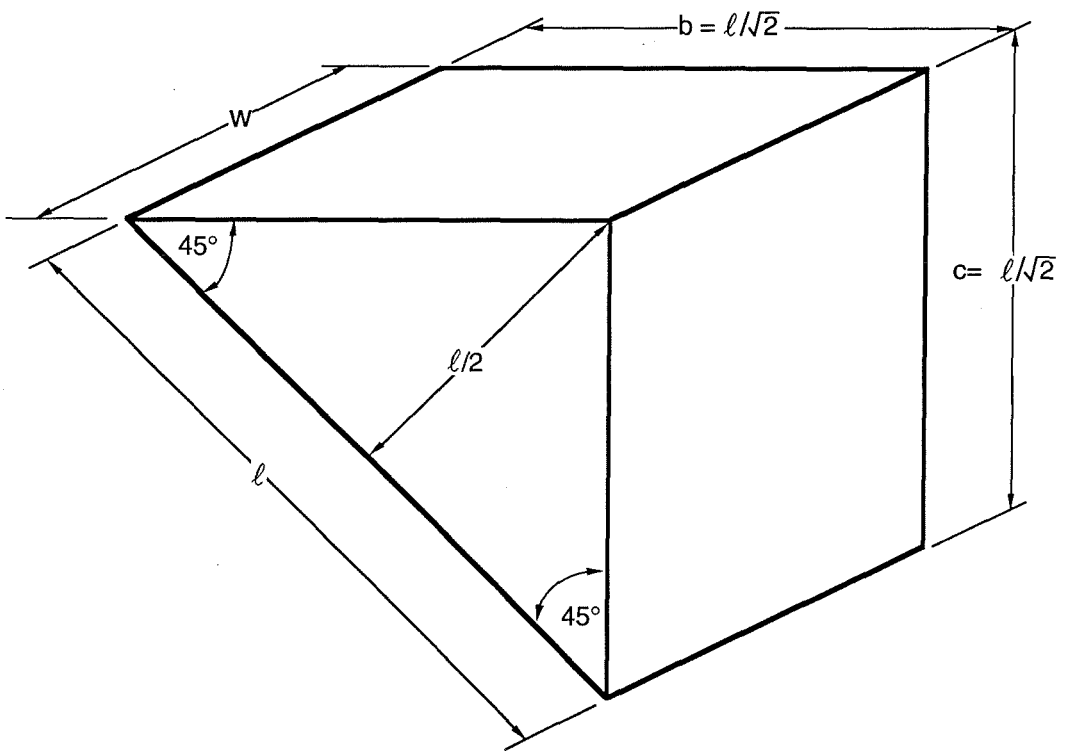

Figure 3.6: Schematic figure defining the length ℓ along the incline, the length b of the top face, the length c of the front face, and the width w of the solid blocks. While the blocks are defined as having a horizontal top face and vertical front face for an arbitrary incline angle, only an angle θ=45° from horizontal was studied experimentally.

Chapter 4

4. Experimental Apparatus and Procedures

This chapter describes the experimental wave tank, wave gauges, solid blocks, and materials used to produce and measure water waves generated by underwater landslides. In addition to describing the wave generation experiments, experiments conducted to determine solid block dynamical coefficients and material characteristics are detailed in this chapter. The methods used to measure landslide motion and shape in time are also described.

4.1 Wave Tank and Wave Gauge Characteristics

Wave generation experiments were conducted in a wave tank 10.1 cm wide, 9.14 m long, and 66 cm high constructed half of Lucite and half of wood lengthwise. An incline 45° from horizontal constructed entirely of Lucite spanned the depth at one end of the wave tank. See Figure 4.1 for a schematic of the wave tank and incline. The incline was sealed with 3.18 mm diameter rubber o-ring chord and held in place by normal forces applied to the side of the wave tank. For a solid block landslide, a 0.62 mm thick Nylon sheet covered the incline from wall to wall during solid block trials in order to smooth over four slots cut into the incline for the vertical gate shown in Figure 1.4. The clean Nylon sheet was placed in the water just prior to performing experiments and each block was put in the water just prior to the trial itself. Th solid block was allowed to slide a few times down the incline in order to remove air bubles trapped on the block surface. Material landslides were impounded behind the gate before it was rapidly drawn into the incline to begin a trial. A wave absorber was placed at the opposite end of the wave tank

that could reduce reflected wave amplitudes by up to 70%. The wave tank was filled with tap water, mixed with a relatively small amount of pool chlorine, and allowed to degas for a day before performing trials. Water temperature was always between 19°C and 20.5°C during experimentation. The water density ρ_o=998.2 kg/m^3 and water dynamic viscosity μ_o=1.002x10^{-3} kg/m·s at 20°C are used for calculations herein.

The wave absorber at the far end of the wave tank was built in two successive parts. The first part consisted of 125 vertical sheets of galvanized screen separated by 1.6 mm of water with each sheet spanning the width and depth of the wave tank. The screen was made of 0.22 mm diameter wire and comprised an orthogonal mesh of 50 wires per decimeter crossed with 70 wires per decimeter. The screen mesh possessed known wave dissipation characteristics based on the work of Goda and Ippen (1963). The second part of the wave absorber consisted of 0.85 m long sheets of rubberized horsehair piled between the screen sheets and the vertical wall at the end of the wave tank. The horsehair sheets filled in the top half of the wave tank since that was where dissipation of wave kinetic energy was most needed. Rubberized horsehair is a common and effective surface *covering for wave absorption on an inclined laboratory beach.*

Resistance wave gauges comprised of two parallel 0.254 mm diameter stainless steel wires stretched taut over 13 cm and separated by 3.18 mm were used to record the wave heights. The frame of each wave gauge was constructed of 4.76 mm stainless steel rod and was electrically grounded to shield the gauge characteristics from nearby metal objects that could change the local electric field. The wires are electrically insulated from the frame and each other except when immersed in a relatively conducting fluid such as tap water. Whenever possible the near-field wave gauge wires were immersed 3 cm in the water while the far-field wave gauge wires were always immersed 7 cm into the water. A 4.5 volt 2400 Hz excitation was provided by a preamplifier to the wave gauge. The output from the bridge circuit was demodulated and amplified before entering a data acquisition system. Schematics of the wave gauge construction and of the wave gauge circuit can be found in Figures 4.2 and 4.3, respectively. Wave gauge signals were acquired by a MacADIOS-8ain analog to digital board controlled with Superscope II software by GW Instruments. The accuracy of the 12 bit digitized signal over a 20 volt range was ±5 mV. Trials were recorded with a sampling rate of either 360 or 720 points per second. Calibration curves were acquired with a sampling rate of 10 points per second.

One wave gauge was positioned above the middle of the initial landslide location at x=0 while another wave gauge was located 4.25 channel depths away. These positions were chosen to provide a characteristic wave height above the wave generator as well as the far-field dispersive characteristics of the generated waves. The need for both near-field and far-field wave characteristics is exemplified by the water waves generated in Prince William Sound, Alaska following the 1964 Good Friday earthquake: some harbors experienced the immediate damage of near-field waves during the earthquake while other harbors experienced groups of large waves arriving several minutes following the earthquake. For simplicity, a constant depth channel has been used to study the far-field wave characteristics. The first wave gauge was positioned above the middle of the initial landslide location using two orthogonal rulers placed along the side of the clear wave tank. The position was accurate to within a millimeter in the direction of the channel. Duct tape attached to the wave gauge frame allowed the gauges to be submerged a similar depth each trial thereby producing consistent wave gauge characteristics. Measuring tape fixed to the top of the wave tank allowed the relative horizontal positions of the wave gauges to be known to within one millimeter. The second wave gauge was located 4.25 channel depths from the first wave gauge using the measuring tape on top of the wave tank. The end of a flexible tape measure was used to ensure that both wave gauges were centered widthwise.

Hand controlled stepper motors were used to calibrate the wave gauges by counting the number of steps and converting steps into a displacement. The calibration of the stepper motor displacement *versus* step number was accomplished with a dial gauge accurate to ±2.5 μm. The linear curve fit shown in Figure 4.4 relating the number of steps N to the wave gauge displacement D

$$D = 0.003299\,N \tag{4.1}$$

was identical for both motors. No backlash or hysteresis was measured, probably because the weight of the wave gauge assembly on the threads was sufficient to maintain continuous contact regardless of the direction of motor rotation. Equation (4.1) was used to relate the number of steps used in the wave gauge calibration to the displacement of the wave gauge.

Wave gauge calibrations were performed at least every 45 minutes and involved repeated departures from an initial zero level to some maximum relative position and back in

about 10 seconds. This type of dynamic calibration has been discussed by Pearlman (1963) and represents an effort to minimize errors due to meniscus reversal, wire wetting, and zero level voltage drift. Dynamic wave gauge calibration essentially simulates a wave coming and going thereby capturing similar behavior of the water near the gauge wires. The meniscus height on a thin wire is described theoretically by Lo (1983). Using a magnifying glass, the meniscus height on the wave gauge wires was estimated to be less than half the wire diameter. Whenever the wave gauge positions were moved along the wave tank, the gauges were calibrated again.

The digital voltage record of each calibration was filtered with a 33% "Smoothing Filter" in Superscope and then smoothed with a sliding average of 10 points prior to extracting calibration data. For a positive displacement the minimum voltage from the zero level and the maximum voltage from the smoothed voltage peak were read to give a voltage difference ΔV; for a negative displacement the opposite voltages were read. Calibration voltage difference ΔV *versus* net displacement ΔD data were fit by a cubic (or up to fifth order) polynomial as shown in Figure 4.5. The fourth order least-squares curve fit in Figure 4.5 is

$$\Delta D = -1.65\text{x}10^{-3} + 3.59\text{x}10^{-1}\,\Delta V + 1.77\text{x}10^{-2}\,\Delta V^2 - \\ - 9.70\text{x}10^{-4}\,\Delta V^3 - 4.12\text{x}10^{-4}\,\Delta V^4 \qquad (4.2)$$

where ΔV is in volts and ΔD is in centimeters. Equation (4.2) shows that the curve fits usually missed the origin of ΔV *versus* ΔD by a small amount since the condition $\Delta D=0$ when $\Delta V=0$ was not imposed on the curve fit.

The calibration curves were used to convert a voltage signal from a trial into a wave amplitude. In order to employ the calibration curve, a zero level voltage had to be chosen about one second before the trial began so that the initial wave amplitude is zero. The zero level voltage was sampled from the trial record after applying a 33% "Smoothing Filter" and then smoothing with a sliding average of 30 points. This single value was then subtracted from the unprocessed voltage signal to yield a trace of voltage differences ready to be converted to wave heights. Small vertical shifts in the calibration curves such as that in equation (4.2) were neglected so that a voltage difference of zero yielded a wave amplitude of zero

4.2 Solid Block Experiments

The interpretation of solid block wave generation experiments depends on the quality of the physical property and solid block motion information. These are provided by a separate set of measurements and experiments from the main body of this work. Measured and calculated solid block properties are provided immediately below. The special methods needed to conduct solid block landslide experiments are then given. The experiments performed to determine solid block dynamical coefficients are described last.

4.2.1 Solid Block Properties

Underwater landslide experiments were conducted with four solid blocks, where block number 2 could be modified to have (at least) eight different densities. All solid blocks were constructed from 8 sheets of PVC nominally 12.4 mm thick and glued together such that each laminate was parallel with the side walls of the tank. A large hole was drilled through the center of mass enabling a brass (or lead) ballast to be inserted into each solid block. All blocks with the subscript "n" (for normal) have a nearly identical density of about $\rho_b \approx 1860$ kg/m^3 achieved by a given-sized brass ballast and water trapped in the remainder of the hole. In the middle of the top face of each block a small metal eyelet 2 mm wide and with an 8 mm outer diameter was screwed into the PVC. A thin Nylon fishing line was attached to the eyelet to hold the block in place prior to a trial.

Figure 3.6 provides a schematic of a solid block and defines five relevant length scales. Table 4.1 provides the relevant physical characteristics of all solid blocks used herein. Since the solid blocks have two angles of $\theta=45°$, it follows that the length along the bottom of a solid block is

$$\ell = \sqrt{2}\ b = \sqrt{2}\ c \tag{4.3}$$

and the volume of the solid block is

$$V_b = \frac{w\ b^2}{2} = \frac{w\ \ell^2}{4}\ . \tag{4.4}$$

All lengths were measured with an accuracy of half of a millimeter. Small variations in solid block thickness and length voided attempts to make more accurate length

measurements. Therefore all lengths are known to within an error of about 1%. The solid block volumes are therefore known to within about 3% since they were calculated from equation (4.4). All four solid blocks are depicted in Figure 4.6. The solid block masses were measured on a Sartorius analytic balance accurate to 0.1 g. This represents a typical error in solid block mass of only 0.02%. The mass of displaced water was calculated from the solid block volume according to

$$m_o = \rho_o V_b \tag{4.5}$$

where the error in m_o is also about 3% since there is negligible error in the water density. The solid block density calculated from the equation

$$\rho_b = \frac{m_b}{V_b} \tag{4.6}$$

has an error that is dominated by the solid block volume V_b. Likewise, a reasonable error in the solid block density is also 3%. These errors determined the accuracy of quantities listed in Table 4.1, although additional decimal places are provided.

Table 4.1: Solid Block Physical Characteristics

Block #	ℓ (cm) $\pm$ 0.05 cm	w (cm) $\pm$ 0.05 cm	m_b (kg) $\pm$ 0.0001 kg	m_o (kg) $\pm$ 0.01 kg	ρ_b (kg/m^3) $\pm$ 60 kg/m^3
4_n	5.60	9.95	0.1431	0.078	1 835
3_n	8.65	9.90	0.3399	0.185	1 835
2_o	12.05	9.90	0.4404	0.359	1 225
2_a	12.05	9.90	0.5250	0.359	1 460
2_b	12.05	9.90	0.6136	0.359	1 710
2_n	12.05	9.90	0.6723	0.359	1 870
2_c	12.05	9.90	0.6958	0.359	1 935
2_d	12.05	9.90	0.7840	0.359	2 180
2_e	12.05	9.90	0.8664	0.359	2 465
2_l	12.05	9.90	0.9872	0.359	2 745
1_n	17.60	9.90	1.4496	0.765	1 890

4.2.2 Solid Block Landslides

The initial configuration of a solid block landslide experiment is shown in Figure 4.7. The wave gauge location is above the middle of the initial solid block position. The Nylon sheet covering the Lucite incline during solid block landslides is barely visible. Solid blocks were released from rest by letting go of the Nylon fishing line that held the block in place prior to an experiment. Just prior to a trial the Nylon fishing line was pinched between the forefinger and the incline so that "letting go" consisted of raising the forefinger. The absolute time of letting go was determined by shining a 10 mW He-Ne laser partially across the front of the solid block and partially onto a photodiode. The photodiode was contained in a black plastic container with a small hole on the front in order to minimize the intensity of 60 Hz fluorescent light flickering. When a systematic change in the photodiode voltage was detected, a very sensitive electronic triggering circuit emitted a voltage pulse along with the actual photodiode signal to the data acquisition system. The voltage pulse could detect the solid block motion before the photodiode signal changed by the resolvable voltage difference of ±5 mV and so was used at all times to establish when a solid block trial began. Experiments were repeated once no waves could be detected on the data acquisition system and fluid motion ceased which could be as short as every three minutes.

Solid block motion for the first 20 solid block trials (25-31, 41-44, and 47-55) was recorded by high speed movie camera. A LOCAM II camera ran a 100 foot roll of Eastman 7222, Double X, 200 ASA, 16 mm film at about 100 frames per second. The precise framing rate was known to within ±0.01 Hz from an LED inside the camera with an electronically controlled flashing rate of 100 Hz. The LED left a light mark on the film that could be seen on the left side of the frame. Since the framing rate was almost never exactly 100 Hz, the position of the light mark moved slowly either up or down the frame as the movie was projected. Let the light mark return to its original position in N frames. If the framing rate f_1 is less than the LED frequency f_2=100 Hz, then the light mark goes up the frame and there will have been $N+1=f_2/(f_2-f_1)$ light marks during the N frames. Solving for the framing rate gives $f_1=100N/(N+1)$. This equation simply means that there are exactly N frames in N+1 full periods of the flashing LED as can be readily verified by examining the movie film. On the other hand, if the framing rate f_1 is greater than the LED frequency, then the light mark goes down the frame and there will have been $N-1=f_2/(f_1-f_2)$ light marks during the N frames. Solving for the framing rate provides $f_1=100N/(N-1)$. The two equations are directly related to using a known

frequency to produce beats in an unknown frequency and then using the beat frequency to calculate the unknown frequency. Since typical values of N were on the order of several hundred, the corrections to the expected framing rate of 100 frames per second were small. Four trials and a calibration grid of 101.6 mm (four inch) squares could be recorded on a single roll of film. The calibration grid was deposited in the water against the near wall of the wave tank and ensured that the projected image was uniformly magnified over the entire projected image with a known magnification factor.

Solid block motion is often detected by eye on the movies four or more frames after the trial has actually begun. A method is described in the LOCAM camera manual whereby the initiation of an event can be recorded on the movie film using another LED. The initiation of solid block motion could be found to within a fraction of a frame by a single LED mark on the movie film triggered by the same photodiode triggering circuit described above. Since a single movie frame lasts about 10 ms and is 8 mm wide, a ruler could be used to locate the relative position of the LED mark and hence the beginning of a trial to within about ±1 ms. The mark was designed to appear on the film about 19.5 cm after the frame being exposed on a region of the film that was still moving through the camera with constant velocity -- the film is held stationary during frame exposure and so cannot be used for timing events more accurately than the framing rate (or ±10 ms for all solid block movies). A calibration procedure is described in the LOCAM camera manual in order to find the precise distance from the exposed frame to the LED mark for each roll of film. The electronic system for recording the LED mark failed to work for Trials 41, 42, 43 so that the initiation of solid block motion had to be inferred from the position *versus* time record of the solid block. This method of locating the beginning of a trial was deemed accurate to within a single frame (or ±10 ms). In addition, the LED calibration procedure failed to leave a detectable mark on the film of Trials 51-54 so that a typical distance of 19.4 cm had to be used to locate the beginning of a trial also to within about one frame of accuracy.

Movies of solid block motion were used to construct position *versus* time records in order to estimate the solid block initial acceleration. The movies were projected onto a surface with a uniform magnification of between 2.2-4.7 times based on a square calibration grid. The position of the top face of the solid block was marked on a large piece of paper for the first 20 frames or so of block motion with an accuracy of about ±1 mm on the sheet of paper. The results were then divided by the magnification factor as well as $\sin 45^\circ = 1/\sqrt{2}$ to obtain the position along the incline in real coordinates. The experimental initial

accelerations were obtained by curve fitting the first 15 frames (about 0.15 s) of the solid block position *versus* time with the parabola $s(t) \approx a_0 t^2/2$, which is the leading term in the Taylor series of equation (3.78) about $t=0^+$. Figure 4.8 shows the curve fit $s(t) \approx a_0 t^2/2$ of the observed solid block position in Trial 48 where error bars indicate one standard deviation. The initial acceleration obtained from the curve fit is $a_0=2.09$ m/s^2.

In order to save image processing time and improve acceleration accuracy, the acceleration of solid blocks during Trials 55-80 was obtained from a solid-state accelerometer. In the following chapter, calculations of solid block inertia based on position *versus* time movie records are shown to incur large errors. The accelerometer was contained within a 6.4 mm diameter cylinder that was 21.6 mm long. The cylinder was centered within a 7.6 mm by 7.6 mm square casing that was 12.7 mm long. The casing was fused to a 12.7 mm by 15.9 mm base that was 1.3 mm thick with screw holes available to fix the accelerometer to the solid blocks. Two screws were used to attach the accelerometer to the top face of either solid block 1, 2, or 3. These blocks were presumed to be massive enough and the accelerometer small enough not to significantly alter solid block and water motion. Solid block 4 was too small to attach the accelerometer onto the top face with screws and so was not studied with an accelerometer.

The accelerometer could measure gravitational acceleration with an amplitude that varied with the cosine of the angle between the accelerometer base and horizontal. The linear relation $V \propto kg\cos\theta$ between accelerometer voltage and effective gravity was verified by fixing solid block 2 to a leveled indexing head from a milling machine. The indexing head was used to rotate the solid block through increments of 15° while recording the accelerometer voltage. Figure 4.9 shows that the response of the accelerometer was linear over the 5-10 m/s^2 acceleration range tested. The zero level voltage and amplitude of the accelerometer signal were controlled by external electronics. Based on the static accelerometer calibration shown in Figure 4.9, the accuracy of accelerometer measurements is typically much less than 1% of actual acceleration values. Most of this error can be attributed to instrument drift over the duration of the static calibration. The accelerometer was used for much shorter durations during a solid block landslide and so would incur much less drift error. For calibration purposes, gravitational acceleration is taken to be $g=9.81$ m/s^2 herein.

In order to overcome the effects of drift, the accelerometer was calibrated for each solid block trial by i) measuring the acceleration prior to releasing the block and ii) by resting

the base of the solid block horizontally in the constant depth channel after the termination of the trial. The influence of solid block acceleration on the accelerometer output must be bounded by the two calibration points which represent known accelerations in the frame of reference of the solid block oriented with the incline. The calibration points were found by filtering the accelerometer signal with a 33% "Smoothing Filter" and then smoothing with a sliding average of 100 points. The two calibration voltages were then extracted from the voltage record -- one before and one after the actual trial. Figure 4.10 provides the unfiltered acceleration *versus* time from Trial 76. The process of letting go of the Nylon fishing line typically lasted between 20-50 ms based on the time taken to reach maximum acceleration and typically incurred no measurable upward acceleration whatsoever. The maximum acceleration in Figure 4.10 was reached just prior to 20 ms after the trial began. This maximum acceleration was taken as the initial acceleration of the solid block. Thereafter, the acceleration steadily declined towards zero with the exception of an unexplained rise and fall at around t=0.3 s. This was a regular feature of solid block acceleration traces and may have reflected a bump in the actual incline.

4.2.3 Experimental Dynamical Coefficient Determination

The dynamical coefficients needed to describe solid block motion are determined experimentally herein. The main effort related to this section involved reducing the errors inherent in measuring solid block initial accelerations and terminal velocities to the point where errors in the characteristic distance s_o and time t_o of solid block motion were acceptable. Since reasonably accurate dynamical data have been obtained, general values for the dynamical coefficients C_n, C_m, and C_d can be found and wave data should collapse in a correct nondimensional wavemaker plot. The dynamical coefficients allow the solid block motion to be generalized beyond the experiments presented herein; the collapse of wavemaker data will indicate a general wavemaker curve for water waves generated by underwater landslides. In passing, the theoretical simplification in Chapter 3 of a constant added mass coefficient can now be justified based on these experimental results.

Trials 25-31 and 41-42 were performed with all of the computerized data acquisition and timing devices described in Section 4.2.2 above. However, when removing the lead ballast from solid block 2 after Trial 42, the PVC laminates comprising the block came apart and needed to be reglued. It will become apparent in the next chapter that the subsequent block dynamics differ just enough to produce generally larger wave

amplitudes. The dynamical analyses performed in this section apply solely to the new solid block 2 used in Trials 47 and onward. Accurate dynamical data for the old block 2 trials are not available. Consequently, the results from this section should be applied to old block 2 trials with caution. However, sufficient trials have been performed such that curve fits of the accumulated data are not significantly affected by the absence or presence of the older block 2 data regardless of the larger dynamical errors.

4.2.3.1 Solid Block Coulombic Friction

The Coulombic friction was analyzed in a separate water tank with the same solid blocks and Nylon incline surface used in the wave generation experiments. The incline angle could be readily adjusted and measured to within less than 1° of accuracy. The dynamic Coulombic friction coefficient can be written

$$C_n = \tan \psi \tag{4.7}$$

where the critical incline angle from horizontal ψ is the critical angle at which a solid block is able to slide without accelerating or decelerating. Three methods were devised to determine ψ experimentally: i) finding the static Coulombic coefficient by increasing the incline angle until the block started sliding, ii) pulling the solid block gently up the incline and finding the angle at which it no longer slid back down and iii) finding the critical angle at which a solid block, once set in motion down the incline, continued moving. Interestingly, none of these methods yielded the same critical angle although they differed by only ±2°. The largest critical angle was found to be that associated with the static Coulombic friction. In general, static Coulombic friction is greater than dynamic Coulombic friction. A solid block set in motion down the incline was always found to continue accelerating down the incline. Hence, the measured angle was typically a little bit above the critical value. However, this critical angle was typically 4° less than the static critical angle and was the smallest critical angle. The intermediate values of ψ obtained by pulling the solid block up the incline were used as the critical incline angle herein and were typically half way between the other two critical angles.

4.2.3.2 Solid Block Initial Acceleration and Added Mass

The initial acceleration of solid blocks was found from movie records for the first 19 solid block trials and directly from an accelerometer for 26 subsequent trials. The initial acceleration a_o of a solid block is an important characteristic of the entire block motion along the incline and depends on the added mass of surrounding water. Since the solid blocks are typically twice as dense as the ambient water and $C_m \approx 1$, the added mass does not dominate block inertia. In general, the added mass coefficient associated with the initial acceleration is a function of two parameters $C_m = C_m(d/b, \theta)$. The number of nondimensional parameters is short, in part because the added mass is evaluated at $t=0^+$ before the solid block has actually gone anywhere. Moreover, the influence of the incline angle θ on the added mass coefficient is not studied herein. By measuring the initial acceleration of solid blocks, the dependence of the added mass coefficient C_m at $t=0^+$ on initial submergence can be found for the given incline angle $\theta=45°$.

4.2.3.3 Solid Block Terminal Velocity and Drag

Accurate measurements of the terminal velocity can be used to determine the drag coefficient of a solid block. Since the apex of the solid block is sharp and forms the starting vortex shown in Figure 1.3, the drag coefficient is assumed to be independent of the instantaneous block Reynolds number $Re = \rho_o b u / \mu_o$ (as are other objects with well-defined points of separation). Hence, a constant value of C_d is able to determine form drag over the entire block motion. For a typical block size and initial acceleration, $Re=1$ when $t \approx 2$ μs which is too early in the solid block motion to account for the rise time in the solid block acceleration shown in Figure 4.10; at terminal velocity the Reynolds number is on the order of 10^5. It has been shown above that the starting vortex has a negligible contribution to the drag coefficient of the solid block. Under these conditions, the drag coefficient should be a function $C_d = C_d(\theta)$ of only the incline angle provided the top face of the solid block is defined as horizontal while the front face is defined as vertical. Theoretically, the terminal velocity is given by

$$u_t = \sqrt{\frac{2\,(m_b - m_o)\,g\,(\sin\theta - C_n \cos\theta)}{C_d\,\rho_o\,w\,\ell\,\cos\theta\,\sin\theta}} =$$

$$= \sqrt{\frac{(\rho_b - \rho_o)\,\ell\,g\,(\sin\theta - C_n \cos\theta)}{C_d\,\rho_o}} \qquad (4.8)$$

where the general definitions of $b \equiv \ell\cos\theta$, $c \equiv \ell\sin\theta$, and $V \equiv wbc/2$ have been used to simplify the expression. The solid block terminal velocity was found by letting the block slide 80 cm down the incline and then counting the number of clock cycles it took to traverse two laser beams. The two laser beams were practically parallel and crossed the wave tank just above the incline surface at the toe of the slope. Two photodiodes and a sensitive trigger circuit were used to begin and end counting clock cycles at $2 \times 10^5 \pm 1$ Hz when the laser beams were cut by a block. A straight 12.5 mm thick Lucite sheet was inserted between the usual incline and the Nylon in order to reduce experimental scatter induced by the wavy incline. Between 10 and 16 measurements of the terminal velocity were taken for each solid block when the laser beams were separated by 77.2 ± 0.1 mm. Three measurements of the terminal velocity were made for each solid block when the laser beams were separated by 29.4 ± 0.1 mm. For the heavier solid blocks, the smaller laser separation distance (farther from the point of release) increased the measured velocity by a few per cent. There was no practical way to further increase the sliding distance or decrease the laser separation in the wave tank.

4.3 Material Experiments

The ability to interpret (and predict) the results of material landslide wave generation experiments depends on a wide variety of measured properties. These are typically provided by a separate set of experiments from the main body of this work. Measured and calculated material properties are described immediately below. The special methods needed to conduct material landslide experiments are then given. The methods used to determine material landslide motion and deformation are described last.

4.3.1 Material Properties

An underwater landslide often has well-defined local material properties prior to failure or away from the failure plane. A list of physical variables that describe the local state of a landslide material was established in Section 3.1.2. One such variable is the material solid volume fraction which is employed in soil mechanics, in suspension rheology, and for granular media properties alike. The material solid volume fraction ν_s in a total volume V_o occupied by material and water is

$$\nu_s = \frac{V_m}{V_o} \tag{4.9}$$

given a solid material volume V_m. Both volumes were measured in a 1 liter graduated cylinder accurate to within ±5 ml since there was practically no air trapped within the material interstices. The material volume V_m was determined by the displacement of the water surface after material was added to the cylinder. The total volume V_o of material and water at the bottom of the cylinder was read from the location of the horizontal material surface. Given a typical total volume $V_o \approx 370$ ml and a typical material volume $V_m \approx 215$ ml, the expected accuracy of the volume measurements is ±1.4% and ±2.3%, respectively. The theoretical accuracy of the typical solid volume fraction $\nu_s \approx 0.58$ is therefore ±0.02 or ±3.7% of its typical value.

The measurements of volumes and solid volume fraction for each landslide material are provided in Table 4.2. Almost all solid volume fractions are between the random loose packing limit $\nu_s \approx 0.50$ and the random close packing limit $\nu_s \approx 0.63$ given by Shapiro and Probstein (1992) for monodisperse suspensions. The more angular crushed calcite and garnet sand have lower solid volume fractions. Almost all spherical particles had solid volume fractions between 0.58-0.61 with the exception of 3 mm lead shot which had a solid volume fraction of 0.65. The oblate spheroid geometry of the 3 mm lead shot in combination with its very high density may have contributed to the high particle packing. Uniform spheres can achieve a theoretical maximum solid volume fraction for a face centered cubic lattice of $\nu_{s.max} = \pi \sqrt{2}/6 \approx 0.74$.

The mass of the landslide materials used in most experiments is provided in Table 4.2 from measurements on a Sartorius analytical balance accurate to ±0.1 g. The error in the measurement is negligible compared to that of the solid volume fraction. There were four trials performed with landslide masses other than those shown in Table 4.2. These are Trial 40 with a 572.7 g mass of crushed calcite, Trial 91 with a 945.4 g mass of 3 mm glass beads, Trial 92 with a 367.3 g mass of 1 mm glass beads, and Trial 93 with a 252.8 g mass of 1 mm glass beads. Most of these experiments were conducted to study the role of particle size divided by landslide size as a nondimensional variable governing landslide motion and wave generation. Additional properties of landslide materials are given in Table 4.3.

The material volume and mass were employed to calculate the material density $\rho_m = m/V_m$ to within about ±4% accuracy for three landslide materials. However, a model S-100 specific gravity balance from Henry Troemner Inc. was used to obtain much more accurate material density values for the majority of the landslide materials. The balance relied on four readings to calculate the specific gravity: m_1 of the empty basket in air, m_2 of the basket containing the material sample in air, m_3 of the empty basket in water, and m_4 of the basket containing the material sample in water. Figure 4.11 shows the four measurements being made for 3 mm steel shot. The equation

$$\frac{\rho_m}{\rho_o} = \gamma = \frac{m_1 - m_2}{m_1 - m_2 - m_3 + m_4} \tag{4.10}$$

yields the specific density, where the density of water ρ_o was given in Section 4.1 to within ±0.1%. Readings from this sensitive balance had a combined accuracy and repeatability of less than ±1 kg/m^3 which means that the material density is actually limited in accuracy by uncertainty in the water density.

The initial suspension density (sometimes called the bulk density) of a material landslide was calculated from

$$\rho_s = \nu_s \rho_m + (1 - \nu_s) \rho_o \tag{4.11}$$

where ρ_m is the known material density. Taking the logarithm of both sides and differentiating the right side with respect to only the solid volume fraction gives

$$\frac{d\rho_s}{\rho_s} = \frac{1}{1 + \dfrac{1}{\nu_s (\gamma - 1)}} \frac{d\nu_s}{\nu_s} \approx \frac{1}{2} \frac{d\nu_s}{\nu_s} \tag{4.12}$$

which shows that the error in the suspension density is reduced to ±1.9% or about half the error in the solid volume fraction for most landslide materials.

Table 4.2: Mass Characteristics of the Landslide Materials Used For Trials

Material	V_o (ml) ± 5 ml	V_m (ml) ± 5 ml	ν_s ± 0.02	m (g) ± 0.1 g	ρ_m (kg/m^3) ± 1 kg/m^3	ρ_s (kg/m^3) ± 40 kg/m^3
Crushed Calcite	355	195	0.55	523.6	2 732	1 950
0.5 mm Glass Beads	375	225	0.60	566.0	2 471*	1 882
1 mm Glass Beads	350	210	0.60	536.9	2 520	1 910
3 mm Glass Beads	365	220	0.60	567.1	2 563	1 935
12 mm Marbles	385	230	0.60	565.9	2 499	1 899
2 mm Lead Shot	360	220	0.61	2 425.4	11 025*	7 114
3 mm Lead Shot	375	245	0.65	2 619.0	10 727	7 321
3 mm Steel Shot	370	220	0.59	1 716.2	7 954	5 102
Garnet Sand	360	190	0.53	776.0	4 097	2 640

* Density calculated from landslide mass and material volume.

Note that additional decimal places are provided for quantities in Table 4.2 in order to avoid propagating round-off errors in calculations. Additional properties of landslide materials are given in Table 4.3. Since the material mass and material density have errors of less than 0.1%, the material volume V_m can be calculated from

$$V_m = \frac{m}{\rho_m} . \tag{4.13}$$

with much higher accuracy than the displaced water volume given in Table 4.2. The solid volume fraction and suspension density can then be recalculated with about half the error shown. However, such accuracy would not assist in the evaluation of experimental results discussed in Chapter 5 since the solid volume fraction varies by at most ±0.01 and the suspension density varies by at most ±1% for steel shot. Experimental errors for landslide motion and deformation are expected to be much bigger in magnitude. Note that the buoyant density of the suspension prior to a landslide is given by

$$\rho_s - \rho_o = \nu_s (\rho_m - \rho_o) \tag{4.14}$$

since the suspension is treated as a separate bulk fluid even though it also contains water in the interstices.

The internal friction angle ϕ and incline friction angle ψ were determined experimentally for most landslide materials. The internal friction angle ϕ governs failure throughout the mass of landslide material while the incline friction angle ψ is related to the Coulombic friction (or sliding) of the landslide material on the Lucite incline. Eight Lucite sheets 10.2 cm by 30.4 cm were given Lucite sides 2.2 cm high to laterally contain the landslide material being tested. The material resting on the sheet approximated an infinite slope in soil mechanics. A material with a nominal diameter of 3 mm could have about 10 random monolayers deposited on the Lucite sheet with 45 particles spanning the width and 150 particles spanning the length. As explained in Section 2.4, failure is governed solely by the angle of inclination in cohesionless materials with no excess pore water pressure and no external load. If the internal friction angle ϕ was being determined, then a random layer of landslide material had been deposited on the Lucite sheet and held in place by a thin layer of silicone sealant. The measurement of the friction angle was made after the silicone dried the random monolayer of particles in place. One end of the Lucite sheet rested on the bottom of a wave tank filled with water while the other end was slowly raised within the water by a point gauge. When the material failed, as shown in Figure 4.12 for the 3 mm steel shot, then the vertical height of the raised end of the Lucite sheet was measured. Clearly, the sine of the friction angle was the measured height divided by the length of the Lucite sheet. Each material was tested three to five times. If the incline friction angle ψ was being determined, then the material was deposited directly onto the Lucite sheet and tested. The average results of the measurements are summarized in Table 4.3 for all landslide materials tested. The errors indicated in Table 4.3 are due solely to repeatability.

Material particles are characterized herein by their nominal diameter, their standard deviation from the nominal diameter, and their shape factor as a measure of particle symmetry. Garnet sand particles are the only landslide particles that are not described in this manner. The size distribution of garnet particles was found from sieving the sand. Therefore, its size analysis deviates somewhat from materials with larger particles that could be readily manipulated and individually measured. Moreover, the sieving results reveal that garnet sand has a log-normal particle size distribution. The garnet sand used herein has a geometric mean of $\mu_g \approx 400$ μm and a geometric standard deviation of $\sigma_g \approx 1.3$; therefore, about 68.3% of all garnet particles have sizes between $\mu_g/\sigma_g = 308$ μm and $\mu_g \sigma_g = 520$ μm. The nominal diameters of all other material particles are distributed in a Gaussian manner as typified by Figure 4.13 for 3 mm lead shot. Crushed calcite also

has a Gaussian distribution of nominal diameter because the particles being used in this work were extracted from only one sieve size fraction.

The nominal diameter of a particle is the diameter of a sphere with the same volume as the particle. Vanoni (1975) provides the nominal diameter as

$$D \equiv \sqrt[3]{\frac{6}{\pi}}\, V_p^{1/3} = 1.2407\, V_p^{1/3} \tag{4.15}$$

where V_p is the volume of a given particle. All particles other than the crushed calcite and garnet sand were assumed to be either spherical or ellipsoidal so that the volume could be calculated based on the measurement of up to three principal axes. The only particles that were visibly ellipsoidal were the 3 mm lead shot particles but the 3 mm glass beads and 12 mm marbles were also measured along three perpendicular axes. The volume of an ellipsoid with principal axes $d_1<d_2<d_3$ is given by

$$V = \frac{\pi\, d_1\, d_2\, d_3}{6} \tag{4.16}$$

where each axis was measured by hand with a Vernier caliper accurate to ±0.01 mm. The 3 mm steel shot and smaller glass and lead particles appeared to be perfectly spherical so that only one diameter was measured per particle. The volume of crushed calcite particles was found first by classifying a given particle into one of three shapes with well known volumetric formulae: prisms, parallelepipeds, or pyramids. For each shape class, three principal lengths d_1, d_2, d_3 were measured with the Vernier caliper. The volume of the particle was then calculated from the appropriate formula and converted into a nominal diameter.

It was decided to continue measuring particle sizes until the mean nominal diameter calculated from the sample particles was known to within chosen bounds. The expected per cent error in the mean for some sample from an unknown probability distribution follows from the Central Limit Theorem of statistics and is given by

$$\%\ \text{Error} \equiv 100\%\ \frac{\sigma}{\mu\sqrt{N}} \tag{4.17}$$

where μ is the sample mean, σ is the sample standard deviation, and N is the sample size. The error for the mean size of crushed calcite particles was ±2.1% from a sample of N=101 particles and that of the 0.5 mm glass beads was ±1.6% from a sample of N=47 particles. All other particle mean sizes were sampled until the expected error in the mean dropped below ±0.4% which required sample sizes ranging from N=20 particles to N=462 particles. The mean nominal diameters are given in Table 4.3 along with the sample standard deviations about the mean.

If one contemplates some of the possible ways to describe mathematically the geometric deviation of a material particle from a sphere, the odds are quite favorable that any given method will be related to the particle shape factor. Vanoni (1975) defines the shape factor of a particle based on the three principal distances that prescribe the particle volume $d_1<d_2<d_3$

$$SF \equiv \frac{d_1}{\sqrt{d_2\, d_3}} \tag{4.18}$$

where SF<1 for any particle other than a cube and a sphere. Strictly speaking, equation (4.18) applies only to oblate spheroids or ellipsoids with well-defined principal axes and round surfaces. However, the extension of the definition to particles with angular edges and rough surfaces is unavoidable for the materials used herein and the shape factor thereby becomes more a measure of particle symmetry than of particle sphericity. The mean shape factor for four landslide materials is given in Table 4.3. The shape factor was calculated from the same three principal measurements used to calculate the particle volume and nominal diameter. Given the mean shape factors of the 3 mm glass beads and 12 mm marbles, the assumption that the smaller glass beads and lead shot are spherical seems justified. In other words, appearances were not deceiving and a shape factor SF=1 can safely be assumed for the smaller glass beads and lead shot. The biggest mean error in the shape factor is 2.4% for the crushed calcite while all other shape factors had mean errors of less than 0.5%. The shape factor was normally distributed for all four landslide materials measured as shown in Figure 4.14 for 3 mm lead shot. There appears to be a direct correlation between shape factor and the incline friction angle. If this observation has a factual basis, then the shape factor for garnet sand should be even less than that of crushed calcite.

Table 4.3: Physical Properties of Landslide Materials

Material	ϕ (°)	ψ (°)	D (mm)	σ (μm)	SF	u_p (m/s)
Crushed Calcite	47 ± 2	20 ± 2	3.328	694	0.653	0.25
0.5 mm Glass Beads	NM	NM	0.500	56	NM	0.07
1 mm Glass Beads	30 ± 2	5 ± 2	1.257	41	NM	0.18
3 mm Glass Beads	29 ± 2	6 ± 2	2.959	43	0.982	0.37
12 mm Marbles	NM	NM	12.16	126	0.995	0.49
2 mm Lead Shot	32 ± 2	5 ± 2	2.059	132	NM	0.82
3 mm Lead Shot	34 ± 2	12 ± 2	3.114	57	0.825	1.00
3 mm Steel Shot	28 ± 2	6 ± 2	3.311	18	NM	0.76
Garnet Sand	38 ± 2	35 ± 2	0.40*	1.3*	NM	0.09

* Geometric mean and nondimensional geometric standard deviation given on page 103.
NM: not measured.

The terminal velocity of a single particle of the landslide material has some potential scaling uses in the discussion of landslide motion and deformation. The particle velocity u_p given in Table 4.3 is the unhindered, theoretical terminal velocity of a mean-sized particle for each landslide material. The nominal diameter was used in the formula for the particle velocity

$$u_p = \sqrt{\frac{4}{3}\left(\frac{\rho_m - \rho_o}{\rho_o}\right)\frac{D\,g}{C_d}} \tag{4.19}$$

where $C_d=C_d(Re)$ is given graphically and analytically by White (1991) and the Reynolds number $Re\equiv\rho_o u_p D/\mu_o$ is based on nominal diameter as well. The corrections for terminal velocity with shape factor given by Vanoni (1975) suggest that the terminal velocity for a typical crushed calcite particle should be $u_p\approx0.25$ m/s (instead of 0.41 m/s) and that there should be no significant shape factor effect on any other material particles including garnet sand. The accuracy of the particle velocities provided in Table 4.3 is typically ±5% since the drag coefficient, with an approximate error of ±10%, was by far the largest source of error in the calculation. The per cent error in the drag coefficient is halved by the square root in equation (4.19).

4.3.2 Material Landslides

A material landslide was initiated by retracting a vertical gate down into the Lucite incline. The gate motion into the incline was rapid enough to release the sediment mass in almost the same shape as when it was initially impounded behind the gate. The lead and steel shot landslides deformed by about a single particle length during gate retraction. The downward motion of the gate was necessary to minimize disruption of both the landslide material and the water free surface. When a gate is pulled up, the shearing induces material motion away from the incline that can completely alter the initial appearance of the sediment mass. In some cases not shown herein, almost all of the material was raised off of the incline due to gate motion towards the water surface. Moreover, the gate must be pulled through the water surface generating small waves and splash that interfere with detection of the underwater landslide-generated waves. Nevertheless, the downward gate motion sheared the landslide material which visibly energized a few adjacent particle layers in most materials studied. However, the main material mass remained intact and the water surface was minimally disturbed by gate motion. It is not yet known if a shear wave propagating through the landslide material affected the subsequent landslide motion or deformation. It is also important to note that retracting the gate must change the state of stress in the landslide material regardless of gate shearing: the landslide material goes from being supported by a solid retaining wall to being unsupported. Therefore, it is difficult to attribute observed landslide failure to either gate motion or a new state of stress. The aim of this thesis work is to describe wave generation based on observed landslide motion and deformation, not to explain the experimental landslide motion and deformation.

Three material landslide experiments (Trials 40, 81, and 82) were recorded with a framing rate of about 400 frames per second. The equations that gave the framing rate in Section 4.2.2 are only slightly modified: if the light mark goes up the frame and returns to its original position in N frames, then the framing rate is f_1=400N/N+1; if the light mark goes down the frame and returns to its original position in N frames, then the framing rate is f_1=400N/N-1. Naturally, the LED mark only appeared just about every fourth frame. All other material landslide trials were recorded at framing rates very close to 100 frames per second.

The gate was sufficiently thin and the incline was sufficiently rigid that gate retraction did not generate significant water waves. The gate was made of 0.4 mm thick stainless steel,

protruded up to 115 mm above the incline, and was 98 mm wide. Figure 4.15 shows the gate fully extended along with some of the Delrin pulleys used to guide the string that retracts the gate. The maximum wave amplitude measured from gate retraction alone was 50 μm and occurred 0.150 s into a trial as shown in Figure 4.16. This wave record was obtained above the middle of solid block 2 as it was held in place immediately behind the gate in water h=0.373 m deep -- in other words, the wave record is the same as many other near-field wave records with the exception that the landslide never moved. The far-field wave gauge did not record any wave amplitudes above the noise level of the wave gauge. The wave pattern shown in Figure 4.16 was not detected in any of the material landslide wave records and peaked too early in time to affect the maximum near-field wave amplitude η_{max} that usually occurred at around $t \approx 0.3$ s. Hence, the water waves generated by the gate retraction are considered negligible in these experiments.

The gate was retracted in about 40 ms by a Nylon braided string connected to a falling weight by a sequence of Delrin pulleys mounted on glass ball bearings. About 15 kg of lead fell vertically almost 0.5 m along sleave bearings before pulling the string taut and retracting the gate. The retraction mechanism is depicted in Figure 4.17. Since a roughly constant string tension was acting on the gate and the only retarding forces were dynamic Coulombic friction and viscous skin friction forces, the gate motion is approximated by

$$\frac{s}{s_o} = 2 - \frac{t}{t_o} - \exp\left(-\frac{t}{t_o}\right) \tag{4.20}$$

where s_o is the initial gate protrusion and t_o is the time constant of gate motion. This solution is identical to equation (3.56) except for the value of the initial gate position. Equation (4.20) is in the same form as equation (3.1) since gate motion can be characterized by one characteristic distance and one characteristic time. The time constant t_o is an unknown constant that depends on the amount and type of landslide material. Figure 4.18 shows a curve fit of the observed gate motion with equation (4.20) where s_o=10.7 cm and t_o=20.9 ms. In order to determine the time of complete gate retraction s=0, the position ratio s/s_o was measured for each high speed movie frame. Since the time interval between movie frames was either 10 ms or 2.5 ms (depending on the framing rate), the time constant t_o could in principle be determined uniquely from the gate position observations.

However, equation (4.20) cannot be inverted in analytical form to provide time as a function of position. Another method was sought whereby the beginning of each trial could be accurately determined to within a fraction of a movie frame. The gate position *versus* time was calculated seven times on a spreadsheet for time constants t_0=16, 18, 20, 22, 24, 26, and 28 ms at time intervals of 0.5 ms. For each material landslide trial, the nondimensional position data for each movie frame were grafted onto the spreadsheet calculations of nondimensional position. The time constant t_0 that correctly reproduced the known time interval (10 ms or 2.5 ms) between the position data was chosen as the best model of the gate motion. The fraction of a movie frame at which s=0 was extrapolated from the spreadsheet with a temporal accuracy of 1/20 of a frame. The fractional movie frame at which s=0 was taken as the beginning t=0 of a material landslide trial. The relative time of each subsequent movie frame was found by subtracting this fractional movie frame and converting frames to time using the framing rate. This method could locate the beginning of a material landslide trial to within ±0.5 ms. For a time constant of t_0=16 ms, the gate would retract in 29.5 ms; whereas, for a time constant of t_0=28 ms, the gate would retract in 51.5 ms. The gate motion was uniformly distributed over all time constants considered with a weighted average of 41 ms to become fully retracted.

The material landslide center of mass motion and deformation rate were found by tracing the landslide outline for individual frames from the high speed movie record. For a typical landslide, every third or fourth frame was traced with the first trace occurring before the trial began. Landslide outlines were traced by hand on 11x17 inch paper using a black felt marker. The accuracy of the tracing process was estimated to be ±1 mm around the landslide perimeter on the sheet of paper. Four registry marks were spaced 101.6 mm (four inches) apart along the outside of the incline. Two of the registry marks were always located with a black dot on the landslide traces. The two black dots were situated exactly 25.4 mm (one inch) below the bottom of the landslide on the paper. Therefore, the absolute vertical and horizontal position of the landslide centroid could be established from the two registry points as described in Appendix B. The traces were reduced 70% onto 8.5x14 inch paper and scanned by an HP ScanJet 4C at 600 dpi. The black and white image was loaded into a Power Mac computer by DeskScan II 2.2 software and saved as a PICT file. The PICT file was imported into NIH Image 1.61 software in order to process and analyze the image.

NIH Image identifies and analyzes particles including particle area, perimeter, and centroid. The area and perimeter are reported as pixel numbers while the geometric center of a particle is given as an absolute pixel position in the coordinate system of the scanned image. The first step in image processing was to fill in the outline of the landslide with solid black. Any spurious pixels remaining from the photocopying process were erased since they would otherwise be counted as a particle. Any particles that had detached from the main body of the landslide had to be connected to the landslide by a thin black line or else they would be counted as separate particles. Any open region surrounded entirely by landslide material had to be cut open with a thin white line or else the program would fill the empty space in and count the area. The two registry points were left as separate particles to be analyzed since their known separation distance would provide the size of a single pixel in the area and perimeter analyses.

Precise error estimates of material landslide motion and deformation rates are provided in Appendix B. However, important sources of error are introduced here in a qualitative manner. When tracing a material landslide, only the profile of the deforming landslide against the near wall was supposed to be traced. However, the lighting of certain materials and the position of the camera occasionally made it difficult to distinguish the top or front of the landslide from the profile. For most material landslides, the first twenty frames (or so) showed part of the front face of the landslide in perspective. This effect was easily compensated for, but, since the demarcation between the landslide profile and front face became blurred by particle motion and surface shearing, the correction may have been less than ideal. Last of all, the garnet sand and 0.5 mm glass bead landslides formed significant wakes behind the landslides where water and particles mixed. These wakes were included in the landslide trace despite the fact that the low particle concentrations implied that very little landslide mass was actually present. This effect needs to be considered when calculating the center of mass motion of a landslide since the centroid of the landslide trace and center of mass are no longer identical.

4.3.3 Experimental Material Deformation Rate

For the material landslides studied herein, material failure involved the acceleration and dilatation of a noncohesive, porous material that underwent deformation due to gravitational and surface shearing forces. Moreover, the eventual gravity current may not have traveled sufficient distance to reach an asymptotic structure along the relatively short experimental incline, thereby limiting the utility of steady state scalings. Last of all,

the prospect of finding an analytical solution of motion based on fundamental, nondimensional coefficients is poor, especially given the complicated fluid dynamic forces that shape the gravity current. Therefore, a descriptive model is used to characterize landslide motion by decomposing the landslide shape and position into a center of mass motion and a rate of strain. The center of mass motion of a material landslide follows directly from the landslide traces and image processing analysis described in the previous section. The rate of strain of the material landslide is inferred from the spreading of an isosceles triangle with the geometric center of the triangle located at the landslide center of mass. The mathematical description of this model was developed in Section 3.2.2.1. The motivation for this phenomenological model is the observation that most material landslides look like spreading triangles at early times. This can be seen, for example, in Figure 1.5 where the crushed calcite landslide appears triangular until around 0.23 s have elapsed. Garnet sand and 0.5 mm glass beads are the only materials for which this simple description of landslide deformation may not apply since the initial material mass essentially split into two distinct pieces early on in the landslide motion. Figure 5.10 shows four frames from the movie of the 0.5 mm glass bead landslide.

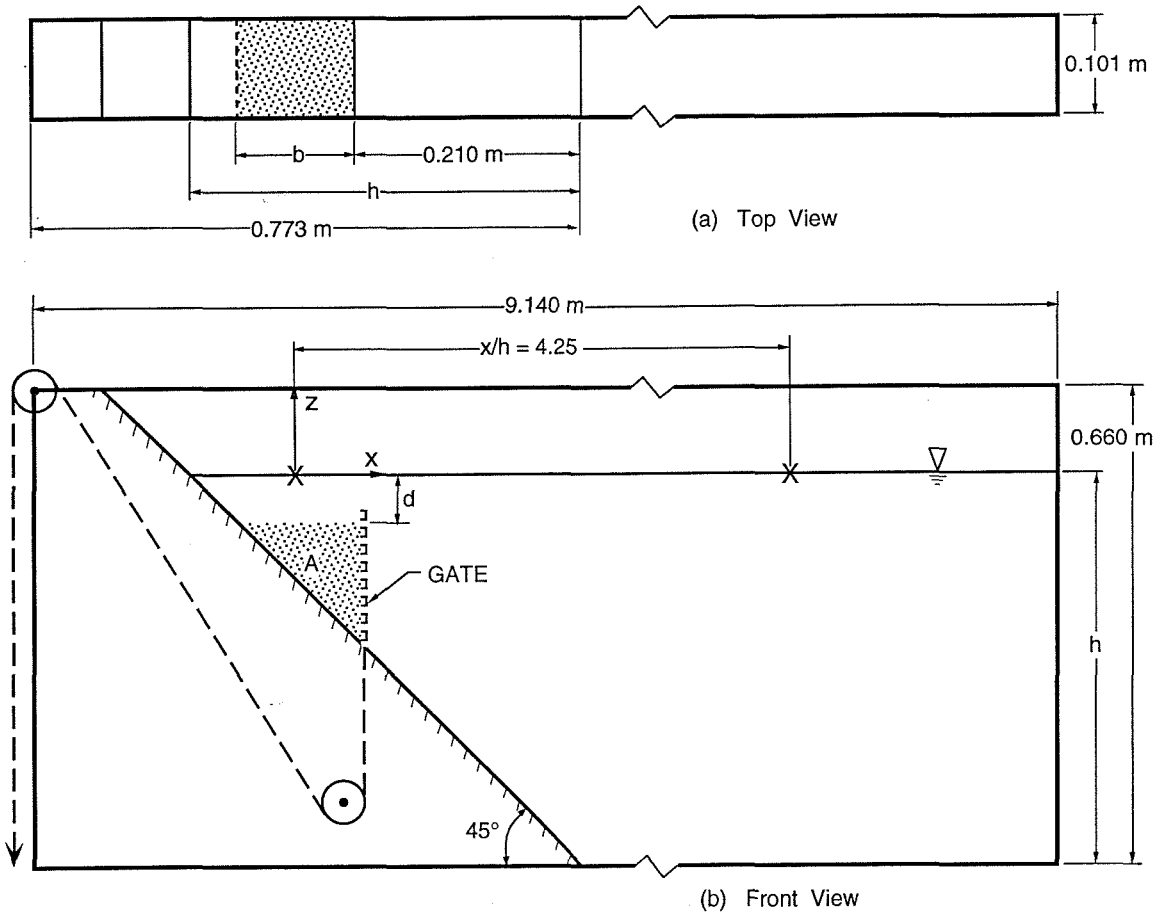

Figure 4.1: Schematic representation of the wave tank and incline with a fully extended gate. Typical near-field and far-field wave gauge locations are indicated by an x on the free surface. The landslide size b, landslide initial submergence d, landslide cross-sectional area A, and constant channel depth h are all defined.

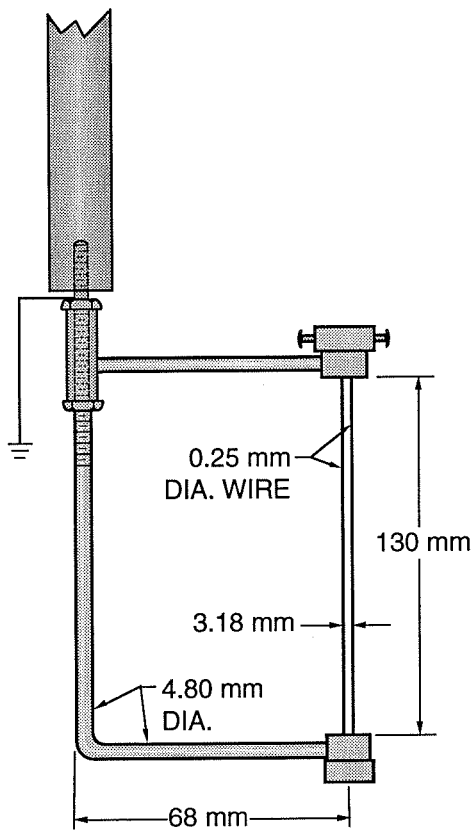

Figure 4.2: Drawing of a typical wave gauge used in this study.

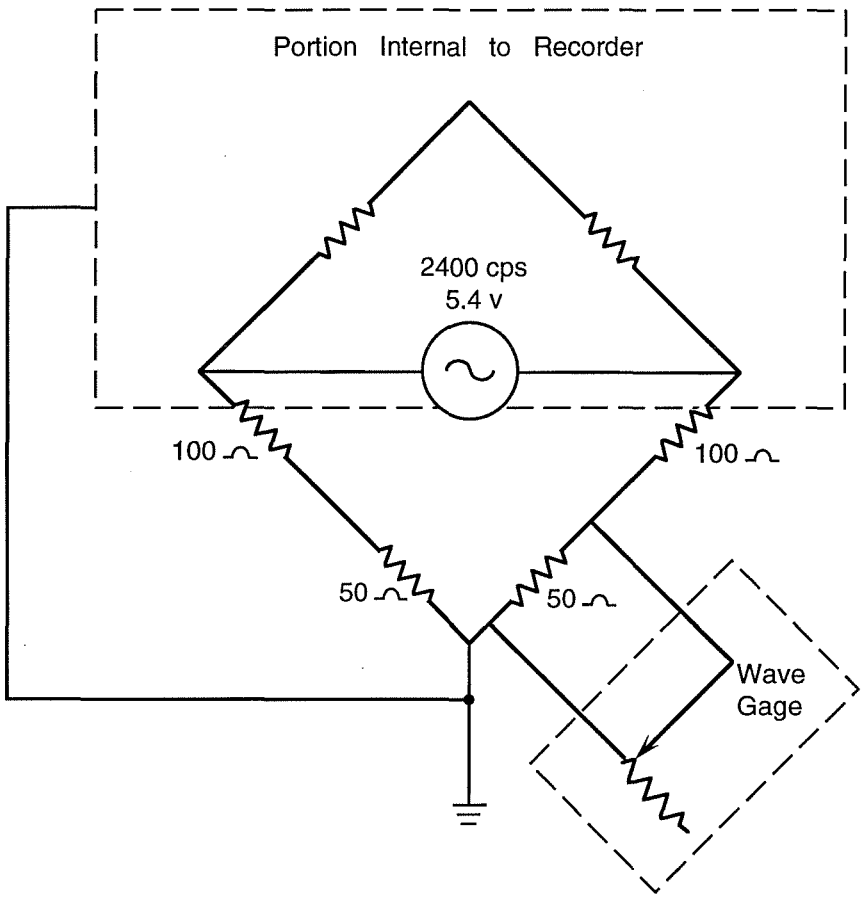

Figure 4.3: Circuit diagram of wave gauge electronics prior to rectifying the alternating voltage output.

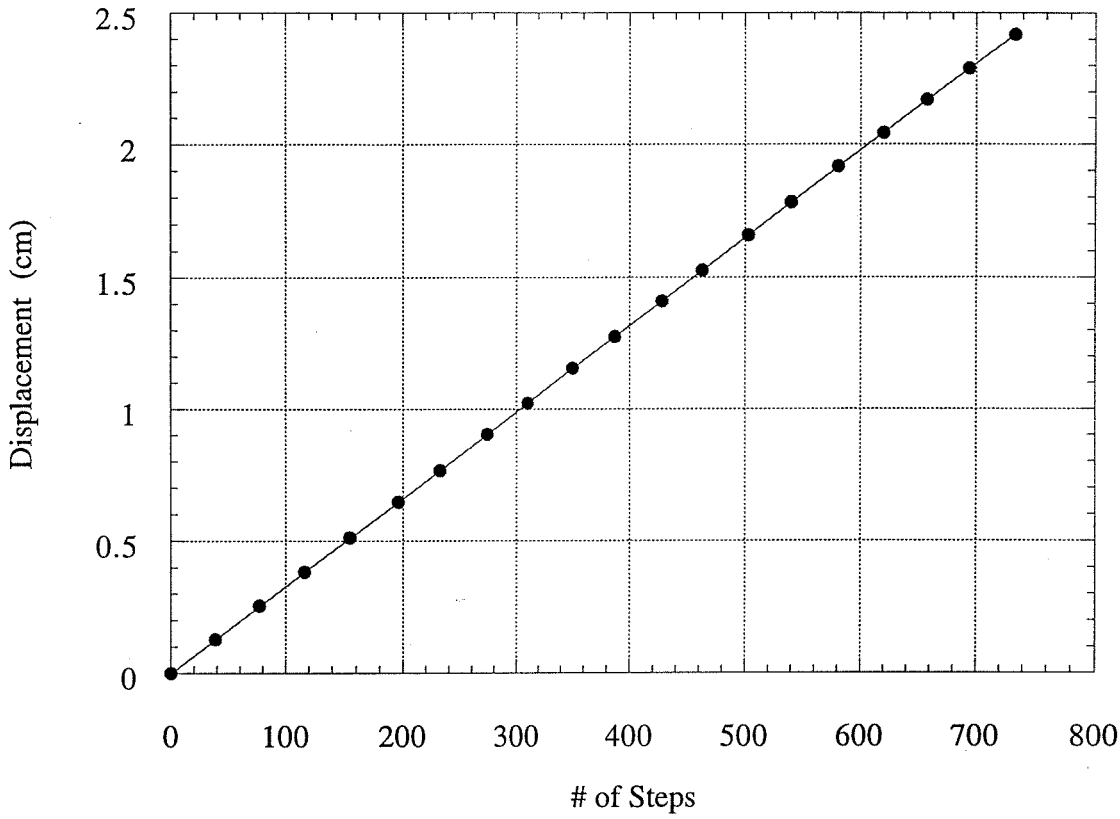

Figure 4.4: Calibration of the stepper motors used in turn to control wave gauge calibration. Displacement is a linear function of the step number and is given explicitly in equation (4.1). There was no measured gear backlash.

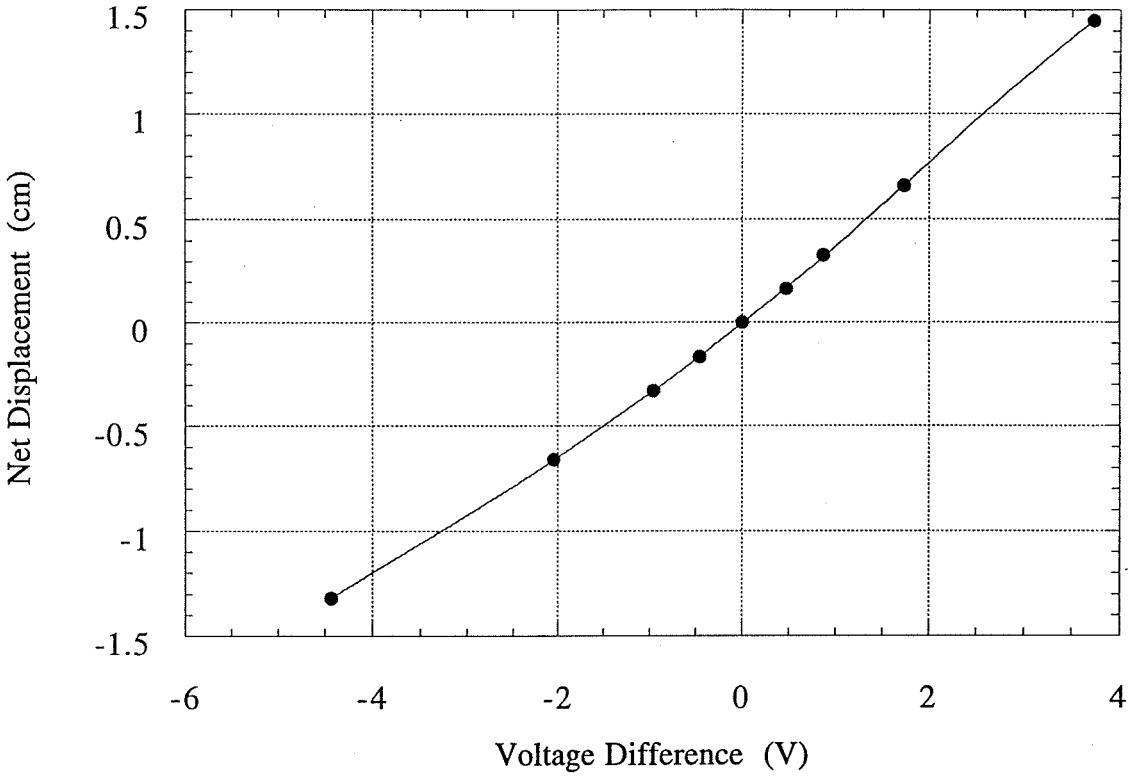

Figure 4.5: Least-squares curve fit of the calibration data of the near-field wave gauge performed for Trial 48. The fourth order polynomial of net displacement as a function of voltage difference is given by equation (4.2) in the text. The calibration curve is a typical example of the results obtained for this work.

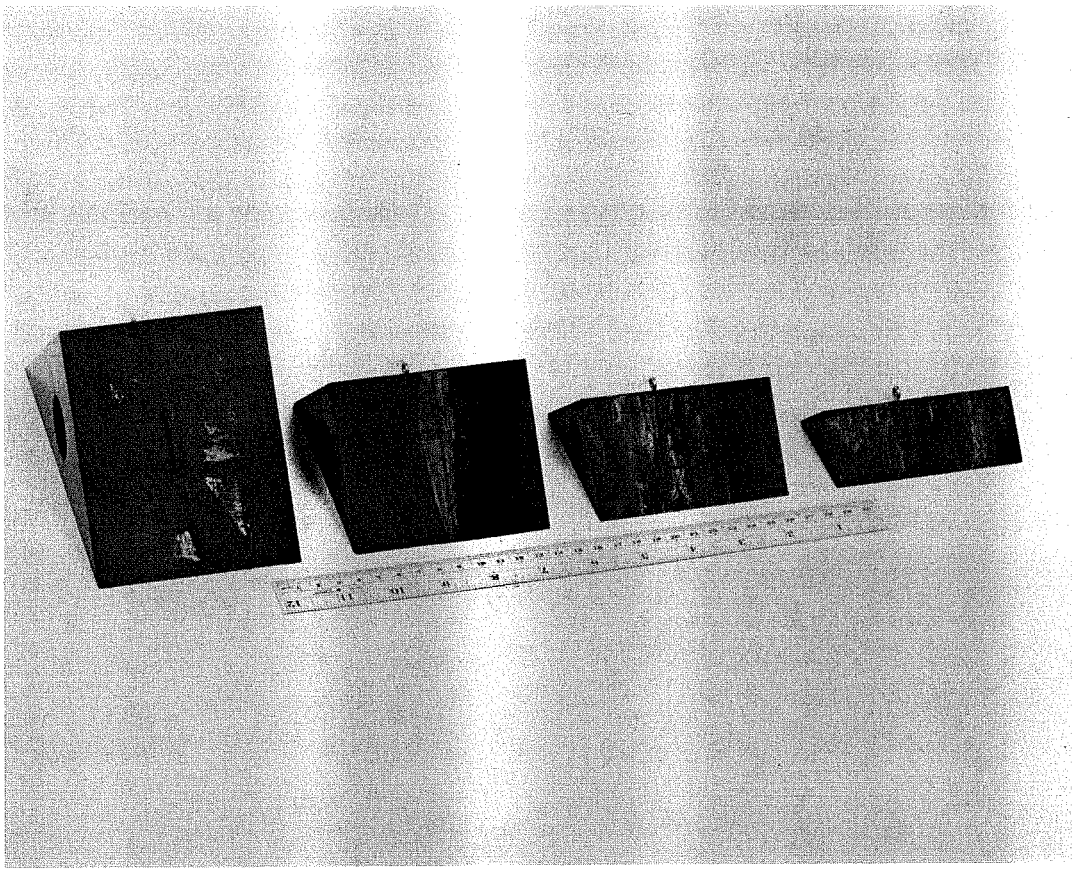

Figure 4.6: Photograph of the four solid blocks used in this work with block 1_n being the largest and block 4_n being the smallest. The subscript n denotes "normal". The eyelets used to support the solid blocks prior to a trial are visible on the top face of each block. The hole containing the brass (or lead) ballast is visible on the side of each block.

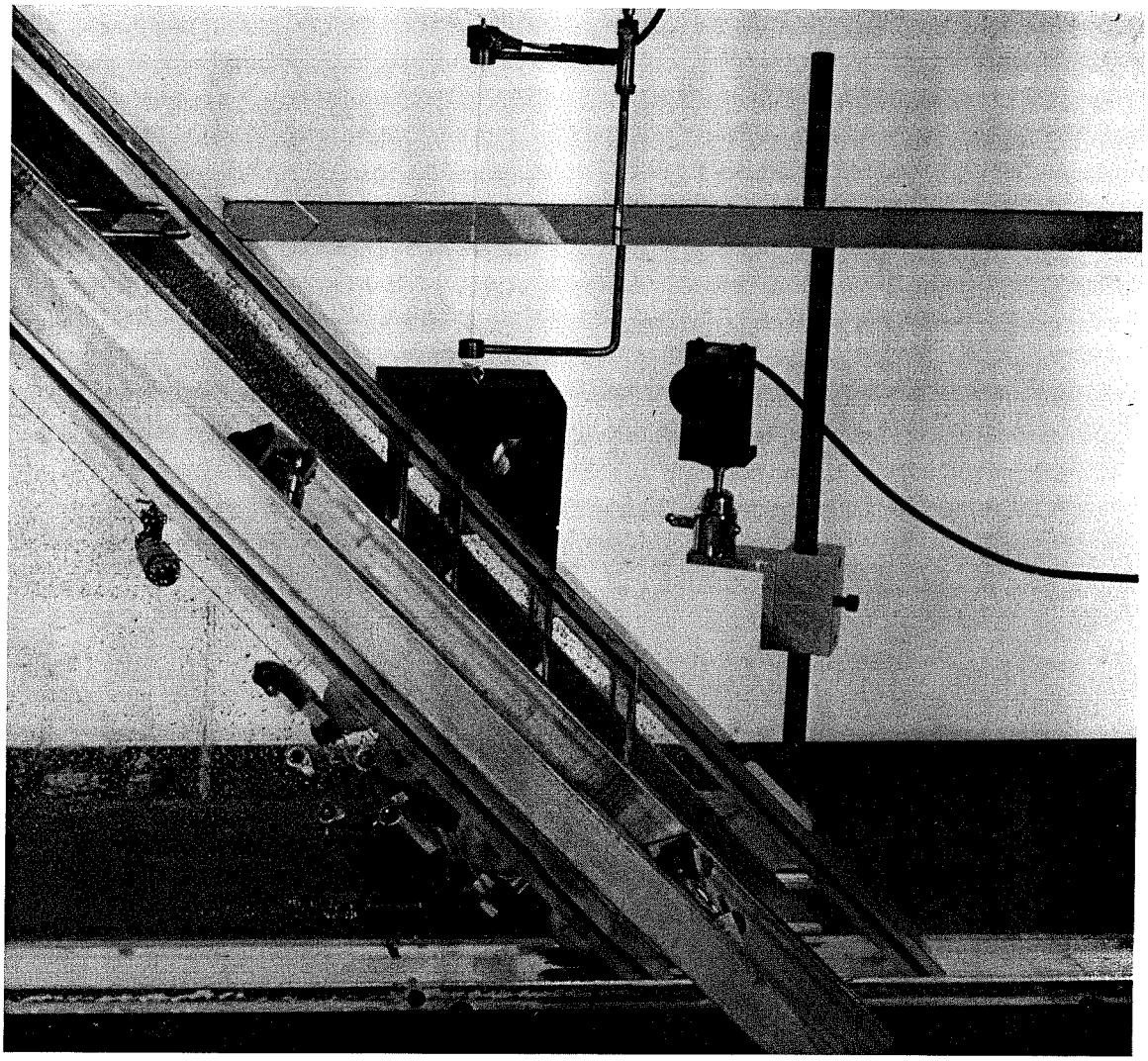

Figure 4.7: Photograph taken just prior to a solid block landslide. Nylon fishing line holds the block in place. Half of the 10 mW laser beam can be seen shining on the lower front face of the block; the other half of the beam is striking the photodiode in the black container. The wave gauge wires are above the middle of the top face of the solid block.

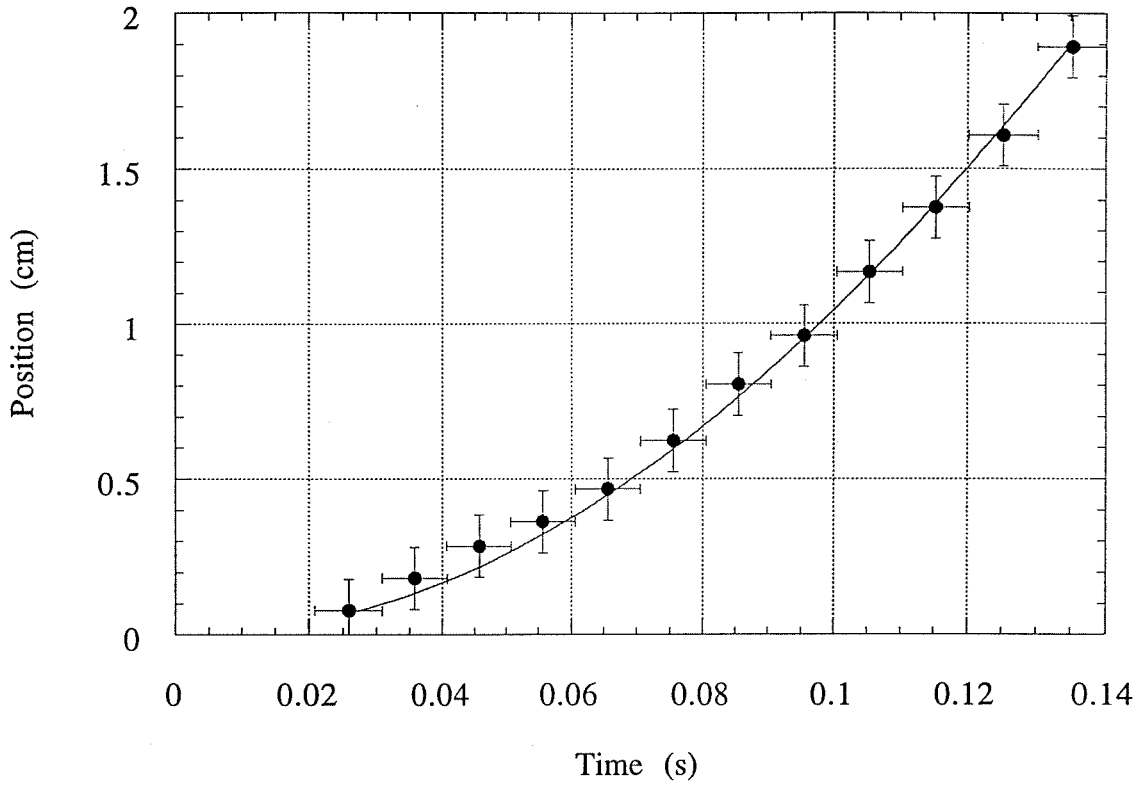

Figure 4.8: Parabolic least-squares fit of the solid block position data from Trial 48. Error bars give the standard error in position and time. The parabolic curve fit represents the first term in the Taylor series expansion of solid block motion and provides the initial acceleration of the block. The initial acceleration is 2.09 m/s^2 here.

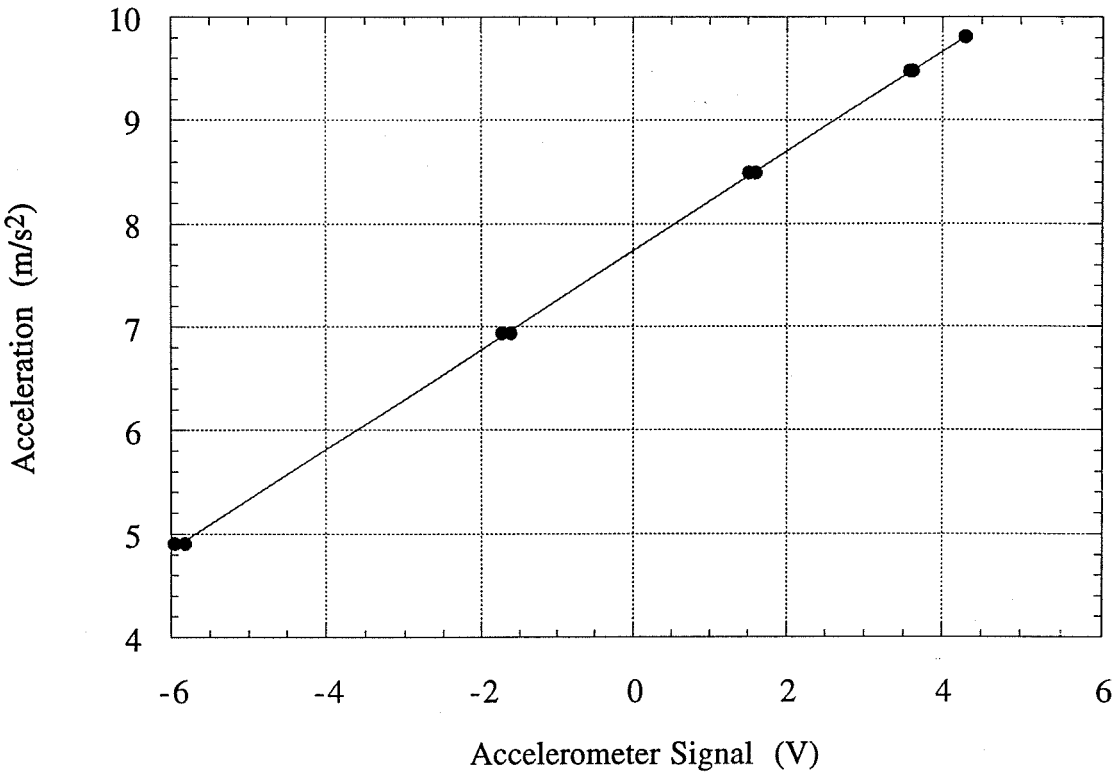

Figure 4.9: Static calibration of the accelerometer by rotation on a level indexing head shows that the voltage signal is linearly proportional to the acceleration given by (g cosθ). The least-squares fit of the calibration data provides a = 7.7421 + 0.48176 V with an accuracy of greater than 99%. The error is due largely to voltage drift during calibration.

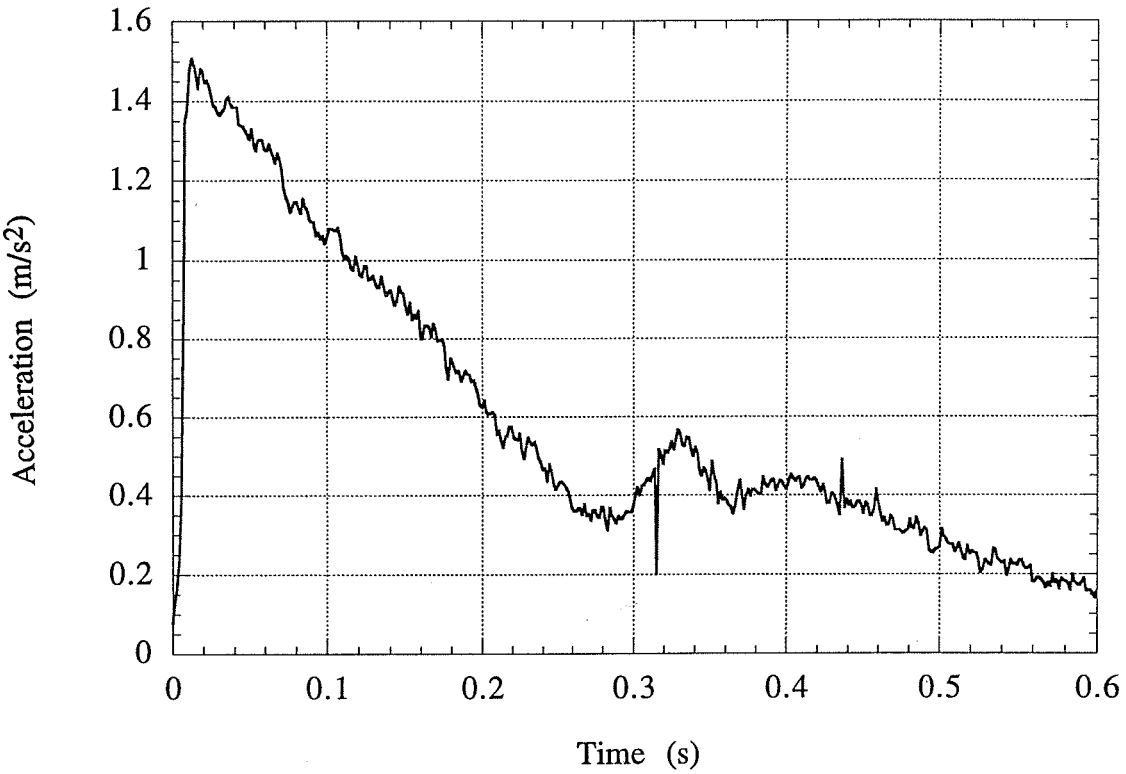

Figure 4.10: Acceleration of solid block 3_n in Trial 76 as measured by the accelerometer. Acceleration rapidly rose to a maximum at about 20 ms and decayed thereafter as the solid block approached terminal velocity. The small rise in acceleration at 0.3 s may be due to waviness of the incline surface.

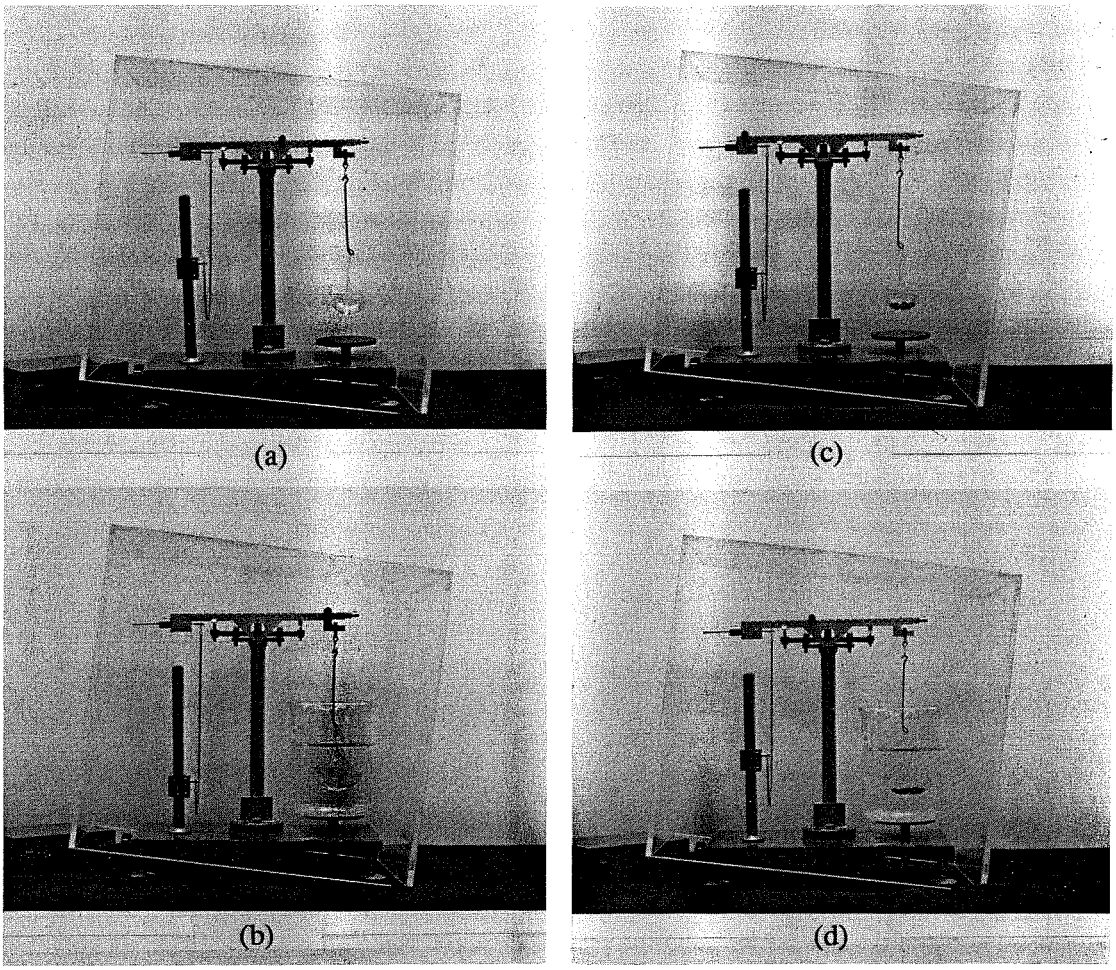

Figure 4.11: Determination of the specific gravity of steel shot by four measurements on a sensitive Troemner balance. Clockwise from top left: empty basket in air, basket with steel shot in air, basket with steel shot in water, and empty basket in water. The specific gravity of the steel shot follows from these measurements in equation (4.10).

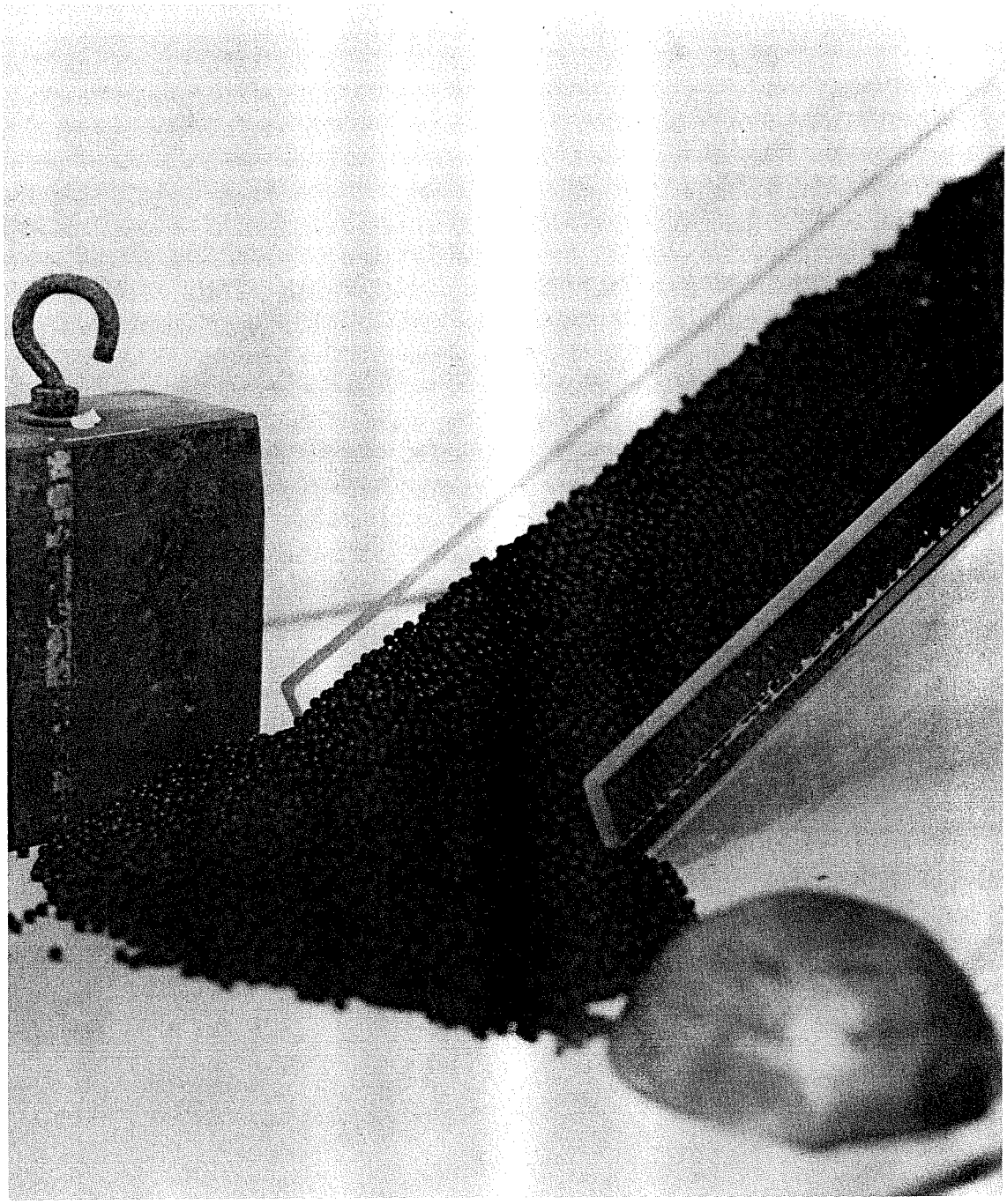

Figure 4.12: Measurement of the internal friction angle of steel shot by tilting a Lucite sheet until the material spilled onto the bottom of the wave tank. The Lucite sheet had a random monolayer of steel particles glued to the bottom to simulate internal failure. Two lead weights held the Lucite sheet in position while it was tilted.

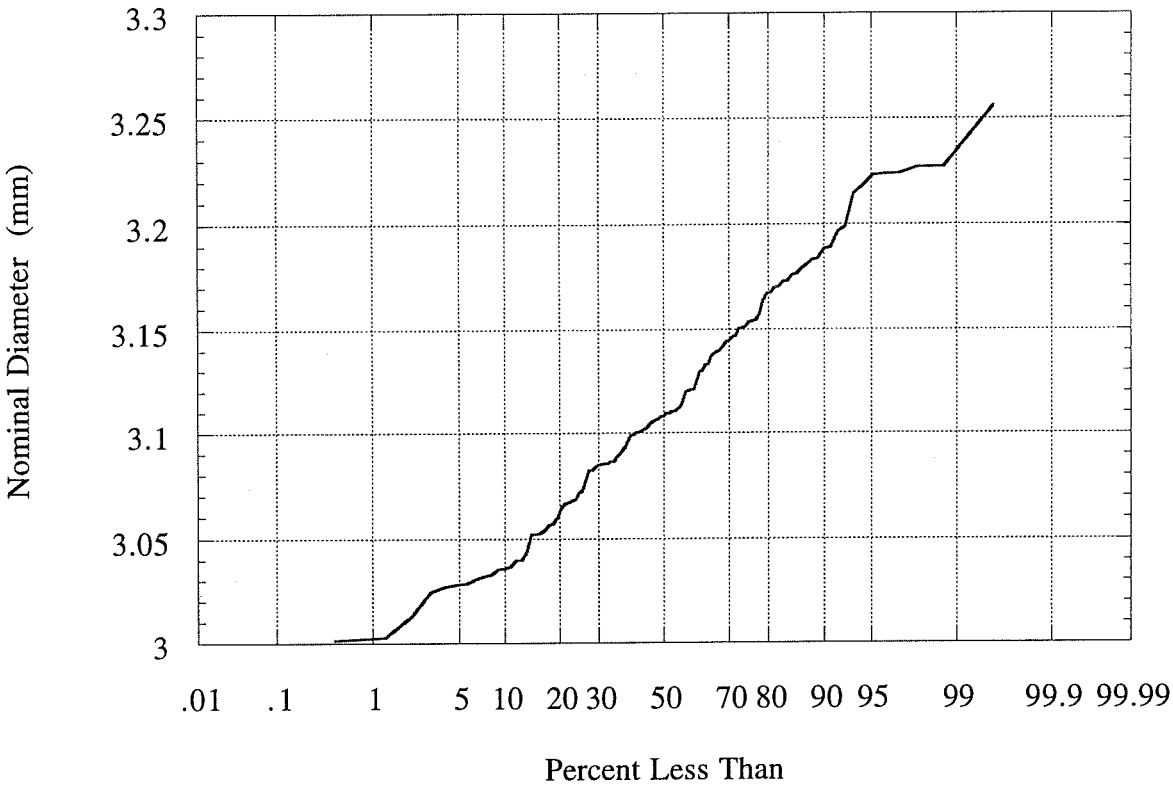

Figure 4.13: Cumulative distribution of the nominal diameter of 3 mm lead shot. The abscissa is plotted in normal coordinates as per cent lass than. A straight line is indicative of a normally distributed nominal diameter. One standard deviation occurs at ±34.1% from the arithmetic mean at 50%.

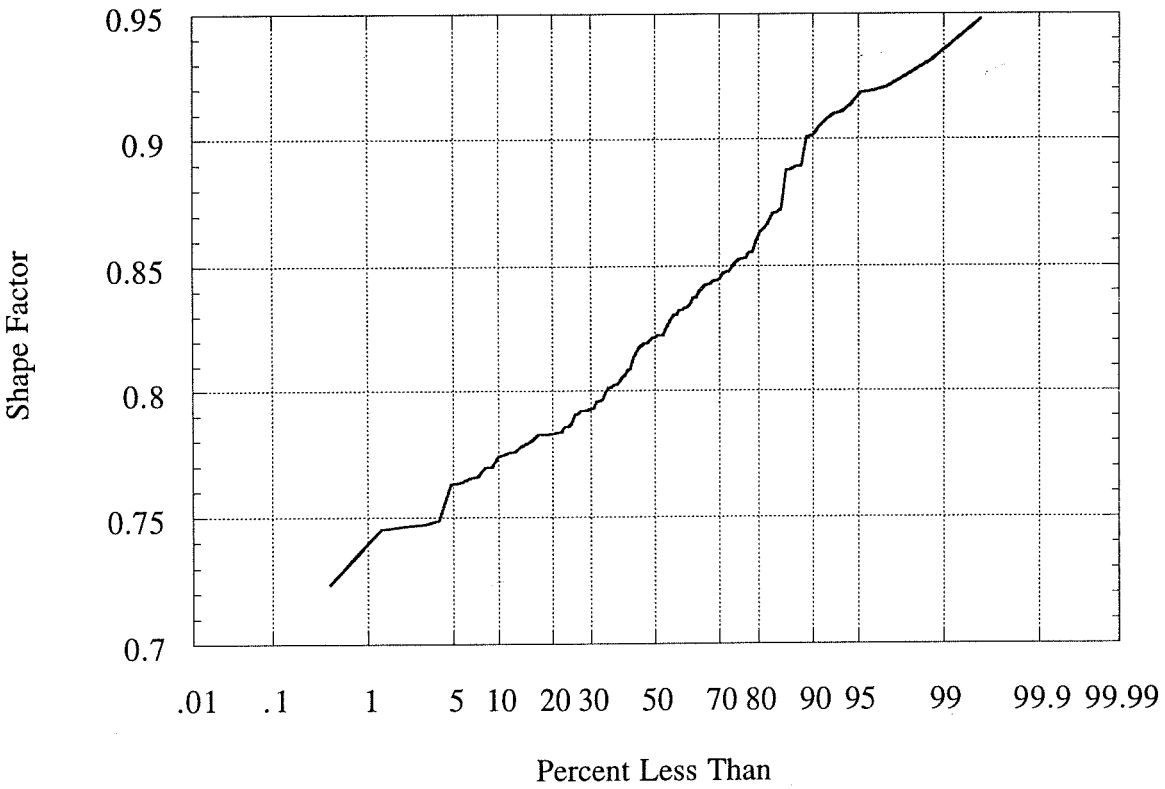

Figure 4.14: Cumulative distribution of the shape factor of 3 mm lead shot. The abscissa is plotted in normal coordinates as per cent lass than. A straight line is indicative of a normally distributed nominal diameter. One standard deviation occurs at ±34.1% from the arithmetic mean at 50%.

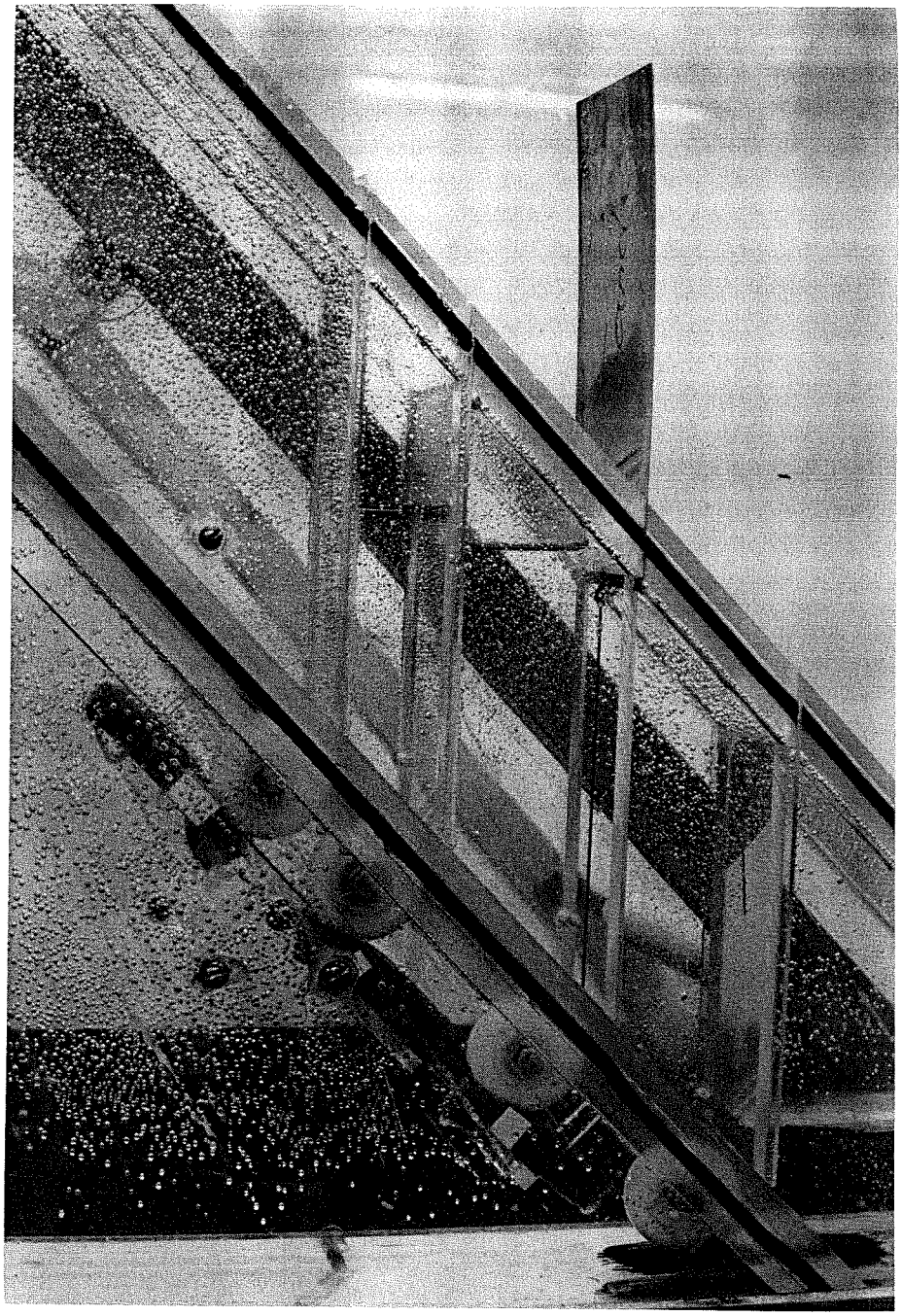

Figure 4.15: Perspective photograph of the back of the fully extended stainless steel gate. Four slots were available on the incline for the gate although only one slot was used. The gate was pulled to the bottom of the incline when retracted. The Delrin pulleys with glass ball bearings can be seen under the Lucite incline. See Figures 4.1 and 4.18 as well.

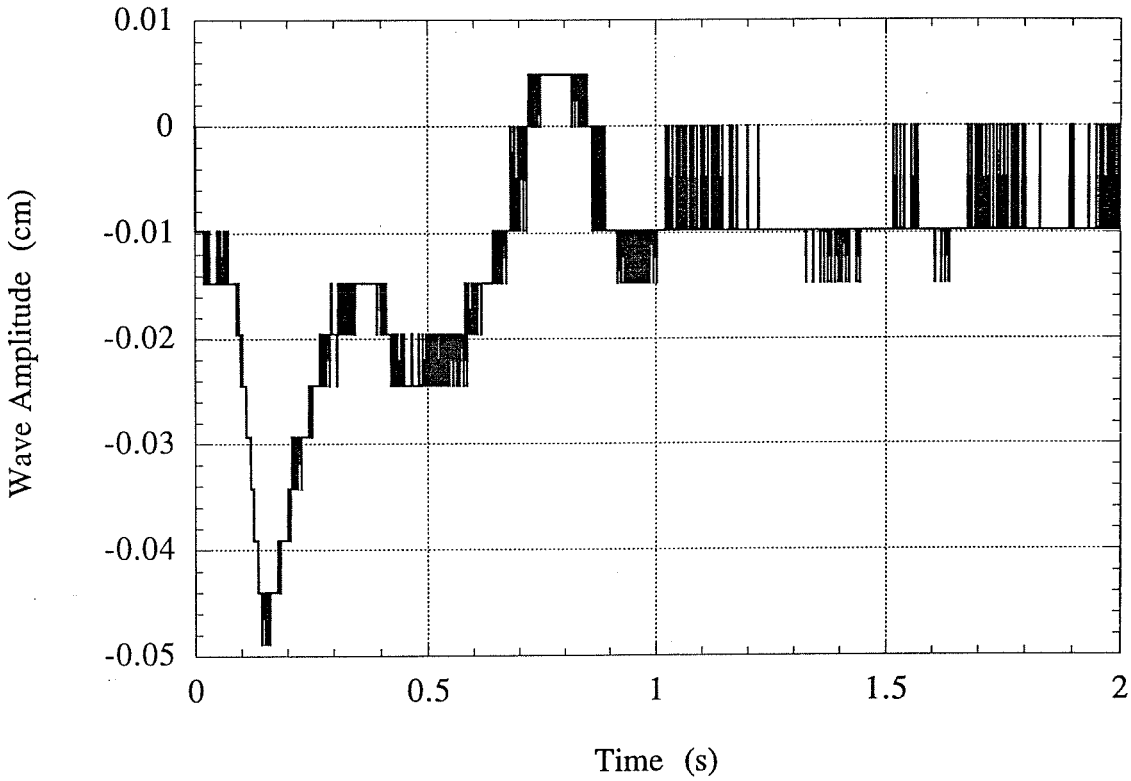

Figure 4.16: Near-field wave record due to gate retraction alone. The amplitude and duration of the wave record is insufficient to alter the wavemaker curves generated from the experimental data. A typical material landslide trial would have a maximum near-field wave amplitude of 0.5 cm at 0.4 s.

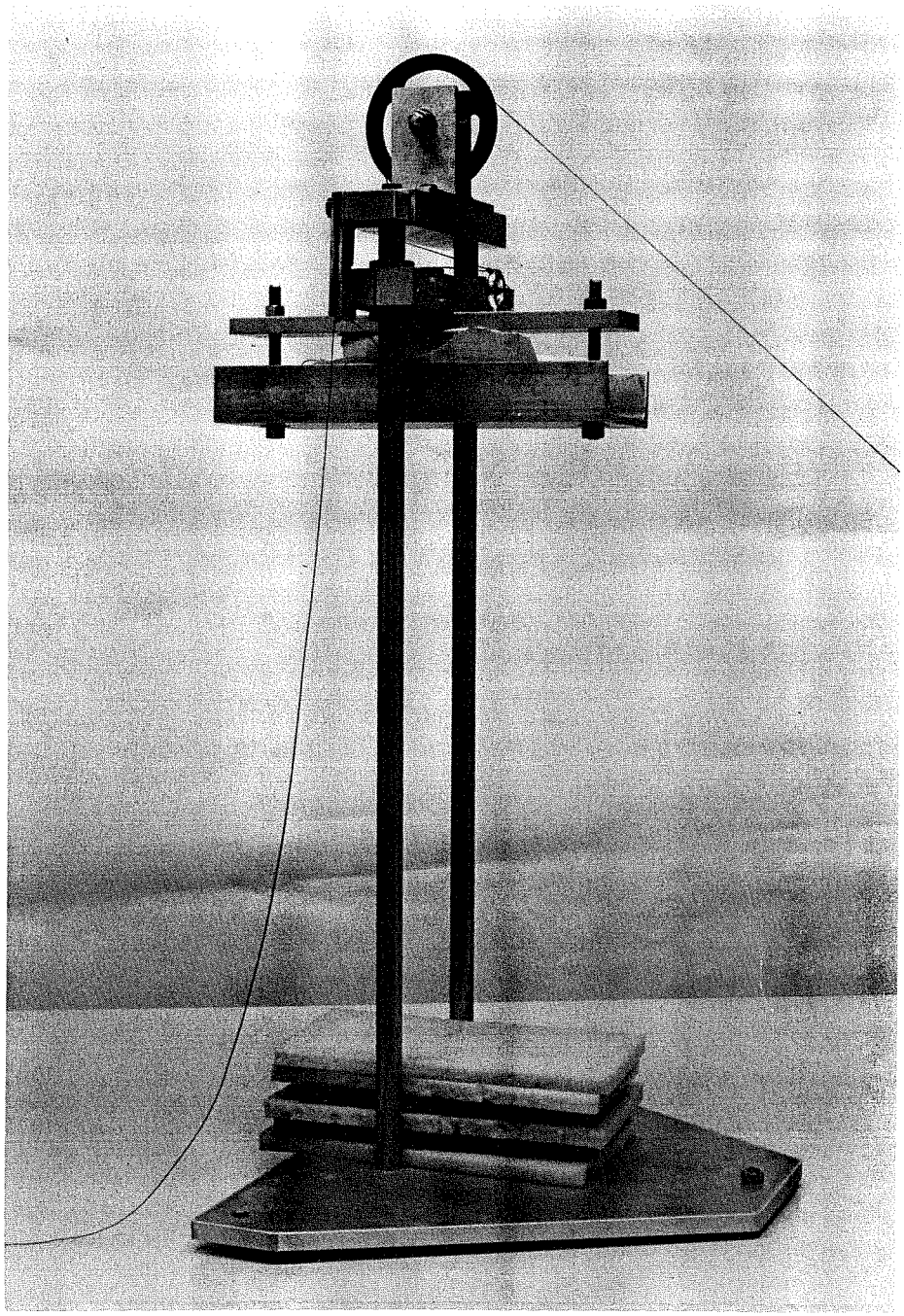

Figure 4.17: Photograph of the gate retraction mechanism. The large pulley on top of the mechanism would guide the braided Nylon cord to the top of the wave tank where the rest of its path is shown in Figures 4.1 and 4.16. Pulling on the cord at the left would release the sliding lead weights. The cord connected to the gate was pulled taut just before the weights struck the padding at the bottom of the mechanism.

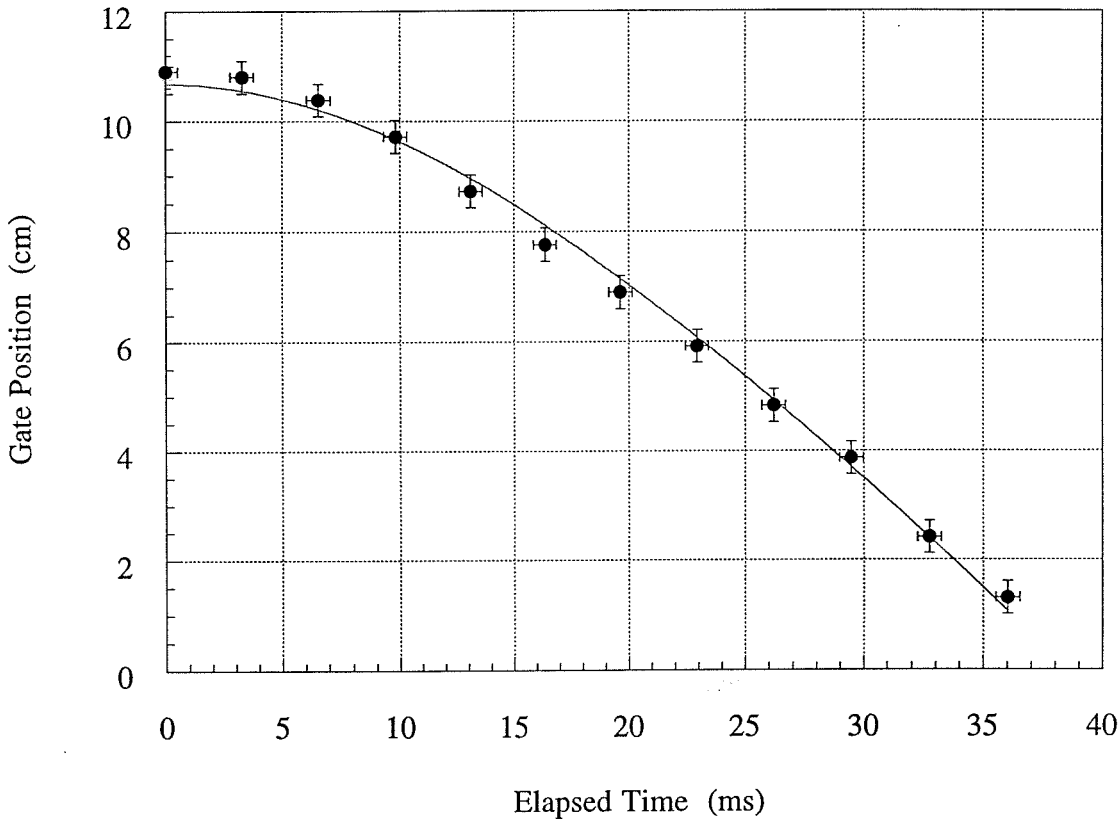

Figure 4.18: Least-squares curve fit of gate position data with equation (4.20). Knowledge of the gate retraction in time allowed the beginning of a material landslide to be determined to within about ±1 ms.

Chapter 5

5. Experimental Results and Discussion

The purpose of this chapter is to describe water waves generated by underwater landslides and to determine how to predict the amplitude of a chosen characteristic wave. The results presented in this chapter support the central claim of this thesis: namely, given an initial landslide geometry along an incline, the characteristic time t_o of landslide motion and the initial landslide rate of deformation Γ suffice to predict the maximum wave amplitude above most underwater landslides. The maximum wave amplitude along with the landslide center of mass motion can in turn be used to determine many other wave characteristics such as per cent conversion of solid block kinetic energy into wave energy. The chapter begins by determining the dynamical coefficients for solid block landslides sliding along an incline at 45°. Following this, the experimental wave results for solid block and material landslides on an incline at 45° are presented. The central thesis of this work will have been verified for an initial landslide submergence $d/b \approx 0.9$. This experimental study is limited to landslides where $Ha_o > 2$ as is commonly found for natural underwater landslides. Numerical simulations of underwater landslides broadened the range of initial geometries (compared to experimental results) while providing a theoretical test of the wavemaker formalism. The error bars shown on all figures represent one standard deviation and are usually found independent of the data in the figure. All corresponding error analyses can be found in Appendix B. The basic data and derived quantities for most trials discussed in this chapter are listed in Appendix C.

5.1 Landslide Motion and Deformation Results

Landslide kinematics are of key importance to constructing nondimensional wavemaker curves and carrying out numerical simulations of water wave generated by underwater landslides. However, it is almost impossible to measure the initial acceleration or terminal velocity of all landslides during an actual trial. The theoretical analyses performed in Chapter 3 describe the solid block and material landslides in terms of measurable dynamical coefficients. Therefore, by independently obtaining the landslide kinematics and dynamical coefficients, accurate estimates of landslide motion are readily available even if experimental values are unavailable for a particular trial.

5.1.1 Solid Block Coulombic Friction

The method used to obtain the dynamic Coulombic friction coefficient is described in Section 4.2.3.1. Table 5.1 provides the experimental results for the critical friction angle ψ between the four PVC solid blocks and the Nylon incline, along with the associated Coulombic friction coefficients C_n and the effective gravitational forcing g_{eff} of the solid blocks down the incline (given that $\rho_b > \rho_o$). Solid block characteristics are provided in Table 4.1. The errors indicated in Table 5.1 are standard errors evaluated in Section B.1.1. The subscript n for a solid block denotes "normal" ballast.

Table 5.1: Solid Block Dynamic Coulombic Friction Data

Block #	ψ (°)	$C_n = \tan\psi$	$g_{eff} = g(\sin\theta - C_n\cos\theta)$
1_n	17 ± 0.5	0.31 ± 0.01	$4.8\ m/s^2 \pm 0.15\ m/s^2$
2_n	17 ± 0.5	0.31 ± 0.01	$4.8\ m/s^2 \pm 0.15\ m/s^2$
3_n	18 ± 0.5	0.33 ± 0.01	$4.7\ m/s^2 \pm 0.15\ m/s^2$
4_n	18 ± 0.5	0.33 ± 0.01	$4.7\ m/s^2 \pm 0.15\ m/s^2$

5.1.2 Solid Block Initial Acceleration and Added Mass

The method used to measure the initial acceleration of solid blocks was described in Section 4.2.3.2. Figures 5.1-5.3 show (typically) three measured initial accelerations of blocks 1_n, 2_n, and 3_n for each chosen initial submergence along with a 3rd or 4th order

polynomial least-squares fit through the data. All measurements of the initial acceleration were made in the wave tank with the same incline, initial solid block positions, and water depth as Trials 55-80. The error bars on the figures represent one standard deviation and are calculated from independent error estimates in Section B.1.2. The initial acceleration of block 1_n can be calculated from

$$a_o(d) \approx 1.8711 - 9.1844\, d + 85.38\, d^2 - 246.79\, d^3 \qquad (5.1)$$

where d is the initial submergence in meters, a_o is expressed in m/s^2, and equation (5.1) is valid for d<180 mm. The initial acceleration of block 2_n can be estimated from

$$a_o(d) \approx 2.0891 - 22.831\, d + 403.9\, d^2 - 2992.3\, d^3 + 7766.7\, d^4 \qquad (5.2)$$

which is valid for d<120 mm. Likewise, the initial acceleration of block 3_n can be calculated from

$$a_o(d) \approx 2.0371 - 16.067\, d + 159.98\, d^2 - 38.921\, d^3 - 2725.1\, d^4 \qquad (5.3)$$

and equation (5.3) is valid for d<130 mm. The initial acceleration of blocks 2_o-2_l was measured five or six times each at one initial submergence (d=74.5 mm) and one incline angle (θ=45°). Once again, this is the same initial solid block submergence and the same incline angle as those used in Trials 55-80. The mean initial accelerations are given in Table 5.2. The mean value of the initial acceleration is used for all solid block trials that are missing an accurate initial acceleration, namely for trials where solid block motion was recorded by high speed movies. The initial accelerations used in solid block trials can be found in Table C.2.

The accelerometer results are about three times more accurate than the movie based initial accelerations according to Figure 5.4 and standard error estimates in Section B.1.2. Accuracy is needed in order to construct unambiguous wavemaker plots. However, it is possible that the presence of the accelerometer (and the wire connecting the accelerometer to the amplifier) altered the initial acceleration when compared with the non-intrusive movie measurements. In order to gauge the influence of the accelerometer, the initial accelerations obtained from high speed movies are correlated with the mean initial accelerations obtained from the accelerometer for solid blocks 1_n, 2_o-2_l, and 3_n. Section 4.2.2 describes how initial accelerations are obtained from high speed movies of

solid block motion. Figure 5.4 shows that the slope of a linear least-squares fit through the origin is almost unity. Therefore, a line of equivalence was not added to the figure. The error bars on Figure 5.4 represent one standard deviation. The relatively poor correlation coefficient r=0.84 can be attributed to the large error in the movie based results since the 16% uncertainty in the curve fit closely resembles the 17% error estimated for the movie based initial accelerations. Given the accuracy of the accelerometer results and the slope of unity in Figure 5.4, the mean initial accelerations given by equations (5.1) to (5.3) and Table 5.2 are substituted for initial accelerations obtained from high speed movies in all plots of experimental data. The substitution is made for all solid block trials performed before Trial 55. Only after making the substitution does the wavemaker curve become evident from the experimental results.

Table 5.2: Mean Initial Acceleration and Added Mass Coefficient for Blocks 2_o-2_l

Block #	a_o (m/s^2)	C_m
2_o	0.83 ± 0.11	0.85 ± 0.07
2_a	1.20 ± 0.14	0.79 ± 0.07
2_b	1.45 ± 0.04	0.88 ± 0.07
2_d	1.95 ± 0.03	0.81 ± 0.07
2_e	2.22 ± 0.27	0.68 ± 0.07
2_l	2.41 ± 0.05	0.77 ± 0.07

The added mass coefficient represents a generalization of the previous initial acceleration results for arbitrary solid block size or initial submergence. The added mass coefficient C_m at $t=0^+$ is calculated from the theoretical equation for the initial acceleration

$$C_m = \frac{(m_b - m_o)\, g_{eff}}{a_o\, m_o} - \frac{m_b}{m_o} \tag{5.4}$$

where the effective gravity is $g_{eff} \equiv g(\sin\theta - C_n \cos\theta)$. Equation (5.4) is dependent on the accuracy of all quantities on the right hand side of the equation. For example, taking the partial derivative of C_m with respect to a_o yields

$$\frac{\partial C_m}{\partial a_o} = \frac{-(m_b - m_o)\, g_{eff}}{a_o^2\, m_o} \tag{5.5}$$

which is around -1.7 s^2/m for all normal solid block trials since $m_b/m_o \approx 2$, $g_{eff} \approx 4.8$ m/s^2, and $a_o \approx 1.7$ m/s^2. Consequently, any random errors in the initial acceleration are amplified when calculating the added mass coefficient. The sensitivity of the added mass coefficient to the initial acceleration is derived from the ratio $m_b/m_o \approx 2$ whereby large changes in added mass are needed to explain small changes in the initial acceleration. The contribution of errors in the gravitational forcing g_{eff} to errors in the added mass coefficient is considered in Section B.1.3.

As shown in Section 4.2.3.2, the added mass coefficient C_m at $t=0^+$ is a function of the nondimensional initial block submergence d/b and the incline angle (fixed at $\theta=45°$). Equation (5.4) is used to convert all acceleration data in Figures 5.1 to 5.3 into added mass coefficients. Figure 5.5 shows a least-squares curve fit of the added mass coefficient C_m at $t=0^+$ *versus* nondimensional initial submergence d/b

$$C_m(d/b;\theta=45°;t=0^+) \approx 0.41469 + 1.4574\, d/b - \\ - 1.3389\, (d/b)^2 + 0.32534\, (d/b)^3 \qquad (5.6)$$

over the range $0<d/b<2$. Equation (5.6) provides a reasonable estimate of the added mass coefficient despite the spread in the data. There are no error bars on Figure 5.5 because they become too dense to be understood. Section B.1.3 derives standard errors of ±28% for added mass coefficients calculated from equation (5.4). Equation (5.6) has the characteristic rise and fall with increasing submergence of related curves given by Brennen (1995). A typical added mass coefficient in Figure 5.5 is $C_m \approx 0.8$. For solid blocks 2_o-2_l listed in Table 5.2, the mean of all six added mass coefficients is $C_m \approx 0.8$. Since the added mass coefficients in Table 5.2 are calculated from mean initial accelerations, they show considerably less scatter than the added mass coefficients in Figure 5.5 (specifically at $d/b \approx 0.87$). All blocks listed in Table 5.2 should have the same added mass coefficient since they are all exactly the same size and had the same initial submergence. Since solid block 4_n was not studied with an accelerometer, an added mass coefficient of $C_m = 0.60 \pm 0.14$ was estimated from Figure 5.5 (given that d/b=2.13) and used to calculate a theoretical initial acceleration of $a_o = 1.75 \pm 0.10$ m/s^2. Only one initial submergence d/b=2.13 was studied for solid block 4_n.

For a two-dimensional square block inclined at 45° to a flow and immersed in an infinite bath of water, i.e., d/b=∞, Sarpkaya and Isaacson (1981) propose the added mass coefficient C_m=0.76. Figure 5.5 covers the opposite limit of zero initial submergence so that C_m=0.76 should be viewed as a reasonable asymptotic value off the right hand side of the figure. However, it is not clear what role separation plays in determining this added mass coefficient. The added mass coefficients given by Figure 5.5 and Table 5.2 are for the initiation of motion before a shear layer has had time to form. Once shear layers are formed, there is no longer any guarantee that the added mass coefficient is single valued *versus* instantaneous submergence and the history of solid block motion may matter. The reason for this is that the fluid domain is no longer simply connected given the presence of a shear layer in the wake of a solid block. Heuristically, fluid separation changes the apparent solid block shape. Hence, the added mass coefficients given in this section should not be used to describe solid block motion for finite times after the block is released. Regardless, variations in the added mass coefficient of a solid block between C_m=0.6-1.0 can arguably be considered negligible for the purpose of calculating the block motion for t>0. Solid block motion is simply not that sensitive to the added mass coefficient because $m_b/m_o \approx 2$. Hence, the analytical solution of solid block motion, equation (3.78), can be considered an accurate approximation of the actual solid block motion using a mean value of $C_m \approx 0.8$. To verify this argument, equation (3.72) was integrated numerically using C_m=0.8 and again using equation (5.6) by replacing the initial submergence d with the instantaneous solid block submergence. At t=0.33 s, the difference in solid block position was no more than 2%.

5.1.3 Solid Block Terminal Velocity and Drag

The method used to obtain the terminal velocities of solid blocks is described in Section 4.2.3.3. The largest of all velocity measurements for a given solid block was taken as the terminal velocity and is shown in Table 5.3. Mean measured velocities gave much larger errors as well as unreasonably large drag coefficients. A drag coefficient was then calculated from the terminal velocity according to the equation

$$C_d = \frac{2\,(m_b - m_o)\,g_{eff}}{u_t^2\,\rho_o\,A} \tag{5.7}$$

where $A = w\ell\cos\theta\sin\theta$ is the solid block projected frontal area. The drag coefficient calculated for each solid block is shown in Table 5.3. Based on these measurements, a

mean drag coefficient of $C_d=1.7 \pm 0.17$ was calculated. The mean drag coefficient was used instead of the minimum drag coefficient in order to provide the most accurate estimates of theoretical terminal velocities for all solid blocks. The standard error estimates in Table 5.3 are derived in Section B.1.4. The analytical solution of solid block motion, equation (3.78) with $C_m=0.8$ and $C_d=1.7$, indicated that all solid blocks should have been within 0.5% of terminal velocity when the velocity was measured at the bottom of the incline. The smaller and less dense solid blocks had much smaller discrepancies. The experimental terminal velocities shown in Table 5.3 were used in the calculation and presentation of all solid block wave data and are listed again in Table C.2. Solid block characteristics are provided in Table 4.1.

Table 5.3: Terminal Velocities and Drag Coefficients of Solid Blocks

Block #	u_t (m/s)	C_d
1_n	0.65 ± 0.020	1.88 ± 0.19
2_o	0.37 ± 0.011	1.60 ± 0.16
2_a	0.44 ± 0.013	1.73 ± 0.17
2_b	0.54 ± 0.016	1.60 ± 0.16
2_n	0.56 ± 0.017	1.75 ± 0.18
2_d	0.65 ± 0.020	1.67 ± 0.17
2_e	0.71 ± 0.021	1.62 ± 0.16
2_l	0.80 ± 0.024	1.57 ± 0.16
3_n	0.43 ± 0.013	2.12 ± 0.21
4_n	0.42 ± 0.013	1.44 ± 0.14

The drag coefficient $C_d=1.7$ found in this section is employed solely for theoretical calculations and numerical simulations. The relatively large error in the drag coefficient is due in part to the square of the terminal velocity in equation (5.7) which ends up doubling the error of the terminal velocity. Conversely, the solid block terminal velocity is not very sensitive to the drag coefficient given the inverse power of $C_d>1$ within the square root. Hoerner (1965) proposes a drag coefficient of $C_d=1.55$ for two-dimensional squares inclined 45° to a uniform flow over a Reynolds number range of $10^4<Re<10^6$. The drag coefficient is constant since bluff bodies with well-defined separation points usually show little Reynolds number dependence once $Re \gg 1$. For most solid block trials,

the Reynolds number based on instantaneous velocity and block size is theoretically of order unity at around $t=v_o/ba_o \approx 10$ μs after releasing a solid block. Hence, almost all of the solid block motion satisfies $Re \gg 1$ for the density of solid blocks studied herein.

5.1.4 Comparison of Block Motion

Figure 4.8 shows a parabolic curve fit of the solid block position data acquired from the high speed movie record of Trial 48. Sections 4.2.2 describes how the position data was obtained. Figure 5.6 compares the same experimental data along with the expected solid block position calculated from equation (3.78). The initial acceleration of block 2_d was taken from Table 5.2 while the terminal velocity was taken from Table 5.3. The values of t_o and s_o are given in Table C.2. The solid line in Figure 5.6 represents the analytical solution of solid block motion and agrees quite well with the data, especially at later times where the relative error in the data is smaller. The two other dashed curves represent solid block motion that results from standard errors in the characteristic distance s_o and time t_o. These standard errors are derived in Section B.1.5. Figure 5.6 shows that relatively small errors in the characteristics of solid block motion can correspond to large differences in block position *versus* time. Therefore, the agreement between the experimental data and the independently derived theoretical prediction is a testament to the accuracy of the acceleration and velocity measurements provided above. Conversely, accurate position *versus* time data can be used to accurately determine the characteristics of motion if a theoretical prediction of motion is available. This is a valuable observation regarding the material landslide center of mass motion described in the next section.

Figure 5.7 compares the acceleration profile from Figure 4.10 of Trial 76 with the theoretical acceleration profile obtained from equation (3.81). The initial acceleration used in equation (3.81) was obtained from the experimental acceleration profile so that the two curves agree at around t=0.02 s. The terminal velocity used in equation (3.81) was taken from Table 5.3 and accounts for the time constant of acceleration decay. The rapid rise of the measured acceleration is probably related to the relaxation time of the Nylon fishing line holding the solid block in its initial position prior to the trial. Figure 5.7 shows that the acceleration has zero slope at $t=0^+$ for an idealized solution of motion that neglects lubrication forces. A sharp decay in the measured acceleration near t=0 is indicative of the action of lubrication. This is shown, for example, by taking the derivative of equation (3.55) with respect to time in Section 3.2.1.2.2. The general comparison of theoretical and measured acceleration decay is acceptable although the

experimental measurement is alternately below and above the theoretical curve. The rise in acceleration at around 0.3 s is a general feature of acceleration measurements for all solid blocks studied. The rise in the acceleration may be associated either with incline waviness or with the coupling between fluid dynamics and solid block motion. The solid block acceleration would increase after going over a rise in the incline due to a simultaneous increase of the effective gravitational forcing and of block lubrication. Examples of coupling between fluid dynamics and solid block motion that may explain the rise in acceleration include the additional drag of the starting vortex at early times and the flow of water above the solid block towards and away from the incline associated with run-up and run-down.

5.1.5 Material Center of Mass Motion

Before discussing the results of the material landslide center of mass motion, it is important to observe landslide dynamics that would otherwise get smoothed over in the integration of cross-sectional area. The methods used to record and study material landslides are described in Sections 4.2.2 and 4.3.2. Figure 5.8 shows movie frames from Trial 91 involving 3 mm glass beads, Figure 5.9 shows movie frames from Trial 84 involving 2 mm lead shot, and Figure 5.10 shows movie frames from Trial 87 involving 0.5 mm glass beads. Four registry marks spaced 101.6 mm (four inches) apart along the outside of the incline are clearly visible in each photograph. As mentioned in Section 4.3.2, gate retraction typically lowered the solid volume fraction near the front face of the initial landslide position. Solid volume fractions slightly lower than random loose packing strongly enhance particle mobility and the flow characteristics of the material. The vertical geometry of the front face of the material may also have induced interior failure of the solid material at short times. The net result of these two effects is to promote the formation of a small gravity current ahead of (both temporally and spatially) the main mass of deforming material. Neither Figure 5.8 nor Figure 5.9 show any significant effects that can be attributed directly to gate retraction. However, the collapse of the front face of the 2 mm lead shot landslide in Figure 5.9 did cause the formation of a jet of material that began accelerating along the incline at around 0.15 s. At early times, the lead shot landslide in Figure 5.9 resembles the experimental results given by Savage and Hutter (1989) for a gravel landslide in air. Figure 5.10 displays the precursor gravity current of the 0.5 mm glass bead landslide at 0.30 s. In the interim leading up to the frame at 0.60 s, the larger mass of material had formed a gravity current that appeared to

feed the precursor gravity current with mass while the two distinct events merged into a single gravity current.

Gravity currents at later times often displayed wave behaviors analogous to wave behavior associated with other fluid dynamic systems. The word "wave" is used to denote a measurable (in this case observable) traveling event in the same sense as Whitham (1973). Figure 5.8 shows that the 3 mm glass bead landslide developed what appears to be three wave events on the gravity current head 0.42 s into the landslide motion. However, by the time the glass bead gravity current reached the bottom of the incline, there remained what appears to be only one large gravity current head quite similar in appearance to the initial landslide shape. The appearance of a typical gravity current head can be found in Ippen and Harleman (1952) or Simpson (1987). A gravity current head itself can be described as a wave event associated with jump conditions in transport quantities. Additional wave events on the surface of a gravity current may be associated with a Kelvin-Helmholtz type shear instability. Figure 5.9 shows that the two wave events at 0.27 s merged into one larger wave event as the lead shot gravity current reached the bottom of the incline. There appears to be a dynamic ordering whereby larger wave events near the back of the gravity current overtake smaller wave events in the front. Single wave events in horizontal gravity currents were observed by Bonnecaze *et al.* (1993) among others but the author knows of no other observation of the superposition of multiple wave events. The 0.5 mm glass bead landslide in Figure 5.10 began to show similar wave behavior until what appears to be a shock wave began forming at around 0.60 s. The apparent shock wave appears to emerge from the separation of the gravity current nose from the surface of the incline and is clearly visible at 0.84 s. The author knows of no other observation of a shock wave leading an underwater gravity current. However, the apparent shock wave in Figure 5.10 does appear very similar to the numerical solutions of Bonnecaze *et al.* (1993) calculated for a horizontal gravity current. Therefore, it appears that the usual gravity current head can evolve into a shock wave on a sufficiently steep underwater incline. None of these local dynamic effects are apparent from the center of mass motion along the incline.

The centroid calculated by NIH Image for a landslide trace assumed that the mass was evenly distributed throughout the cross-sectional profile; the image analysis was performed on a black and white image of the landslide profile that could not indicate density variations. For early times and for materials with either large densities or large particles, the assumption of a uniform solid volume fraction throughout the landslide

profile appeared to be valid. Therefore, the centroid of the landslide profile is directly associated with the center of mass of the landslide. At later times, closer attention is given to the center of mass position of material landslides with large entrainment of water (or particle dilution) in the landslide wake. For three glass bead landslides near the bottom of the incline, one trace was made of the gravity current profile while another trace was made of the dense core of the landslide excluding the landslide wake. Naturally, neither trace had the same centroid position. In all cases studied, the complete gravity current centroid had not progressed as far along the incline and was situated higher above the incline. By arbitrarily assigning a relative density of one half to the landslide wake, errors in the centroid position along the incline of 5% and in the centroid height above the incline of 3% were found. These errors were neglected for all landslides not composed of glass beads or garnet sand since landslide wakes were either easily discernible or non-existent. A more complete description of this analysis can be found in Section B.1.6.

Figure 5.11 shows the landslide centroid position of a 3 mm glass bead landslide as a function of time. Figure 5.12 shows the landslide centroid position of the 3 mm steel shot landslide as a function of time. Figure 5.13 shows the landslide centroid position of the 0.5 mm glass bead landslide as a function of time. The error bars in the position data of Figures 5.11 and 5.13 indicate the potential error between the centroid and the center of mass for these rapidly deforming landslides. The motion of all three landslides appears very similar in shape. In fact, the center of mass motion of a material landslide along the incline appears to follow the same analytical solution as solid block motion down the incline as anticipated in Section 3.2.2. The agreement is still surprising not least because the analytical solution assumes constant values of the Coulombic friction and drag coefficients whereas all material landslides underwent significant deformation and some material agitation. The analogy between material landslide motion and solid block motion should fail once random particle collisions and particle rolling motions become important. However, the agreement appears to be excellent regardless of the material density, material particle size, particle angularity, mode of landslide deformation, or landslide rate of deformation. Therefore, equation (3.78) is used to curve fit the position data in order to extract a characteristic distance s_o and time t_o for material landslide motion. These characteristics of motion are needed in order to construct a wavemaker curve for material landslides.

One explanation for the center of mass motion of material landslides lies in the observation that densely packed arrays of particles several monolayers thick were observed sliding along the incline in the core of 12 mm marble and 3 mm steel shot gravity currents. In other words, significant particle collisions and particle rolling motions never developed within the landslide along the incline. Figure 5.18 shows pictures of a crushed calcite landslide sliding along the incline. Similar behavior for the other landslide materials would indicate that all landslides were sliding along the Lucite surface even if the top surface was being deformed and mixed by, among other causes, the shearing action of surrounding water. Naturally, material sliding may simply be a by-product of having chosen a smooth Lucite incline for the experimental apparatus. This observation should not be extrapolated to natural underwater landslides. For example, equation (3.70) suggests that large landslides should be dominated by Coulombic friction. However, Shaller (1991) shows that this is actually a very poor assumption and that large landslides can experience much longer run-out in air and water than would otherwise be predicted by Coulombic friction. Campbell *et al.* (1995) suggest that long run-out landslides are a consequence of macroscopic rheology that results from particle interactions.

Table 5.4 summarizes the results of the curve fits of landslide centroid position along the incline as a function of time. All curve fits appeared very similar to those shown in Figures 5.11 to 5.13. Table 5.4 also provides the standard errors given by the KaleidaGraph general curve fitting algorithm described in Section B.1.6. Regardless of the material, most material landslides studied have characteristic lengths s_0 between 15-30 cm as well as characteristic times t_0 between 0.25-0.40 s. These characteristics of motion resemble typical solid block characteristics of motion given in Table C.2. All three crushed calcite trials were repeated trials and have reasonably similar characteristic motions. Trials 89 and 90 involving 1 mm glass beads were similar to Trial 35 in initial volume but had different initial submergences. Trial 92 involved a smaller mass of 1 mm glass beads so that significantly different characteristics of motion are to be expected. Trials 34 and 82 are repeated 3 mm glass bead landslides and both landslides have very similar characteristics of motion. Trials 37 and 83 are repeated 12 mm marble landslides and both landslides have characteristics of motion that agree to within the normal errors shown. Table 5.4 provides one extra decimal place to avoid round off errors. The reader should note that curve fits for Trial 38 involving 3 mm lead shot, Trial 84 involving 2 mm lead shot, Trial 85 involving garnet sand, and Trial 93 involving 1 mm glass beads failed to converge to accurate characteristics of landslide motion. In all four cases, the

final values of s_o and t_o were highly sensitive to the desired accuracy of the curve fit and in some cases failed to converge whatsoever. The standard errors when the curve fitting algorithm stopped (or was stopped) were on the order of 100 per cent of the characteristics of motion. These four trials are therefore excluded from all further analyses involving material landslide motion including some aspects of wave generation and propagation that incorporate the characteristic time t_o.

Table 5.4: Material Landslide Center of Mass Motion

Material	Trial	s_o (cm)	t_o (s)
Crushed Calcite	32	13.5 ± 0.6	0.290 ± 0.008
Crushed Calcite	33	12.4 ± 0.9	0.272 ± 0.014
Crushed Calcite	40	11.6 ± 0.9	0.271 ± 0.014
0.5 mm Glass Beads	87	26.3 ± 2.3	0.531 ± 0.029
1 mm Glass Beads	35	17.9 ± 1.0	0.342 ± 0.014
1 mm Glass Beads	89	20.7 ± 1.4	0.379 ± 0.019
1 mm Glass Beads	90	21.4 ± 1.9	0.390 ± 0.022
1 mm Glass Beads	92	14.8 ± 3.6	0.312 ± 0.028
3 mm Glass Beads	34	18.1 ± 1.2	0.319 ± 0.014
3 mm Glass Beads	82	17.1 ± 0.5	0.324 ± 0.006
3 mm Glass Beads	91	19.2 ± 0.8	0.317 ± 0.009
12 mm Marbles	37	26.0 ± 2.7	0.353 ± 0.022
12 mm Marbles	83	28.0 ± 1.0	0.364 ± 0.008
2 mm Lead Shot	39	30.4 ± 5.4	0.252 ± 0.028
3 mm Lead Shot	86	38.4 ± 5.1	0.295 ± 0.024
3 mm Steel Shot	81	29.5 ± 3.9	0.271 ± 0.021

There is no essential difference between a sliding material mass and a sliding solid block at early times in their respective center of mass motions. Therefore, the initial acceleration of a material landslide is given by equation (3.73) with $C_n=\tan\psi$ found from Table 4.3 and $C_m\approx 0.8$ borrowed from the solid block motion studies described in Section 5.1.2. The two materials in Table 4.3 for which the incline friction angle was not measured had to be excluded from the calculation. The experimental value of the initial acceleration was given by

$$a_o \approx \frac{s_o}{t_o^2} \tag{5.8}$$

where s_o and t_o were taken from Table 5.4. The data are tabulated in Table C.10. Figure 5.14 shows that the agreement between the theoretical predictions and the observed initial accelerations is quite good. A least-squares linear curve fit through the origin has a slope of m=0.92 and a correlation coefficient r=0.96 indicating that the theoretical prediction is in general a little large. The per cent error between the two initial accelerations is on average 10.6% with a standard deviation of ±14.6% about the mean. Given the normal errors in s_o and t_o, Section B.1.6 shows that the error in the initial acceleration should actually be ±30.3%. Therefore, the theoretical prediction does better than could be expected and equation (3.73) is justified to describe the center of mass motion of deforming landslides in numerical simulations.

Figure 5.14 also shows that glass sphere initial accelerations do not collapse to nearly a single point as suggested by equation (3.73). Rather, the initial accelerations derived from equation (5.8) exhibit ordering by particle size. Material characteristics that depend on nominal diameter represent the only significant differences between the glass spheres. Figure 5.15 compares the ratio of experimental to theoretical initial acceleration of glass sphere landslides with the nondimensional particle size D/b. The data for Figure 5.15 can be found in Tables C.9 and C.14. For nondimensional particle sizes D/b ranging from 0.015-0.15, the ratio of initial accelerations can be approximated by the curve fit

$$\frac{s_o}{t_o^2\, a_o} \approx 1.384 \left(\frac{D}{b}\right)^{0.16} \tag{5.9}$$

which has a correlation coefficient r=0.92. The theoretical initial acceleration becomes a better predictor of the actual initial acceleration for larger particle sizes. For 12 mm marbles, the observed initial acceleration matches the theoretical prediction. For 1 mm glass beads, the experimental initial acceleration is typically about 30% smaller than expected. This discrepancy may be attributed to negative pore water pressures within the deforming landslide that increase Coulombic friction with the incline by increasing the normal force. Since 1 mm glass bead landslides are observed to form a dilatational flow, negative pore water pressures must be induced within the landslide core to draw in water.

The idea that gravity currents have terminal velocities assumes that an asymptotic gravity current structure can be achieved and maintained over sufficiently long distances. Kuenen (1952), Striem and Miloh (1976) and Harbitz (1992) all employ simple analytical expressions for the gravity current terminal velocity that resemble equation (2.1) based on the landslide thickness. However, the work of Parker *et al.* (1986) reveals the complicated dynamics governing gravity current deformation and motion, especially when sediment entrainment and deposition with a sediment bed are taken into account. Regardless, the exceptional agreement between the observed centroid motion and equation (3.78) for all landslide materials studied allows a gravity current terminal velocity to by predicted based on experimental results. Even if this velocity is hypothetical, it will still serve the same scaling purposes as the terminal velocity of a solid block landslide. An *a priori* prediction of the gravity current terminal velocity is available from equation (3.74) using the drag coefficient $C_d \approx 1.7$ found for solid blocks in Section 5.1.3 and the initial suspension density from Table 4.2. The experimental prediction of the gravity current terminal velocity is calculated from

$$u_t \approx \frac{s_o}{t_o} \tag{5.10}$$

where s_o and t_o are given in Table 5.4. The agreement between both predictions of the gravity current terminal velocity is indicated in Figure 5.16. Table C.11 contains the corresponding data. A least-squares linear curve fit through the origin has a slope of m=0.83 and a correlation coefficient of r=0.94 showing that the *a priori* prediction is in general a little large as would be expected. Still, the agreement is rather surprising given that the initial suspension density is used in equation (3.74) whereas gravity current densities typically drop with distance traveled down the incline. The per cent error between the two terminal velocities is on average 9.4% with a standard deviation of ±17.4% about the mean. Given the normal errors in s_o and t_o, the error in the terminal velocity should actually be ±22.4%. Once again, the theoretical prediction does better than expected and equation (3.74) can be used to describe material landslide center of mass motion in numerical simulations of deforming landslides.

Figure 5.16 also exhibits ordering by glass sphere and lead shot nominal diameter. However, equation (3.74) should be considered a fortuitous scaling quantity rather than a prediction of material landslide terminal velocities. Instead of using equation (3.74), the relation between the experimentally inferred terminal velocity and the single particle fall

velocity is examined here. The particle fall velocity relative to the material landslide terminal velocity probably controls the degree of mixing in the landslide wake, where relatively small settling velocities allow for the development of a significant material landslide wake. Figure 5.17 plots the ratio of experimental terminal velocity to single particle fall velocity *versus* the nondimensional particle size of glass sphere landslides. The data for Figure 5.17 is located in Tables 4.3, C.9 and C.14. The approximate equation

$$\frac{s_o}{t_o u_p} \approx 1.26 + 0.00471 \left(\frac{D}{b}\right)^{-1.39} \tag{5.11}$$

describes the variation of nondimensional terminal velocity with a correlation coefficient r=0.99 and is valid for nondimensional particle sizes D/b ranging from 0.015-0.15. The exponent -1.39 in equation (5.11) is too large to be induced solely by the particle fall velocity dependence on nominal diameter given by equation (4.19). Therefore, additional curvature must arise from either i) the smaller or ii) the larger nominal diameter spheres permitting larger experimental terminal velocities. Inspection of Table C.11 reveals that it is the 12 mm marble landslides that had the larger experimental terminal velocities. The conclusion is straightforward: larger particles permit larger experimental terminal velocities through less mixing and smaller landslide wakes. Mixing incorporates surrounding water with no intrinsic inertia into the moving landslide mass. Mixing also lowers the instantaneous suspension density. Hence, mixing slows down a material landslide. For a given material density, mixing can be suppressed by larger particle sizes.

5.1.6 Material Landslide Rate of Deformation

As in the previous section, this discussion begins with photographic records of deforming material landslides. Trials 40, 82, and 81 contained marked particles that can be observed on each movie frame and tracked during landslide failure. In order to resolve the marked particles, each landslide was recorded with the movie camera close to the wave tank and tilted 45° clockwise so that the landslide traverses the frame horizontally from left to right. The experimental methodology is described in Section 4.3.2. Figures 5.18-5.20 show movie frames from Trial 40 involving crushed calcite, Trial 82 involving 3 mm glass beads, and Trial 81 involving 3 mm steel shot, respectively. Figure 5.18 shows that crushed calcite underwent very little strain in the core of the gravity current. This is not surprising for a granular material with an internal friction angle of 47° sliding along an

incline 45° from horizontal. While particles were being sheared from the surface at t=0.39 s, most of the particles within the landslide core still had very similar relative positions. Figure 5.19 demonstrates the significantly higher rate of deformation associated with glass bead landslides. Moreover, particle motion within the gravity current was sufficiently strong that marked particles regularly appeared and disappeared from view due to transverse particle mixing. The steel shot in Figure 5.20 underwent very rapid stretching of the landslide nose while the tail of the gravity current deformed relatively little. The steel shot landslide rapidly acquired sufficient velocity for a few particles to detach from the gravity current. Similar behavior was observed in the two-dimensional simulations of a granular medium landslide along a 45° incline (in the absence of interstitial fluid) performed by Campbell *et al.* (1995). For all three materials described here, the use of an isosceles triangle to describe the initial landslide rate of deformation as described in Section 3.2.2.1 is seen to be justified. At early times, the simulated landslides of Campbell *et al.* (1995) also appeared like isosceles triangles.

If the mean particle size of a landslide material is much smaller than the initial size of the landslide, then the material can be considered as a continuum that has no inherent length scale other than the size of the landslide -- although the constitutive properties of the continuum may still depend on the particle size. Therefore landslide size should grow in relation to the distance traveled down the incline. In fact, Figures 5.21 and 5.22 show that the landslide cross-sectional area of Trial 91 involving 3 mm glass beads and the 3 mm steel shot landslide grew linearly proportional to the elapsed time of landslide motion. The error bars represent one standard deviation and are derived in Section B.1.8. Hence, the initial rate of area change in time needed for equation (3.85) can be found from a linear curve fit of the data as a function of time as shown on Figures 5.21 and 5.22. On the other hand, Figure 5.23 shows that the landslide area of the 0.5 mm glass bead landslide grew linearly proportional to the distance traveled down the incline. Garnet sand was the only other landslide material with an area that grew in proportion to the distance traveled. Clearly, the larger internal friction angle, the larger material density, and the angularity of garnet sand did inhibit significant cross-sectional area growth. Therefore, a completely different landslide dynamic appears to govern the deformation of landslides with smaller nominal diameters. The analysis of Figure 5.17 suggests that particle size and material density control the degree of mixing between material particles with surrounding water and thereby determine the mechanism of cross-sectional area growth. Or, linear growth of cross-sectional area in time may be the short time asymptotic behavior of landslide growth for all materials and the incline was too

short to capture growth in proportion to distance traveled for most materials. The initial rates of area change in time for the 0.5 mm glass bead and garnet sand landslides were found from a linear curve fit of the data at early times.

The results of all linear curve fits for the initial rate of area change in time can be found in Tables 5.5 and C.12. The standard errors are estimated in Section B.1.8. The initial rate of area change in time is a measure of material dilatation induced by gate retraction, gravitational forcing, particle interactions, and landslide surface shearing to name the primary sources of cross-sectional area growth. Area growth in Table 5.5 seems to reflect particle size more than any other material characteristic in Tables 4.2 and 4.3. A more detailed attribution of the initial rate of area change to different material characteristics is not possible due to the limited number of materials studied and the errors inherent in the measurements. For an identical material density, large particles resist mixing due to their relatively large settling velocities. However, small particles may also resist mixing at early times due to their relatively low hydraulic diffusivity that permits negative pore water pressures to develop during dilatational flows. For all material landslides, water apparently flowed into the material landslide from all directions except through the incline. Uniform flow into a sink may change the absolute pressure near the sink but it would not impart any directionality to the flow. Therefore, a uniform change in the absolute pressure around an underwater landslide would not alter its center of mass motion. The surface waves induced by landslide growth alone can be approximated by a submerged line sink with a corresponding flow rate and initial submergence. This calculation is made in Section 5.3.1 below. It is highly unlikely that there is any significant water flow through the material landslides due to center of mass motion. Material landslide cross-sectional area is inversely proportional to the mean solid volume fraction of particles in the landslide. Therefore, the suspension density of material landslides is continually decreasing with time.

Material landslides with small particles rapidly become diluted by the entrainment of water, most notably in their wakes. Some difficult questions arise. For example, does part of the landslide continue to contribute dynamically to landslide motion while other parts get left behind? Or, is area even a meaningful characteristic of a highly deformed gravity current displaying nonlinear wave activity? Excluding the wake area from landslide traces could reduce the landslide area by 40% for 0.5 mm glass beads and 25% for 1 mm and 3 mm glass beads. In fact, excluding the wake area from the last trace of the 0.5 mm glass bead landslide produced a landslide cross-sectional area that appears to

suggest linear growth of area in time of the dense landslide core. However suggestive, these issues are best left to studies devoted specifically to gravity current deformation. Wave generation is inherently tied to earlier events in an underwater landslide. That is why the initial rate of deformation is sought in this section rather than some more complicated measure of landslide deformation over time. It is worth noting here that these experiments had the benefit of not undergoing entrainment of sediment during landslide motion and deformation.

Table 5.5: Material Landslide Initial Rates of Deformation

Material	Trial	$1/A_0\ dA/dt$ (s^{-1})	$1/z_{c.o}\ dz_c/dt$ (s^{-1})	$\Gamma = d\alpha/dt$ (rad/s)
Crushed Calcite	32	1.55 ± 0.20	-0.40 ± 0.09	-1.17 ± 0.20
Crushed Calcite	33	1.92 ± 0.25	-0.46 ± 0.11	-1.41 ± 0.24
Crushed Calcite	40	1.83 ± 0.24	-0.52 ± 0.12	-1.42 ± 0.24
0.5 mm Glass Beads	87	0.83 ± 0.11	-0.52 ± 0.12	-0.93 ± 0.16
1 mm Glass Beads	35	2.35 ± 0.31	-0.60 ± 0.14	-1.77 ± 0.30
1 mm Glass Beads	89	2.33 ± 0.31	-0.33 ± 0.08	-1.49 ± 0.25
1 mm Glass Beads	90	2.62 ± 0.34	-0.49 ± 0.11	-1.79 ± 0.30
1 mm Glass Beads	92	2.26 ± 0.29	-0.70 ± 0.16	-1.83 ± 0.31
1 mm Glass Beads	93	2.82 ± 0.37	-0.55 ± 0.13	-1.96 ± 0.33
3 mm Glass Beads	34	2.41 ± 0.31	-0.98 ± 0.23	-2.18 ± 0.37
3 mm Glass Beads	82	1.75 ± 0.23	-0.89 ± 0.20	-1.75 ± 0.30
3 mm Glass Beads	91	1.61 ± 0.21	-0.55 ± 0.13	-1.34 ± 0.23
12 mm Marbles	37	1.17 ± 0.15	-0.59 ± 0.14	-1.15 ± 0.20
12 mm Marbles	83	1.44 ± 0.19	-0.55 ± 0.13	-1.26 ± 0.21
2 mm Lead Shot	39	2.16 ± 0.28	-1.50 ± 0.34	-2.53 ± 0.43
2 mm Lead Shot	84	1.57 ± 0.20	-1.67 ± 0.38	-2.41 ± 0.41
3 mm Lead Shot	38	1.92 ± 0.25	-1.48 ± 0.34	-2.41 ± 0.41
3 mm Lead Shot	86	0.83 ± 0.11	-1.59 ± 0.37	-1.99 ± 0.34
3 mm Steel Shot	81	1.53 ± 0.20	-1.71 ± 0.39	-2.42 ± 0.41
Garnet Sand	85	0.52 ± 0.07	-0.82 ± 0.19	-1.07 ± 0.18

The definition of the centroid height above the incline can be found in Figure 3.1. Error analyses are carried out in Section B.1.7. Figure 5.24 shows the change in centroid height above the incline as a function of time for Trial 91 involving 3 mm glass beads. It is noticed that a change in the landslide deformation takes place at around $t \approx 0.2$ s. Before that time, the landslide is spreading and the center of mass is dropping; after that time, the landslide centroid begins to rise, probably on account of stronger mixing with surrounding water. A linear curve fit over the first seven height measurements yields the initial normal rate of strain given in Table 5.5 and needed for equation (3.85). The term "normal" is used to denote the direction normal to the incline. This behavior was also typical of crushed calcite, 1 mm glass bead, and marble landslides. Such a change in landslide deformation is absent from Figure 5.25 probably because the 3 mm steel shot was too dense for these size particles to have begun significant mixing by the time the landslide reached the bottom of the incline. The normal rate of strain was therefore found from a linear curve fit over all data. All lead shot landslides had similar behavior in the normal rate of strain as the steel shot landslide. Figure 5.26 shows that the 0.5 mm glass bead landslide underwent a change in landslide deformation similar to that seen in Figure 5.24 before a marked rise in the landslide centroid occurred. The garnet sand landslide also underwent a marked rise in the landslide centroid height above the incline probably on account of the strong mixing experienced by that landslide. Since the minima in Figures 5.24 and 5.26 occur around the same time, it follows that the rate of landslide mixing is highly dependent on the size of the glass bead particles. This effect was first discussed in connection with Figure 5.17 above.

Regardless, all material landslides experienced an initial drop in the center of mass height above the incline as seen by the negative signs in Tables 5.5 and C.12. Error analyses for the initial normal rate of strain are described in Section B.1.7. Rapid spreading of a material landslide at early times almost certainly lowers the landslide center of mass. The initial normal rate of strain appears to depend on the material density more than any other material characteristic. It is the component of gravitational forcing normal to the incline that is primarily responsible for the spreading failure of material landslides at short times. The gravitational forcing is in turn proportional to the landslide mass in Table 4.2. A comparison of 3 mm glass bead and crushed calcite initial normal rates of strain may indicate that a large internal friction angle inhibits landslide spreading. This observation is also apparent from Figure 1.6. However, a more detailed analysis of the initial normal rates of strain was not pursued due to the limited number of materials studied and the errors inherent in the measurements.

The initial landslide rate of deformation Γ was calculated from equation (3.85) with data from Table 5.5. Values of the initial landslide rates of deformation are given in Tables 5.5 and C.13. The error provided in Table 5.5 represent one standard deviation and were calculated based on an analysis in Section B.1.9. The initial landslide rates of deformation shown in Table 5.5 are a measure of how fast the initially horizontal top face of a material landslide rotates clockwise. Given the assumption that the landslide retains the shape of an isosceles triangle at early times, the vertical front face of the landslide is assumed to rotate a similar amount counter-clockwise. Figures 5.18 to 5.20 show that this does indeed occur. Therefore, the initial landslide rate of deformation is a direct measure of the geometrical departure of material landslides from solid block geometry at early times. Unlike the growth in landslide cross-sectional area, the change in landslide shape should actually affect the pressure distribution along the surface of the landslide and hence alter wave generation. All three crushed calcite trials have reasonably similar initial rates of deformation. All five 1 mm glass bead trials also had similar initial rates of deformation. Trials 34 and 82 as well as Trials 38 and 86 demonstrate the differences in the initial rate of deformation that can be expected for repeated trials. The initial rates of deformation Γ vary from -50°/s to -140°/s so that after a time Δt=0.1 s the angle α has varied between $-5° < \Delta\alpha \approx \Gamma\Delta t < -14°$. It is shown in Section 5.3 that these rates of deformation are significant enough to affect wave amplitudes. Table 5.5 provides an extra decimal place in order to avoid round off errors.

The nondimensional quantity Γt_o is the hypothetical angle change in radians of the top face of a triangular material landslide if the initial landslide rate of deformation were maintained over the entire characteristic time of center of mass motion. The nondimensional landslide deformations Γt_o were calculated from data in Tables 5.4 and 5.5 and are given in Tables 5.6 and C.13. Additional calculations provided in Section B.1.9 show that the nondimensional landslide deformations are typically accurate to within ±25% at one standard deviation. Figure 5.24 shows that the initial rate of normal strain can be maintained up to at least t=0.2 s while a typical characteristic time for center of mass motion is $t_o \approx 0.3$ s from Table C.10. Hence, Γt_o provides a meaningful characteristic landslide deformation. Based on the material landslide center of mass motion described in Section 5.1.5 as well as the preceding analyses of landslide growth and normal rates of strain, it is not surprising to be unable to attribute the nondimensional landslide deformation to particular material characteristics. In Section 3.2.2.1, the nondimensional landslide deformation was proposed as a perturbation to water waves

generated by solid block landslides. The values of the nondimensional landslide deformation in Table 5.6 do not necessarily satisfy the usual idea of a perturbation quantity $|\Gamma t_o| \ll 1$. However, the discussion in Section 5.3.2 shows that the initial landslide rate of deformation is in fact a perturbation parameter relative to wave generation. Table 5.6 provides an extra decimal place to avoid round off errors.

Table 5.6: Nondimensional Material Landslide Deformations

Material	Trial	$-\Gamma t_o$ (radians)
Crushed Calcite	32	0.34 ± 0.07
Crushed Calcite	33	0.38 ± 0.09
Crushed Calcite	40	0.38 ± 0.09
0.5 mm Glass Beads	87	0.50 ± 0.11
1 mm Glass Beads	35	0.60 ± 0.13
1 mm Glass Beads	89	0.57 ± 0.12
1 mm Glass Beads	90	0.70 ± 0.16
1 mm Glass Beads	92	0.57 ± 0.15
3 mm Glass Beads	34	0.70 ± 0.15
3 mm Glass Beads	82	0.57 ± 0.10
3 mm Glass Beads	91	0.42 ± 0.08
12 mm Marbles	37	0.41 ± 0.10
12 mm Marbles	83	0.46 ± 0.09
2 mm Lead Shot	39	0.64 ± 0.18
3 mm Lead Shot	86	0.59 ± 0.15
3 mm Steel Shot	81	0.66 ± 0.16

Bagnold (1954) discovered two distinct asymptotic regimes for the behavior of large, neutrally buoyant particles in a uniform shear flow. Zeininger and Brennen (1985) have shown that the ideas of Bagnold (1954) can be applied to the characteristic flow rate of hopper flows for a variety of granular media in air and water. The initial landslide rate of deformation Γ given in Table 5.5 allows for the regimes of material landslides to be estimated for underwater landslides. Bagnold (1954) showed that the "grain-inertia" regime has shear stresses proportional to

$$\tau \propto \rho_m D^2 L^2 \Gamma^2 \tag{5.12}$$

where ρ_m is the material density, D is the particle nominal diameter, Γ is a characteristic rate of strain, and L is a nondimensional geometrical packing factor. According to Bagnold (1954), the geometrical packing factor

$$L \equiv \frac{\nu_s^{1/3}}{\nu_{s.max}^{1/3} - \nu_s^{1/3}} \tag{5.13}$$

represents the ratio of particle diameter to mean particle separation, where $\nu_{s.max} \approx 0.74$ is the theoretical maximum solid volume packing of monodisperse spheres. Larger values of the solid volume fraction ν_s can produce significantly larger values of the geometrical packing factor L since equation (5.13) diverges as $\nu_s \to \nu_{s.max}$. The "macro-viscous" regime was found experimentally to have shear stresses proportional to

$$\tau \propto \mu_o L^{3/2} \Gamma \tag{5.14}$$

where μ_o is the dynamic viscosity of water. The ratio of equation (5.12) to equation (5.14) forms the nondimensional Bagnold number

$$Ba \equiv \frac{\rho_m D^2 L^{1/2} \Gamma}{\mu_o} \tag{5.15}$$

that describes the relative importance of the two flow regimes. According to experimental results, a Bagnold number $Ba<40$ constitutes "macro-viscous" behavior whereas a Bagnold number $Ba>400$ corresponds to "grain-inertia" behavior. A "macro-viscous" mixture can be considered as a conventional suspension whereas a "grain-inertia" mixture can be considered as a granular medium.

The observation that the lead shot landslide in Figure 5.9 resembles the experimental results given by Savage and Hutter (1989) for a gravel landslide in air can be reinterpreted as saying that the 2 mm lead shot is behaving like a granular medium even though the landslide is immersed in water. The same can be said about the comparison of the steel shot landslide in Figure 5.20 with the two-dimensional granular media simulations of Campbell *et al.* (1995). More to the point, Zeininger and Brennen (1985) have shown that the nondimensional flow rates of lead shot in air and in water are

identical in a hopper flow with a Bagnold number Ba≈1000. The regime of each material landslide performed for this work can be checked by evaluating the initial Bagnold number using the values in Tables 4.2, 4.3, and 5.5. The Bagnold number will of course vary in time and only the initial Bagnold number is considered. In fact, the only material landslides for which Ba>400 were the marble experiments. All lead and steel shot trials had initial Bagnold numbers between 100<Ba<300 so that the initial motion and deformation of these landslides may actually be slightly different in air. The crushed calcite, glass bead, and garnet sand landslides all had Bagnold numbers Ba<50 and therefore behaved more or less like suspensions when liquefied. While these constitute interesting calculations, the "macro-viscous" shear stress in equation (5.14) was apparently not correlated with the initial gravitational shear stress along the bottom of the landslides with Ba<40. Therefore, it appears that these concepts cannot be used for quantitative or predictive analyses of underwater landslides.

5.2 Solid Block Landslide Results

Solid block landslide experiments form an important benchmark from which more complicated underwater landslide experiments can expand the wavemaker formalism of Section 3.1.3. Water waves generated by solid block landslides are described first. Solid block motion is then combined with the observed water wave records to produce wavemaker data. While the wavemaker curves provided in this section are limited to the chosen solid block and incline geometries, they provide the correct (albeit primitive) formalism for studying water waves generated by general underwater landslides. The experiments performed with material landslides merely modify the present results based on landslide rates of deformation.

5.2.1 Near-field Wave Characteristics

In section 1.1, Figures 1.3 and 1.4 demonstrated that the vertical face of a landslide generated a positive wave in front of the landslide while the horizontal face of a landslide generated a negative wave above the landslide. In addition, Figure 1.3 demonstrated the initial flow of water from the front face of the landslide along streamlines connected to the top face of the landslide. As noted in Section 1.1, the essential features of such a flow field are captured by a submerged flow doublet at the block vertex. Figure 5.27 superposes near-field wave records of Trials 20 and 22 for different wave gauge positions. In both trials, the old block 2_n was released from rest with an initial

submergence of d=59 mm. Solid block Trial 60 is almost a repeat of Trials 20 and 22. Given that the wave gauges were in the near-field above the incline, the solid block size is used to nondimensionalize wave gauge positions. A wave gauge with measuring wires above the middle of the initial solid block position is considered to be at x/b=0. Immediately above the initial solid block position, the free surface is drawn down by block motion and then rebounds. About two block lengths away, the leading positive wave can be seen prior to the arrival of a large negative wave. Given $s_o \approx 0.203$ m and $t_o \approx 0.365$ s for Trial 60 in Table C.2, equation (3.78) shows that the free surface minimum at x/b=2.09 and $t \approx 0.8$ s corresponds to passage of the solid block under the wave gauge. The free surface trough following the landslide motion was first pointed out in the discussion of Figures 1.3 and 1.4. The maximum wave amplitude at $x/b \approx 2$ is nearly twice as large as that immediately above the initial solid block position. At x/b=4.18, a larger positive wave is measured far ahead of the solid block along with passage of a significant negative wave. The free surface minimum at x/b=4.18 occurs a little bit ahead of the solid block position at $t \approx 1.1$ s. Hence, the ability of solid block motion to create a trough above the top face of the block is apparently lessened with increasing depth. Wiegel (1955) notes that the trough in the free surface above the landslide is analogous to the trough found above a moving hydrofoil. The comparison is interesting because in both cases the trough is generated by the pressure distribution along the surface of the wavemaker and in both cases the trough follows the position of the wavemaker.

Figure 5.28 shows the superposed near-field wave records at x/b=0 for solid block 2 Trials 28-31, 41 and 42. Each trial had the same initial submergence d=74 mm and was conducted on a 45° incline. The initial geometry of each solid block trial is given in Table C.1. The dynamical coefficients of the solid block trials shown in Figure 5.28 are assumed to be constant in time and identical for the six wave records. Therefore, only the solid block mass (or density) changed in equations (3.6) and (3.78). Error analyses of near-field wave records are conducted in Section B.2.1. In Figure 5.28, larger solid block densities are clearly associated with larger wave amplitudes as was also found by Wiegel (1955). A change in solid block density changes the characteristics of motion appearing in the Hammack number and the nondimensional wave amplitude in equation (3.27). Therefore, the block density becomes the central parameter used to find the loci of the wavemaker curve for a given initial landslide geometry and identical dynamical coefficients.

Despite several noteworthy differences in the wave records, the general characteristics of each wave record look remarkably similar: the free surface forms a relatively large negative wave followed by a free surface rebound with decaying oscillations. Appendix A provides the near-field wave records of all trials repeated more than once for the sake of wave record comparison. All wave records in Figure 5.28 appear to share a similar motion at very early times. Near $t=0^+$, the initial wave motion at $x/b=0$ follows the quadratic behavior of the solid block motion given by equations (3.97) and (3.99)

$$\eta(t,0) \approx -\frac{a_o \sin\theta\, t^2}{2} \frac{2}{\pi} \int_0^\infty \frac{\sin(\beta y)}{y \cosh y} dy =$$

$$= -\frac{a_o \sin\theta\, t^2}{2\pi} \left\{ 4 \tan^{-1}\left[\exp\left(\frac{\pi\beta}{2}\right)\right] - \pi \right\} \qquad (5.16)$$

where $\beta=b/2d$ and the term in the braces is always less than π. All assumptions made in deriving equation (5.16) are described in Section 3.3.1. The subsequent large amplitude negative wave is the single most important feature of wave generation at $x/b=0$.

In fact, the maximum near-field wave amplitude (taken as a positive number) is used below as a characteristic wave amplitude for the entire wave generation and propagation problem. Figure 5.27 shows that wave records obtained at different near-field locations offer different values of the maximum near-field wave amplitude. One is free to choose the location that will be used to characterize other wave amplitudes. For this work, the location $x/b=0$ is chosen. From now on, the term "maximum near-field wave amplitude" is reserved for the positive number η_{max} recorded at $x/b=0$. However, one must acknowledge that completely different choices for a characteristic wave amplitude are also possible. For example, one might choose instead a characteristic wave amplitude far from the generation region or a time averaged wave amplitude at some important location relevant to some other wave problem. Equation (3.27) does not depend on the definition of the characteristic wave amplitude in order to guarantee the existence of a wavemaker curve.

The shoreward side of the negative wave propagating away from the incline is highly dispersive and can give rise to higher frequency water waves observed in the wave records of Figure 5.28 at around one second. Following the negative wave, there is a free

surface rebound in the form of a smaller positive wave. The rebound occurs sooner for more massive blocks although the amplitude of the rebound is nearly constant. Wiegel (1955) also observed free surface rebounds with amplitudes comparable to the maximum near-field wave amplitude. The free surface oscillations that follow the free surface rebound are exponentially damped in what appears to be a nearly critical manner. To see this, let the Hammack number $Ha=t\sqrt{gd}/b$ represent nondimensional time. It follows from the method of Laplace (or steepest descent) applied to the integral solution equation (3.94) of Section 3.3.1 that the wave amplitude above the middle of the solid block decays proportional to

$$\eta(t,0) \propto \frac{s_o}{Ha \cosh \frac{Ha^2}{4}} \tag{5.17}$$

for sufficiently long times after the wave front has left the wave generation region. The exponential damping of free surface oscillations above an underwater landslide can therefore be predicted by linear water wave theory. Equation (5.17) highlights the facts that the nondimensional, linear wave amplitude is a continuous function of the Hammack number and that the use of the characteristic time t_o in the wavemaker formalism was meant to imply that the maximum near-field amplitude occurs at around $t \approx t_o$. For most experiments, $t_o \approx 0.35$ s which is close to the actual time of the maximum near-field wave amplitude. While the time of the maximum near-field amplitude can only be expected to be proportional to the characteristic time of motion, the similarity between the two times is an important clue as to the connection between solid block motion and wave generation.

Section 4.2.3 noted the existence of old and new block 2 results. Having chosen a characteristic wave amplitude, one can now examine if the maximum near-field wave amplitudes of repeated trials differ significantly. Figure 5.29 compares the maximum near-field wave amplitudes of 10 repeated trials. The maximum near-field wave amplitude η_{max} was found by taking the absolute value of the maximum wave amplitude extracted from a near-field wave record using the subroutine "Pulse Analysis" in the Superscope software. The results of the analysis are given in Table C.3. The standard error in the maximum near-field wave amplitude is estimated in Section B.2.1. The abscissa denotes the wave amplitudes for block motion recorded with a high speed movie camera whereas the ordinate denotes wave amplitudes for block motion recorded by an accelerometer. The purpose of Figure 5.29 is to show that trials performed with the old

block 2 typically had smaller wave amplitudes than similar trials performed with the new block 2. This is seen by the fact that all circular symbols are located to the left of the line of equivalence. There was probably a difference in the block Coulombic friction with the incline between the old and new block 2. There is also a noticeable trend for the new block 2 to have slightly smaller wave amplitudes with the accelerometer present, but the trend is not statistically significant. Smaller wave amplitudes would indicate that the accelerometer retarded solid block motion.

The maximum near-field wave amplitude measured above the middle of the initial landslide position was chosen as a characteristic wave amplitude. However, other measures of near-field wave amplitude can be devised and two of these are now examined. For example, a plausible measure of the near-field wave amplitude would be the area between the negative wave and the horizontal axis $\eta=0$. The amplitude integral extends from t=0 s until the wave crosses $\eta=0$ at time t_x and is therefore dependent on the shape of the wave record The nature of the near-field wave records is such that differences in the time of zero crossing t_x from one trial to another have little effect on the value of the amplitude integral. The amplitude integral I(0) can be made nondimensional by the characteristic quantity $t_o\eta_{max}$. The dimensionless ratio $I(0)/t_o\eta_{max}$ is expected to depend on wave interactions with the incline, wave nonlinearity, and the underwater landslide geometry. For a fixed incline angle, these effects are all related to the nondimensional initial submergence d/b. Figure 5.30 shows the resulting plot. Error bars represent one standard deviation and are calculated in Section B.2.2. The data for Figure 5.30 can be found in Tables C.1 and C.6. A power law curve fit through the origin yields

$$\frac{I}{t_o\,\eta_{max}} \approx 1.824\left(\frac{d}{b}\right)^{0.36} \tag{5.18}$$

over the range $0.3<d/b<2.2$ with a correlation coefficient r=0.77. Equation (5.18) should probably be a function of incline angle θ since the shape of the near-field wave record would depend on wave interactions with the incline. Figure 5.30 indicates that the amplitude integral I(0) of the near-field wave record remains relatively large compared to the scaling quantity $t_o\eta_{max}$ for large initial submergences. Regardless, the amplitude integral is seen to provide no new information about the wave amplitude as its value can be predicted uniquely from the characteristic quantities t_o and η_{max} as well as the initial landslide geometry. Since the maximum near-field wave amplitude is ultimately a

function of geometry and kinematics, wave shape is seen to also be a function of geometry and kinematics.

Another measure of near-field wave amplitude can be obtained by squaring the near-field wave record and integrating from time t=0 to infinity. The integral that results is a measure of the total wave potential energy passing through the wave gauge location in addition to being another measure of wave shape. The near-field energy integral was integrated until the wave amplitude was less than the (voltage) drift away from the axis η=0. In practice, the integral extended until 4 s from the beginning of the trial. The energy integral can be compared to the characteristic quantity $t_o\eta_{max}^2$. Figure 5.31 shows the variation of $E_p(0)/t_o\eta_{max}^2$ with nondimensional initial block submergence. Error analyses of the nondimensional ratio $E_p(0)/t_o\eta_{max}^2$ are located in Section B.2.3. The data corresponding to Figure 5.31 can also be found in Tables C.1 and C.6. A power law curve fit through the origin provides

$$\frac{E_p(0)}{t_o\,\eta_{max}^2} \approx 1.586\left(\frac{d}{b}\right)^{0.40} \tag{5.19}$$

over the range 0.3<d/b<2.2 with a correlation coefficient r=0.79. The exponent in equation (5.19) is very similar to the exponent in equation (5.18). Equation (5.19) should also be a function of incline angle θ. The total potential energy measured at the origin $E_p(0)$ remains relatively large compared to the scaling quantity $t_o\eta_{max}^2$ for large initial submergences. The near-field energy integral is seen to provide no new information about the wave amplitude since the total wave potential energy can be predicted from the characteristic quantities t_o and η_{max} as well as initial landslide geometry. Hence, the near-field energy integral can also be predicted solely from landslide geometry and motion. In general, there appears to be no need for a separate measure of the wave amplitude other than the maximum near-field wave amplitude η_{max}.

5.2.2 Far-field Wave Characteristics

Dispersive waves propagating down a constant depth channel disperse according to the nondimensional product κh, where κ is the wavenumber and h is the channel depth. Therefore, distances down the channel in the far-field are often expressed as fractions of the channel depth as x/h. This basic fact of water wave propagation introduces a new length scale into the geometry of the wavemaker problem and one may inquire under

what conditions the channel depth is important to the characteristics of far-field waves. For example, if water waves generated by underwater landslides propagate as deep water waves, then it is safe to assume that the channel depth plays little to no role in the characteristics of far-field waves. More to the point, it is convenient to seek a channel depth criterion whereby water waves generated by underwater landslides will indeed produce deep water waves. If far-field waves propagate as deep water waves, then the nondimensional product κh in the dispersion relation

$$\omega = \pm\sqrt{\kappa\, g \tanh \kappa\, h} \tag{5.20}$$

no longer contributes to wave propagation since $\tanh(\kappa h)\approx 1$. For deep water waves, it follows that the only horizontal length scale far from the wave generation region is the wavelength λ contained in the definition of the wavenumber κ in equation (5.20). Therefore, distances down the constant depth channel should be expressed nondimensionally as x/λ for deep water waves.

This section begins with some basic observations of far-field wave records measured at the location $x/h=4.25$, where the near-field wave gauge is located at $x/h=0$. As shown in Section 5.2.4, $x/h=4.25$ is far enough away from the wave generation region to provide the features of the dispersive wave train. Figure 5.32 shows the far-field wave records corresponding to Figure 5.28. An error analysis of far-field wave records can be found in Section B.2.4. The characteristics of each wave record in Figure 5.32 look similar: the wave front consists of a leading positive wave followed by a dispersive wave train of modulated wave amplitude. The leading positive wave is generated by the front face of the accelerating solid block as shown in Figure 5.27. Once again, denser solid blocks generated larger wave amplitudes as in the previous section and as shown by Wiegel (1955). The peaks and troughs of the dispersive wave trains in Figure 5.32 are not aligned and appear to show varying degrees of wave dispersion. This may be an indications that these are deep water waves and the far-field wave gauge should have been located at the same value of x/λ rather than the same value of x/h. Appendix A provides the far-field wave records of all trials repeated more than once for the sake of wave record comparison.

As shown in Section 3.3.2, the leading waves in Figure 5.32 are Airy waves that accomplish the transformation from exponential wave growth to dispersive wave oscillations. The wave amplitude decays with distance according to

$$\eta \propto \frac{\eta_{max}}{x^{1/3}} \tag{5.21}$$

while the celerity of the Airy wave is the long wave celerity $\sqrt{gh}$ in the channel. Wiegel (1955) observed far-field waves generated by submerged solid blocks and confirmed these properties of the Airy wave. Therefore, while the dispersive wave train may propagate as deep water waves independent of the channel depth, the Airy wave always propagates at a celerity controlled by the channel depth. The maximum Airy wave amplitude is used as a characteristic far-field wave amplitude. The Airy wave is followed by a damped sinusoidal wave envelope that contains groups of water waves. For linear water waves, the nodes of the wave envelope separate distinct wave numbers in the wave train through which no energy may be transferred. Whitham (1973) shows that nodes travel at the group velocity of their respective wavenumber. For the experiments described herein, it is shown immediately below that almost all of the wave energy is contained within the first group of waves. Therefore, the first node has a large enough wavenumber (or small enough wavelength) that the largest waves travel ahead of the first node. Indeed, the maximum far-field wave amplitude occurs near the middle of the first wave group rather than at the leading positive wave.

If the waves in the constant depth channel are deep water waves, then the far-field wave characteristics depend on only two general characteristics of the wavemaker itself: the ability to generate a leading positive wave followed by a negative wave and the fact that water waves leave the generation region faster than they are generated, i.e., $Ha_o \gg 1$. These characteristics should hold for most underwater landslides in nature except perhaps for the largest earthquake induced underwater landslides on slopes less than several degrees or very shallow landslides induced by nearshore human activity. These possibilities are explored in more detail immediately below. A criterion needs to be established to estimate if landslide-generated water waves propagate as long waves, deep water waves, or with some intermediate behavior. The conventional boundary $\kappa h > \pi$ used to denote deep water waves can be converted to a criterion on the channel depth h. If the far-field wave train is comprised of deep water waves, then water waves propagating along the incline towards the constant depth channel cease to feel the incline prior to reaching the toe of the incline. This is why the toe of the incline was not used as a reference position in this work.

A typical far-field wavelength should be related to a characteristic wave period which in turn should be proportional to the characteristic time of landslide motion. Wiegel (1955) observed that the wave period increases with increasing block size and smaller incline angles but appears independent of water depth, initial submergence, or solid block mass. Equation (3.73) for the initial acceleration and equation (3.74) for the terminal velocity can be combined with equation (3.75) to yield

$$t_o = \frac{\sqrt{2}\ (m_b + C_m\, m_o)}{\sqrt{(m_b - m_o)\, g\, (\sin\theta - C_n \cos\theta)\, C_d\, \rho_o\, w\, \ell \cos\theta \sin\theta}} \tag{5.22}$$

where equation (5.22) is proportional to $\ell^{1/2}$ and increases with decreasing θ. These trends correspond with the observations of Wiegel (1955). Since the characteristic wavelength $\lambda \approx t_o\sqrt{gd}$ also depends on the time scale t_o, it follows that the wavelength is also proportional to $\ell^{1/2}$ which explains the observations of Wiegel (1955) regarding wavelength. The volume of a solid block landslide

$$V_b = \frac{w\,\ell^2}{2} \cos\theta \sin\theta \tag{5.23}$$

can be used to simplify equation (5.22) since $m_b=\rho_b V_b$ and $m_o=\rho_o V_b$. The characteristic time scale t_o becomes for any incline angle θ

$$t_o = \frac{\sqrt{\ell}\ (\rho_b + C_m\, \rho_o)}{\sqrt{C_d\, \rho_o\, (\rho_b - \rho_o)\, g\, (\sin\theta - C_n \cos\theta)}} \tag{5.24}$$

and the dependence of the time scale on the length of the landslide has been made explicit. Equation (5.24) can be applied to material landslides if ρ_s is used in place of ρ_b and suitable dynamical coefficients are known. Equation (5.24) shows that the Hammack number Ha_o is proportional to $\ell^{-1/2}$ since $b \equiv \ell\cos\theta$. Therefore, for a given landslide density and initial submergence, longer landslides have smaller Hammack numbers. The increase in the characteristic time scale t_o with increasing landslide length is not strong enough to offset the growth in landslide size.

The far-field wave records are naturally amenable to Fast Fourier Transform (FFT) analysis because the wave records begin and end with negligible wave amplitudes (and slopes) and because wave dispersion makes the different frequency components visually

recognizable. A typical far-field wave record sampled at 720 points per second could provide 4096 points for an FFT of base 2. However, the resulting frequency step $\Delta f=720/4096\approx 0.18$ Hz in the FFT analysis was too large to resolve the dominant wave frequency of around $f\approx 1$ Hz because almost all of the wave energy was contained within the first six or seven frequency bins. The frequency resolution was so poor that a figure depicting a typical FFT analysis is not included. Consequently, a direct correlation between the dominant wave frequency and the characteristic time scale of landslide motion was not sought. Since the dominant frequency is related to the dominant wave period by $T=1/f$, it is apparent that $T\approx 1$ s is a typical dominant wave period for this work. Since $t_o\approx 0.35$ s, it follows that $T\approx 2t_o$ is a better predictor of far-field wave periods than the characteristic time of landslide motion alone. This fact is readily apparent from near-field wave records as well: the duration of the large initial trough is approximately $2t_o$. Hence, typical far-field wavelengths

$$\lambda \approx 2\, t_o \sqrt{g\, d} \tag{5.25}$$

follow from Section 3.1.3. The factor of two was added to convert the characteristic wavelength into a better estimate of the dominant wavelength. A longer estimate of the dominant wave period clearly increases the dominant wavelength. The additional factor of two probably arises from the fact that the scaling analysis assumed a channel of depth d whereas waves rapidly propagated beyond the solid block into deeper water where the long wave celerity would be higher.

Since the dominant far-field period and wavelength can now be estimated, it is possible to classify the far-field waves shown in Figure 5.32. For the typical time scale $t_o\approx 0.35$ s and submergence $d\approx 75$ mm encountered in this work, a dominant wavelength $\lambda\approx 600$ mm can be expected from equation (5.25). Figure 5.32 shows typical wave heights of around $H\approx 7$ mm in a constant depth channel $h\approx 373$ mm. The nondimensional ratios $H/\lambda\approx 0.012$ and $h/\lambda\approx 0.62$ describe waves that can be classified as linear, deep water waves according to Dean and Dalrymple (1991). Therefore, in hindsight, the far-field wave gauge should have been positioned based on characteristic wavelengths propagated by the wave train rather than channel depths propagated by the wave train. If the near-field waves are not deep water waves at the time of generation, then they would experience wave shoaling as they propagate over the incline into deeper water. At some particular depth, the waves would no longer feel the incline and disperse according to their wavelengths as given by the deep water dispersion relation. The next paragraph provides a criterion for that depth.

In order to find a criterion for water waves generated by underwater landslides to propagate as deep water waves in a constant depth channel, equation (5.25) for the dominant wavelength is combined with the deep water wave criterion. It follows that the far-field waves have a product $\kappa h > \pi$ (or equivalently $h > \lambda/2$) only if

$$h > t_o \sqrt{g\, d} \tag{5.26}$$

since the wavenumber is defined as $\kappa \equiv 2\pi/\lambda$. For a typical characteristic time $t_o \approx 0.35$ s and a typical submergence $d \approx 75$ mm encountered in this work, far-field waves propagate as deep water waves whenever $h > 300$ mm. The typical channel depth used in this work was $h \approx 373$ mm. Therefore, equation (5.26) was satisfied by all but the block 2_o Trials 41 and 68 which had small characteristic times of motion. A few trials with large initial submergences came close to not satisfying equation (5.26) as seen in Table C.7. This fact explains the highly dispersive nature of the wave train, but also results from an arbitrary choice of the channel depth h employed herein. In general, far-field wave characteristics depend not only on the near-field landslide characteristics but also on the channel bathymetry (and specifically on some characteristic water depth compared to the dominant wavelength).

For some large, natural underwater landslides induced by earthquakes, long waves with little dispersion can be expected. For example, the numerical simulations of Harbitz (1992) showed that the Storegga landslides off Norway generated long waves. The criterion $\kappa h < \pi/10$ (or $h < \lambda/20$) associated with long waves gives the criterion

$$h < \frac{t_o \sqrt{g\, d}}{10} \tag{5.27}$$

for the channel depth. For large underwater landslides along mild slopes, the approximation $d \approx h$ turns equation (5.27) into the criterion

$$h < \frac{g\, t_o^2}{100} \tag{5.28}$$

in order for far-field water waves to propagate as long waves. An example of long wave generation is in order here. If one uses the dynamical coefficients $C_n \approx 0$, $C_d \approx 1.7$, and $C_m \approx 0.8$ in equation (5.24) along with $\rho_s \approx 2000$ kg/m^3 and $\theta \approx 4°$, then the time scale of

wave generation becomes $t_o \approx 2.6\ell^{1/2}$ where the numerical coefficient has units 2.6 $s/m^{1/2}$. Introducing this time scale into equation (5.28) gives the nondimensional criterion $h/\ell < 0.66$ in order to generate long waves on a 4° slope. A number of approximations have been made before arriving at the depth criterion $h/\ell < 0.66$, but it is clear that an underwater landslide several kilometers long would generate long waves in most coastal waters. The Hammack number in this example is given by $Ha_o \approx 8.2\sqrt{h/\ell}$ where the approximation $d \approx h$ has been used once again. The Hammack number will usually be greater than unity for long underwater landslides, although it is quite likely that $Ha_o < Ha_{o.min}$ and a power law approximation to the wavemaker curve is not available.

Far-field wave amplitudes can be related to near-field wave amplitudes. The reader should keep in mind that this section applies only to far-field waves that are deep water waves and that have propagated briefly along a 45° incline. The objective is to demonstrate that two characteristic wave amplitudes generated by a given solid block landslide can be related. Since most of the waves studied herein are linear dispersive waves, the characteristic near-field wave amplitude must be linearly proportional to a characteristic far-field wave amplitude. The maximum Airy wave amplitude at x/h=4.25 was chosen as the characteristic far-field wave amplitude. Figure 5.33 shows a linear curve fit through the origin between the two characteristic wave amplitudes

$$\eta_{airy}(4.25) \approx 0.30\, \eta_{max} \tag{5.29}$$

with a correlation coefficient r=0.87. Standard errors in the maximum near-field wave amplitude are evaluated in Section B.2.1 while standard errors in the maximum Airy wave amplitude are evaluated in Section B.2.4. The data for Figure 5.33 can be found in Tables C.3 and C.4. The maximum Airy wave amplitude at x/h=4.25 is typically 30% of the maximum near-field wave amplitude. Given the larger standard errors in the far-field wave records as well as the reduced wave amplitudes, the scatter in Figure 5.33 is unavoidable.

As discussed above, the leading positive wave far from the generation region behaves as an Airy wave, travels at the long wave celerity, and decays algebraically with distance with a -1/3 power. Therefore, the maximum Airy wave amplitude is given for the constant depth channel used in these experiments by

$$\eta_{airy}(x/h) \approx 0.48\,\eta_{max}\left(\frac{h}{x}\right)^{1/3} \tag{5.30}$$

in the far-field delineated by x/h>2.5. Given that the maximum near-field wave amplitude can be predicted from landslide geometry and motion, it follows that the maximum Airy wave amplitude can also be predicted anywhere in the far-field provided the incline angle is 45°. While the Airy wave travels at the long wave celerity $\sqrt{gh}$ away from the wave generating region, the hypothetical origin of the Airy wave is not located at x=0 when t=0. In fact, a hypothetical origin $x=x_o<0$ results from the incline being shallower than the constant depth channel and leads to the wave train arriving later than expected. The simplistic approach that x=0 when t=0 does no harm. However, a typical correction for the hypothetical origin would be $x_o/h\approx-2$ based on the block 2 far-field wave records in Appendix A. Hence, a single near-field wave amplitude η_{max} suffices to predict far-field damage potential while the channel depth suffices to predict time of wave arrival. Since the maximum near-field wave amplitude can be predicted, then so can the maximum Airy wave amplitude for all distances far from the generation region along a constant depth channel.

5.2.3 Solid Block Wavemaker Plot

A wavemaker plot is more than a tool to predict wave amplitudes for arbitrary landslide motion. As the Hammack number approaches $Ha_{o.min}$ from large values, wave generation increasingly follows the motion of the wavemaker. That is, waves can no longer escape the wave generation region faster than the wavemaker moves. Therefore, the shape of a wavemaker curve is directly associated with the mechanics of wave generation and propagation. Much of the experimental work presented in this section has Hammack numbers close to $Ha_{o.min}$. This results mainly from the size of the experimental system and the density of the solid blocks. One set of solid block 2 experiments and some linear theory solutions based on Section 3.3.1 permit evaluation of Hammack number exponents in equation (3.29). The linear theory results also suggest values for $Ha_{o.min}$ that vary with the initial landslide submergence. A criterion for underwater landslides to generate linear water waves is derived that can be directly associated with different wavemaker curves.

As in the "creeping" wavemaker analysis presented by Hammack (1972) and repeated in Section 3.1.3, the maximum near-field wave amplitude is presented as a function of the

Hammack number Ha_o and the nondimensional submergence d/b for a fixed incline angle θ=45°. The characteristic distance and time scales were calculated from equations (3.75) or $s_o=u_t^2/a_o$ and $t_o=u_t/a_o$. Experimental values for the initial acceleration were either obtained from an accelerometer during the experiment (for Trials 55-80) or from the mean acceleration data given in Section 5.1.2 above (for all previous solid block trials). Experimental values from Table 5.3 were used for the terminal velocity. The maximum near-field wave amplitude was extracted from the wave record as described in Section B.2.1. The initial submergence d of each solid block was measured just prior to performing the trial. Standard errors appearing on solid block wavemaker plots are estimated in Section B.2.5. All experimental data used to construct solid block wavemaker plots can be found in Tables C.1 and C.3.

Figure 5.34 shows the wavemaker plot of all solid block trials with initial submergences between d/b=0.85-0.87 on an incline with θ=45°. Wavemaker data were generated by varying the density of block 2 which in turn changes s_o and t_o. The Coulombic friction coefficient should be the same for all trials shown on Figure 5.34. Hence, the two nondimensional quantities γ and ψ given in equation (3.6) are interchangeable with s_o and t_o since the number of independent variables is conserved. The substitution is always justified for solid block landslides by equations (3.1), (3.4), and (3.5). Figure 5.34 is considered to represent the typical degree of data collapse that can be expected from these wavemaker experiments. Nevertheless, small errors in the characteristics of motion simply displace the experimental wavemaker data by a small amount. Hammack (1972) appears to get better data collapse in part because data are presented with log-log axes over almost three decades of Hammack numbers and in part because the wavemaker motion was hydraulically controlled. Curve fits of the data can yield useful analytical approximations of the wavemaker curve. A power law least-squares curve fit of the data in Figure 5.34 yields

$$\frac{\eta_{max}}{s_o} = \frac{0.33}{Ha_o^{2.01}} \tag{5.31}$$

with a correlation coefficient r=0.87 over the range $3<Ha_o<4.5$. Equation (5.31) applies only to an incline θ=45° from horizontal and initial submergences between d/b=0.85-0.87. The term $\sin\theta$ given in equations (3.21) and (3.27) has been dropped since all experiments reported herein were performed with an incline angle of 45°. This curve fit

gives no information regarding the minimum Hammack number $Ha_{o.min}$ for which equation (3.29) can be expected to be valid.

Figure 5.35 shows the resulting wavemaker plot for the maximum near-field wave amplitude of all solid block trials reported in Appendix C. The data are seen to be ordered by the nondimensional submergence of the solid block with larger submergences located farther to the right. In order to clarify that Figure 5.35 contains a family of wavemaker curves, the approximate linear wavemaker theory from Section 3.3.1 was used to evaluate nondimensional maximum near-field wave amplitudes. The experimental block size b, initial submergence d, initial acceleration a_o, and terminal velocity u_t from Tables C.1 and C.2 were assumed to be exact and input into equation (3.97) to calculate theoretical wavemaker data based on experimental inputs. The Hammack numbers are unaltered but the nondimensional maximum near-field wave amplitudes differ. The results of the approximate linear theory calculations are summarized in Table C.4. The standard errors in the nondimensional maximum near-field wave amplitudes incurred by using approximate experimental data are evaluated in Section B.2.6. Figure 5.36 shows the theoretical wavemaker data calculated from the approximate linear theory developed in Section 3.3.1. The ordering of the theoretical results with nondimensional initial submergence d/b is clearly seen in Figure 5.36.

The approximate linear theory results should be able to provide a criterion for the generation of linear water waves by underwater landslides. Given that the theoretical equation (3.97) can give rise to wavemaker data that appear similar to experimental results, one should ask under what conditions the theoretical maximum near-field wave amplitudes becomes proportional to the experimental results. Figure 5.37 shows that the linear theory nondimensional wave amplitudes can be used to predict experimental nondimensional wave amplitudes provided the nondimensional initial submergence $d/b>0.8$. The horizontal error bars in Figure 5.37 arise from uncertainty in the experimental solid block motion as described in Section B.2.6. A linear curve fit through the origin of the data with initial submergence $0.8<d/b<0.87$ provides

$$\text{Experimental } \frac{\eta_{max}}{s_o} \approx 0.273 \text{ Theoretical } \frac{\eta_{max}}{s_o} \tag{5.32}$$

with a correlation coefficient r=0.83. All experimental results with $d/b>0.8$ appear to fall along the curve fit whereas all experimental results with $d/b<0.75$ are situated above the

curve fit. The approximate linear theory underpredicts wave amplitudes when d/b<0.75, which can be interpreted as a nonlinear effect. Equation (5.32) should be independent of the incline angle provided the leading long wave does not have time to reflect off the incline and propagate back to x=0 prior to the occurrence of the maximum near-field wave amplitude. Equation (3.88) provides the minimum time for reflected long waves to return to the origin for an incline 45° from horizontal. A more general criterion for the generation of linear water waves by underwater landslides is now sought.

Equation (5.32) provides a useful tool for predicting linear water wave amplitudes above an underwater landslide. However, the criterion for linear water waves to be generated by underwater landslides

$$\frac{d}{b} > 0.8 \tag{5.33}$$

is insufficient as provided. Landslide kinematics must somehow determine the linearity of water waves and so one must reconsider the role of the Submergence number Sg in wave generation. In order for equations (3.16) and (3.17) to be linear, the criterion $Sg/Ha_o \ll 1$ in equation (3.23) or equivalently the criterion

$$\frac{d}{b} \gg \frac{u_t \sin\theta}{\sqrt{g\,d}} \tag{5.34}$$

must be met, where equations (3.20) and (3.75) have been employed. Equations (5.33) and (5.34) may in fact be the same linearity criteria given typical values of the terminal velocities $u_t \approx 0.5$ m/s and initial submergences $d \approx 75$ mm studied herein. With these typical values and an incline angle $\theta=45°$, one finds the linearity criterion $d/b \gg 0.4$. In fact, the only trials that did not satisfy equation (5.34) were the block 1_n trials and block 2_n Trials 52, 56, and 57 with d<50 mm. These are the same trials that showed considerable scatter in the far-field wave characteristics in Section 5.2.2 above. For linear water waves, it follows from equation (3.24) that any characteristic wave amplitude in the wave basin can be linearly correlated with any other characteristic wave amplitude as shown in Figure 5.33. One simply evaluates the wave height H once and for all based on one chosen characteristic wave amplitude at some given x and t. This is the basis behind equations (5.29) and (5.30) that relate the maximum near-field wave amplitude to the maximum Airy wave amplitude. In addition, linearity guarantees that one can make

an equivalent wavemaker plot with any chosen characteristic wave amplitude. This fact has not been exploited in this work.

Equation (5.34) is readily evaluated for a variety of practical underwater landslide scenarios. The implications for long underwater landslides on shallow inclines are particularly interesting. In particular, the left hand side of equation (5.34) is proportional to ℓ^{-1} since $b \equiv \ell\cos\theta$ while the right hand side is proportional to $\ell^{1/2}$ from equation (4.8). If $C_n \approx 0$, then the right hand side of equation (5.34) is also proportional to $\sin^{3/2}\theta$. Hence, for a given initial submergence, linearity in water waves generated by long underwater landslides would arise from a tenuous balance between landslide length and incline angle from horizontal. For example, an underwater landslide initially submerged $d \approx 100$ m on a 4° incline that has a terminal velocity of $u_t \approx 30$ m/s must be less than $b \approx 1500$ m in length in order to satisfy a basic inequality in equation (5.34). It is simply not possible to make a blanket statement such as "long underwater landslides generate nonlinear water waves." Nor can the converse be asserted. Each case must be examined individually.

Now that a reliable linearity criterion has been established and most solid block experiments have been shown to produce linear water waves that are proportional to equation (3.97), linear theory calculations can be used with confidence to construct wavemaker curves and provide values of $Ha_{o.min}$. Theoretical wavemaker curves are calculated by first choosing a nondimensional initial block submergence along the 45° incline. Choosing the initial landslide geometry fixes the wavemaker curve for a given Coulombic friction coefficient. A solid block number (or density) is then chosen. The initial acceleration of the solid block landslide is then calculated from one of equations (5.1) to (5.3). Initial accelerations can also be calculated from equations (3.73) and (5.6) with Coulombic friction data from Table 5.1. Terminal velocities for solid blocks studied in this work can be taken from Table 5.3. Equation (5.34) can be verified before evaluating equation (3.97). Varying the solid block density (or mass) and calculating the Hammack number and the nondimensional maximum near-field wave amplitude then produces a few loci for the approximate theoretical wavemaker curve. As the solid block density increases, Hammack numbers decrease and an inflection point in the wavemaker curve appears. The value of the Hammack number at the inflection point is designated $Ha_{o.min}$. To the right of the inflection point, a power law least-squares curve fit of the nondimensional wavemaker data yields values for k and n in equation (3.29). Multiplying the numerical value found for k by 0.273 then provides a prediction of the

actual solid block wavemaker curve. The wavemaker curve to the left of $Ha_{o.min}$ may still involve linear water waves but cannot be described analytically by equation (3.29).

Four wavemaker curves are now calculated from equation (3.97) and compared with experimental solid block results with d/b≥0.8 on an incline at 45°. A power law curve fit of block 2 wavemaker predictions with nondimensional submergence d/b=0.87 provided

$$\frac{\eta_{max}}{s_o} \approx \frac{0.210}{Ha_o^{1.625}} \tag{5.35}$$

over the range $3.3<Ha_o<4.5$ with $Ha_{o.min}\approx 3.3$. Despite the different exponents in equations (5.31) and (5.35), the two curves cross near $Ha_o\approx 3.3$ and differ by at most 14% (at $Ha_o=4.5$) over the entire range $3.3<Ha_o<4.5$. A power law curve fit of block 2 wavemaker predictions with nondimensional submergence d/b=1.0 gave

$$\frac{\eta_{max}}{s_o} \approx \frac{0.275}{Ha_o^{1.743}} \tag{5.36}$$

over the range $3.6<Ha_o<7.6$ with $Ha_{o.min}\approx 3.6$. A power law curve fit of block 2 wavemaker predictions with nondimensional submergence d/b=1.5 yielded

$$\frac{\eta_{max}}{s_o} \approx \frac{0.297}{Ha_o^{1.628}} \tag{5.37}$$

over the range $4.2<Ha_o<8.5$ with $Ha_{o.min}\approx 4.2$. A power law curve fit of block 2 wavemaker predictions with nondimensional submergence d/b=2.0 provided

$$\frac{\eta_{max}}{s_o} \approx \frac{0.311}{Ha_o^{1.562}} \tag{5.38}$$

over the range $4.6<Ha_o<9.3$ with $Ha_{o.min}\approx 4.6$. Figure 5.38 compares the approximate linear theory wavemaker curves with experimental solid block wavemaker data. Half of the experimental data are seen to lie to the left of the corresponding values of $Ha_{o.min}$. Nevertheless, agreement is within one standard deviation for most of the experimental data that fall within the range of the curve fits. In general, equation (3.29) need not be used to describe the wavemaker curve. Hence, the approximate linear theory can be used to predict wavemaker curves for underwater landslides that generate linear water waves.

Wiegel (1955) found experimentally that underwater landslides on smaller incline angles had smaller wave amplitudes if all other parameters were held constant. Equation (3.27) suggests an approximate way of collapsing nondimensional wave amplitudes for different incline angles. The characteristic near-field wave amplitude is proportional to the sine of the incline angle since only the vertical block motion is considered for near-field wave generation. However, this simple approach to collapsing characteristic wave amplitudes obtained from different incline angles would almost surely fail since it is nearly impossible to have the same characteristics of motion for different incline angles. Consider instead landslide motion with $C_n \approx 0$ as well as nearly constant C_d and C_m over a range of incline angles including 45°. Water waves generated by an underwater landslide at an incline angle other than 45° are compared with water waves generated by an underwater landslide at $\theta=45°$. Similar near-field geometries are created by keeping the nondimensional initial submergences d/b of the two solid block landslides constant while allowing the incline angle to vary. The characteristics of solid block motion s_o and t_o are assumed to be known for the given incline angle other than 45°. Equations (3.73) to (3.75) show that the characteristic distance

$$s_o \sin\theta = \frac{m_b + C_m m_o}{C_d \rho_o w b} \tag{5.39}$$

is invariant with incline angle for a given solid block mass m_b and a given length of the top face b of the block. The solid block density must therefore decrease as the incline angle is increased in order to keep m_b and b constant. Equation (5.24) shows that the characteristic time of solid block motion t_o is proportional to $1/\sin\theta$ given that $C_n \approx 0$ and $b \equiv \ell\cos\theta$. It follows immediately that the Hammack number Ha_o at an angle other than 45° should be multiplied by $\sqrt{2}\sin\theta$ in order to find the corresponding Hammack number at 45°. If $\sqrt{2}\sin\theta\ Ha_o$ is greater than the inflection point in the wavemaker curve, then the wavemaker curve at $\theta=45°$ with the correct nondimensional submergence d/b yields an approximate nondimensional wave amplitude for wave generation at the given incline angle. If $\sqrt{2}\sin\theta\ Ha_o$ is less than the inflection point in the wavemaker curve, then the wavemaker curve at 45° represents a different physical mechanism of wave generation altogether and cannot be used. It should be noted that this analysis is approximate not only because $C_n \approx 0$ but also because the interaction between the waves and the incline would be different for different incline angles. Incidentally, equations (5.23) and (5.39)

demonstrate that the characteristic distance s_o of landslide motion is proportional to the landslide size ℓ.

Considerable insight can be gained into the wave generation problem if one examines equation (3.29) a little more closely. By examining the cases when the exponent n=1 and n=2 in equation (3.29), two expressions for the maximum near-field wave amplitude can be derived that no longer involve the Hammack number. If the whole integer n=2 is assumed to be generally correct for solid block landslides, then the maximum near-field wave amplitude is given by

$$\eta_{max} = \frac{k\, a_o\, b^2}{g\, d} \tag{5.40}$$

and any dependence of wave generation on the terminal velocity disappears. In the case where n=1, the maximum near-field wave amplitude is given by

$$\eta_{max} = \frac{k\, u_t\, b}{\sqrt{g\, d}} \tag{5.41}$$

and any dependence of wave generation on the initial acceleration disappears. Sabatier (1983) derives a similar equation for the maximum near-field wave amplitude in the case of a two-dimensional compact landslide moving down an incline at constant velocity. The two results in equations (5.40) and (5.41) are given to show that any power $1<n<2$ between the two cases given here influences the theoretical mixture of terminal velocity and initial acceleration acting on the wavemaker process. Moreover, equations (5.40) and (5.41) show that a larger near-field wave amplitude results from larger landslides and smaller initial submergences as shown by Wiegel (1955). Similar results would be found for any value $1<n<2$. This is important since the ordering of the nondimensional wavemaker curves for a given Hammack number in Figure 5.38 yield larger nondimensional wave amplitudes for larger nondimensional initial submergences. The result in nondimensional space is therefore counterintuitive.

It is interesting that in neither the experimental nor the theoretical wavemaker results just shown was the exponent n=1 found by Hammack (1972) recovered for the wavemaker curves. This observation leads to some fascinating conclusions. While the wavemaker geometries in Hammack (1972) and this work differ significantly, the approximate linear theory results from Section 3.3.1 are able to predict the maximum near-field wave

amplitude when the experiments satisfy d/b>0.8. Therefore, the original assumption that the wave amplitudes immediately above the solid block at short times only feel the motion of the top face of the block appears justified. Hence, the differences in exponent n cannot be readily attributed to differences in geometry. This implies that the exponent in the wavemaker formalism is a function of the wavemaker kinematics and in particular of the analytical expressions for the characteristics of motion s_o and t_o. The exponent n is not a function of the precise definition of the characteristic time t_o and distance s_o of landslide motion since the choices made by Hammack (1972) are linearly proportional to the more general definitions implied by equation (3.1). The exponent in the wavemaker curve would be unaltered by any linear rescaling of the characteristic time t_o of landslide motion. However, Hammack (1972) could control s_o and t_o separately whereas the characteristics of landslide motion are coupled according to equations (3.4) and (3.5) herein. Physical quantities such as the landslide density are therefore able to alter the shape of the wavemaker curve through equations (3.73) to (3.75).

The wavemaker curve is central to water waves generated by underwater landslides. It is a powerful predictive tool for calculating the maximum near-field wave amplitude. Should the dynamics of a given underwater landslide not be known whereas the bathymetry and landslide size are known, then the loci of nondimensional maximum near-field wave amplitudes -- i.e., the wavemaker curve -- can still be found. For sufficiently large Hammack numbers, the exponent of the Hammack number in equation (3.29) can be assumed to have a value $n \approx 1.6$ that approximates the theoretical results in this section. All that is required to complete the wavemaker curve is a single simulation with some arbitrary landslide motion (provided $Ha_o > Ha_{o.min}$) that allows one to solve for the coefficient k. If the actual landslide motion can be pinned down, then so can the maximum near-field wave amplitude. The power of the method lies in coupling the wavemaker motion to the wave generation in a nondimensional curve.

5.2.4 Description of the Total Wave Potential Energy

The propagation of large water waves incurs relatively small energy losses provided wave breaking does not occur. However, the dispersive properties of a linear wave train propagating down a channel of constant depth superficially conceals the fact that energy is in fact being conserved. Closer inspection reveals that the wave train travels at the group velocity of energy propagation rather than the individual wave celerity. Hence, waves exist only where there is energy and waves can be interpreted as a physical

manifestation of the wave energy. It follows that a measure of the wave train energy is more relevant far from the generation region than any single measure of wave amplitude. This section examines how the far-field wave energy is related to the near-field wave generation process.

The simplest measure of wave energetics available from wave gauge records is the total wave potential energy passing through a given point in the constant depth channel. The total wave potential energy passing through the wave gauge location x/h is proportional to the energy integral

$$E_p(x/h) \equiv \int_0^\infty \eta^2(t,x/h)\, dt \qquad (5.42)$$

where the temporal extent of the wave train changes with nondimensional distance x/h and the free surface eventually comes to rest at some large value of time. Error estimates for the energy integral are described in Section B.2.3.

Figure 5.39 shows the variation of the energy integral E_p with wave gauge position for a solid block trial repeated 3 times with three wave gauge records per trial. The first and last wave gauge positions were each measured twice in order to verify that the second and third trials produced similar wave amplitudes. The two results farthest to the left are above the middle of the initial solid block position and have energy integral values around $E_p(0)\approx 0.19$ cm^2·s. In the vicinity of $x/h\approx 0.5$, a peak in the energy integral occurs that is nearly twice as high as the value recorded above the solid block. Hence, at a near-field position $x/b\approx 1$, almost all of the wave energy appears to be invested in potential energy. Half of the potential energy is steadily transferred to kinetic energy over the next two depths of wave propagation and dispersion. Once equipartition of energy (or wave equilibrium) is achieved, the wave potential energy is seen to remain constant with distance from the wave generation region at about $E_p(\infty)\approx 0.15$ cm^2·s. The kinetic energy of a linear wave train need not be measured far from the generation region because of the equipartition of wave energy between kinetic and potential energies. The first location of equipartition of wave energy actually serves as a reasonable indicator of where the far-field wave propagation region begins -- e.g., in this case about $x\approx 2.5h$. Therefore, wave gauges located a distance $x/h\approx 4.25$ from a landslide are demonstrably in the far-field. It is desirable to convert the far-field criterion $x/h>2.5$ into a form applicable to deep water wave propagation in the far-field. Given a characteristic wavelength $\lambda\approx 300$ mm

calculated in Section 5.2.2 and a typical channel depth h=373 mm, the far-field criterion for deep water waves becomes $x/\lambda>3.0$.

From dimensional and physical considerations, it seems logical to expect the far-field wave potential energy at x/h=4.25 to be related to the near-field wave potential energy at x/h=0. In practice, the far-field energy integral was summed for 5.5-6 s or until waves reflected off of the far end of the wave tank reached the wave gauge. The energy integrals $E_p(0)$ and $E_p(4.25)$ calculated for solid block landslides are given in Tables C.5 and C.6. Figure 5.40 shows that a unique relation between the two energy integrals exists since the ratio $E_p(0)/E_p(4.25)$ is a nearly constant function of the nondimensional initial submergence. A power law curve fit yields

$$\frac{E_p(4.25)}{E_p(0)} \approx 0.702 \left(\frac{d}{b}\right)^{-0.19} \tag{5.43}$$

over the range $0.3<d/b<2.2$ with a correlation coefficient r=0.19. Considerable scatter exists in the energy integral ratio, however a clear trend is established. In order for equation (5.43) to be unique, deep water waves must exist in the far-field. These results do not indicate how the near-field and far-field energy integrals would be related if the depth of the constant depth channel no longer gave rise to deep water waves. Moreover, equation (5.43) can be expected to be a function of the incline angle as well as any intervening bathymetry that might alter wave propagation. There is also no obvious way to isolate how much wave energy is trapped within the near-field and how much energy is dissipated on the inclined beach. Both of these effects would clearly be a function of the incline angle θ.

Figure 5.31 shows that the near-field energy integral is a function of the characteristic landslide quantities η_{max} and t_o and initial landslide geometry. Figure 5.40 shows that the near-field energy integral is directly related to the far-field energy integral through initial landslide geometry. Hence, wave energetics are in general a function of the characteristic landslide quantities η_{max} and t_o and initial landslide geometry. Given that the maximum near-field wave amplitude η_{max} can be predicted for a given t_o and initial landslide geometry, the wave energetics are ultimately reduced to landslide geometry and motion. There must therefore exist an energetics curve for some characteristic measure of wave energetics that parallels the wavemaker curve.

5.2.5 Solid Block Energy Conversion

Previous authors have considered the conversion of solid block potential energy into wave energy for free falling blocks. This idea only works when there is a clear starting point and end point in the landslide center of mass motion or else the landslide could have a theoretically infinite potential energy. For example, Wiegel (1955) found typical energy conversions of 1-2% using this method for solid blocks sliding along an incline. These energy conversion values were subsequently used by Striem and Miloh (1976) as well as Murty (1979) to estimate characteristic tsunami heights. Using a similar definition of efficiency, Sabatier (1983) derives theoretical energy conversion maxima of around 5% provided the underwater landslide length is shorter than the water depth and landslide velocity is smaller than the long wave celerity. However, given that solid blocks sliding down an incline dissipate energy due to Coulombic friction and deposit energy into the fluid medium through viscous dissipation, the kinetic energy acquired by the solid block at terminal velocity is used herein instead of the potential energy. In a non-dissipative system, the two energies are naturally interchangeable. Both kinetic and potential energy approaches were used by Striem and Miloh (1976) in order to estimate characteristic wave heights. Both methods yielded similar wave height estimates. However, Striem and Miloh (1976) assumed that a single solitary wave was formed by an underwater landslide.

Section 5.2.2 showed that the far-field dispersive wave trains measured in this work propagate as deep water waves while Section 5.2.3 showed that most of the observed far-field waves can be considered as linear waves. Therefore, a linear water wave energy per unit width is used here to estimate kinetic energy conversion into wave energy. General properties of linear wave trains can be found in Dean and Dalrymple (1991). For an infinite wave train of sinusoidal waves, the energy per wavelength per unit width is

$$E \equiv \frac{\rho_o g \eta_{max}^2 \lambda}{2} \tag{5.44}$$

where η_{max} is the characteristic wave amplitude and λ is the wavelength. There is no conflict in using the maximum near-field wave amplitude for a far-field measure of energy conversion because Section 5.2.4 shows that far-field wave train energy is directly related to the maximum near-field wave amplitude. For the wave generation process studied herein, the characteristic wavelength (or horizontal length scale) is $\lambda \approx t_o \sqrt{gd}$. This

is the same horizontal length scale used in the scaling analysis of Section 3.1.3 and the same wavelength used in Section 5.2.2 above. Assuming that the water waves generated by underwater landslides are linear, the characteristic energy conversion from solid block kinetic energy to water wave energy per unit width is

$$e \equiv \frac{\rho_o g t_o \eta_{max}^2 \sqrt{g d}}{\rho_b u_t^2 A} = \frac{2 m_o g \eta_{max}^2 \sqrt{g d}}{m_b a_o u_t b^2} \tag{5.45}$$

where $A=b^2/2$ is the cross-sectional area of the solid block and $t_o=u_t/a_o$. The energy conversion is a nondimensional quantity that can be viewed as a characteristic efficiency of the wave generation process. The energy density of linear water waves is independent of the water depth and the specific wavelength of the water waves. Therefore, the energy conversion should not depend explicitly on the channel depth h or the incline angle θ.

Figure 5.41 shows that a single function can predict the energy conversion of a solid block landslide as a function of the nondimensional initial submergence. The energy conversion was calculated from equation (5.45). The masses m_b and m_o were obtained from Table 4.1 while all other data needed to calculate energy conversion were obtained in the same manner as in Section 5.2.3. The resulting values of the energy conversion are listed in Table C.7. Error bars in Figure 5.41 represent one standard deviation and were calculated in Section B.2.7. Most solid block experiments converted between 2-8% of the maximum solid block kinetic energy into a characteristic near-field wave energy. The per cent energy conversion naturally increased as the initial submergence of the solid block decreased. The power least-squares curve fit of the characteristic energy conversion

$$e\ 100\% \approx 3.82 \left(\frac{d}{b}\right)^{-0.62} \tag{5.46}$$

has a correlation coefficient r=0.69. Equation (5.46) is valid over the range $0.5<d/b<2$ for an incline at $\theta=45°$. Equation (5.46) can be used to predict the maximum near-field wave amplitude if landslide geometry and kinematics are known. In fact, solving for η_{max} yields the square root of the product $a_o u_t$ in the numerator which suggests a power law of n=1.5 in the wavemaker curve of equation (3.29). A similar power was suggested by the theoretical results curve fit by equation (5.35).

5.2.6 Example of an Application

A simple example demonstrates the utility of the results presented so far in this work. This example shows how practical engineering estimates can be extracted from the more fundamental aspects of this research. The example may seem somewhat simplistic and contrived since it has been chosen to match the experimental work, however, there are some important lessons to be drawn. For example, the solid block wavemaker on a 45° incline can serve as a practical upper bound for water waves generated by a natural underwater landslide along a steep bank.

Consider a long row of rectangular concrete blocks submerged along a 30° slope of loosely consolidated sediment such that half of each block is buried. For the purpose of this approximate calculation, the bank is assumed to have a slope of 45°. The blocks stretch along the edge of a straight shoreline and moor vessels that traverse a relatively narrow lake lengthwise. The blocks extend b=1.5 m along upper surfaces that are parallel to the lake surface and are submerged by d=1.3 m. The lengths are designed to match most of the block 2 experiments. For the purpose of clarity, this end of the lake can be considered a popular destination for tourists who paddle a 400 m distance in canoes from a town at the other end of the lake. The lake has a nearly constant depth of h=6.5 m from the toe of the steep bank to the town where there exists a vertical retaining wall along which a promenade and stores are situated. The lake depth also corresponds to the geometry of the block 2 experiments. The promenade is elevated one meter above the mean water level of the lake. The town council is concerned that a local earthquake may induce waves in the lake that might endanger people or property. Do water waves generated by soil failure around the concrete blocks pose a credible hazard to the town? And how long after an earthquake would water waves arrive?

Soil stability analyses indicate that the soil would fail during a modest earthquake and that the concrete blocks would have an initial acceleration of about $a_o \approx 2$ m/s^2 based on the failed soil shear strength along the failure plane. An estimate of the theoretical terminal velocity of the concrete blocks sliding (or tumbling) down the bank is $u_t \approx 4$ m/s assuming that $\rho_b/\rho_o \approx 5$. Using the standard landslide motion theory, it follows that the characteristic time of motion is $t_o \approx 2$ s and the characteristic distance of motion is $s_o \approx 8$ m. The initial submergence of the generation region is $d/b \approx 0.87$ and the Hammack number is $Ha_o \approx 4.8$. The solid block wavemaker curve equation (5.31) from Section 5.2.3 provides

$\eta_{max} \approx 0.015 s_o = 12$ cm. Solving for the energy conversion from equation (5.46) yields $e \approx 0.042$ along with another maximum near-field wave amplitude estimate of $\eta_{max} \approx 23$ cm from equation (5.45). Neglecting the effective displacement of the wave origin x_o, the wave travels a distance of approximately x/h=62. Therefore, the Airy wave arriving at the retaining wall has an amplitude $0.12\eta_{max}$ or $\eta_{airy} \approx 1.4$ cm and arrives 50 s after the earthquake. Given that the process of wave run-up would approximately double the wave amplitude at the retaining wall, the water height should reach 3-6 cm above normal water level. The wave amplitude is small enough to be negligible for the postulated mechanism of wave generation. The town would not be endangered by these water waves.

5.3 Material Landslide Results

The material landslides studied herein deform rapidly enough to alter the waves that are generated. This section demonstrates the extent that landslide rates of deformation can alter the nondimensional wave amplitudes observed for solid block landslides. In order to relate material landslide results to solid block landslide results, material landslide motion is decomposed into the center of mass motion s(t) and a rate of deformation $\Gamma(t)$. The material landslide center of mass motion is described by the same analytical solution used to describe solid block motion. The initial rate of landslide deformation is taken as the characteristic rate of deformation and considered to have the strongest ability to alter wave generation. For a given landslide center of mass motion, a large initial rate of deformation implies a rapid flattening of the material landslide. Since a perfectly flat and thin underwater landslide cannot generate significant water waves, landslide deformation would likely lead to smaller water waves for a given center of mass motion. Note that an increase in landslide cross-sectional area must be accompanied by an influx of water so that a material landslide is also acting like a submerged sink. Overall, volume is still conserved within the wave tank.

5.3.1 Material Landslide Wave Records

Wave records from Trials 87, 35, 34, and 37 involving glass spheres of nearly identical initial landslide geometry, initial solid volume fraction, material density, and incline friction angle yet significantly different nominal diameters (0.50, 1.26, 2.96, and 12.2 mm, respectively) are shown in Figures 5.42 and 5.43. Error analyses for near-field and far-field wave records are located in Sections B.2.1 and B.2.4, respectively. Figure 5.42 compares near-field wave records measured at x=0. Near-field wave characteristics of

material landslides closely resemble those of solid block landslides shown in Figure 5.28. Figure 5.43 shows the far-field wave records corresponding to Figure 5.42. Far-field wave characteristics of material landslides also resemble those of solid block landslides shown in Figure 5.32. The results presented in Section 5.2.2 regarding solid block landslides suffice to describe the features of far-field water waves generated by material landslides. As mentioned in Section 3.3.2, Mei (1983) shows that water waves generated by a tilting body decay more rapidly with propagation distance down a constant depth channel than the far-field Airy waves. This implies that the dominant far-field wave amplitude and wave period depend primarily on the center of mass motion. Far-field wave records for water waves generated by deforming material landslides are given in Appendix A and do not show any qualitative difference with far-field water waves generated by solid block landslides.

If the four trials shown in Figures 5.42 and 5.43 had been solid block landslides, then the water wave amplitudes would have been nearly identical because the glass particles all have similar material densities and solid volume packing fractions. However, larger glass spheres are seen to produce larger wave amplitudes in both Figure 5.42 and Figure 5.43. Therefore, water waves generated by material landslides can be highly sensitive to material properties such as nominal diameter, at least at laboratory scale where $D/b \approx 100$. One is tempted to attribute the wave amplitude differences in Figures 5.42 and 5.43 solely to differences in the landslide rates of deformation that depend on material particle size. However, Tables 5.4 through 5.6 as well as Figures 5.15 and 5.17 reveal that in fact the center of mass motions and the initial rates of deformation differ significantly for all four materials. The apparently simple correlation between wave amplitude and particle nominal diameter is actually concealing more complicated coupled nonlinearities that one may assume govern material landslide shape, motion, and wave generation. For example, hydraulic diffusivity, pore water pressure and suspension viscosity all depend on particle nominal diameter. The correct analysis of wave amplitudes must therefore be made in the five-dimensional space of nondimensional wavemaker parameters: the dependent quantity $\eta_{max}/s_o \sin\theta$, and the four independent quantities θ, d/b, Ha_o, and Γt_o.

A deforming material landslide acts as a flow sink for surrounding water through a variety of mechanisms including shear thinning of granular material at the landslide base and shear induced mixing with the surrounding water. Tyvand (1992) has considered the water wave generated by a submerged line source initiated at time t=0. Shortly after turning on the sink, the free surface is approximated by

$$\eta(t,x) \approx -\frac{d\, Q_o\, t}{\pi\,(x^2 + d^2)} \tag{5.47}$$

where d is the submergence of the sink and Q_o is the volumetric sink rate per unit width. Given a typical sink rate of $Q_o=dA/dt\approx 0.01$ m^2/s from Tables C.11 and C.12 as well as a submergence of $d\approx 80$ mm, the free surface displacement at $x=0$ for a time $t=t_o\approx 0.3$ s is approximately $\eta(t_o,0)\approx 80$ μm. Clearly, the action of the granular landslide as a sink of water does not affect the free surface considerably. This result justifies neglecting the initial rate of area change in time as a source of wave generation as discussed in Section 5.1.6. The initial rate of deformation Γ has a much more pronounced effect on the pressure distribution about material landslides and hence on water wave generation.

5.3.2 Material Wavemaker Plot

The role of landslide deformation was assumed *a priori* to be a separable modifier of the maximum near-field wave amplitude. However, Section 5.1.6 showed that the initial landslide rate of deformation is comparable in duration to the characteristic time of the center of mass motion since $|\Gamma t_o|$ is of order unity. The time scale associated with landslide deformation $1/\Gamma$ is typically 0.6 s in Table 5.5 or about twice a typical time scale of center of mass motion t_o in Table 5.4. Therefore, landslide deformation was slower than the center of mass motion for all materials studied. The nondimensional landslide deformation Γt_o is based on a comparison of time scales of landslide motion. However, the initial rate of deformation could have also been made nondimensional by the characteristic time scale of wave propagation out of the generation region. In this case, there results the nondimensional group

$$\frac{\Gamma\, b}{\sqrt{g\, d}} \ll 1 \tag{5.48}$$

where the largest value is 0.25 for the 3 mm lead shot Trial 38 and a typical value of equation (5.48) is 0.15 for most material landslides reported herein. The inverse of equation (5.48) is a deformation Hammack number that is even larger than Ha_o since $1/\Gamma > t_o$. Therefore, material landslide deformation is a perturbation of wave generation even though $|\Gamma t_o|$ is of order unity. Deformation of long underwater landslides has the potential to significantly affect wave generation provided there is a measurable rate of

deformation. The rate of deformation of long underwater landslides in nature is apparently still an open question.

The discussion accompanying Figures 5.42 and 5.43 demonstrates that density no longer plays a central role in determining the loci of a material landslide wavemaker curve. For example, Figures 5.15 and 5.17 showed that material landslide center of mass motion can depend on the particle nominal diameter. In other words, material landslide center of mass motion is coupled to the initial landslide rate of deformation in an apparently complicated manner. In fact, both material landslide center of mass motion and initial rate of deformation can be expressed as functions of the material quantities as shown by equation (3.8). The solution to understanding water waves generated by material landslides lies in constructing wavemaker plots that relate nondimensional wave amplitudes to nondimensional landslide motions. Material properties and identifying characteristics are entirely ignored other than their role in prescribing the material landslide center of mass motion and the initial rate of deformation. Solid block maximum near-field wave amplitudes defined a single wavemaker curve for a given initial landslide geometry. For a given initial material landslide geometry, maximum near-field wave amplitudes define regions of the $(\eta_{max}/s_o\sin\theta, Ha_o)$ plane dependent on the initial landslide rate of deformation. A unique wavemaker curve no longer exists for a given landslide initial geometry and center of mass motion.

Figure 5.44 shows a wavemaker plot for material landslides with $d/b \approx 0.9$ and $\theta = 45°$. The initial geometry of these material landslides corresponds closely to the initial geometry of the solid block landslides represented by Figure 5.34. The characteristic distance s_o and time t_o of landslide motion were obtained from Table 5.4. The nondimensional landslide deformation Γt_o was obtained from Table 5.6. The relevant error estimates for Figure 5.44 are contained in Sections B.1.6, B.1.9 and B.3. The data used to construct the wavemaker plot can be found in Tables C.8, C.13 and C.14. The nondimensional wave amplitudes are seen to fall below equation (5.31) found by curve fitting the wavemaker results in Figure 5.34. Moreover, there is a general trend for larger nondimensional landslide deformations to be associated with smaller nondimensional wave amplitudes. Figure 5.45 shows the same data as Figure 5.44 indexed by landslide material rather than nondimensional landslide deformation. Wavemaker data for repeated trials are seen to agree to within the error bars of one standard deviation. Over the range of Hammack numbers shown in Figures 5.44 and 5.45, nondimensional wave amplitudes generated by deforming material landslides vary from 0.5-0.9 times the nondimensional wave

amplitudes generated by solid block landslides with similar initial geometries and center of mass motions. It follows that a hazard mitigation study conducted in a region susceptible to underwater landslides can use solid block results to obtain a maximum possible wave amplitude while completely ignoring landslide deformation. In general, one can hypothesize that solid block landslides with $\alpha<\theta=45^\circ$ would generate smaller waves on an incline at $\theta=45^\circ$. This hypothesis was never tested in this work.

5.4 Numerical Simulations of Wave Generation

The focus of numerical simulations was the generation of water waves in the near-field above the incline. In particular, the simulation domain was designed to simulate water waves generated by underwater landslides slightly beyond the occurrence of the maximum near-field wave amplitude. Longer simulations in the same domain would have placed the landslide below the constant depth channel while a larger simulation domain would have become a prohibitively long computation. Numerical simulations provide wavemaker data for some solid block landslides not studied experimentally. The numerical simulations are shown in Section B.4 to have a typical error in the maximum near-field wave amplitude of 5.6% due to errors in the conservation of volume. Simulation results are summarized in Tables C.15, C.16 and C.17.

5.4.1 Application of the BEM Code

It is desirable to run numerical simulations with entirely nondimensional quantities. For nondimensional simulations, the number of independent inputs is lowered, the simulations are readily scaled to any reasonable size, and the computer manipulates quantities that are almost all of O(1) away from singular regions of the computational domain. The correct length scale with which to nondimensionalize near-field lengths is the solid block size b. According to the requisite Froude scaling, the characteristic time scale is given by $\sqrt{b/g}$. Therefore, equation (4.8) for the landslide terminal velocity becomes nondimensional without introducing any new nondimensional quantities. It follows that all dimensional accelerations are divided by the gravitational acceleration g. A characteristic mass scale is established by dividing all densities with the density of water ρ_o. The net result is that simulations are conducted with the same dimensional equations as given in Sections 3.2 and 3.4 but with b=1, g=1, ρ_o=1, and $\rho_b=\gamma$.

As mentioned in Section 3.4.3, a separate computer program was written that would convert user chosen inputs into a simulation domain and landslide center of mass motion. The solid block density ρ_b and the nondimensional initial submergence d/b had to be chosen by the user. The dynamical coefficients also needed to be specified in order to calculate center of mass motion. The Coulombic friction coefficient C_n had to be input by the user. The values for the drag coefficient $C_d \approx 1.7$ and the added mass coefficient $C_m=0.8$ were fixed in the simulations. The shape of the simulation domain is discussed in Section 3.4.3 and is identical to the wave tank depicted in Figure 4.1. The node density along the free surface was set at 40 nodes per characteristic wavelength. There were 5+4h nodes along the vertical right side of the numerical wave tank. Along the horizontal bottom, the node density was 5 nodes per characteristic wavelength plus an additional five nodes. The node density along the incline was set at 30 nodes per characteristic wavelength. The front and top face of the solid block both consisted of 21 nodes, which typically represented a node density twice that of the free surface.

The first 10 time steps of a single simulation were repeatedly run with different values for the Courant number and the solid block corner size in order to characterize rates of volumetric change. The results for the different Courant numbers are discussed first. Over a range $0.2<Co<0.6$, the volumetric rate of change was found to be proportional to

$$\frac{dV}{dt} \propto Co^{1.82} \tag{5.49}$$

so that a smaller time step leads to significantly increased simulation accuracy. A Courant number Co=0.2 was chosen for the simulations reported in this work. The BEM code was run on a Sun Ultra-170 at the University of Rhode Island. For a typical simulation consisting of 300 nodes total, each time step in the simulation would take roughly 20 seconds. With a Courant number Co=0.2, a typical simulation required around five hundred time steps and therefore took approximately three hours to complete. Smaller Courant numbers would have made the simulations considerably more time consuming. An actual experiment lasted at most two seconds.

The three corners of a solid block landslide were described by an approximate geometry and treated with approximate boundary conditions. Two new points were defined a distance ε on either side of each solid block corner. A new corner point with a less acute angle was joined to these two new points. The location of the new corner was calculated

as half of the old corner position and a quarter of both new points located a distance ε from the corner. The two line segments joining each new point consisted of seven nodes. The boundary condition along a line segment was expressed as three quarters of the adjacent solid block boundary condition and one quarter of the boundary condition from the opposite face. The volumetric rate of change was found to be proportional to

$$\frac{dV}{dt} \propto \varepsilon^{-1} \tag{5.50}$$

over the range $10^{-4}<\varepsilon<10^{-2}$. The inverse power in equation (5.50) indicates that the singularity at the block vertex is responsible for most of the volumetric change in the simulation domain. To verify this conjecture, the accumulated volume change from an entire simulation was plotted as a function of time. The plot appeared to be a graph of solid block position *versus* time. Therefore, the rate of volume change was proportional to the solid block velocity. In order to minimize the simulation error, the nondimensional corner size was chosen to be $5x10^{-3}$ for all simulations reported in this work.

5.4.2 Results from the BEM Code

Computer simulations of water waves generated by underwater landslides offer detailed profiles of the free surface that can depict wave generation. Figure 5.46 shows three free surface profiles from early times during Run 1, a nondimensional computer simulation of Trial 67. The characteristic time of motion for the simulation is $t_o\sqrt{g/b}$ =3.83 and can be found in Table C.15. The three free surface profiles therefore occur at about $0.1t_o$, $0.2t_o$ and $0.3t_o$, respectively. The left hand side of Figure 5.46 corresponds to the initial intersection of the free surface with the incline at position x/b=-d/b-1/2=-1.37 since d/b=0.87 and the nondimensional length of the top face of the solid block is unity. The right hand side of Figure 5.46 is approximately at the toe of the incline which occurs at x/b=3.12 in this simulation. The top face of the solid block initially extends from x/b=±0.5. In the simulation, the free surface trough is centered over the rear half of the solid block at early times. Run-down along the incline is evident on the far left of Figure 5.46 although the different axis scales make the run-down appear vertical. The run-down corresponds qualitatively to the sea level drawdown described by Striem and Miloh (1976). The positive wave generated in front of the solid block has a maximum wave amplitude initially one landslide length ahead of the front face of the block at about

x/b≈1.5. For these nondimensional computer simulations, the characteristic wavelength is given by

$$\frac{\lambda}{b} = \frac{t_o \sqrt{g\,d}}{b} = 3.57 = Ha_o \tag{5.51}$$

which provides a new interpretation of the Hammack number as a nondimensional wavelength. Regardless, the characteristic wavelength appears to be a reasonable predictor of the wavelength evident in Figure 5.46. The idea that the initial water flow about an underwater landslide acts like a flow doublet located near the landslide vertex has been mentioned before in Sections 1.1 and 5.2.1. The free surface profiles in Figure 5.46 depict the expected result if water were injected by the front face of an immobile solid block and withdrawn from the top face at an equal flow rate. The initial horizontal location of the flow doublet appears to be slightly ahead of the block vertex at x/b=0.5 and shows very little horizontal motion at these early times. An asymmetry in the free surface is clearly evident that would not be present for water waves generated by a real flow doublet in a constant depth channel. Iwasaki (1990) considers an analytical model of a horizontal underwater landslide traveling at constant velocity in a two-dimensional channel that generates water waves with similar wave profiles.

Since the simulation domain was designed to contain the landslide dynamics for a simulations duration of $t=2t_o$, it is not possible to compare a simulated near-field wave record with an entire experimental wave record. Figure 5.47 compares the wave record at x/b=0 for Run 1 to the near-field wave record of Trial 67 up to a time t=0.8 s. The two wave records agree until about 0.1 s but then diverge from 0.1 s to 0.3 s. For this particular comparison, the form of the simulated wave record is correct although the amplitude is too small by a factor of about 1.7. The fact that the experimental results are approximately two times larger than the simulation results is superficially hard to explain. Gaps between the solid blocks and the wave tank sides should result in slightly smaller waves than the conceptually perfect seal that exists in numerical simulations. Also, the small volumetric excess of water appearing during the numerical simulations increases the computed wave amplitudes. Both of these errors are in the opposite sense of the observed difference in nondimensional wave amplitudes. The real explanation probably lies in the fact that an inviscid simulation cannot inherently reproduce fluid separation and therefore generates a different pressure distribution over the block surface. In particular, the simulated pressure distribution cannot produce form drag. However, form

drag only becomes important after about one time scale or $t_o \approx 0.33$ s from Table C.2. Before form drag becomes important to wave generation, added mass effects generate water waves. Added mass effects should be properly simulated by an inviscid code at early times. This probably accounts for the good initial agreement between wave records in Figure 5.47. It follows that the wave profiles in Figure 5.46 are probably realistic.

Figure 5.48 compares the nondimensional wave amplitudes of Trials 50, 51, 57, 67, 68, 73, and 79 with nondimensional wave amplitudes from analogous simulations. Simulation analogs had nearly identical initial landslide geometries, solid block densities, and Coulombic friction coefficients as the corresponding experiment. Table C.17 indicates which simulation runs correspond to which solid block trials. The data can be found in Tables C.3 and C.17. Because the comparison is made between nondimensional wave amplitudes, small errors in the characteristics of motion that affect the dimensional wave amplitude should result in a negligible difference on a nondimensional wavemaker plot. Experimental results are seen to be larger than the simulation results by about 40%. Harbitz (1992) found that shear stresses between a gravity current and the surrounding water accounted for 40% of water wave generation. The straight line curve fit through the origin provides the relation

$$\text{Experimental } \frac{\eta_{max}}{s_o} \approx 1.42 \text{ Numerical } \frac{\eta_{max}}{s_o} \tag{5.52}$$

with a correlation coefficient r=0.89. The correlation between the two sets of results is quite good given the standard errors in the data. The error bars represent one standard deviation and are derived in Sections B.2.5 and B.4. Equation (5.52) is not meant to suggest that a linear relation should exist between nondimensional wave amplitudes.

The scaling of time in Section 3.1.3 was based on the time it takes the leading long wave to travel over the top face of the solid block. This quantity naturally represents the shorter time scale since $t_o \gg b/\sqrt{gd}$ whenever $Ha_o \gg 1$. However, in Section 5.2.2, it was pointed out that the dominant wave period and wavelength scaled with the characteristic time t_o of landslide motion rather than the characteristic time scale of wave propagation. The self-consistency of numerical simulations enables one to compare both time scales to a chosen characteristic time scale from available wave records. The occurrence of the maximum near-field wave amplitude t_{max} was chosen as a characteristic time from the numerical simulations. The characteristic time scale of wave propagation

$$\frac{b}{\sqrt{g\,d}}\sqrt{\frac{g}{b}} = \sqrt{\frac{b}{d}} \tag{5.53}$$

reduces to a simple function of the initial submergence d/b in the nondimensional simulations. Figure 5.49 shows that the occurrence of the maximum near-field wave amplitude t_{max} found from simulations depends primarily upon the characteristic time of landslide motion t_o. Table C.15 contains all of the data shown in Figure 5.49. The time of the maximum near-field wave amplitude is approximately given by

$$t_{max} \approx 0.69\, t_o \tag{5.54}$$

with a correlation coefficient r=0.89. A relation such as equation (5.54) was originally postulated to exist in Section 5.2.2 but was not verified with experimental results. This correlation is the first direct link between the characteristic time of landslide motion and a characteristic time associated with the observed water waves. However, Figure 5.49 also shows that, at $t_o\sqrt{g/b} \approx 3.8$, the value of $t_{max}\sqrt{g/b}$ is ordered somewhat by initial submergence. In addition, the data for d/b=0.87 and d/b=2.13 show an interesting crossover near $t_o\sqrt{g/b} \approx 6$. So, while the characteristic time of landslide motion dominates the occurrence of the maximum near-field wave amplitude, the characteristic time of wave propagation has subtle influences of its own.

Figure 5.50 shows the simulated wavemaker results obtained from solid block landslides with block densities ranging from ρ_b=1100 kg/m^3 to ρ_b=2745 kg/m^3 and a Coulombic friction coefficient C_n=0.344. The incline angle was held constant for these solid block landslides at θ=45°. Wavemaker data are provided for nondimensional initial submergences of d/b=0.87 and d/b=2.13. Both sets of wavemaker data display a power law behavior for larger Hammack numbers. For d/b=2.13, a power of n≈1.55 is found while, for d/b=0.87, a power of n≈1.20 is found. The simulation results also demonstrate the inflection point indicative of where Equation (3.29) ceases to be valid. For d/b=2.13, the power law behavior ceases to apply around $Ha_{o.min}$≈5.5. When d/b=0.87, the power law behavior ceases to apply around $Ha_{o.min}$≈3.5. These values agree quite well with those displayed in Figure 5.38. While these transition Hammack numbers are different for different nondimensional initial submergences, they both correspond to the solid block with density ρ_b=2745 kg/m^3. In fact, the wavemaker data for the different initial submergences appear primarily to have been translated along both axes.

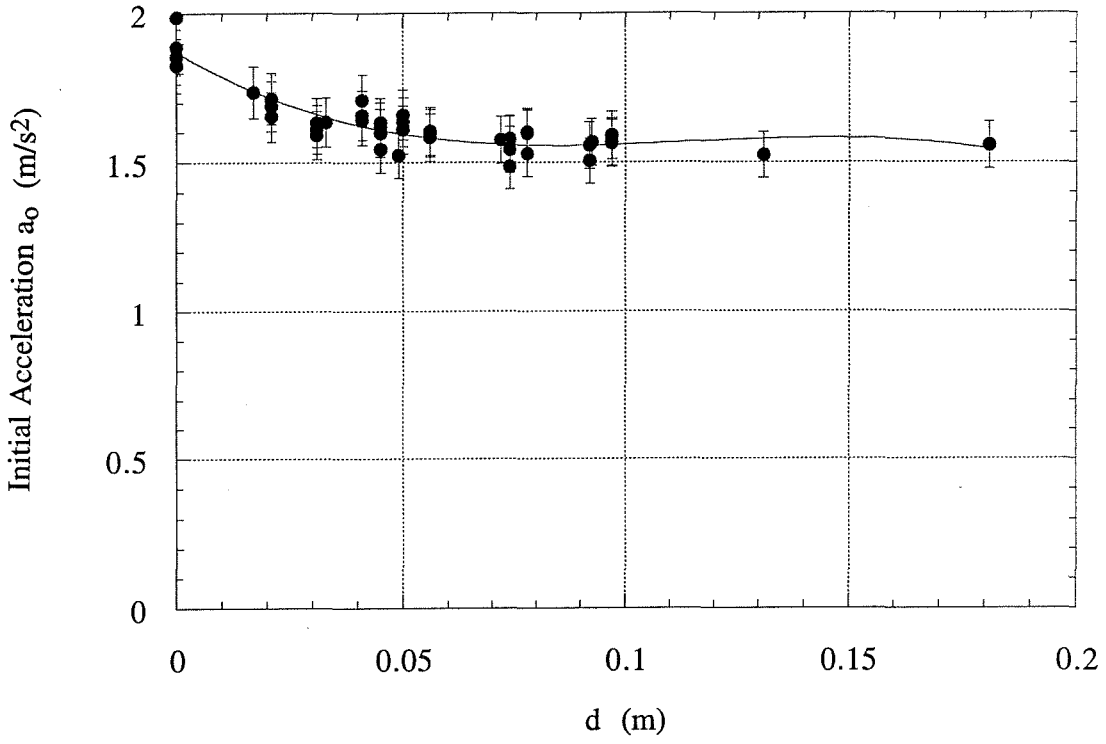

Figure 5.1: Initial acceleration of solid block 1_n as a function of initial submergence measured with a solid-state accelerometer. The least-squares polynomial curve fit is provided in equation (5.1). The initial acceleration is generally between 1.6-1.7 m/s^2 over a wide range of initial submergences.

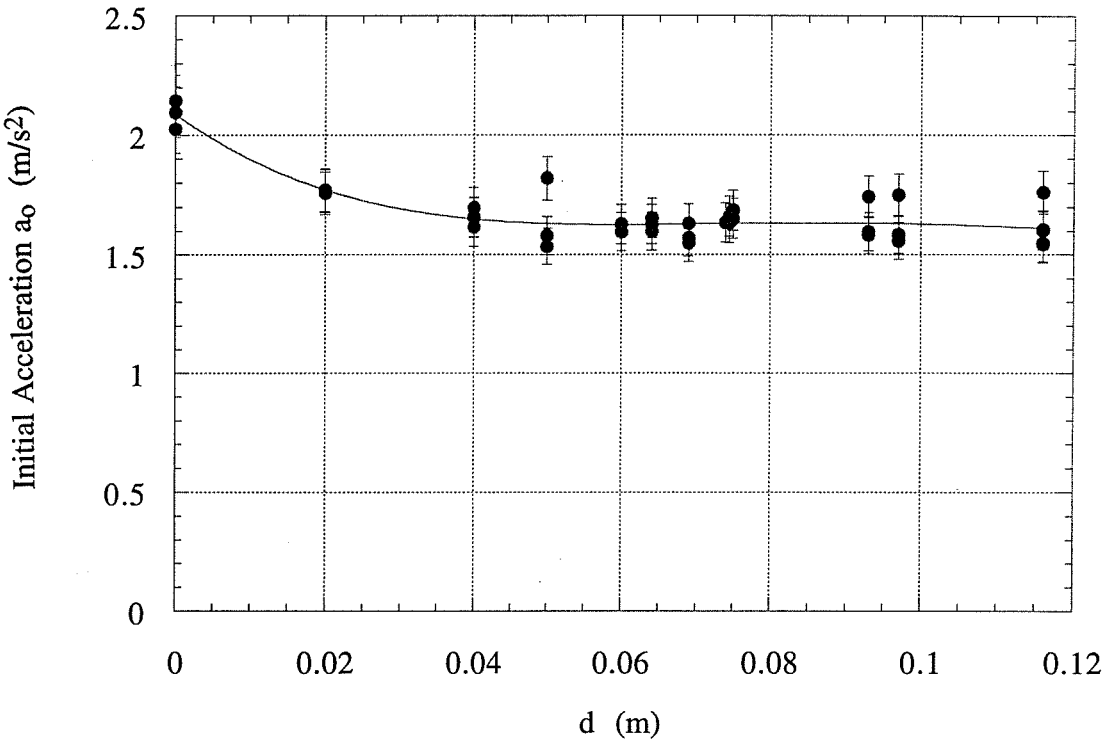

Figure 5.2: Initial acceleration of solid block 2_n as a function of initial submergence measured with a solid-state accelerometer. The least-squares polynomial curve fit is provided in equation (5.2). The initial acceleration is generally between 1.5-1.8 m/s^2 over a wide range of initial submergences.

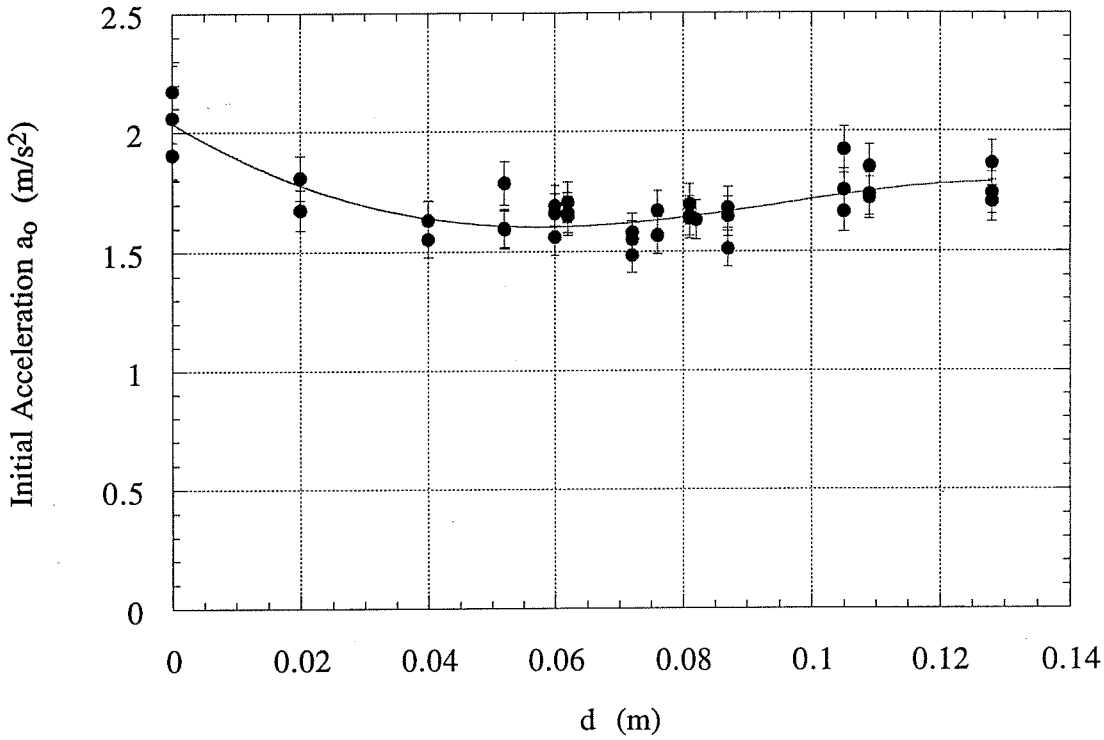

Figure 5.3: Initial acceleration of solid block 3_n as a function of initial submergence measured with a solid-state accelerometer. The least-squares polynomial curve fit is provided in equation (5.3). The initial acceleration is generally between 1.5-1.9 m/s^2 over a wide range of initial submergences.

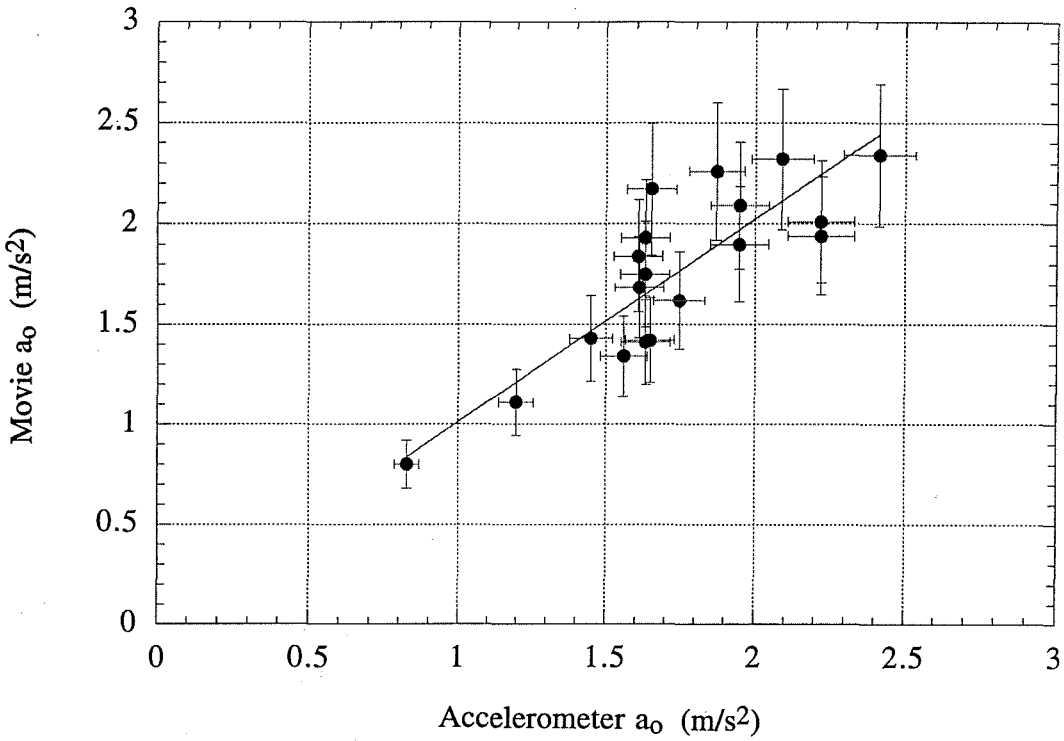

Figure 5.4: Correlation between mean accelerometer measurements of initial acceleration and high speed movie based curve fits of initial acceleration for particular solid block experiments. The least-squares linear curve fit through the origin yields a slope of 1.01. The accelerometer results can therefore be used in place of the high speed movie results.

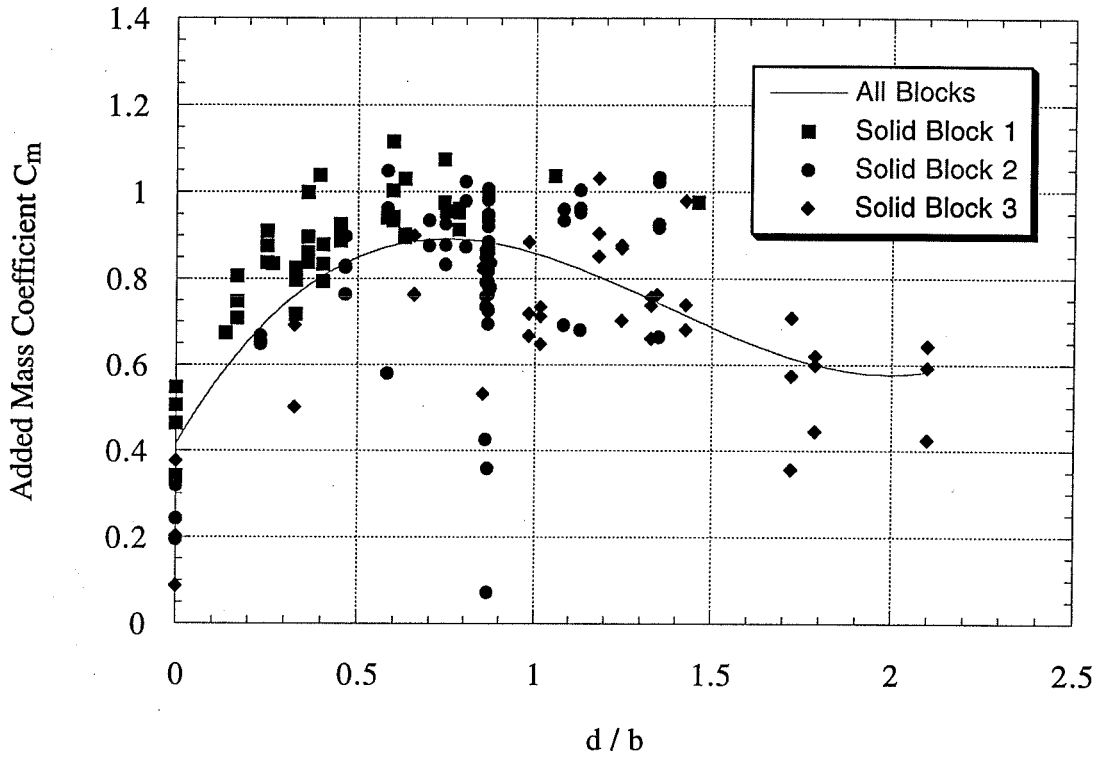

Figure 5.5: Raw data of added mass coefficient computed from equation (5.4) as a function of the nondimensional initial submergence d/b at time $t=0^+$. The least-squares polynomial curve fit through all data is given in equation (5.6). The amplification of random errors in the acceleration data is clearly evident.

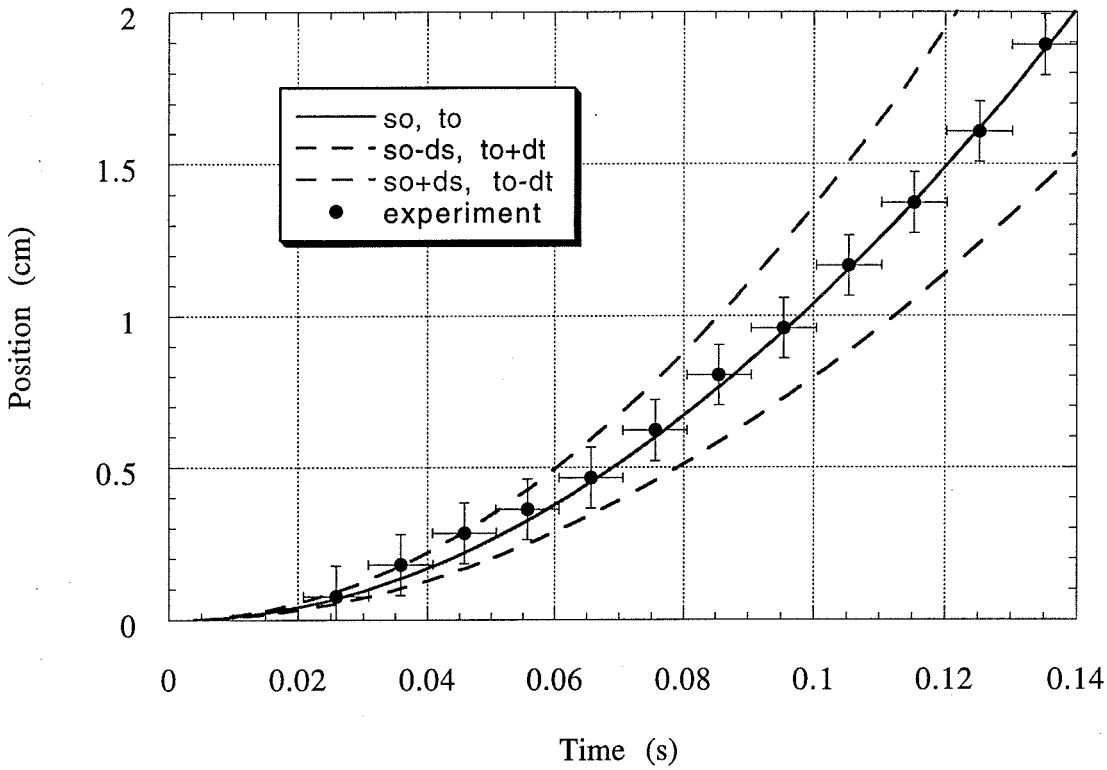

Figure 5.6: Comparison of solid block position data from Trial 48 with the analytical solid block motion of equation (3.78). The independent values $s_o=u_t^2/a_o=0.216$ m and $t_o=u_t/a_o=0.333$ s follow from Table C.2. The error in the characteristic distance is $ds=0.11s_o$ while the error in the characteristic time is $dt=0.08t_o$.

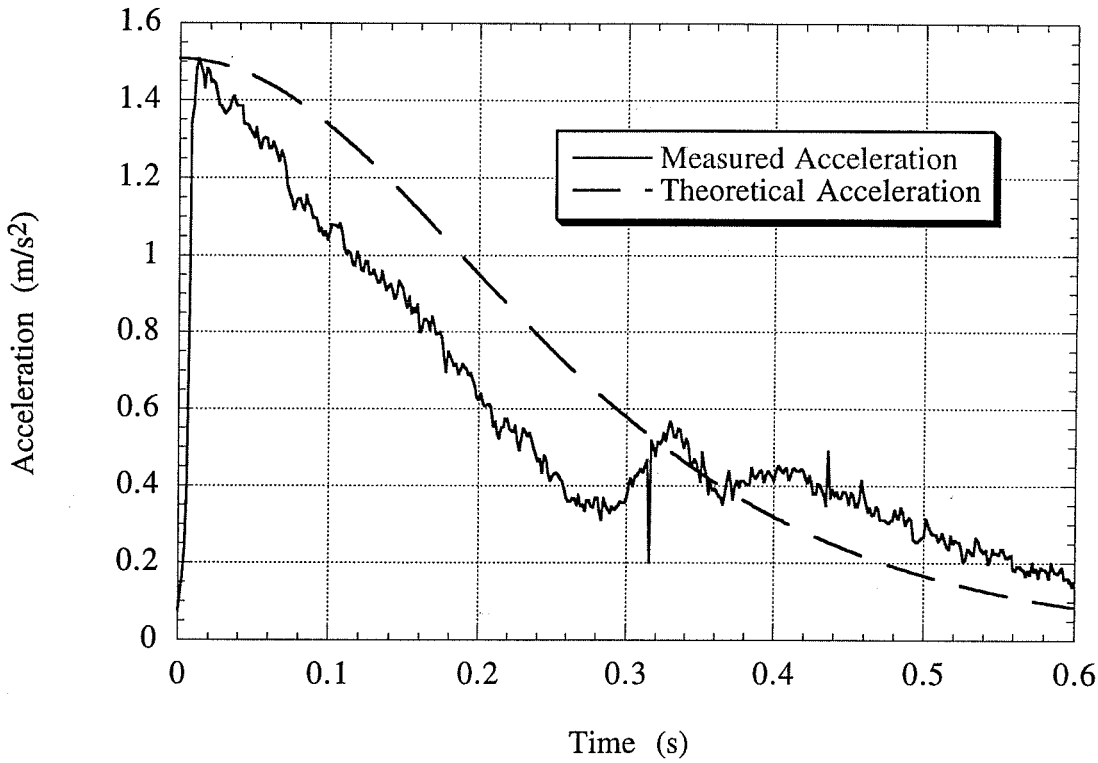

Figure 5.7: Comparison of acceleration data from Trial 76 with the analytical acceleration equation (3.81). The initial acceleration was obtained from the acceleration record while the terminal velocity came from Table 5.3.

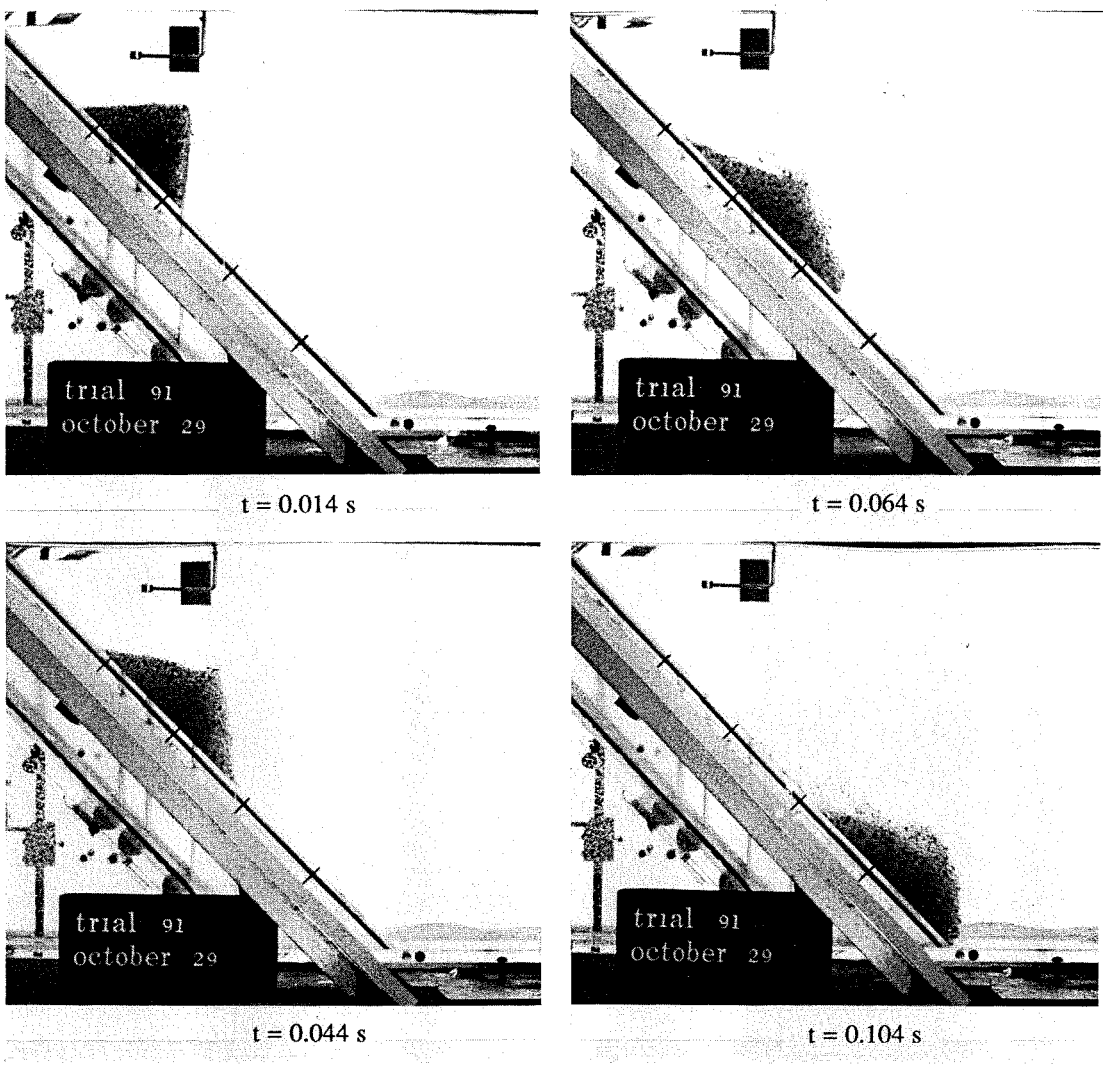

Figure 5.8: Four frames from the movie records of the 3 mm glass bead landslide of Trial 91. The initial frame was exposed shortly after complete retraction of the stainless steel gate. The evolution of material landslides from deforming triangular material masses into a gravity current is seen to involve various wave events.

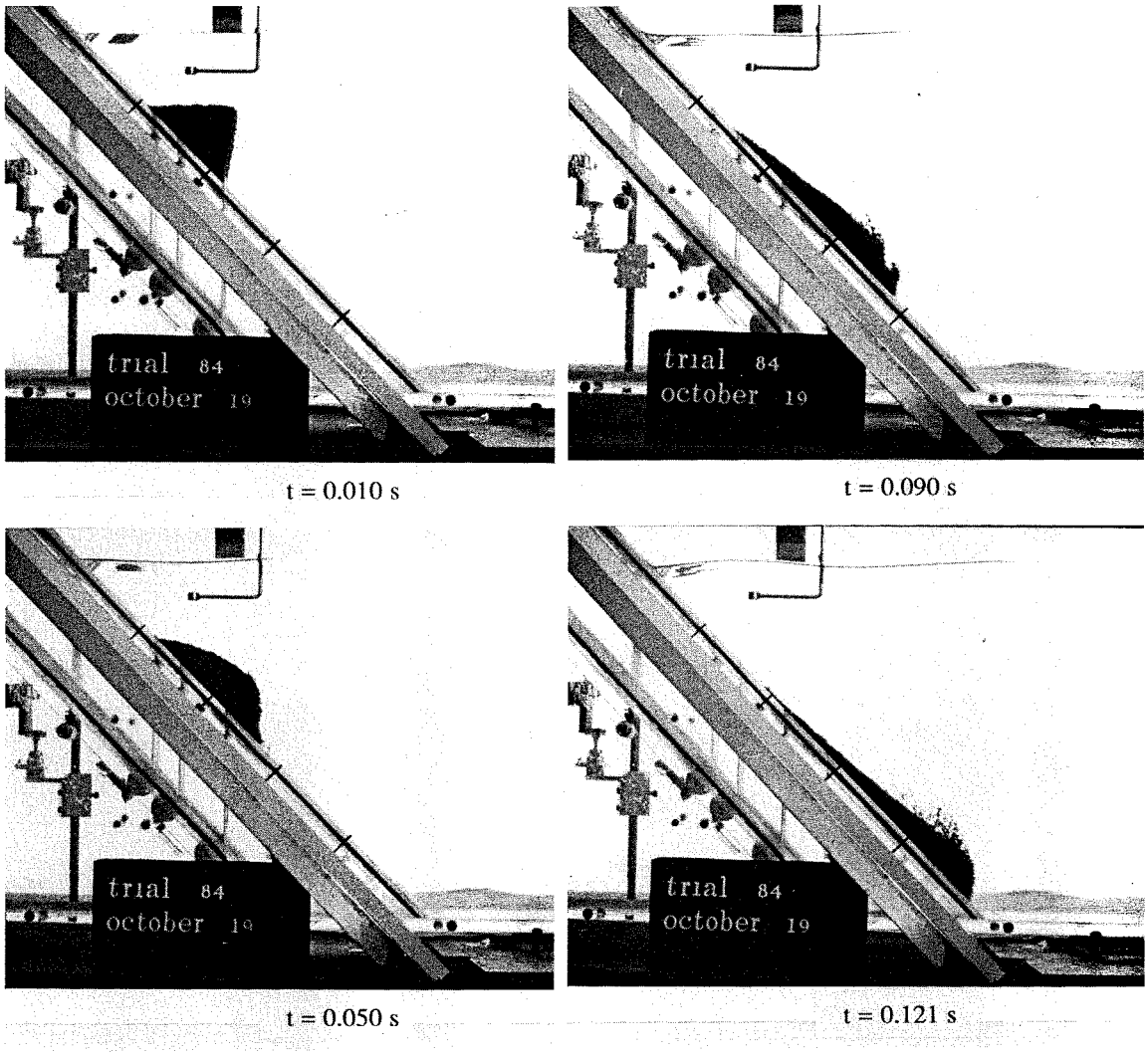

Figure 5.9: Four frames from the movie records of the 2 mm lead shot landslide of Trial 84. The initial frame was exposed shortly after complete retraction of the stainless steel gate. The evolution of material landslides from deforming triangular material masses into a gravity current is seen to involve various wave events.

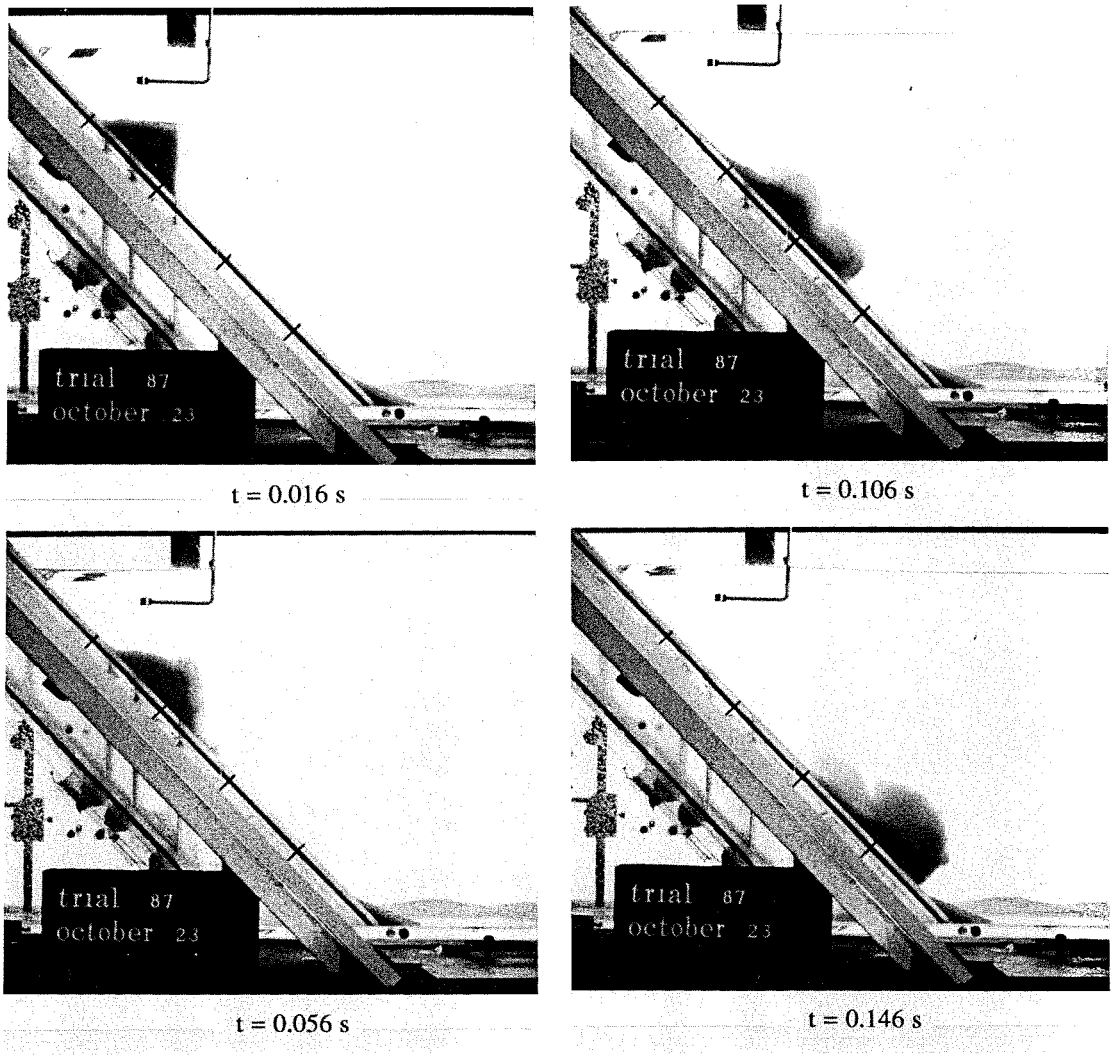

Figure 5.10: Four frames from the movie records of the 0.5 mm glass bead landslide of Trial 87. The initial frame was exposed shortly after complete retraction of the stainless steel gate. The evolution of material landslides from deforming triangular material masses into a gravity current is seen to involve various wave events.

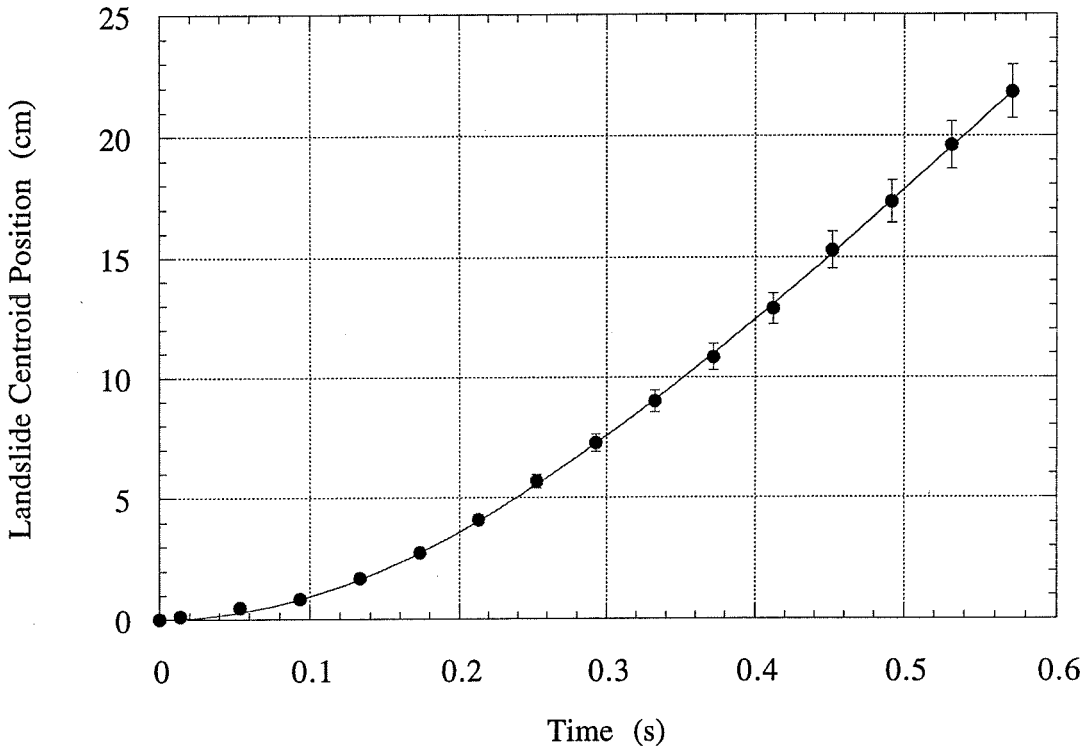

Figure 5.11: Position of the material landslide cross-sectional centroid along the incline as a function of time for Trial 91 composed of 3 mm glass beads. The data are curve fit by equation (3.78) to yield a characteristic distance $s_o \approx 19.2$ cm and time $t_o \approx 0.32$ s. The landslide initial size was b=112 mm with initial submergence d=97 mm.

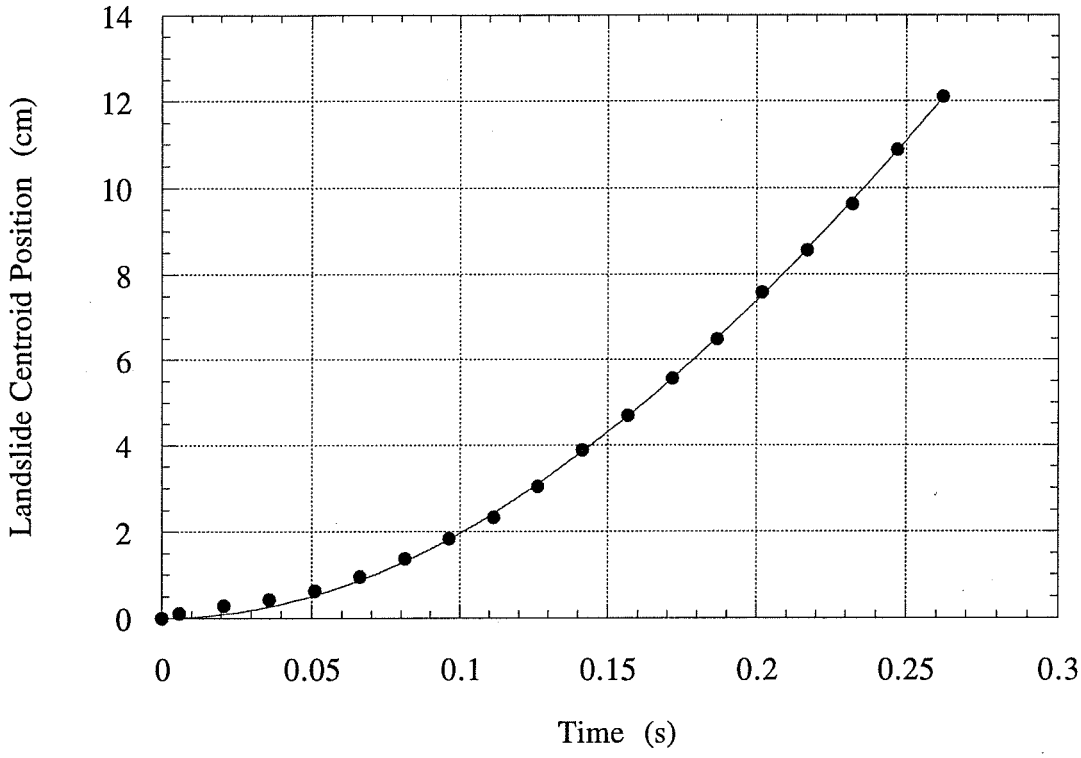

Figure 5.12: Position of the material landslide cross-sectional centroid along the incline as a function of time for Trial 81 composed of 3 mm steel shot. The data are curve fit by equation (3.78) to yield a characteristic distance $s_o \approx 29.5$ cm and time $t_o \approx 0.27$ s. The landslide initial size was b=85 mm with initial submergence d=74 mm.

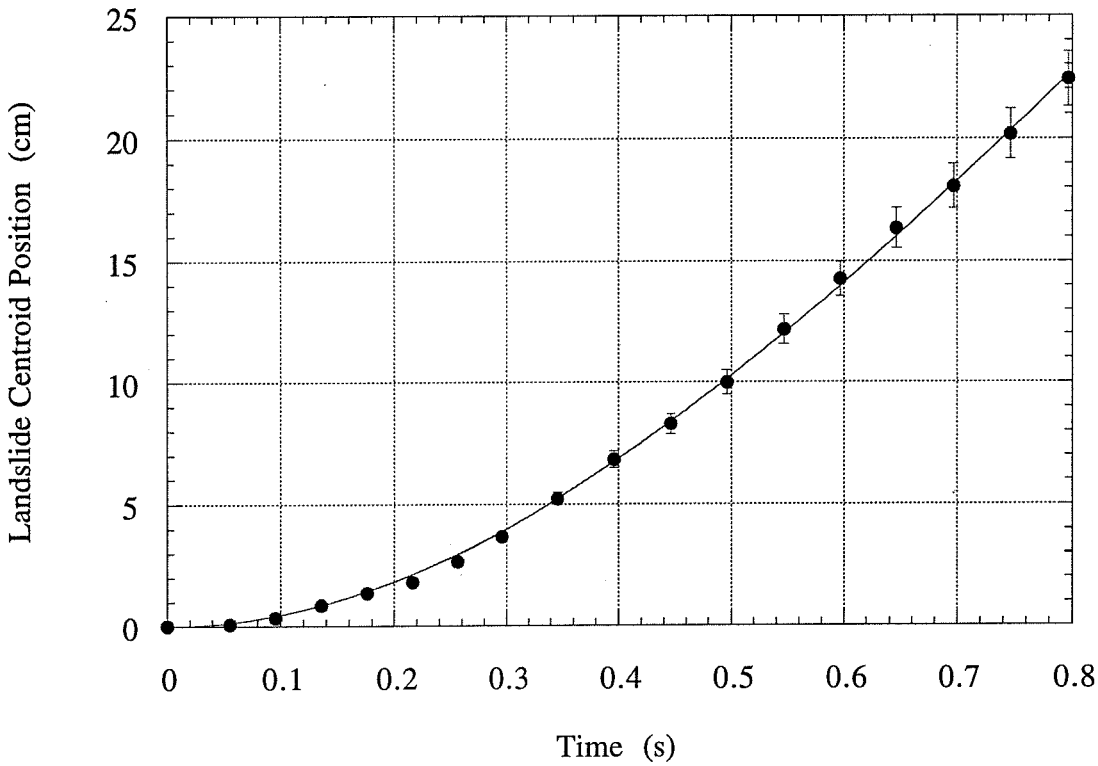

Figure 5.13: Position of the material landslide cross-sectional centroid along the incline as a function of time for Trial 87 composed of 0.5 mm glass beads. The data are curve fit by equation (3.78) to yield a characteristic distance $s_o \approx 26.3$ cm and time $t_o \approx 0.53$ s. The landslide initial size was b=85 mm with initial submergence d=75 mm.

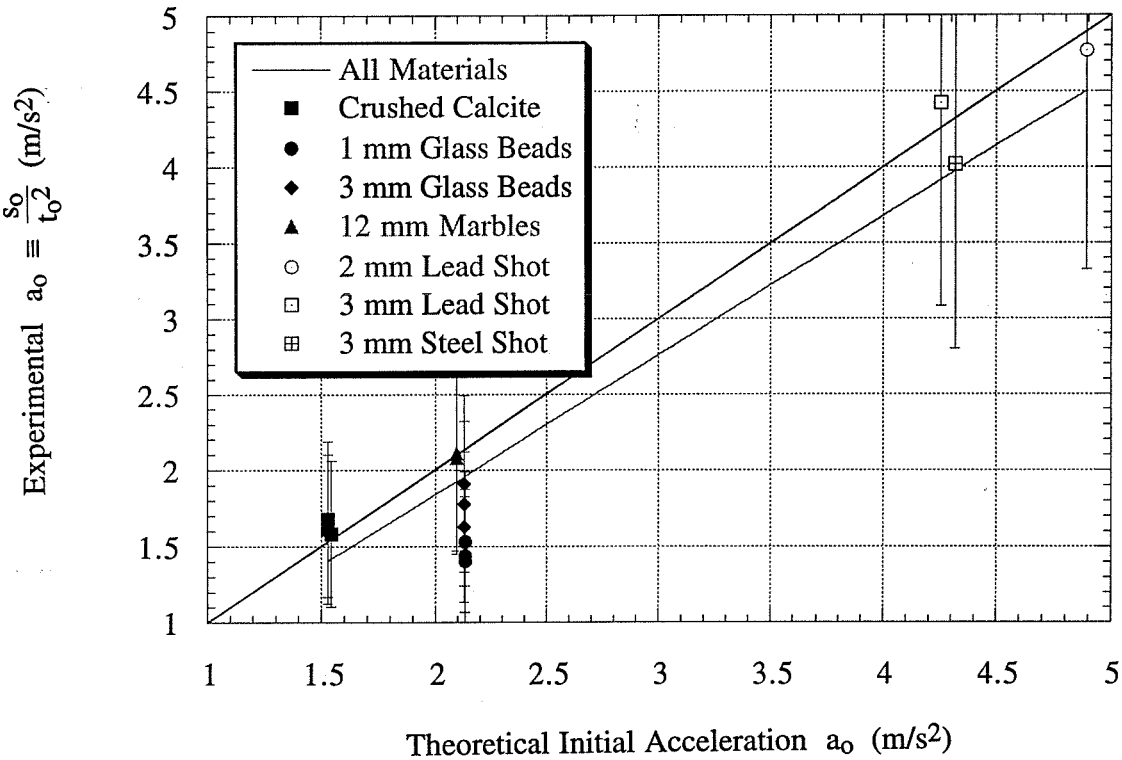

Figure 5.14: Correlation between the theoretical initial acceleration predicted by equation (3.73) and the initial acceleration s_o/t_o^2 obtained by curve fitting the landslide centroid motion down the incline. The least-squares linear curve fit through the origin has a slope of 0.92. The line of equivalence is also shown on the figure.

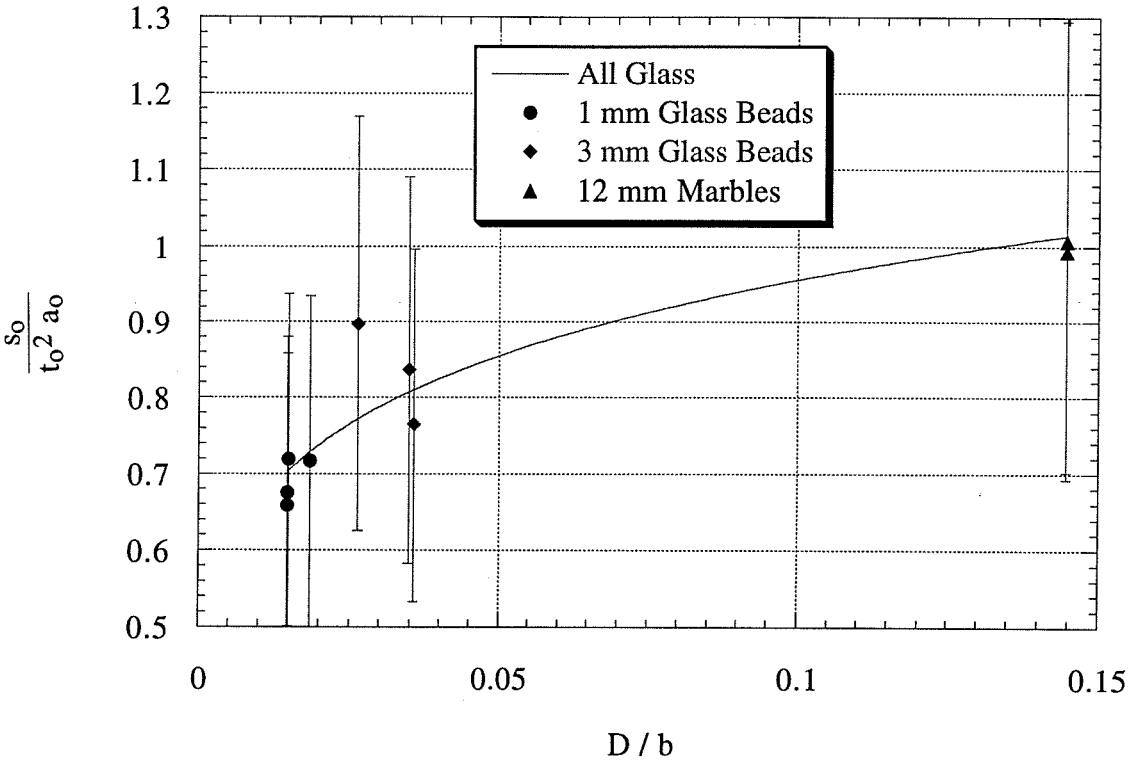

Figure 5.15: Ratio of experimental to theoretical initial acceleration as a function of nondimensional particle size for glass bead landslides. Only material characteristics dependent on the particle size varied significantly. The theoretical initial acceleration becomes a better predictor of the actual initial acceleration with larger particle size.

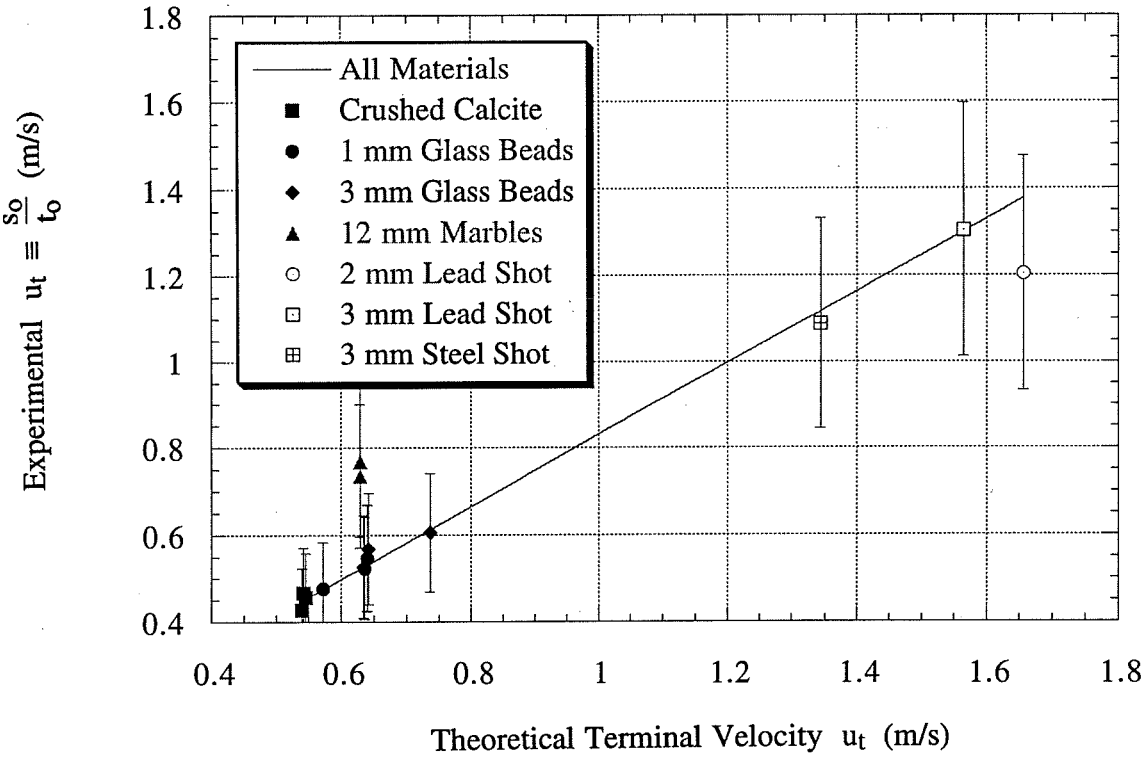

Figure 5.16: Correlation between the theoretical terminal velocity predicted by equation (3.74) and the experimental terminal velocity s_o/t_o obtained by curve fitting the landslide centroid motion down the incline. The least-squares linear curve fit through the origin has a slope of 0.83.

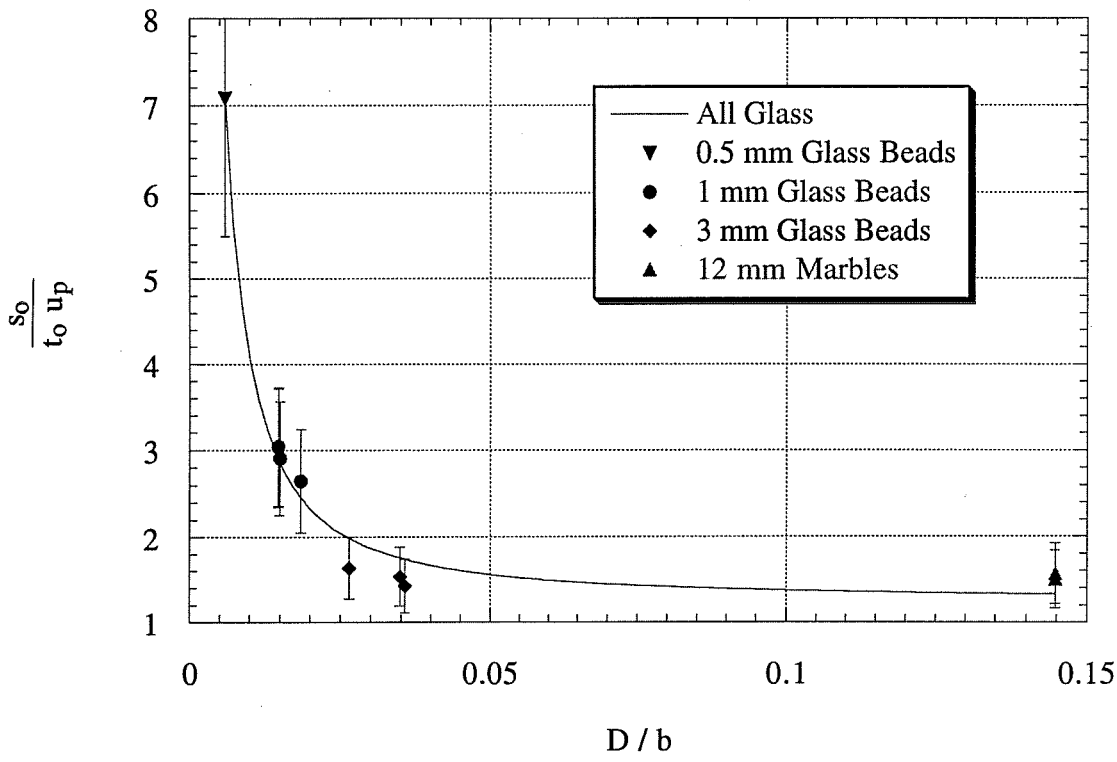

Figure 5.17: Ratio of experimental terminal velocity to single particle fall velocity as a function of nondimensional particle size for glass bead landslides. The power -1.4 in the curve fit is too strong to be induced by only the particle fall velocity dependence on D. Larger particles permit larger experimental terminal velocities through less mixing.

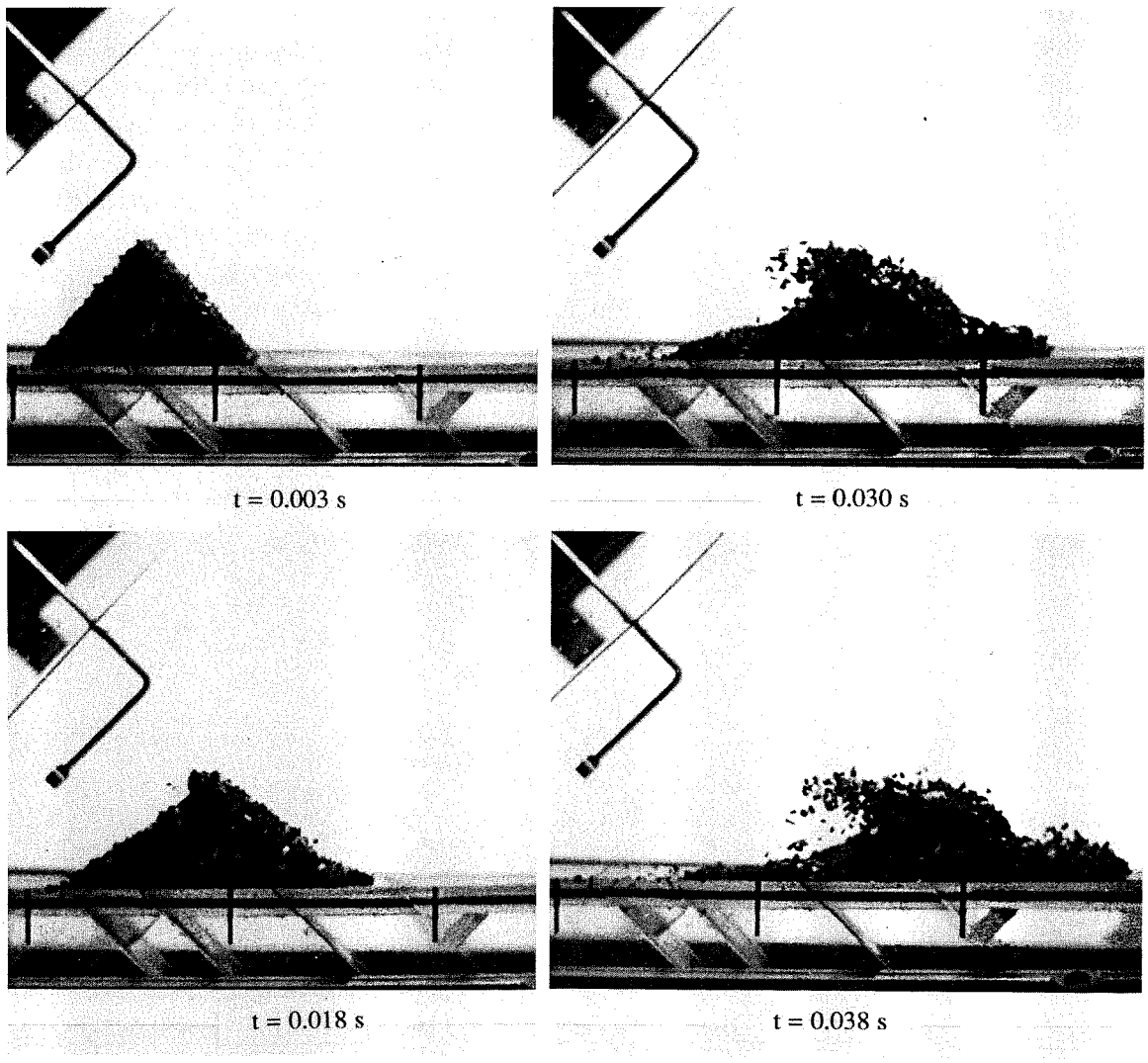

Figure 5.18: Four frames from the movie records of the crushed calcite landslide of Trial 40. The initial frame was exposed shortly after complete retraction of the stainless steel gate. Marked particles in the landslide core demonstrate very little relative displacement until they appear close to the landslide surface.

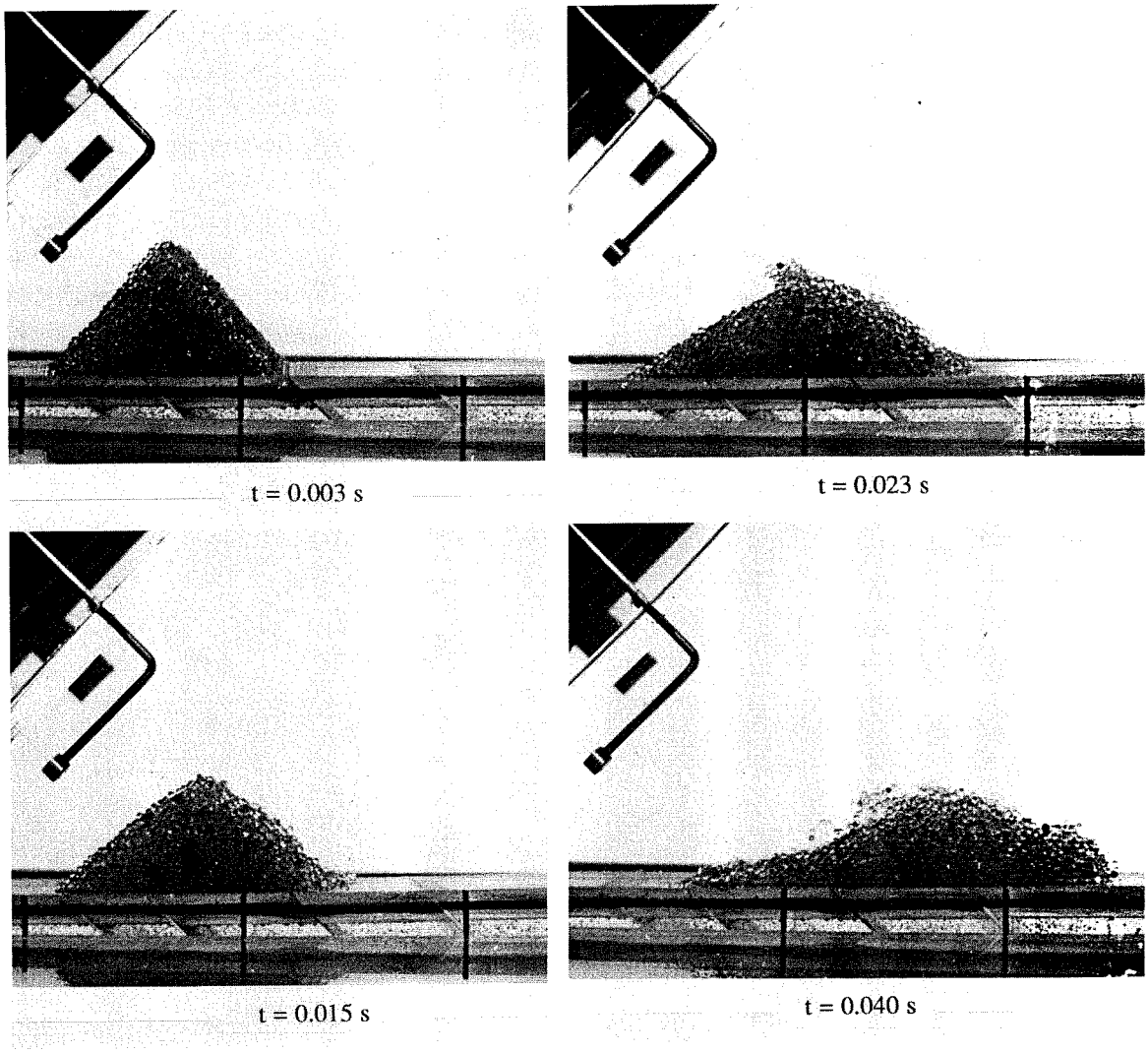

Figure 5.19: Four frames from the movie records of the 3 mm glass bead landslide of Trial 82. The initial frame was exposed shortly after complete retraction of the stainless steel gate. Marked particles in the landslide core demonstrate significant relative motion over the entire landslide cross-section.

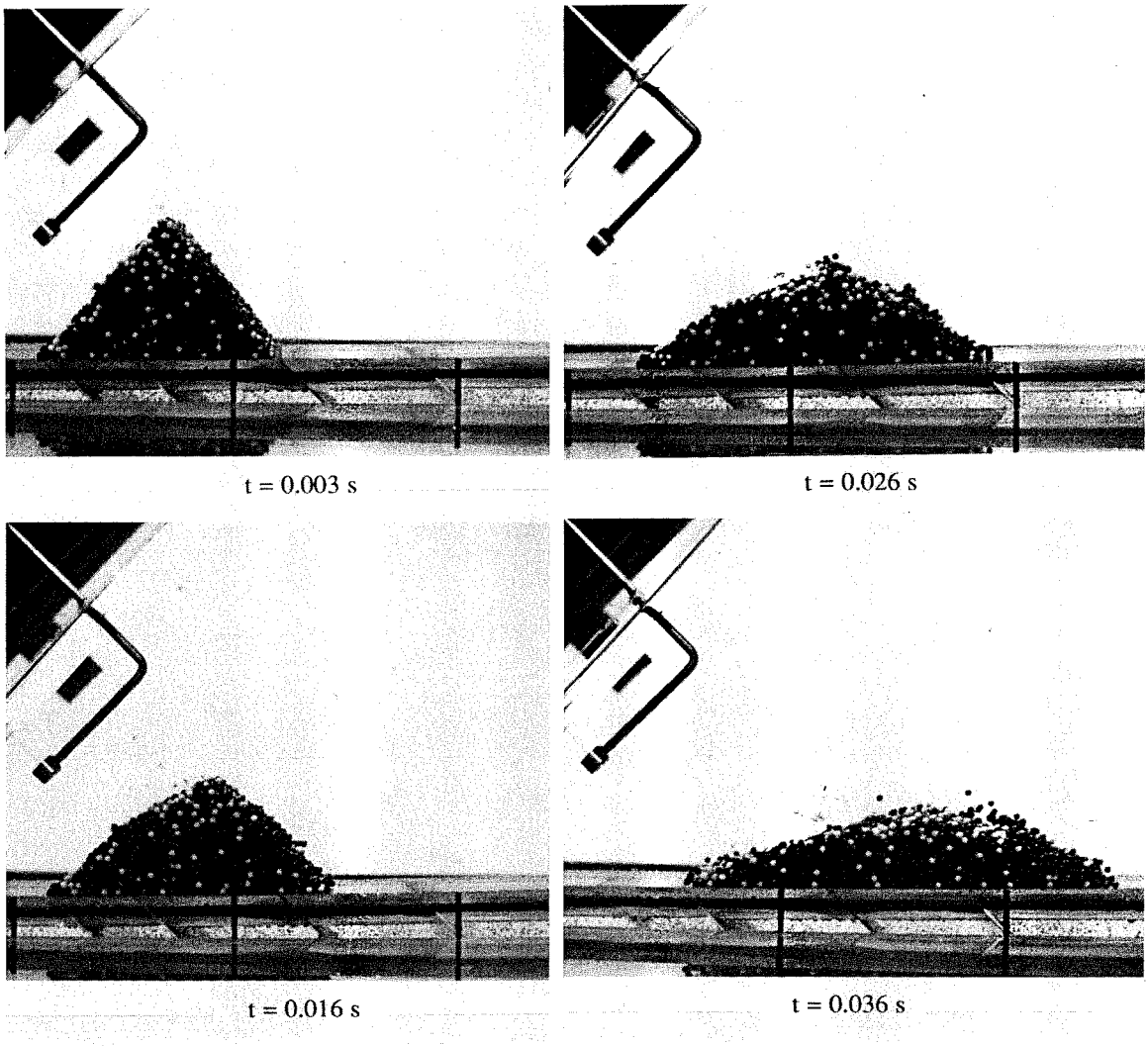

Figure 5.20: Four frames from the movie records of the 3 mm steel shot landslide of Trial 81. The initial frame was exposed shortly after complete retraction of the stainless steel gate. Marked particles in the landslide core demonstrate more relative displacement near the nose of the landslide.

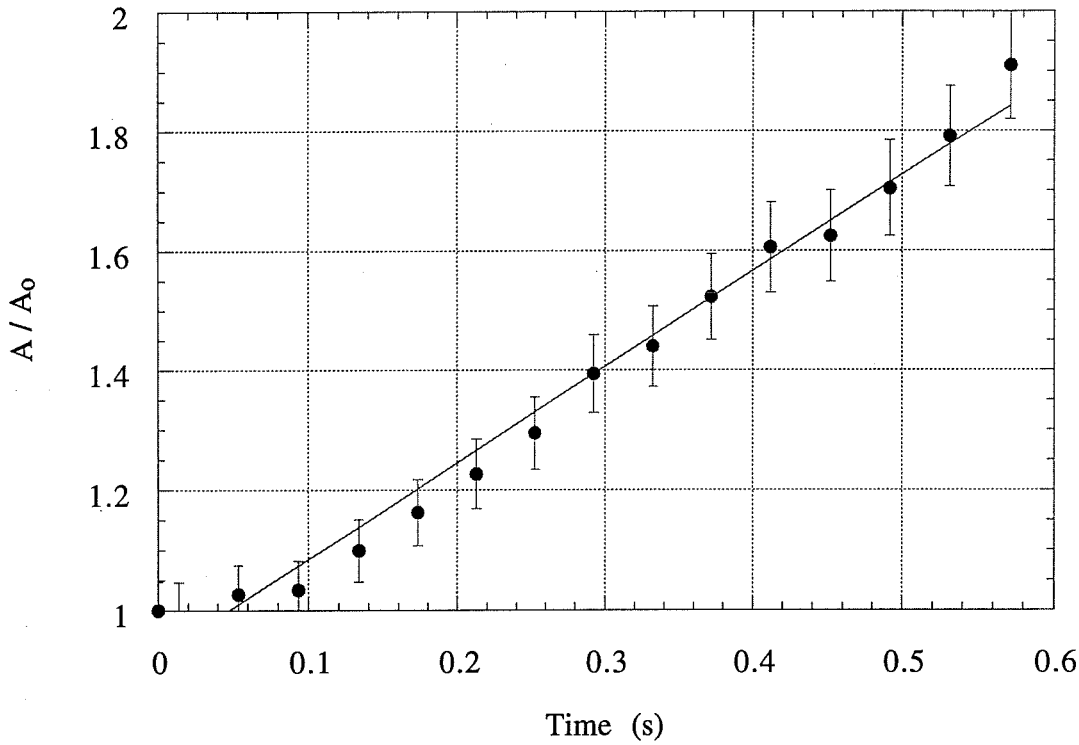

Figure 5.21: Normalized cross-sectional area of a 3 mm glass bead landslide as a function of time. The rate of strain associated with area growth is 1.61 s^{-1} over all of Trial 91. There is additional uncertainty in the area for short times due to perspective.

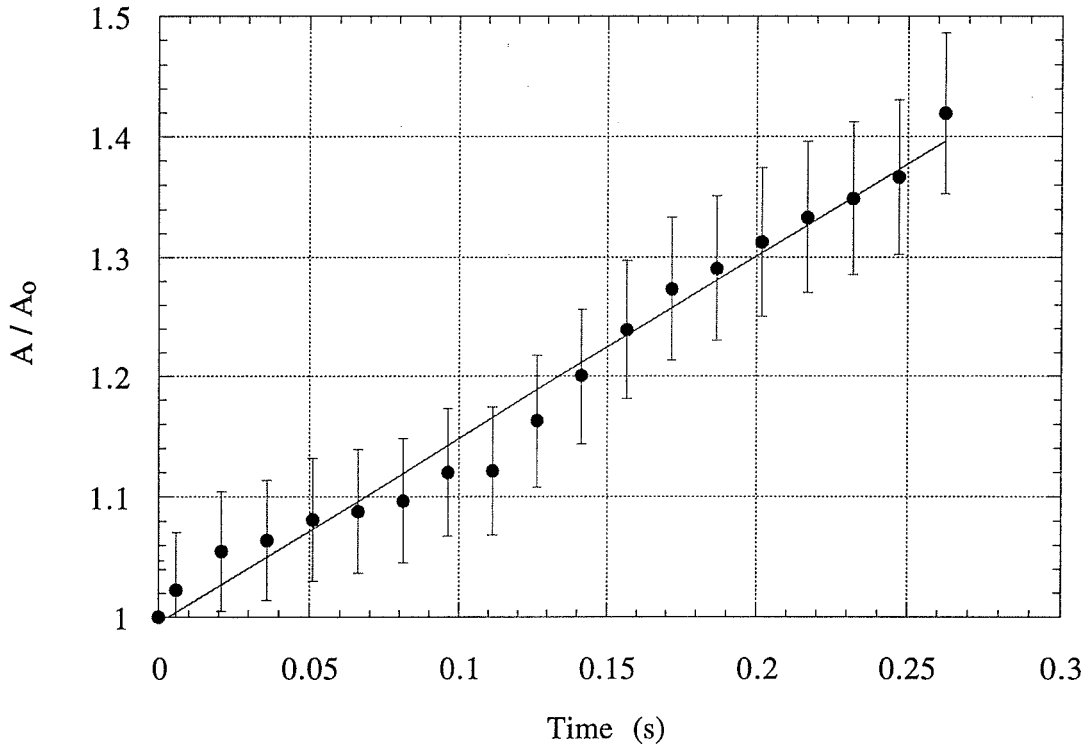

Figure 5.22: Normalized cross-sectional area of a 3 mm steel shot landslide as a function of time. The rate of strain associated with area growth is 1.53 s^{-1} over all of Trial 81. There is considerably less uncertainty in the area of the steel shot landslide.

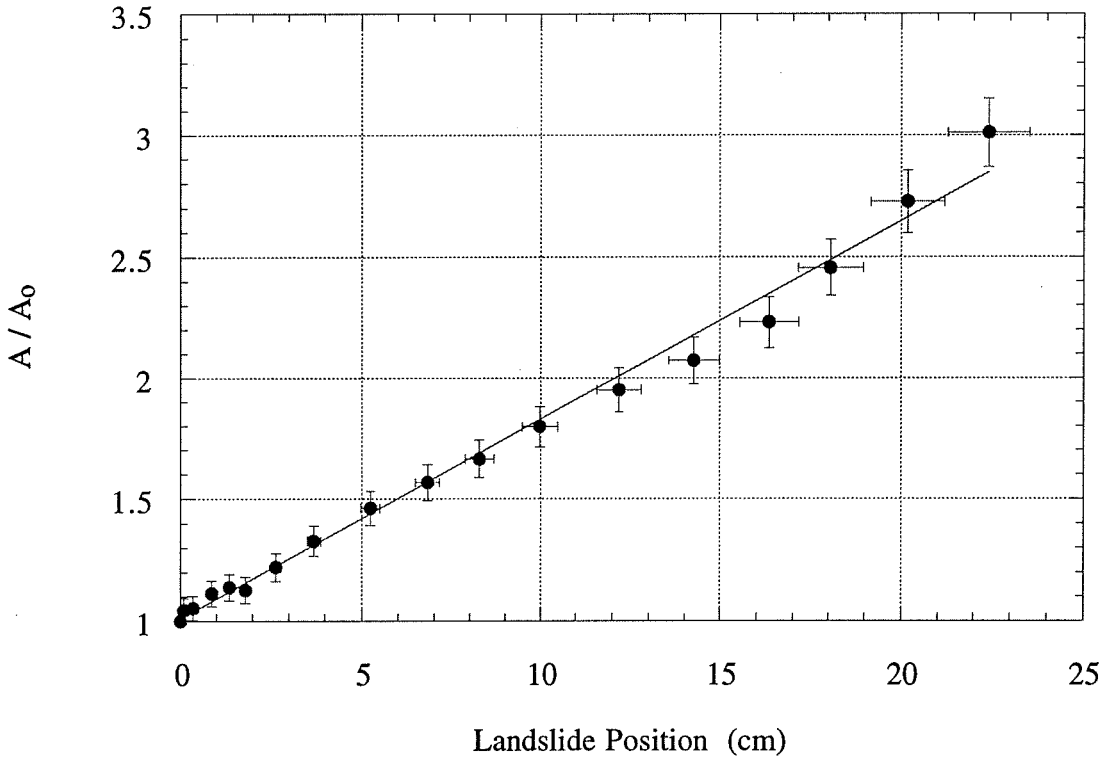

Figure 5.23: Normalized cross-sectional area of a 0.5 mm glass bead landslide as a function of landslide centroid position along the incline. The derivative of the area with respect to position is 0.082 cm^{-1} for all of Trial 87.

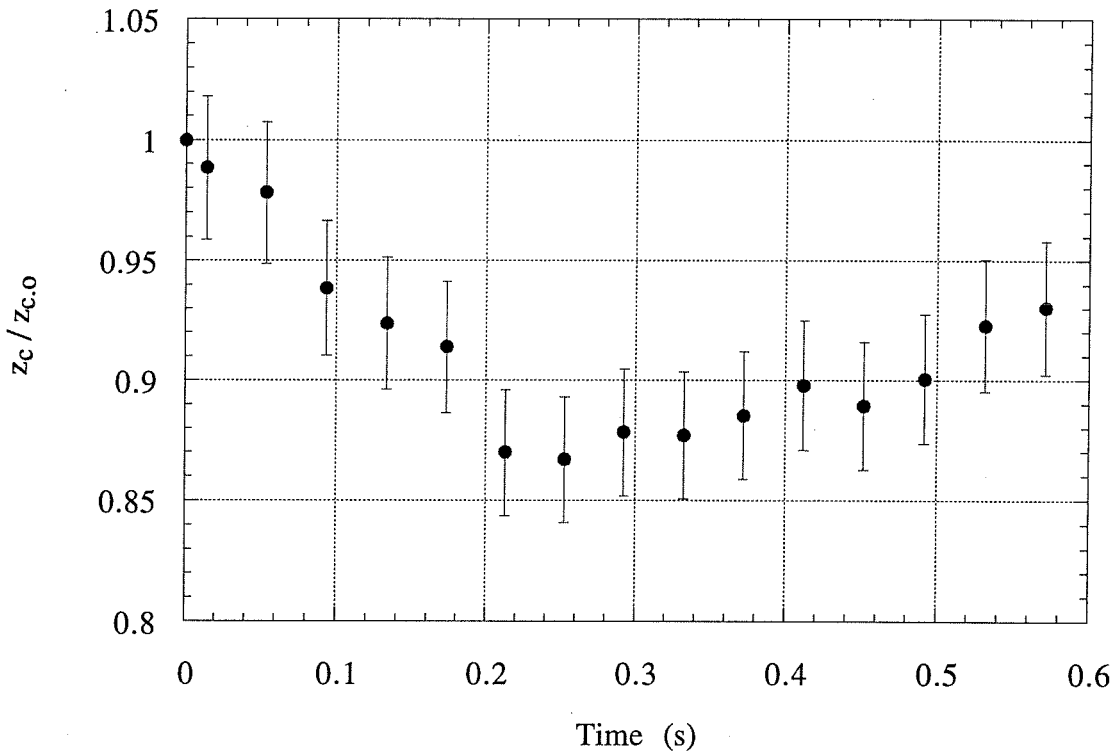

Figure 5.24: Normalized centroid height above the incline for a 3 mm glass bead landslide as a function of time. The initial rate of strain associated with centroid lowering is -0.55 s^{-1} for Trial 91. After 0.2 s have elapsed, the centroid begins to rise due to the formation of a growing gravity current.

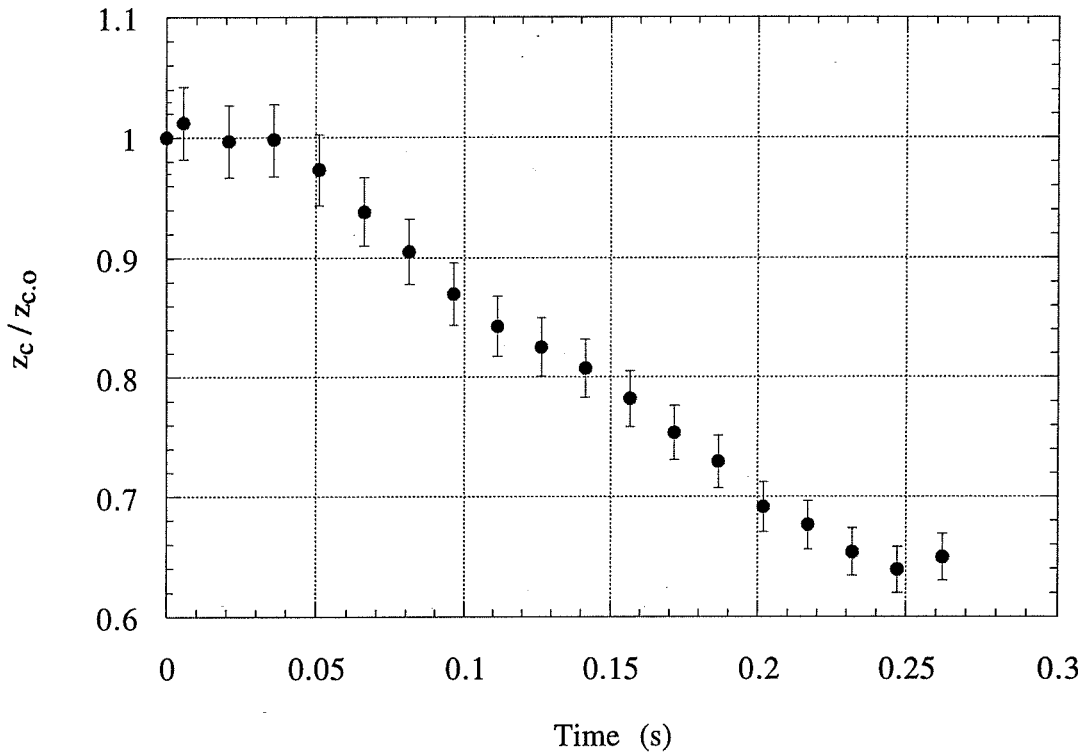

Figure 5.25: Normalized centroid height above the incline for a 3 mm steel shot landslide as a function of time. The rate of strain associated with centroid lowering is -1.71 s^{-1} over the entire Trial 81. The large density of steel shot does not permit the formation of a gravity current.

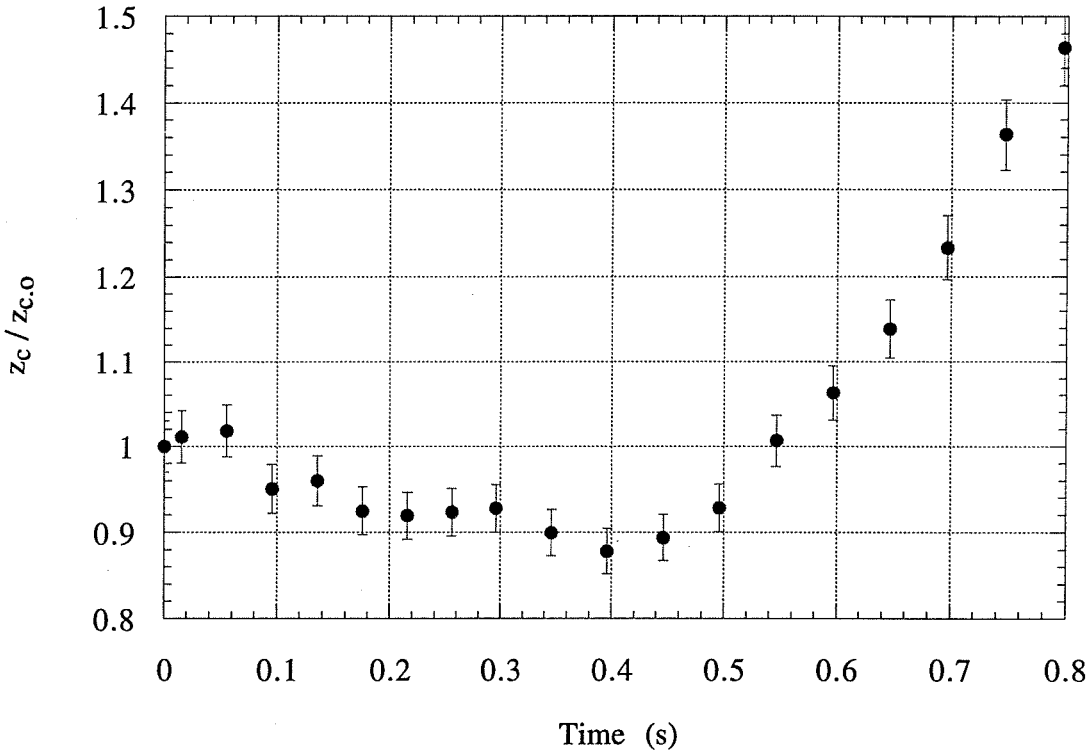

Figure 5.26: Normalized centroid height above the incline for a 0.5 mm glass bead landslide as a function of time. The initial rate of strain associated with centroid lowering is -0.52 s^{-1} for Trial 87. After 0.4 s have elapsed, the centroid begins to rise rapidly as landslide particles are mixed with the surrounding water.

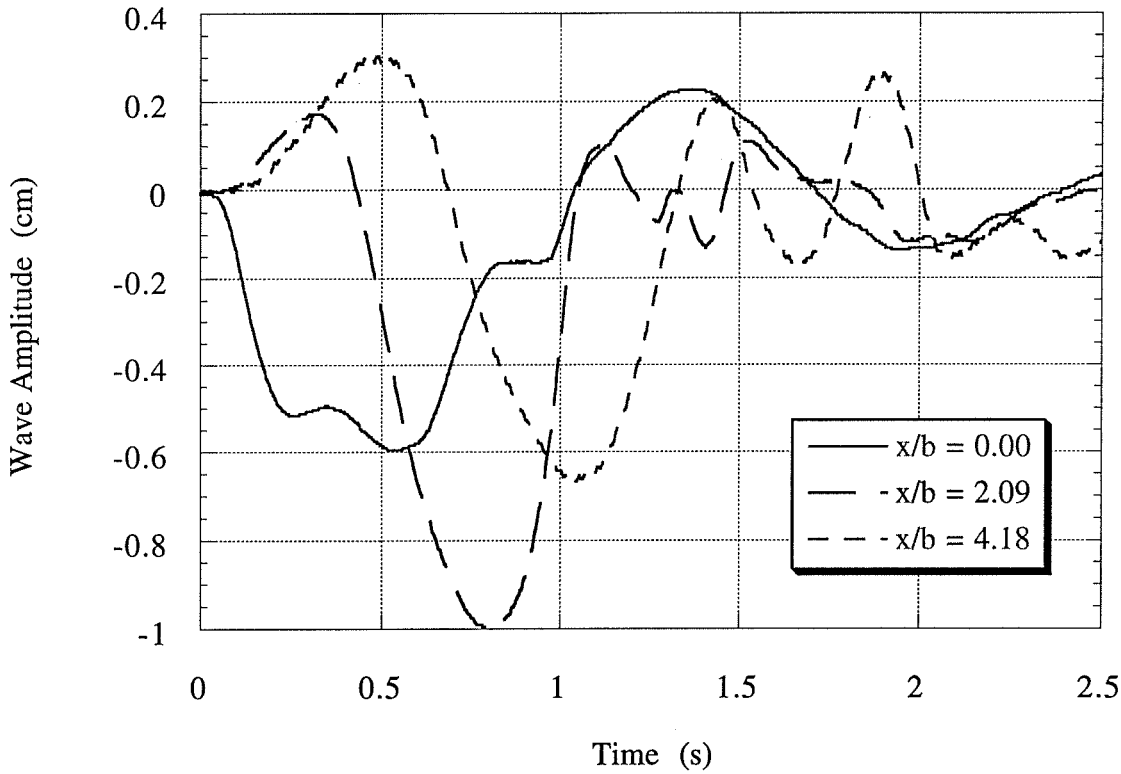

Figure 5.27: Three near-field wave records measured at different positions x/b for a repeated solid block 2_n trial with initial submergence d=59 mm. The maximum negative wave amplitude follows the solid motion while a positive wave is generated ahead of the front face of the solid block.

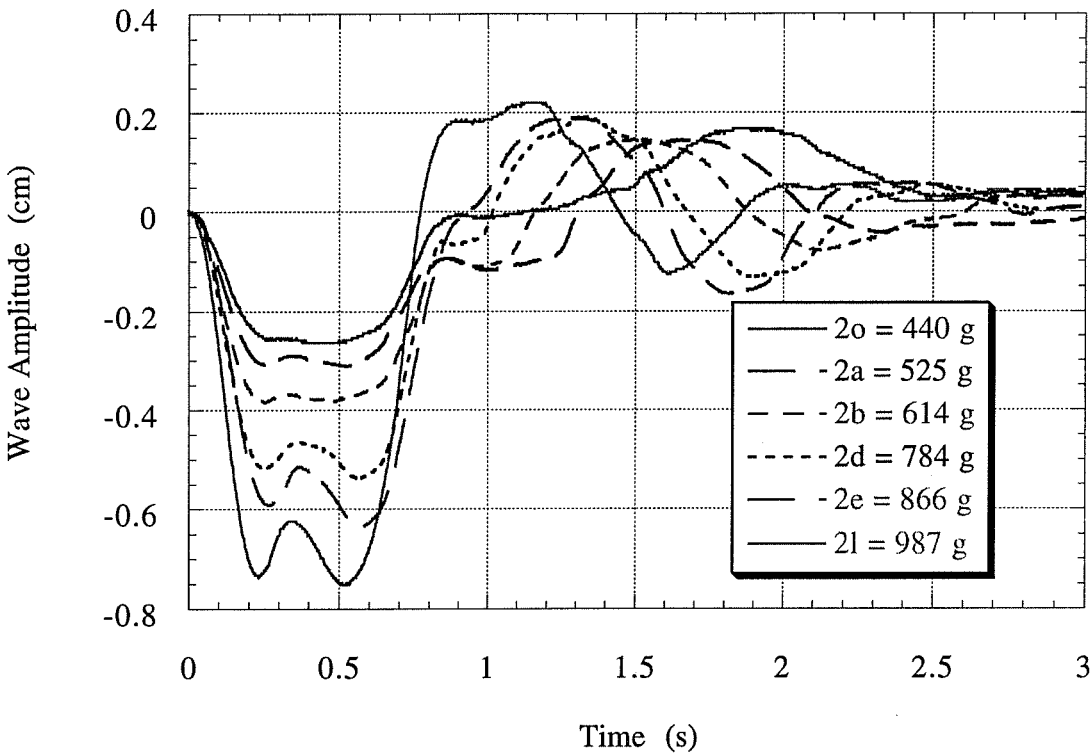

Figure 5.28: Comparison of six near-field wave records obtained at x/b=0 above the middle of the initial landslide position. Different density blocks were released from rest with an initial submergence of d=74 mm. The maximum near-field wave amplitude depends on the block 2 density whereas the rebounding positive wave does not.

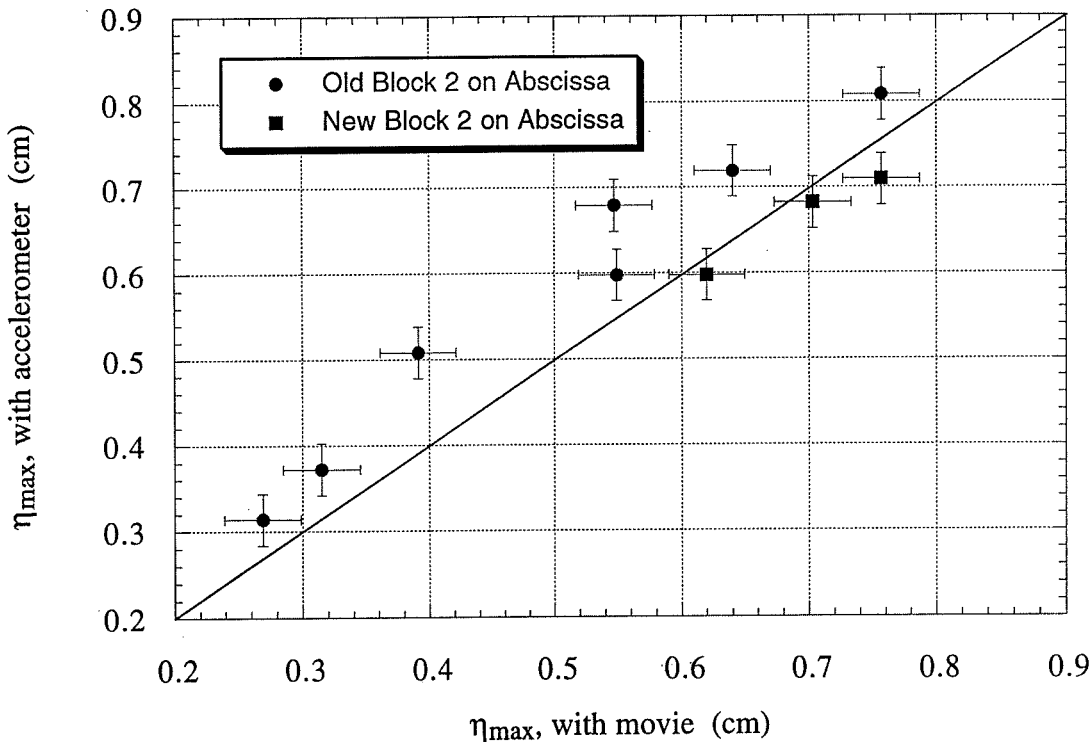

Figure 5.29: Comparison of maximum near-field wave amplitudes for solid block trials observed with a high speed movie camera *versus* similar trials measured with an accelerometer. Old block 2 waves are seen to be consistently smaller than the new block 2 results plotted along the ordinate. The accelerometer may affect waves slightly.

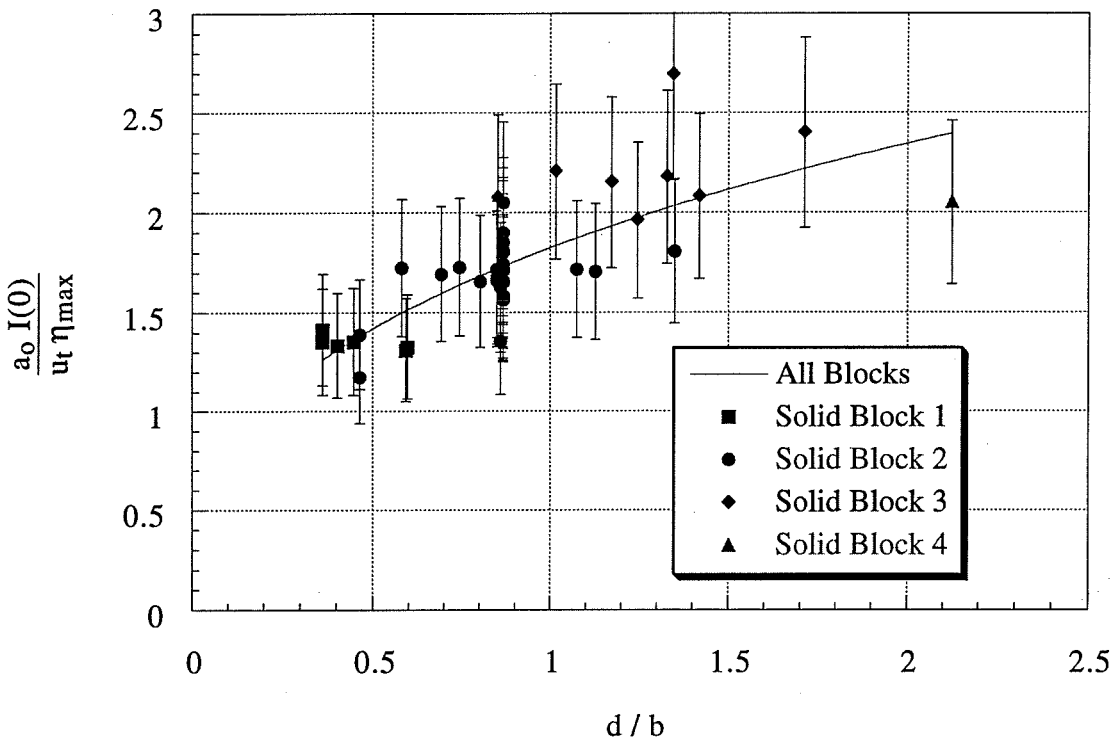

Figure 5.30: Ratio of the near-field amplitude integral I(0) to the scaling quantity $t_o\eta_{max}$ as a function of nondimensional initial submergence. The initial submergence is a measure of wave nonlinearity and alters the interaction of waves with the incline. The amplitude integral I(0) remains relatively large for large initial submergences.

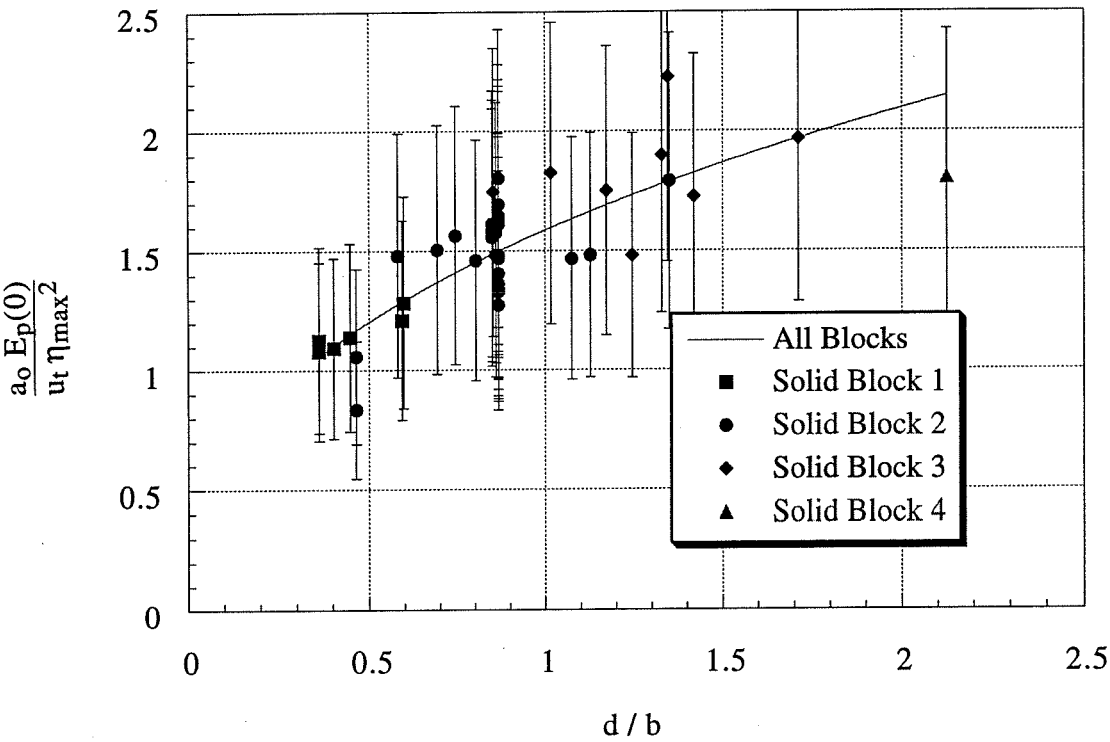

Figure 5.31: Ratio of the near-field energy integral $E_p(0)$ to the scaling quantity $t_o\eta_{max}^2$ as a function of nondimensional initial submergence. The initial submergence is a measure of wave nonlinearity and alters the interaction of waves with the incline. The total potential energy measured at the origin remains relatively large.

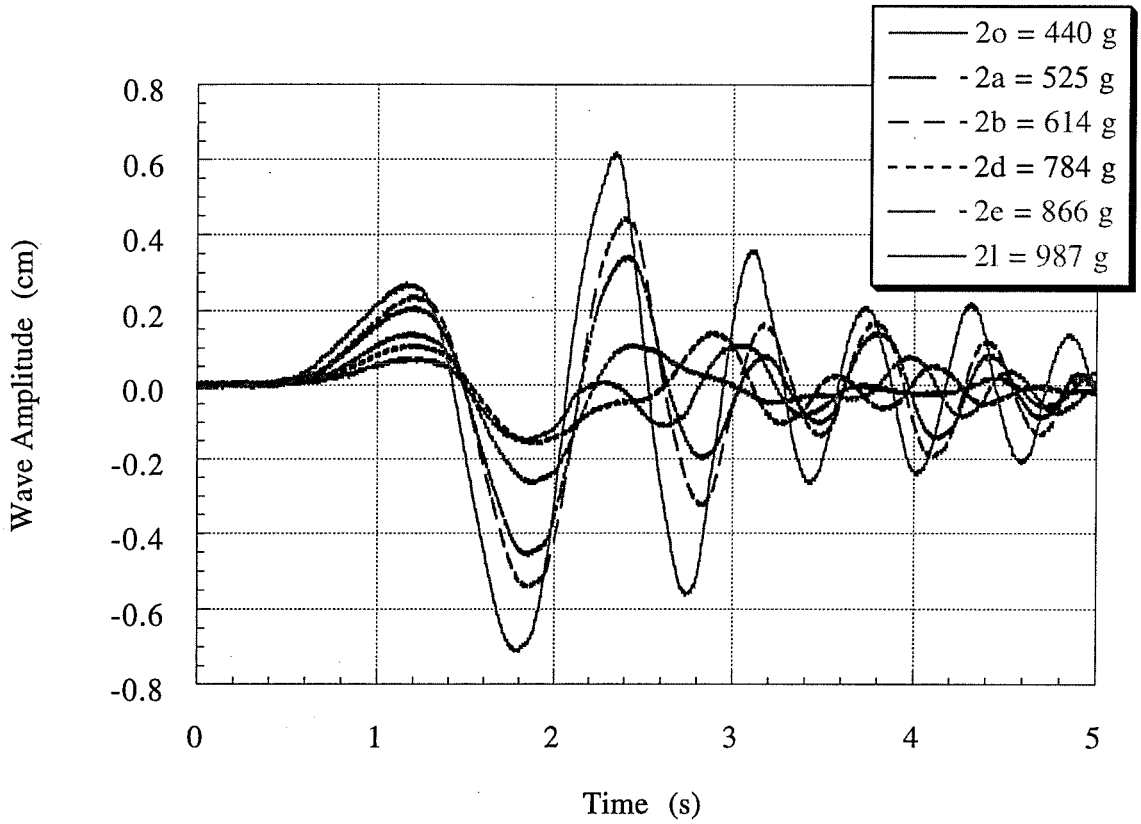

Figure 5.32: Comparison of six far-field wave records obtained at x/h=4.25 in the constant depth channel. Different density blocks were released from rest with an initial submergence of d=74 mm. The far-field maximum Airy wave amplitude depends on the block 2 density.

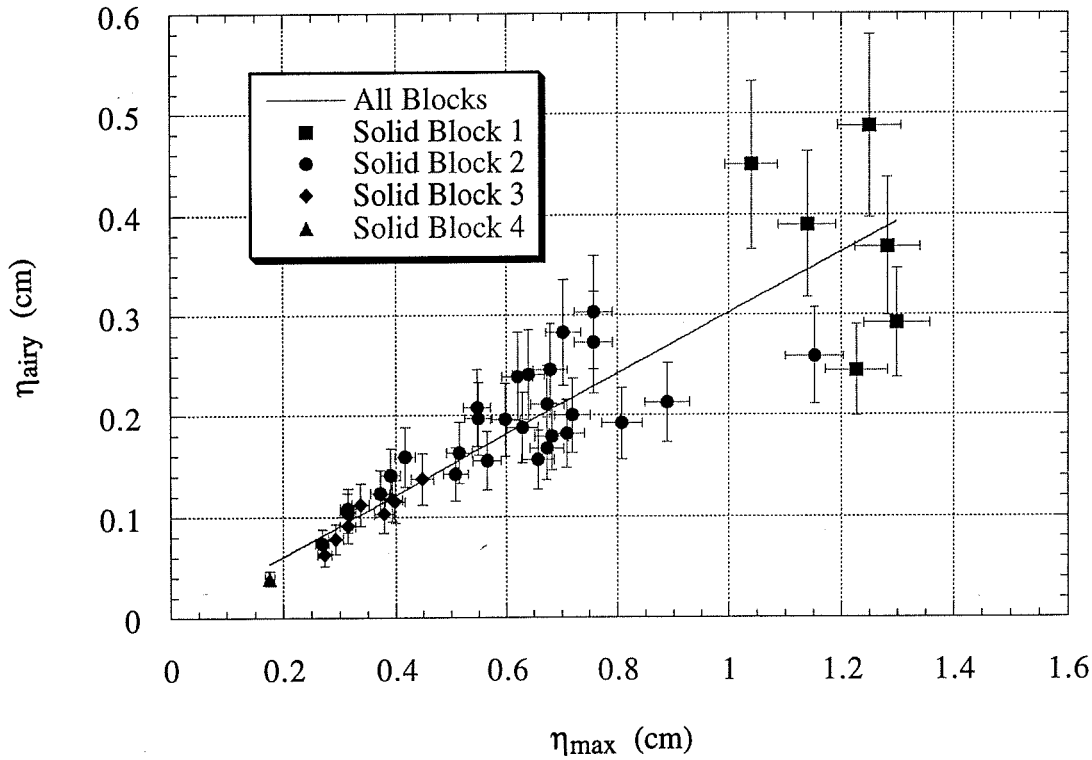

Figure 5.33: Maximum near-field wave amplitude correlation with Airy wave maximum measured 4.25 channel depths from x=0. The linear least-squares correlation through the origin is given by equation (5.29).

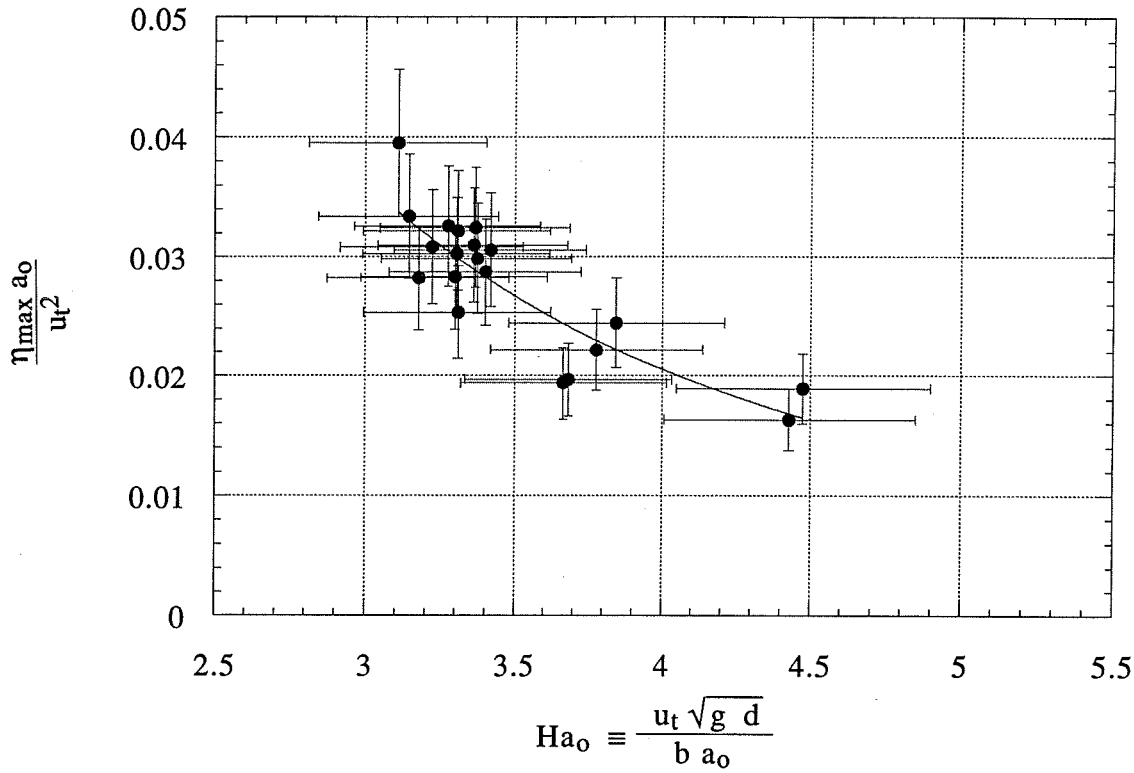

Figure 5.34: Wavemaker plot for solid blocks with d/b=0.85-87 on an incline at θ=45°. A power law least-squares curve fit of the data yields the exponent n=2.01 and the coefficient k=0.33 given by equation (5.31). The wavemaker curve is defined in this figure by changes in block density while Coulombic friction remains constant.

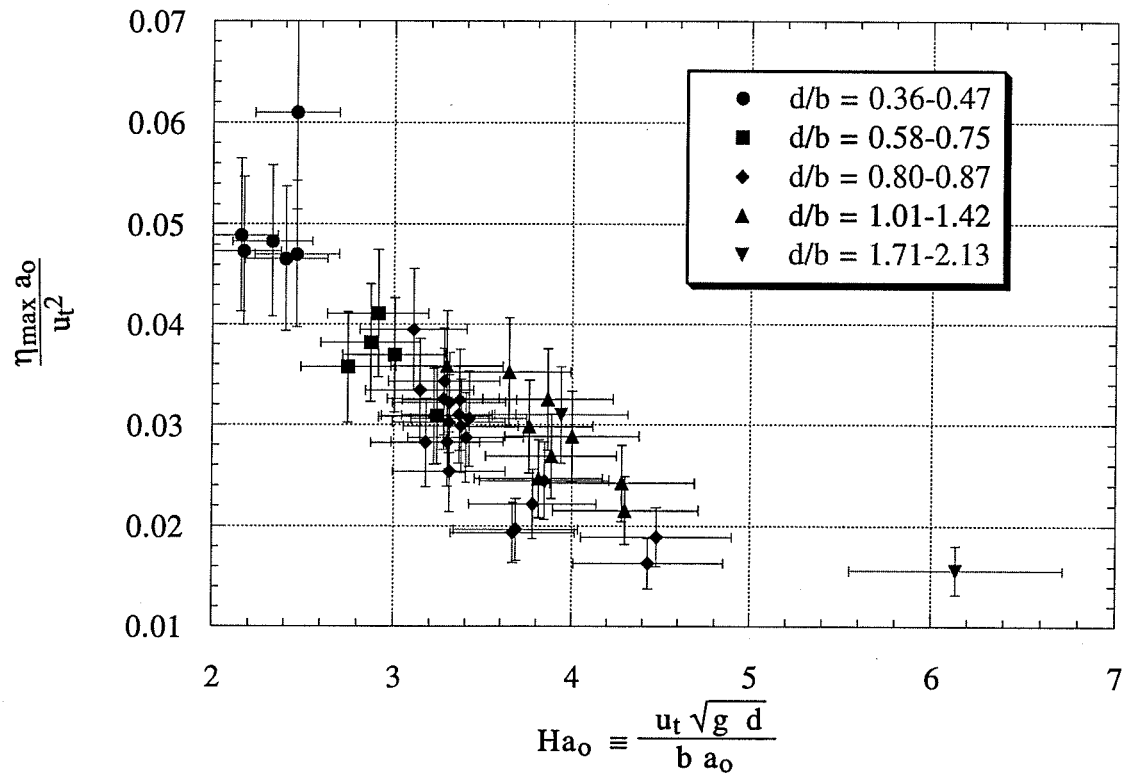

Figure 5.35: Wavemaker plot for solid blocks over a wide range of nondimensional submergences d/b on an incline with θ=45°. The data are organized into families of wavemaker curves depending on the value of d/b. All solid block trials analyzed in this work are presented on this figure.

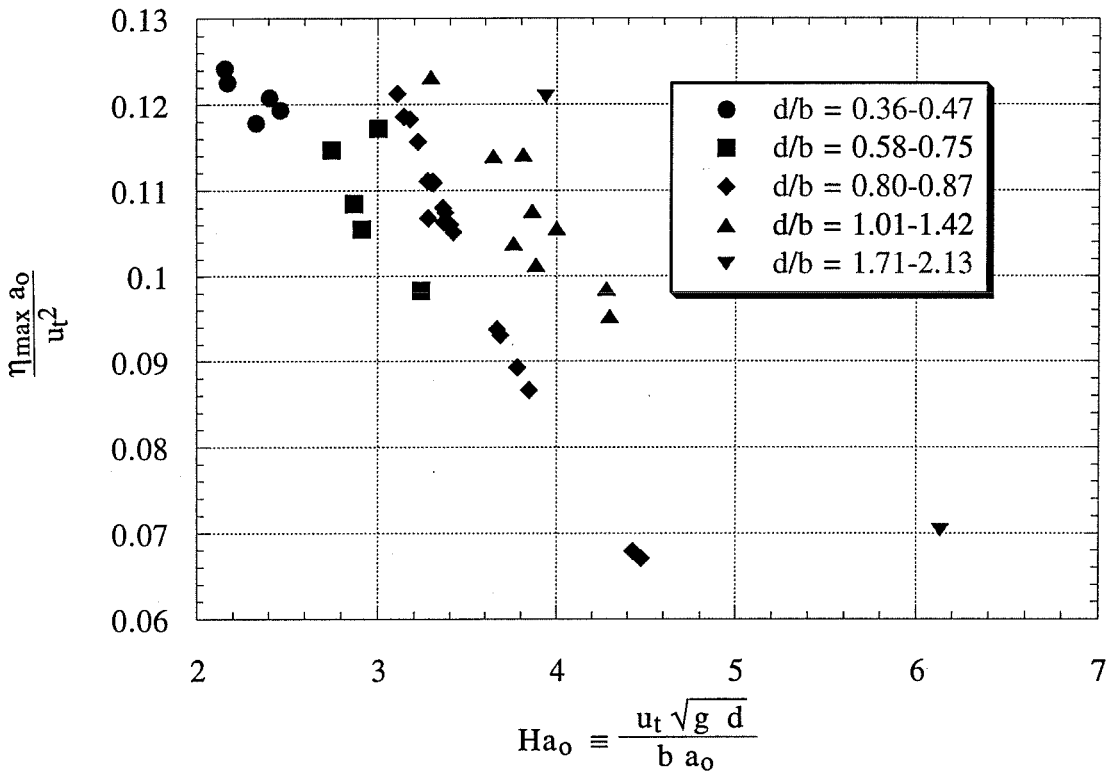

Figure 5.36: Approximate linear theory wavemaker data based on the actual landslide initial geometry and motion of all solid block trials shown in Figure 5.35. The families of wavemaker curves are more evident. The predicted nondimensional wave amplitudes are about three times too large.

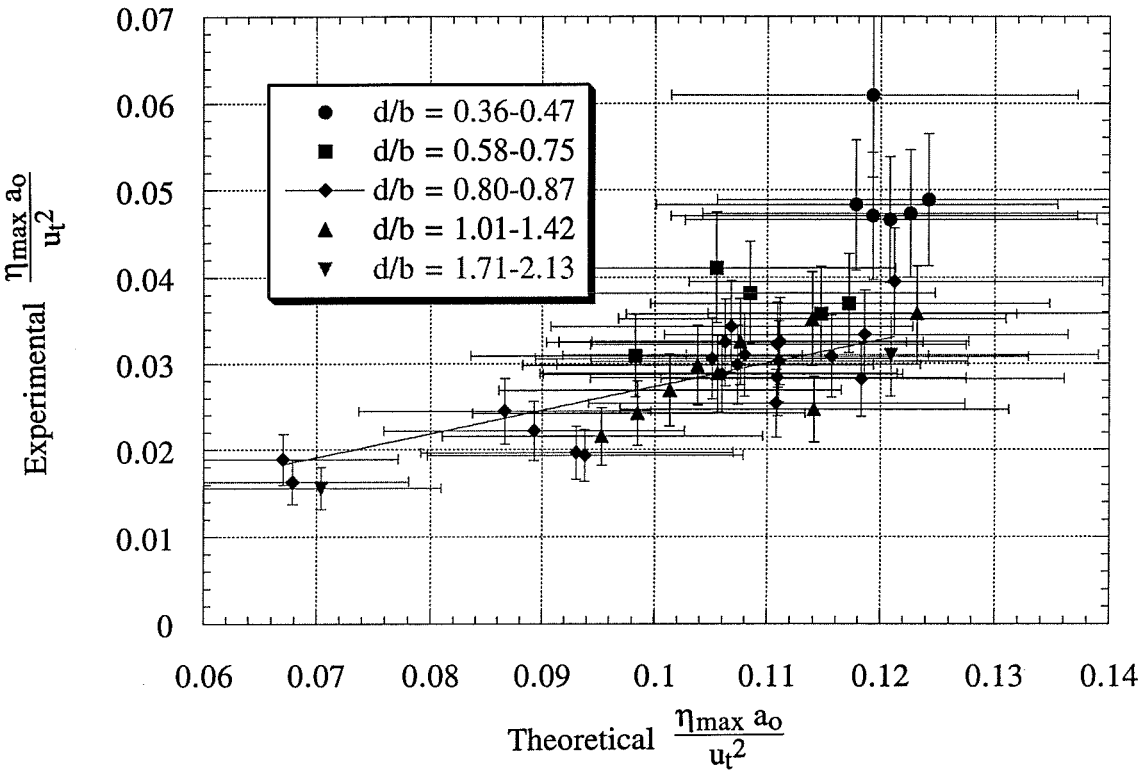

Figure 5.37: Correlation between linear theory predictions of the nondimensional maximum near-field wave amplitude and measured experimental values of the nondimensional maximum near-field wave amplitude. The linear curve fit through the origin for 0.80<d/b<0.87 is given by equation (5.32).

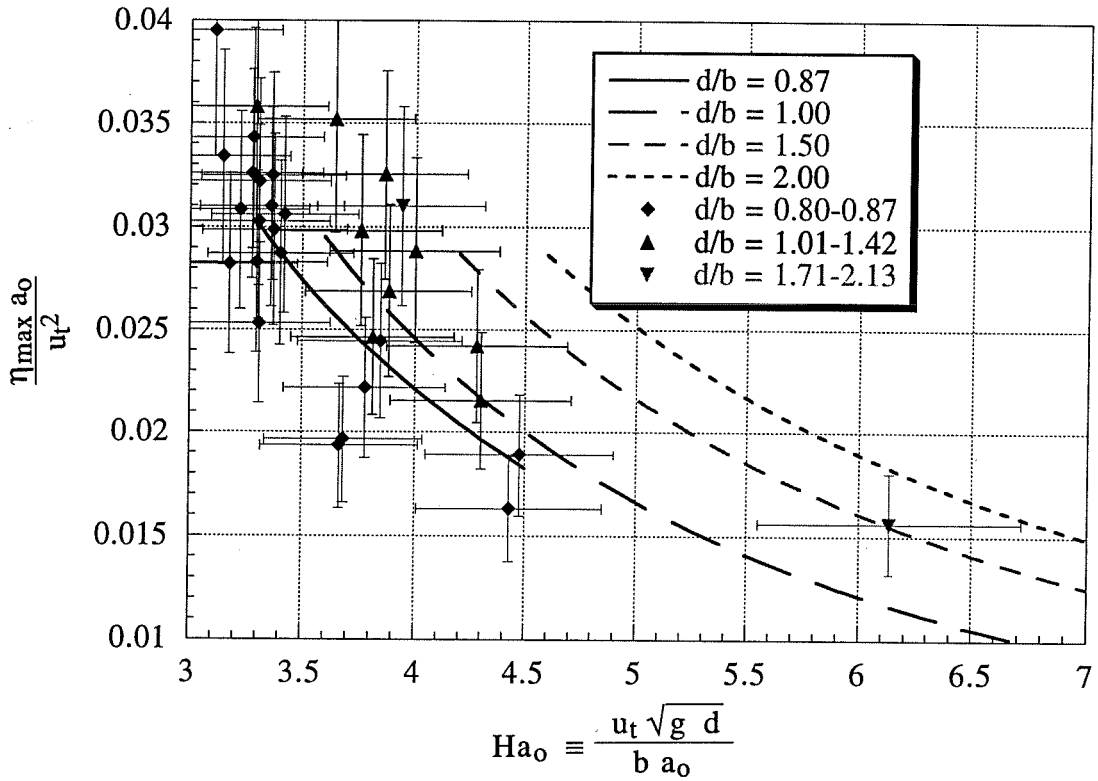

Figure 5.38: Comparison of corrected linear theory wavemaker curves and experimental results expected to generate linear water waves. Most experimental results are within one standard deviation of the appropriate wavemaker curve. The power law curve fits of the linear theory wavemaker curves cease to be valid above η_{max}/s_o of about 0.03.

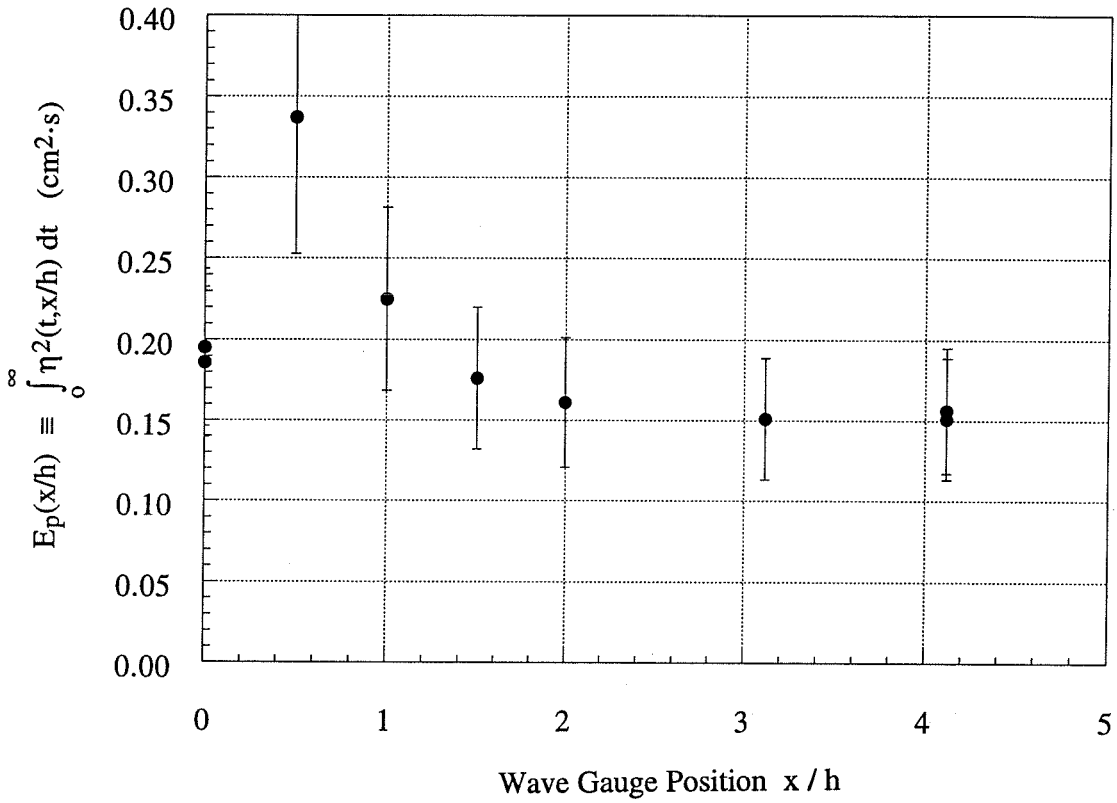

Figure 5.39: Distribution of the energy integral E_p with distance x/h. The energy integral is proportional to the total wave potential energy passing through a given location. The peak near x/h≈0.5 is induced by the large trough shown in Figure 5.27 at x/b≈2. Far away from the wave generation region, the energy integral E_p has a constant value.

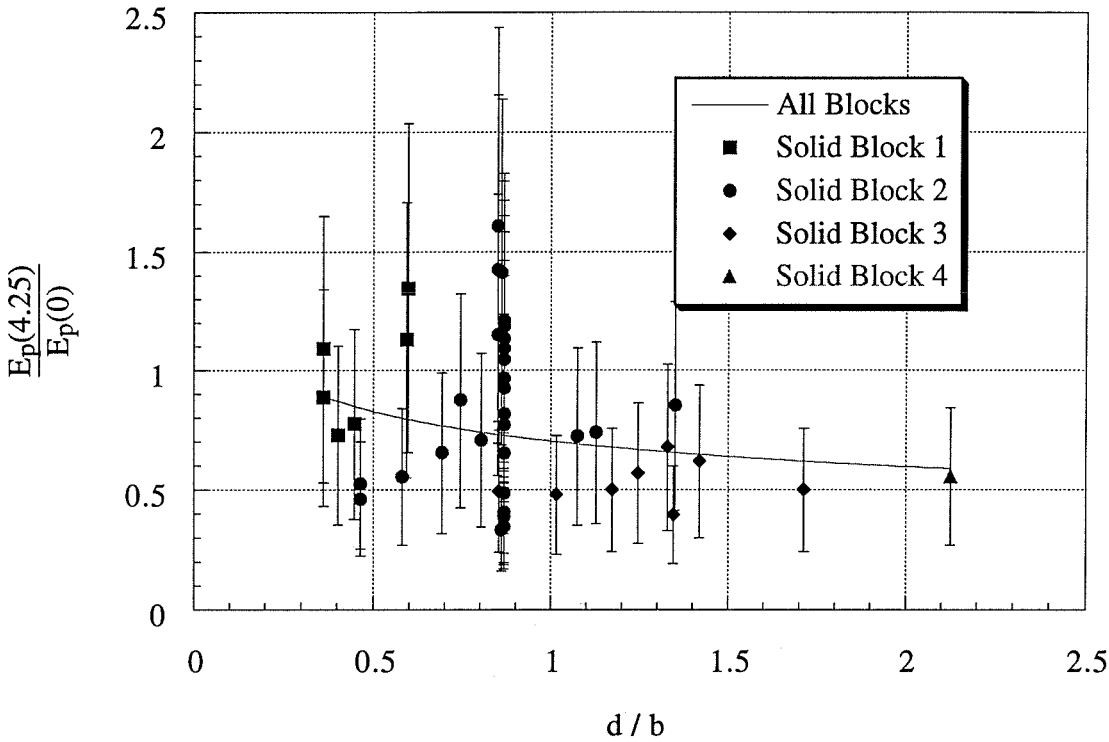

Figure 5.40: Ratio of the far-field energy integral $E_p(4.25)$ to the near-field energy integral $E_p(0)$ as a function of nondimensional initial submergence. The initial submergence is a measure of wave nonlinearity and alters the interaction of waves with the incline. More energy escapes the incline with decreasing initial submergence.

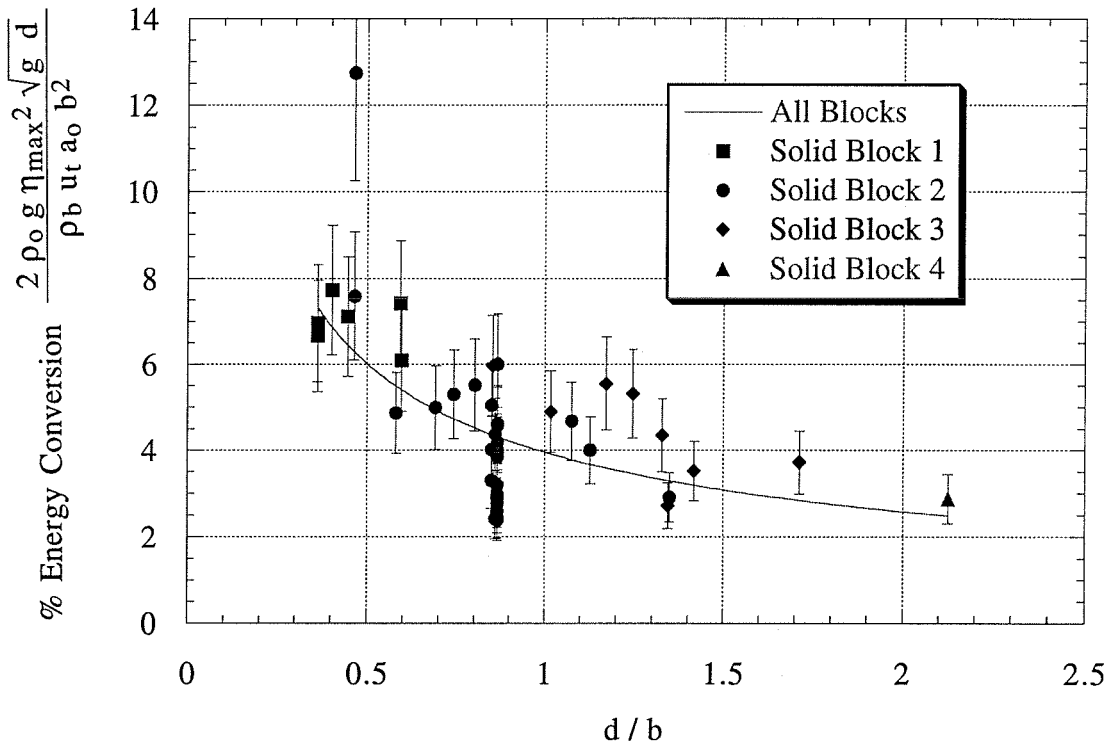

Figure 5.41: Characteristic conversion of solid block kinetic energy into wave potential energy. The power law least-squares curve fit is provided in equation (5.46). Most solid block landslides convert between 3-7% of their ultimate kinetic energy into wave potential energy that propagates down the channel.

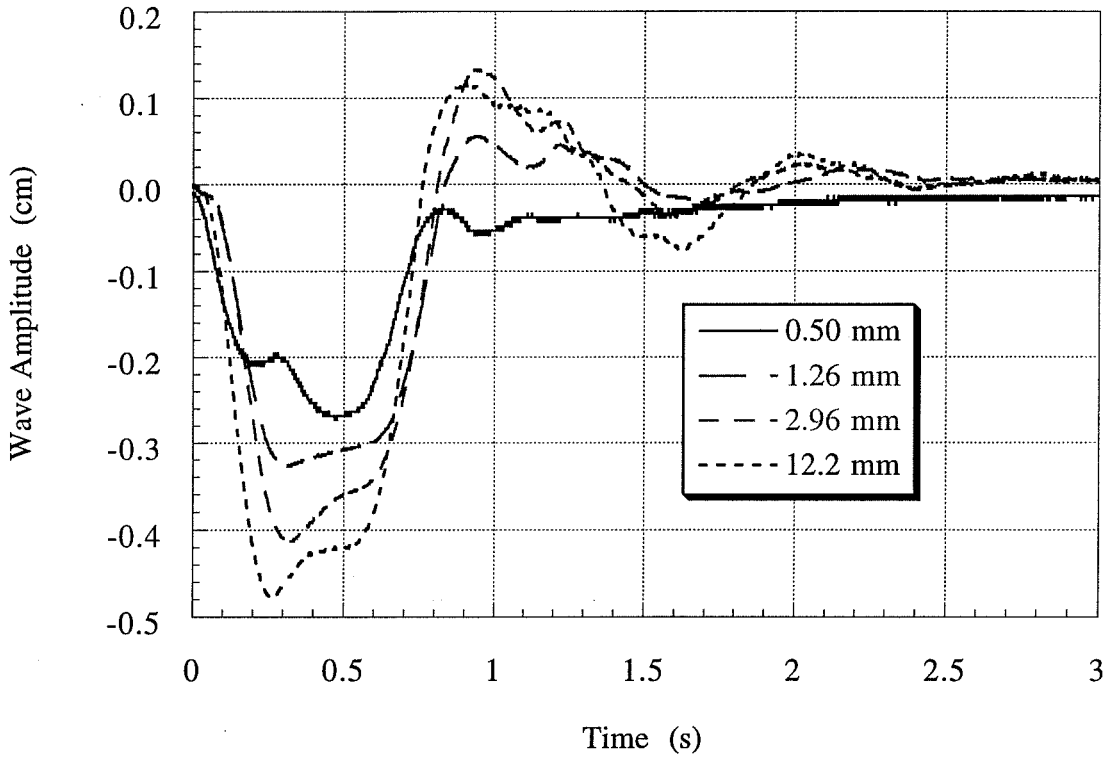

Figure 5.42: Four near-field wave records of material landslides involving different diameter glass spheres. Materials composed of larger spheres generated larger waves even though the suspension densities were nearly identical. Both centers of mass motion and initial rates of deformation varied for all four landslides.

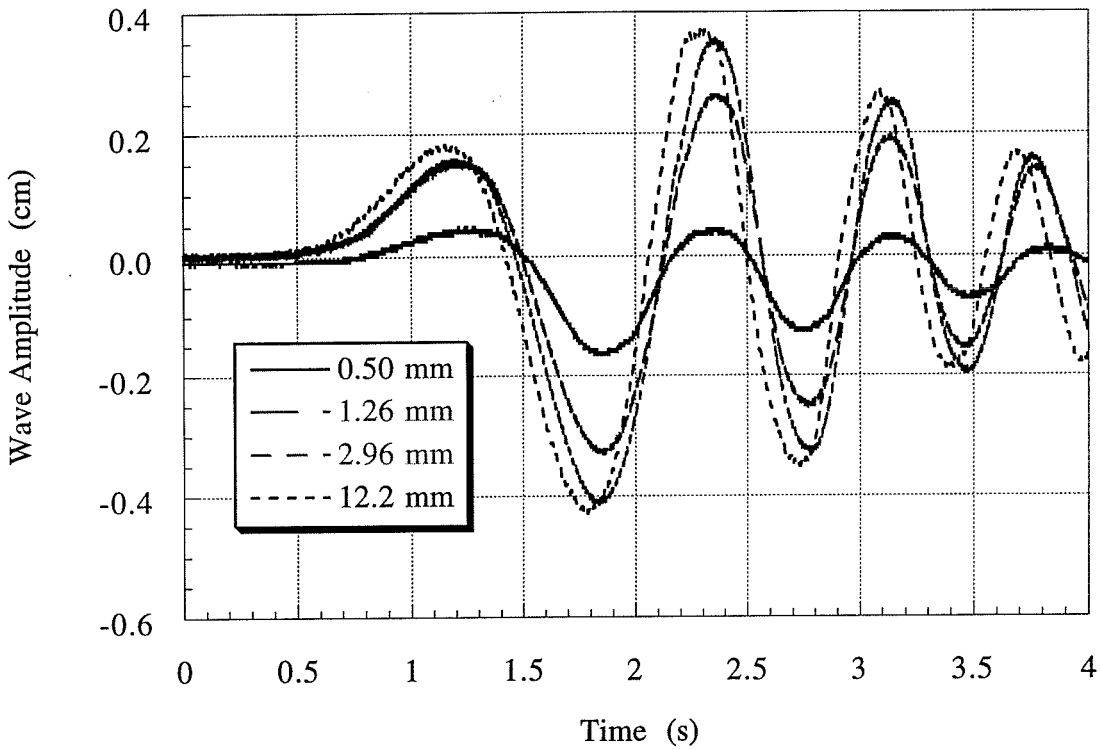

Figure 5.43: Far-field wave records of the same material landslides shown in Figure 5.42. Materials composed of larger spheres typically generated larger waves. The appearance of waves generated by material landslides is very similar to those generated by solid block landslides.

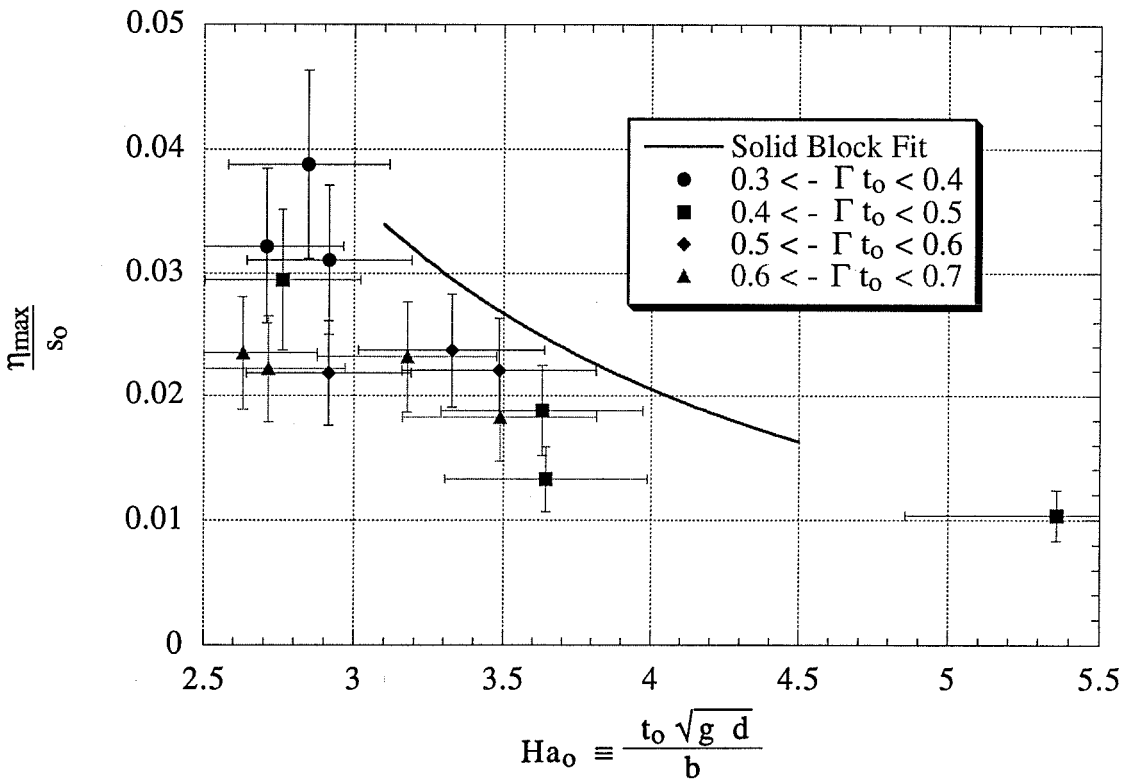

Figure 5.44: Wavemaker data of deforming material landslides with initial submergences d/b=0.88-0.90. The material landslides are characterized by their nondimensional landslide deformation Γt_o. Rapidly deforming landslides can reduce nondimensional wave amplitudes to half of solid block wave amplitudes.

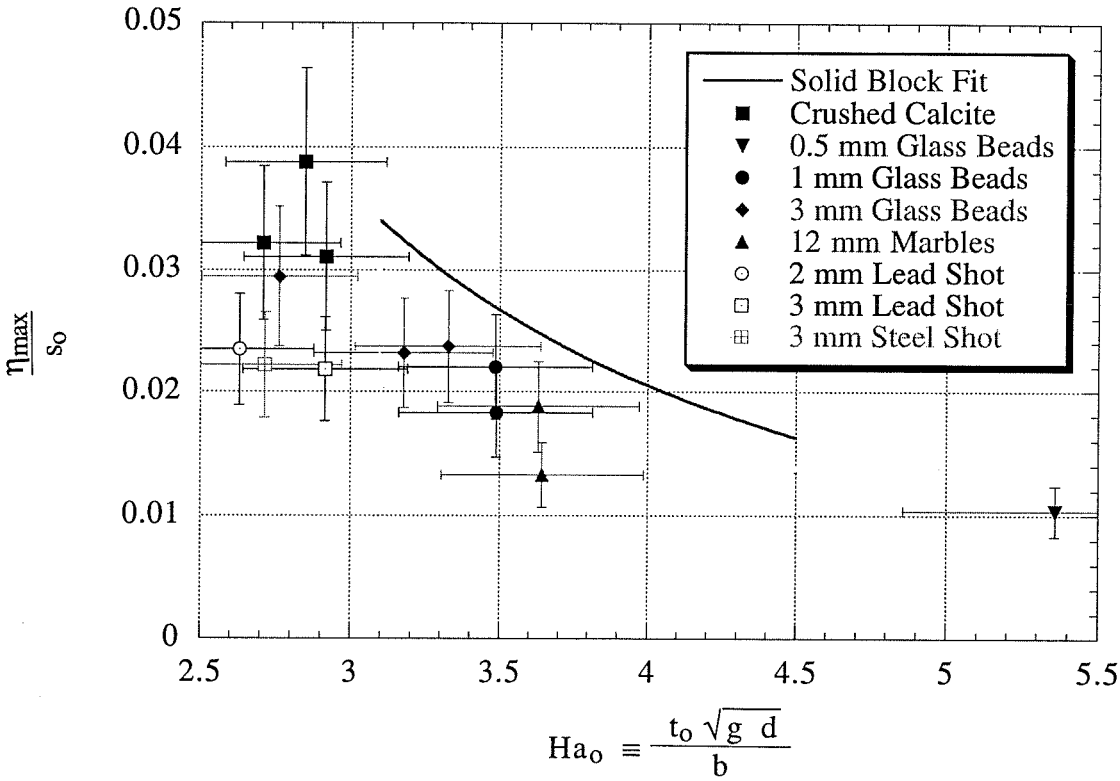

Figure 5.45: Same wavemaker data as Figure 5.44 of deforming material landslides with initial submergences d/b=0.88-0.90. Material landslides involving identical materials can cover a wide range of Hammack numbers and nondimensional wave amplitudes. The absolute size of the 1 mm glass bead landslides varies significantly.

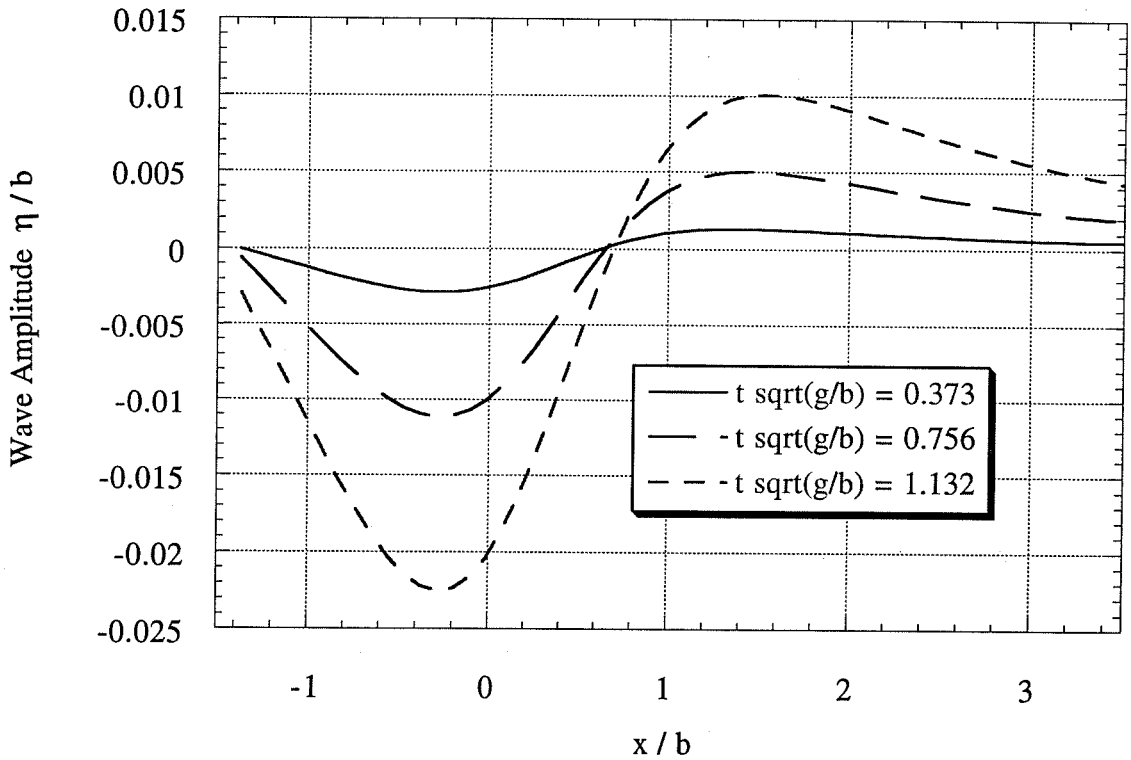

Figure 5.46: Simulated wave profiles at three different nondimensional times early in the wave generation process. The origin x/b=0 is located above the middle of the initial solid block position. The intersection of the incline and the still water level is at x/b=-1.37. The nondimensional solid block size is unity. Positive wave generation is clear.

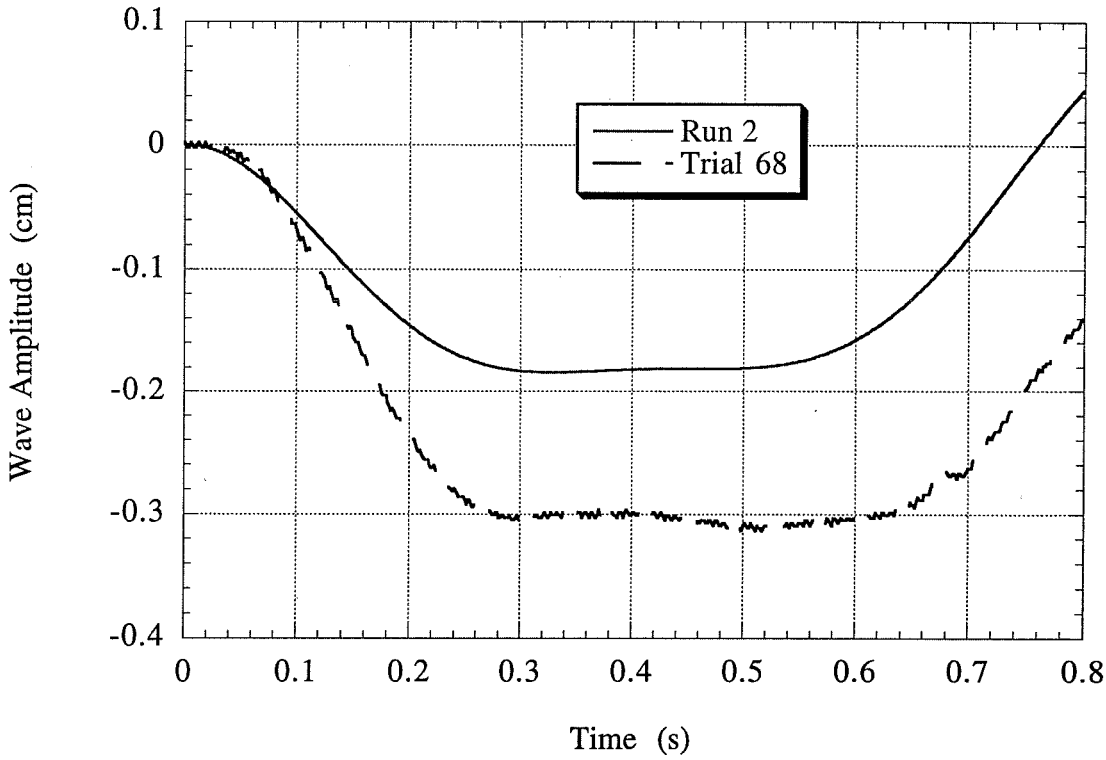

Figure 5.47: Comparison of simulated wave record with corresponding solid block landslide wave record. The two wave records agree up to about 0.1 s but then diverge until about 0.3 s. The form of the simulated wave record is correct although the amplitude is too small by a factor of about 1.7.

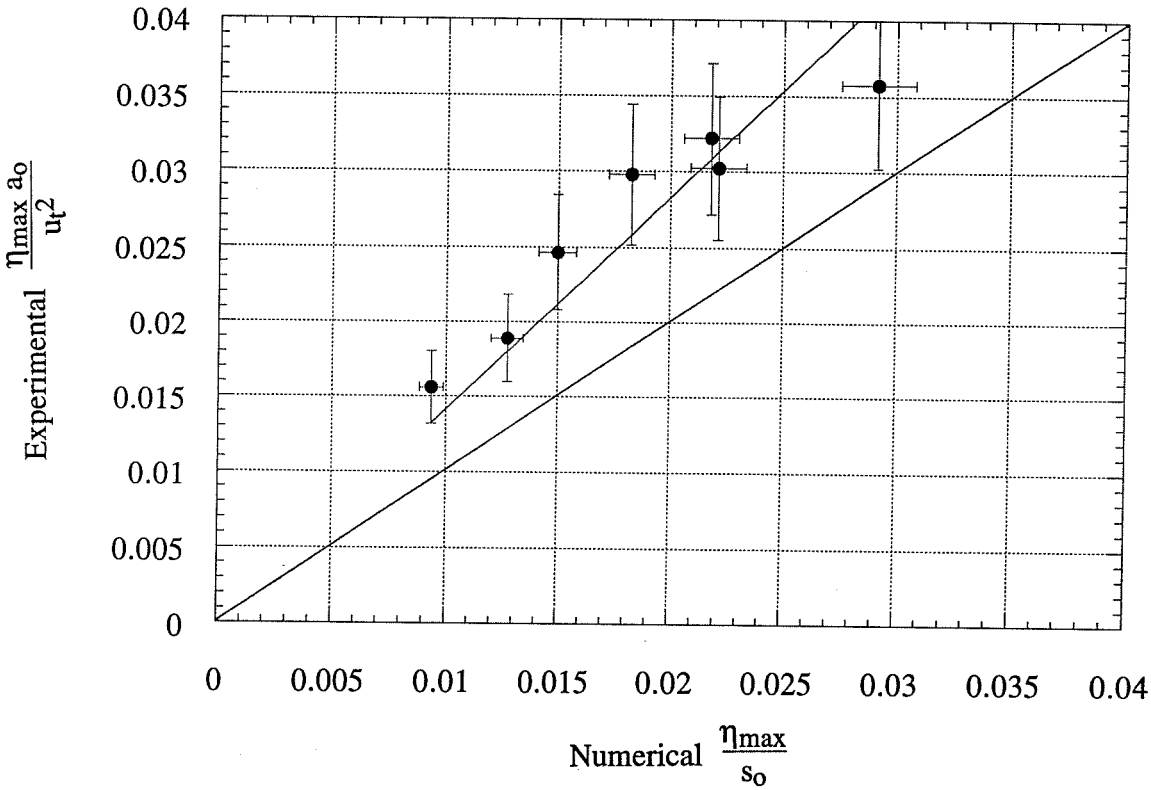

Figure 5.48: Comparison of simulated nondimensional maximum near-field wave amplitudes with corresponding experimental results. Experimental results are consistently larger by about 40%. The inviscid simulations could not produce separation and therefore had a different pressure distribution over the block surface.

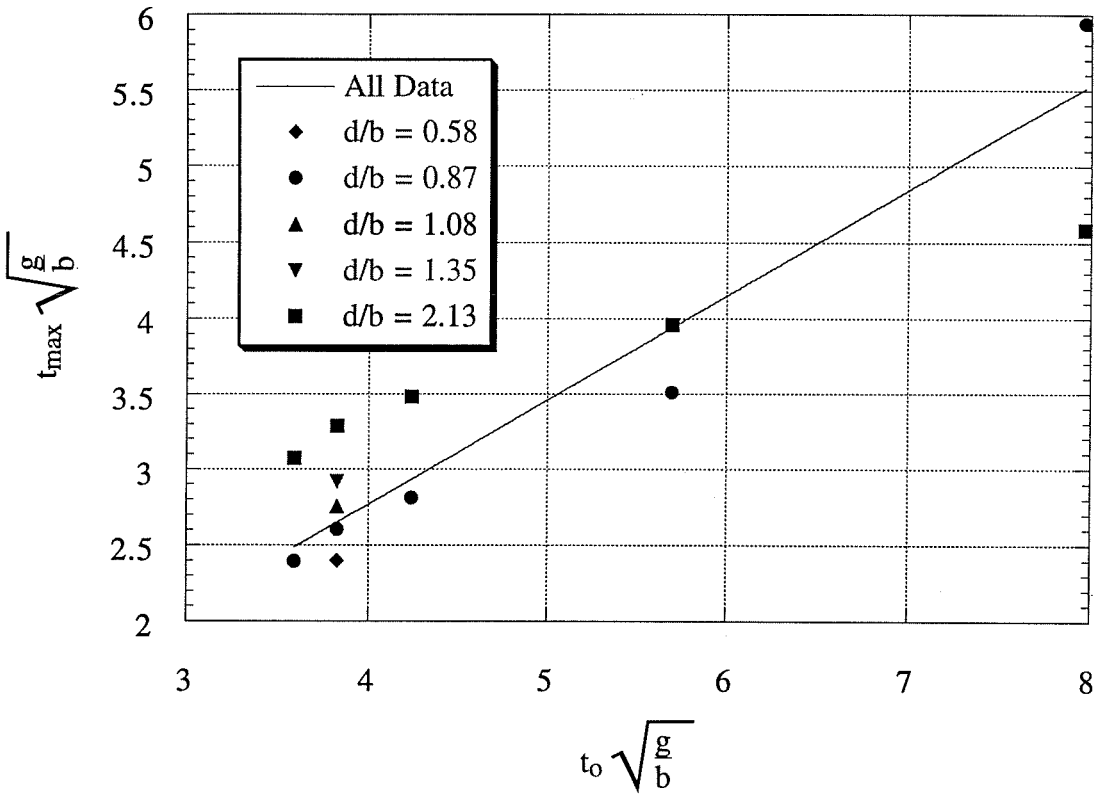

Figure 5.49: Correlation between the simulated nondimensional characteristic time of solid block motion and the nondimensional occurrence of the maximum near-field wave amplitude. Some of the variability is due to the different initial geometries of the simulations. All incline angles were fixed at 45°.

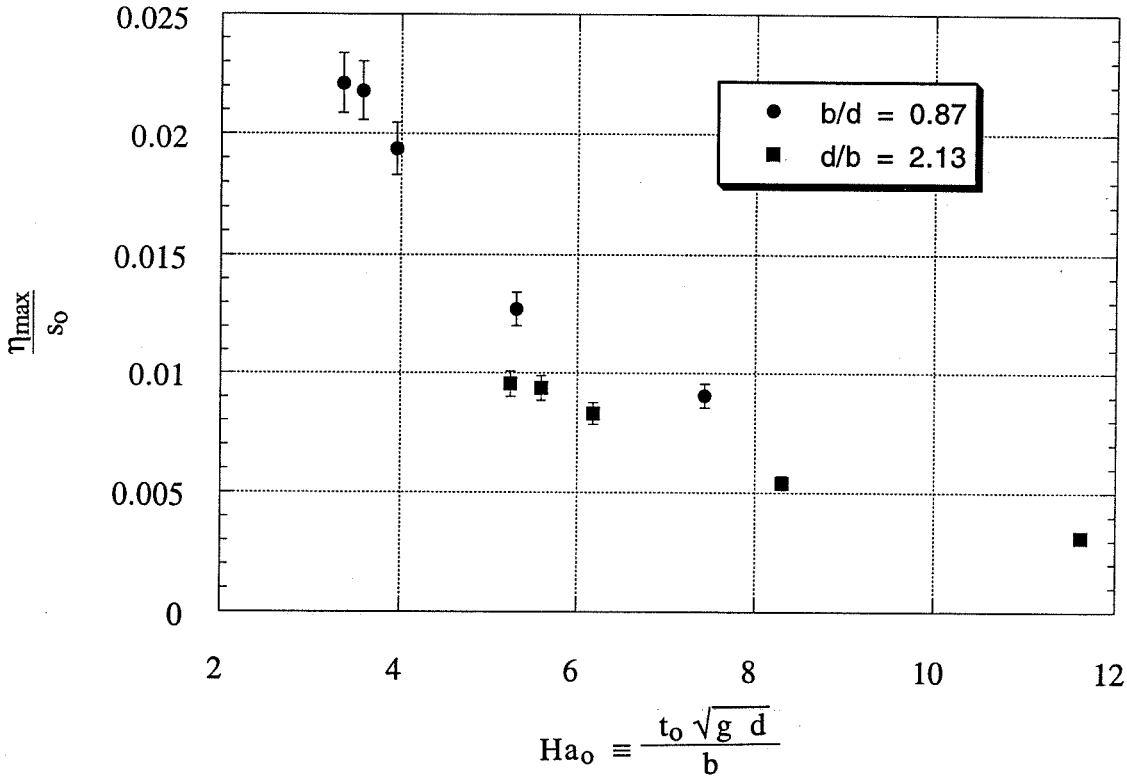

Figure 5.50: Wavemaker data depicting two simulated wavemaker curves are shown for solid block landslides at two different initial submergences along an incline at 45°. Values for $Ha_{o.min}$ are evident from the inflection points in the wavemaker curves and are in agreement with the values inferred from approximate linear theory wavemaker data.

Chapter 6

6. Summary and Conclusions

This chapter summarizes the thesis results, restates the major conclusions, and describes some future research considerations.

6.1 Summary

The goal of this thesis is to be able to predict water wave amplitudes above an underwater landslide. Of particular concern has been the damage potential of water waves generated by underwater landslides. A review of the underwater landslide literature showed the wide variety of sizes and circumstances associated with landslide occurrence and wave generation. It was argued in Section 1.1 that a steep incline would be needed to study laboratory scale landslides so a single incline angle $\theta=45^\circ$ was chosen. A distinct separation of wave generation mechanisms was achieved by choosing two-dimensional landslides with a horizontal top face and a vertical front face. Underwater landslide motion was assumed to be governed by only one characteristic distance s_o and one characteristic time t_o in equation (3.1). A scaling analysis of the governing differential equations yielded the nondimensional form of a wavemaker curve provided in equation (3.21). An analysis of solid block motion revealed the analytical forms of the characteristics of landslide motion in equations (3.73) to (3.75). Experiments conducted on an incline at 45° from horizontal proved the existence of the nondimensional wavemaker curve for solid block landslides. The wavemaker curve was obtained by varying the mean block density for the same initial landslide submergence d/b=0.87. A power law curve fit of the data is given by equation (5.31). The approximate linear

wavemaker model result in equation (3.97) was shown to predict nondimensional wave amplitudes whenever d/b>0.8 on an incline 45° from horizontal after being multiplied by an empirical coefficient 0.273. In addition, far-field wave characteristics such as total wave train potential energy and conversion of solid block kinetic energy into wave potential energy were shown to scale with near-field wave characteristics whenever linear, deep water waves were generated by the landslide. The underwater landslides studied in this work converted between 2-8% of the kinetic energy acquired by a solid block into wave potential energy. The criterion to generate linear water waves when $Ha_o \gg 1$ is given by equation (5.34) while the criterion to have deep water waves in the far-field is given by equation (5.26). Numerical simulations covering a wide range of landslide densities and two nondimensional initial submergences provided a more complete picture of the water wave amplitudes generated by underwater landslides. The numerical simulations also provided minimum Hammack numbers $Ha_{o.min}$ above which power law wavemaker curves are valid. Experiments conducted with deforming material landslides revealed nondimensional wave amplitudes 50-90% smaller than those of solid block landslides with identical initial geometries and center of mass motions.

6.2 Conclusions

The unsteady motion of any underwater object that is governed by only one characteristic distance s_o and one characteristic time t_o generates water waves according to one of two wavemaker formalisms. Both formalisms are given by Hammack (1972) while the case of slow landslide motion relative to wave propagation is repeated here in Section 3.1.3. For the generation of two-dimensional water waves, a characteristic near-field wave amplitude can be expressed as an unknown function

$$\frac{\eta}{s_o \sin\theta} = \frac{1}{Ha_o} f\left(\frac{b}{d}, \theta, Sg, Ha_o\right) \tag{3.21}$$

where the Hammack number $Ha_o \equiv t_o\sqrt{gd}/b$ is the correct nondimensional time for water waves generated by underwater landslides and the Submergence number $Sg \equiv s_o \sin\theta/d$ relates the vertical component of the characteristic distance of motion to the initial landslide submergence.

Two characteristic wave amplitudes are given particular attention in this work. The maximum near-field wave amplitude is the absolute value of the largest wave amplitude

measured above the initial landslide position at x/b=0. The maximum Airy wave amplitude is the maximum amplitude of the leading wave in the wave train at x/h=4.25. It was decided to construct wavemaker curves based on the maximum near-field wave amplitude.

Two criteria are given for the generation of linear deep water waves by an underwater landslide. These linearity criteria are $Ha_o \gg 1$ and

$$\frac{d}{b} \gg \frac{u_t \sin\theta}{\sqrt{g\,d}} \quad . \tag{5.34}$$

Underwater landslides satisfying these criteria generate water waves with significantly simpler wave behavior. For linear water waves, the maximum Airy wave amplitude is directly proportional to the maximum near-field wave amplitude as shown in Figure 5.33. Most water waves generated by underwater landslides studied herein were linear water waves. Equation (5.34) scales with landslide length raised to an exponent of half $\ell^{0.5}$.

The near-field water waves recorded at x/b=0 all appeared very similar: the free surface formed a relatively large negative wave followed by a free surface rebound with decaying oscillations. In the far-field at x/h=4.25, the wave front consisted of a leading Airy wave followed by a dispersive wave train of modulated wave amplitude. Far-field wave propagation was shown to exist when x/h>2.5 or $x/\lambda>3$. For linear water waves generated on a 45° incline, the maximum Airy wave amplitude

$$\eta_{airy}(x/h) \approx 0.48\,\eta_{max}\left(\frac{h}{x}\right)^{1/3} \tag{5.30}$$

can be predicted any distance down a constant depth channel. The Airy wave always propagates as a long wave at the long wave celerity. The remaining wave train propagates as deep water waves if the channel depth satisfies

$$h > t_o\sqrt{g\,d} \tag{5.26}$$

where $\lambda=t_o\sqrt{g\,d}$ is a characteristic wavelength of water waves generated by underwater landslides. Much of the wave train propagates as long waves if the channel depth satisfies the criterion

$$h < \frac{t_o \sqrt{g\,d}}{10} \,. \tag{5.27}$$

The leading Airy wave in the far-field wave train propagates at the long wave celerity and therefore always depends on the channel depth.

Experimental maximum near-field wave amplitudes measured at x/b=0 above solid block landslides sliding down a 45° incline confirmed the existence of nondimensional wavemaker curves in Figures 5.34 and 5.35 as a function of the nondimensional initial submergence and of the Hammack number Ha_o. For θ=45° and d/b=0.87, a power law curve fit of the experimental data gave

$$\frac{\eta_{max}}{s_o} = \frac{0.33}{Ha_o^{2.01}} \tag{5.31}$$

where the factor sinθ in equation (3.21) was omitted. Maximum near-field wave amplitudes of solid block landslides can be predicted from a wavemaker curve if the landslide initial geometry, initial acceleration and terminal velocity are known.

Equations (5.40) and (5.41) show that an analytical form of the wavemaker curve allows absolute wave amplitudes to be predicted above a solid block landslide provided $Ha_o > Ha_{o.min}$. Results from Sections 5.2.3 and 5.2.5 suggest a typical exponent n≈1.5 for solid block landslides on an incline at 45°. If this exponent can be generalized to different incline angles, then a scaling for water wave amplitudes generated by underwater landslides is obtained. For a vanishing dynamic friction coefficient $C_n \approx 0$ and $Ha_o > Ha_{o.min}$, equations (3.73), (3.74) and (5.23) provide a maximum near-field wave amplitude that is proportional to

$$\eta_{max} \propto \frac{\ell^{1.75} \sin^{1.75}\theta \cos^{1.5}\theta}{d^{0.75}} \propto \frac{c^{1.75}}{d^{0.75}} \tag{6.1}$$

where ℓ is the landslide length along the incline, d is the initial landslide submergence, and $c \equiv \ell \sin\theta$ is the height of the vertical front face of the landslide.

Numerical simulations of water waves generated by underwater landslides were conducted with a fully nonlinear inviscid boundary element code. Figure 5.48 indicates

the agreement between numerical simulations and experimental results: water waves simulated by the BEM code are typically 30% smaller than experimental results. Wavemaker data were constructed from simulation results for nondimensional initial submergences d/b=0.87 and d/b=2.13. A power law wavemaker curve was shown to apply only if $Ha_o>3.5$ when d/b=0.87 and $Ha_o>5.5$ when d/b=2.13.

An approximate solution of linear near-field water waves generated by a solid block landslide is provided by equation (3.97). Figure 5.37 shows that the linear water wave solution can be used to predict maximum near-field wave amplitudes that are proportional

$$\text{Experimental } \frac{\eta_{max}}{s_o} \approx 0.273 \text{ Theoretical } \frac{\eta_{max}}{s_o} \tag{5.32}$$

to experimental wave amplitudes provided linear water waves are generated.

Initially triangular material landslides deformed in a manner very similar to a spreading isosceles triangle at early times. The initial rate of change of area in time depended most strongly on the nominal particle diameter. The initial normal rate of strain depended primarily on the bulk density of the landslide. The initial landslide rate of deformation is calculated from

$$\Gamma \equiv \frac{d\alpha}{dt} = \frac{1}{\frac{A}{9\,z_c^2} + \frac{9\,z_c^2}{A}} \left[\frac{2}{z_c}\frac{dz_c}{dt} - \frac{1}{A}\frac{dA}{dt} \right] \tag{3.85}$$

and combined with the characteristic time of center of mass motion to give a new nondimensional number in the wavemaker formalism Γt_o. The nondimensional landslide deformation Γt_o is a measure of the isosceles triangle spreading during the characteristic time of center of mass motion.

As a gravity current developed, multiple wave events were observed superposed on the gravity current head with larger wave events traveling faster down the incline. A material landslide composed of 0.5 mm glass beads was observed to form a leading shock wave rather than the usual gravity current head.

Material landslides and solid block landslides generate similar wave records with similar nondimensional wave amplitudes. For an identical initial geometry and center of mass motion, solid block landslides have larger nondimensional wave amplitudes than deforming material landslides. Figures 5.44 and 5.45 show that nondimensional wave amplitudes generated by deforming material landslides range from 0.5-0.9 times the nondimensional wave amplitudes generated by solid block landslides. Material landslides with larger nondimensional landslide deformations tend to produce smaller nondimensional wave amplitudes for a given initial geometry and center of mass motion.

6.3 Future Research Considerations

Two future research directions are being considered at this moment. The first direction involves further numerical simulations of water waves generated by underwater landslides. The boundary element code used in this work can be further refined for studies of underwater landslide-generated waves. For example, landslide shapes that are not susceptible to flow separation could be simulated. Also, a more complete analysis of the wavemaker parameters can be carried out. A viscous, finite volume, fluid dynamics code can also be employed to study water waves generated by partially aerial landslides or underwater landslides with very small initial submergences. Lagrangian free surface updating in a finite volume code enables the wave breaking expected during such landslides to be simulated. Therefore, highly nonlinear water waves generated by underwater landslides can be studied. Viscous simulations would allow for more accurate near-field wave amplitude predictions over a wider variety of initial conditions.

The second research direction involves the dynamics of underwater landslides. A wide range of landslide phenomena were observed in the course of studying water wave generation for this work. The initiation, propagation and deposition of an underwater landslide appears to provide ample research opportunities covering the entire gamut of experimental, theoretical, and computer based fundamental research.

References

Bagnold, R. A. Experiments on a Gravity-Free Dispersion of Large Solid Spheres in a Newtonian Fluid Under Shear. Proc. Royal Society London, Vol. 225A, pp. 49-63, (1954).

Bak, P. Self-Organized Criticality and Gaia. Thinking About Biology, edited by Stein, W. D. and Varela, F. J., Addison-Wesley, pp. 255-268, (1993).

Bjerrum, L. Subaqueous Slope Failures in Norwegian Fjords. Norwegian Geotechnical Institute Bulletin, No. 88, pp. 1-8, (1971).

Bonnecaze, R. T., Huppert, H. E., Lister, J. R. Particle-Driven Gravity Currents. Journal of Fluid Mechanics, Vol. 250, pp. 339-369, (1993).

Bornhold, B. D., Ren, P., Prior, D. B. High-Frequency Turbidity Currents in British Columbia Fjords. Geo-Marine Letters, Vol. 14, pp. 238-243, (1994).

Brady, J. F. The Rheological Behavior of Concentrated Colloidal Dispersions. Journal of Chem. Phys., Vol. 99, No. 1, pp. 567-581, (1993).

Brennen, C. E. Cavitation and Bubble Dynamics. Oxford University Press, (1995).

Britter, R. E., Linden, P. F. The Motion of the Front of a Gravity Current Traveling Down an Incline. Journal of Fluid Mechanics, Vol. 99, pp. 531-543, (1980).

Buckingham, E. On Physically Similar Systems. Physical Review, Vol. 4, pp. 354-376, (1914).

Campbell and Associates. Report of a Seafloor Instability at Skagway, Alaska. Contact P, N & D Inc., North America phone number (907) 561-1011, (1995).

Campbell, C. S., Cleary, P. W., Hopkins, M. Large-Scale Landslide Simulations: Global Deformation, Velocities and Basal Friction. Journal of Geophysical Research, Vol. 100, No. B5, pp. 8267-8283, (1995).

Chester, C., Friedman, B., Ursell, F. An Extension of the Method of Steepest Descent. Proc. Cambridge Phil. Soc., Vol. 53, Part 3, pp. 599-611, July, (1957).

Cornforth, D. H., Landslide Technology. The 1994 Submarine Slope Failure at Skagway, Alaska. Contact the State of Alaska, Department of Transportation and Public Facilities, North America phone number (907) 465-1763, (1995).

Das, M. M., Wiegel, R. L. Water Waves Generated by Horizontal Motion of a Vertical Wall. University of California at Berkeley, Hydraulic Engineering Laboratory, HEL 16-7, (1971).

Dean, R. G., Dalrymple, R. A. Water Wave Mechanics for Engineers and Scientists. World Scientific, (1991).

Gardner-Taggart, J. M., Barminski, R. F. Short Period Wave Generation in Moss Landing Harbor Caused by Offshore Landslides Induced by the Loma Prieta Earthquake. Geophysical Research Letters, Vol. 18, No. 7, pp. 1277-1280, July, (1991).

Goda, Y., Ippen, A. T. Theoretical and Experimental Investigation of Wave Energy Dissipation Composed of Wire Mesh Screens. Massachusetts Institute of Technology, Department of Civil Engineering, Report No. 60, August, (1963).

Grantz, A., Plafker, G., Kachadoorian, R. Alaska's Good Friday Earthquake, March 27, 1964. U.S. Geological Survey Circular 491, (1964).

Greene, H. G., Gardner-Taggart, J. M., Ledbetter, M. T., Barminski, R. F., Chase, T. E., Hicks, K. R., Baxter, C. Offshore and Onshore Liquefaction at Moss Landing Spit, Central California -- Result of the October 17, 1989, Loma Prieta Earthquake. Geology, Vol. 19, pp. 945-949, September (1991).

Grilli, S. T., Skourup, J., Svendsen, I. A. An Efficient Boundary Element Method for Nonlinear Water Waves. Engineering Analysis with Boundary Elements, Vol. 6, No. 2, pp. 97-107, (1989).

Grilli, S. T., Losada, M. A., Martin, F. Characteristics of Solitary Wave Breaking Induced by Breakwaters. ASCE Journal of Waterway, Port, Coastal, and Ocean Engineering, Vol. 120, No. 1, pp. 74-92, (1994a).

Grilli, S. T., Subramanya, R., Svendsen, I. A., Veeramony, J. Shoaling of Solitary Waves on Plane Beaches. ASCE Journal of Waterway, Port, Coastal, and Ocean Engineering, Vol. 120, No. 6, pp. 609-628, (1994b).

Grilli, S. T., Subramanya, R. Quasi-Singular Integrals in the Modeling of Nonlinear Water Waves in Shallow Water. Engineering Analysis with Boundary Elements, Vol. 13, pp. 181-191, (1994).

Hamilton, T. S., Wigen, S. O. The Foreslope Hills of the Fraser Delta: Implications for Tsunamis in Georgia Strait. Science of Tsunami Hazards, Vol. 5, pp. 15-33, (1987).

Hammack, J. L. Discussion. ASCE Journal of the Waterways, Harbors, and Coastal Engineering Division, Vol. 97, No. 2, May, pp. 417-423, (1971).

Hammack, J. L. Tsunamis - A Model of their Generation and Propagation. Ph.D. Thesis, California Institute of Technology, (1972).

Hammack, J. L. A Note on Tsunamis: Their Generation and Propagation in an Ocean of Uniform Depth. Journal of Fluid Mechanics, Vol. 60, pp. 769-799, (1973).

Hammack, J. L. Personal communication, (1996).

Harbitz, C. B. Model Simulations of Tsunamis Generated by the Storegga Slides. Marine Geology, Vol. 105, pp. 1-21, (1992).

Heezen, B. C., Ewing, M. Turbidity Currents and Submarine Slumps, and the 1929 Grand Banks Earthquake. American Journal of Science, Vol. 250, pp. 849-873, December, (1952).

Heinrich, P. Nonlinear Water Waves Generated by Submarine and Aerial Landslides. ASCE Journal of Waterway, Port, Coastal, and Ocean Engineering, Vol. 118, No. 3, pp. 249-266, (1992).

Hoerner, S. F. Fluid-Dynamic Drag. Published by the Author, (1965).

Hughes, S. A. Physical Models and Laboratory Techniques in Coastal Engineering. World Scientific, (1993).

Inman, D. L. Areal and Seasonal Variations in Beach and Nearshore Sediments at La Jolla, California. Department of the Army, Corps of Engineers, Beach Erosion Board, Technical Memorandum No. 39, (1953).

Ippen, A. T., Harleman, D. R. F. Steady-State Characteristics of Subsurface Flow. Gravity Waves: Proceedings of the NBS Semicentennial Symposium on Gravity Waves, National Bureau of Standards Circular 521, pp. 79-93, (1952).

Iwasaki, S. Experimental Study of a Tsunami Generated by a Horizontal Motion of a Sloping Bottom. Bulletin of the Earthquake Research Institute, Vol. 57, pp. 239-262, (1982).

Iwasaki, S. On the Estimation of a Tsunami Generated by a Submarine Landslide. Proceedings of the International Tsunami Symposium, NOAA/Pacific Marine Laboratory, pp. 134-138, (1987).

Iwasaki, S. A Tsunami Generated by a Horizontal Motion of a Landslide in an Ocean. Proceedings of the International Tsunami Symposium, NOAA/Pacific Marine Laboratory, pp. 1-5, (1990).

Jaeger, H. M., Liu, C.-H., Nagel, S. R., Witten, T. A. Friction in Granular Flows. Europhys. Letters, Vol. 11, No. 7, pp. 619-624, (1990).

Jiang, L., LeBlond, P. H. The Coupling of a Submarine Slide and the Surface Waves Which it Generates. Journal of Geophysical Research, Vol. 97, No. C8, pp. 12731-12744, (1992).

Jiang, L., LeBlond, P. H. Numerical Modeling of an Underwater Bingham Plastic Mudslide and the Waves Which it Generates. Journal of Geophysical Research, Vol. 98, No. C6, pp. 10303-10317, (1993).

Kajiura, K. Tsunami Source, Energy and Directivity of Wave Energy. Bulletin of the Earthquake Research Institute, Vol. 48, pp. 835-869, (1970).

Komar, P. D. Beach Processes and Sedimentation. Prentice-Hall, (1976).

Kuenen, Ph. H. Estimated Size of the Grand Banks Turbidity Current. American Journal of Science, Vol. 250, pp. 874-884, December, (1952).

Kulikov, E. A., Rabinovich, A. B., Thomson, R. E., Bornhold, B. D. The Landslide Tsunami of November 3, 1994, Skagway Harbor, Alaska. Journal of Geophysical Research, Vol. 101, No. C3, pp. 6609-6615, (1996).

Lander, J. F., Lockridge, P. A. United States Tsunamis 1890-1988. U.S. Department of Commerce, National Oceanic and Atmospheric Administration, National Environmental Satellite, Data, and Information Service, National Geophysical Data Center, Boulder, Colorado, Publication 41-2, (1989).

Lander, J. F., Lockridge, P. A., Kozuch, M. J. Tsunamis Affecting the West Coast of the United States 1806-1992. U.S. Department of Commerce, National Oceanic and Atmospheric Administration, National Environmental Satellite, Data, and Information Service, National Geophysical Data Center, Boulder, Colorado, No. 29, (1993).

Lander, J. F. Tsunamis Affecting Alaska 1737-1996. U.S. Department of Commerce, National Oceanic and Atmospheric Administration, National Environmental Satellite, Data, and Information Service, National Geophysical Data Center, Boulder, Colorado, No. 31, (1996).

LeBlond, P. H., Jones, A. T. Underwater Landslides Ineffective at Tsunami Generation. Science of Tsunami Hazards, Vol. 13, pp. 25-26, (1995).

Lo, L. L. The Meniscus on a Needle -- A Lesson in Matching. Journal of Fluid Mechanics, Vol. 132, pp. 65-78, (1983).

Ma, K.-F., Satake, K., Kanamori, H. The Origin of the Tsunami Excited by the 1989 Loma Prieta Earthquake -- Faulting or Slumping. Geophysical Research Letters, Vol. 18, No. 4, pp. 637-640, April, (1991).

McCarthy, R. J., Bernard, E. N., Legg, M. R. The Cape Mendocino Earthquake: A Local Tsunami Wakeup Call? Coastal Zone 1993, Proceedings of the 8th Symposium on Coastal and Ocean Management, New Orleans, ASCE, Vol. 3, pp. 2812-2828, (1993).

Meakin, P., Skjeltorp, A. Application of Experimental and Numerical Models to the Physics of Multiparticle Systems. Advances in Physics, Vol. 42, No. 1, pp. 1-127, (1993).

Mei, C. C. The Applied Dynamics of Ocean Surface Waves. World Scientific, (1983).

Murty, T. S. Submarine Slide-Generated Water Waves in Kitimat Inlet, British Columbia. Journal of Geophysical Research, Vol. 84, No. C12, pp. 7777-7779, (1979).

Nagel, S. R. Instabilities in a Sandpile. Reviews of Modern Physics, Vol. 64, No. 1, pp. 321-325, (1992).

Noda, E. K. Theory of Water Waves Generated by a Time-Dependent Boundary Displacement. University of California at Berkeley, Hydraulic Engineering Laboratory, HEL 16-5, (1969).

Noda, E. K. Water Waves Generated by Landslides. ASCE Journal of the Waterways, Harbors, and Coastal Engineering Division, November, pp. 835-855, (1970).

Noda, E. K. Water Waves Generated by a Local Surface Disturbance. Journal of Geophysical Research, Vol. 76, No. 30, pp. 7389-7400, (1971).

Parker, G., Fukushima, Y., Pantin, H. M. Self-Accelerating Turbidity Currents. Journal of Fluid Mechanics, Vol. 171, pp. 145-181, (1986).

Pearlman, M. D. Dynamic Calibration of Wave Probes. Massachusetts Institute of Technology, Department of Naval Architecture and Marine Engineering, Report No. 39, July, (1963).

Press, W. H., Teukolsky, S. A., Vetterling, W. T., Flannery, B. P. Numerical Recipes in FORTRAN: the Art of Scientific Computing, Second Edition. Cambridge University Press, (1992).

Prins, J. E. Characteristics of Waves Generated by a Local Disturbance. Transactions, American Geophysical Union, Vol. 39, No. 5, pp. 865-874, (1958).

Prior, D. B., Wiseman, W. J., Bryant, W. R. Submarine Chutes on the Slopes of Fjord Deltas. Nature, Vol. 290, March 26, pp. 326-328, (1981).

Prior, D. B., Bornhold, B. D., Coleman, J. M., Bryant, W. R. Morphology of a Submarine Slide, Kitimat Arm, British Colombia. Geology, Vol. 10, pp. 588-592, (1982).

Quadfasel, D., Kudrass, H., Frische, A. Deep-Water Renewal by Turbidity Currents in the Sulu Sea. Nature, Vol. 348, November 22, pp. 320-322, (1990).

Raichlen, F., Lee, J. J., Petroff, C., Watts, P. The Generation of Waves by a Landslide: Skagway, Alaska -- A Case Study. Proceedings of the 25th International Conference on Coastal Engineering, Orlando, Florida, (1996).

Sabatier, P. C. On Water Waves Produced by Ground Motions. Journal of Fluid Mechanics, Vol. 126, pp. 27-58, (1983).

Sarpkaya, T., Isaacson, M. Mechanics of Wave Forces on Offshore Structures. Van Nostrand Reinhold, (1981).

Savage, S. B., Hutter, K. The Motion of a Finite Mass of Granular Material Down a Rough Incline. Journal of Fluid Mechanics, Vol. 199, pp. 177-215, (1989).

Savage, S. B. Flows of Granular Materials with Applications to Geophysical Problems. Lecture notes from the IUTAM International Summer School on Mechanics, International Centre of Mechanical Sciences, Udine, Italy, (1992).

Scott, R. F. Principles of Soil Mechanics. Addison-Wesley, (1963).

Scott, R. F. Centrifuge and Modeling Technology: A Survey. *Revue Française de Geotechnique*, Vol. 48, pp. 15-34, (1989).

Shaller, P. J. Analysis and Implications of Large Martian and Terrestrial Landslides. Ph.D. Thesis, California Institute of Technology, (1991).

Shapiro, A. P., Probstein, R. F. Random Packings of Spheres and Fluidity Limits of Monodisperse and Bidisperse Suspensions. Physical Review Letters, Vol. 68, No. 9, pp. 1422-1425, (1992).

Shepard, F. P., Dill, R. F. Submarine Canyons and Other Sea Valleys. Rand McNally and Co., (1966).

Simpson, J. E. Gravity Currents: In the Environment and the Laboratory. Halstead Press, Wiley, (1987).

Stoker, J. J. Water Waves. Interscience, (1957).

Striem, H. L., Miloh, T. Tsunamis Induced by Submarine Slumpings off the Coast of Israel. International Hydrographic Review, Vol. 2, pp. 41-55, (1976).

Terzaghi, K. Varieties of Submarine Slope Failures. Proc. 8th Texas Conf. Soil Mech. Found. Eng., pp. 1-41, (1956).

Tuck, E. O., Hwang, L.-S. Long Wave Generation on a Sloping Beach. Journal of Fluid Mechanics, Vol. 51, No. 3, pp. 449-461, (1972).

Turner, J. S. Buoyancy Effects in Fluids. Cambridge University Press, (1979).

Tyvand, P. A. Unsteady Free-Surface Flow due to a Line Source. Physics of Fluids A, Vol. 4, No. 4, April, pp. 671-676, (1992).

Vanoni, V. A. Sedimentation Engineering. ASCE, (1975).

Villeneuve, M., Savage, S. B. Nonlinear, Dispersive, Shallow-Water Waves Developed by a Moving Bed. Journal of Hydraulic Research, Vol. 31, No. 2, pp. 249-266, (1993).

Wehausen, J. V., Laitone, E. V. Surface Waves. Encyclopedia of Physics (*Handbuch der Physik*), Vol. 9, pp. 446-778, Springer-Verlag, (1960).

White, F. M. Viscous fluid flow. McGraw Hill, (1991).

Whitham, G. B. Linear and Nonlinear Waves. Wiley-Interscience, (1973).

Wiegel, R. L. Laboratory Studies of Gravity Waves Generated by the Movement of a Submarine Body. Transactions, American Geophysical Union, Vol. 36, No. 5, pp. 759-774, (1955).

Wiegel, R. L., Noda, E. K., Kuba, E. M., Gee, D. M., Tornberg, G. F. Water Waves Generated by Landslides in Reservoirs. ASCE Journal of the Waterways, Harbors, and Coastal Engineering Division, May, pp. 307-333, (1970).

Yehle, L. A., Lemke, R. W. Reconnaissance Engineering Geology of the Skagway Area, Alaska, with Emphasis on Evaluation of Earthquake and Other Geological Hazards. Open File Report, USGS, (1972).

Zeininger, G., Brennen, C. E. Interstitial Fluid Effects in Hopper Flows of Granular Material. Cavitation and Multiphase Flow Forum, Joint ASCE/ASME Mechanics Conference, Albuquerque, New Mexico, Vol. 23, pp. 132-136, (1985).

Appendix A

A. Wave Records

The wave records of all solid block and material landslide trials that were repeated more than once are provided here. Since roughly half of all trials were repeated more than once, this appendix displays a large portion of the near-field and far-field wave records obtained for this work.

A.1 Solid Block Near-field Wave Records

Figures A.1-A.11 show 27 out of the 43 near-field wave records obtained above the middle of the initial solid block position. The eleven figures show the superposed near-field wave records of all experiments that were repeated more than once for the purpose of comparison. Some interesting differences emerge from the comparisons. For example, Figure A.5 shows the influence that the accelerometer wire can have on the near-field wave record by creating rapidly oscillating ripples in the free surface as it entered the water; solid block motion in Trial 29 was recorded by a movie camera. For all accelerometer trials, most of the wire was folded under the water free surface to minimize this complication. The differences in the maximum wave amplitudes present in Figure A.6 remain unexplained as does the fact that Trial 56 fits patterns established by solid block experiments better than Trial 52. Figure A.8 clearly shows how Trial 30 (performed with the old block 2) has a smaller wave amplitude than similar trials repeated with the new block 2. Recall that all block 2 trials up to and including Trial 42 involved the old block 2. Regardless, Figures A.8 and A.9 indicate the agreement that can be obtained in the near-field wave records with the experimental apparatus and method described in Chapter 4. Figure A.11 has several unexplainable differences in the wave records and yet the important characteristics of both trials agree to within independently established error bars that are provided in Appendix B.

A.2 Solid Block Far-field Wave Records

The eleven Figures A.12-A.22 show the superposed far-field wave records of all experiments that were repeated more than once for comparison. Once again, some

interesting differences emerge from the comparisons. Figures A.14-A.16 demonstrate the increased noisiness of the far-field wave gauge as well as the degree of repeatability that can be expected from very small wave amplitude trials. Figures A.18-A.20 provide another indication of the agreement that can be obtained in the far-field wave records with the experimental apparatus and method described in Chapter 4. The old block 2 results are no longer obviously smaller than the new block 2 results. The only figures for which both the near-field and far-field wave records had substantial differences were Figures A.11 and A.22 involving Trials 51 and 64.

A.3 Material Near-field Wave Records

Figures A.23-A.27 show 11 out of the 21 near-field wave records obtained above the middle of the initial material position. The five figures show the superposed near-field wave records of all experiments that were repeated more than once for the purpose of comparison. Figure A.24 stands out as the only figure in which the agreement is not exceptional. Nevertheless, the differences between Trials 37 and 83 are almost within standard errors.

A.4 Material Far-field Wave Records

Figures A.28-A.32 show the superposed far-field wave records of all experiments that were repeated more than once for comparison. Figures A.29-A.31 agree to within standard errors despite the apparently large discrepancies between the wave records. Figures A.24 and A.29 involving Trials 37 and 83 are the only two repeated material landslide trials where both the near-field and far-field wave records differ substantially.

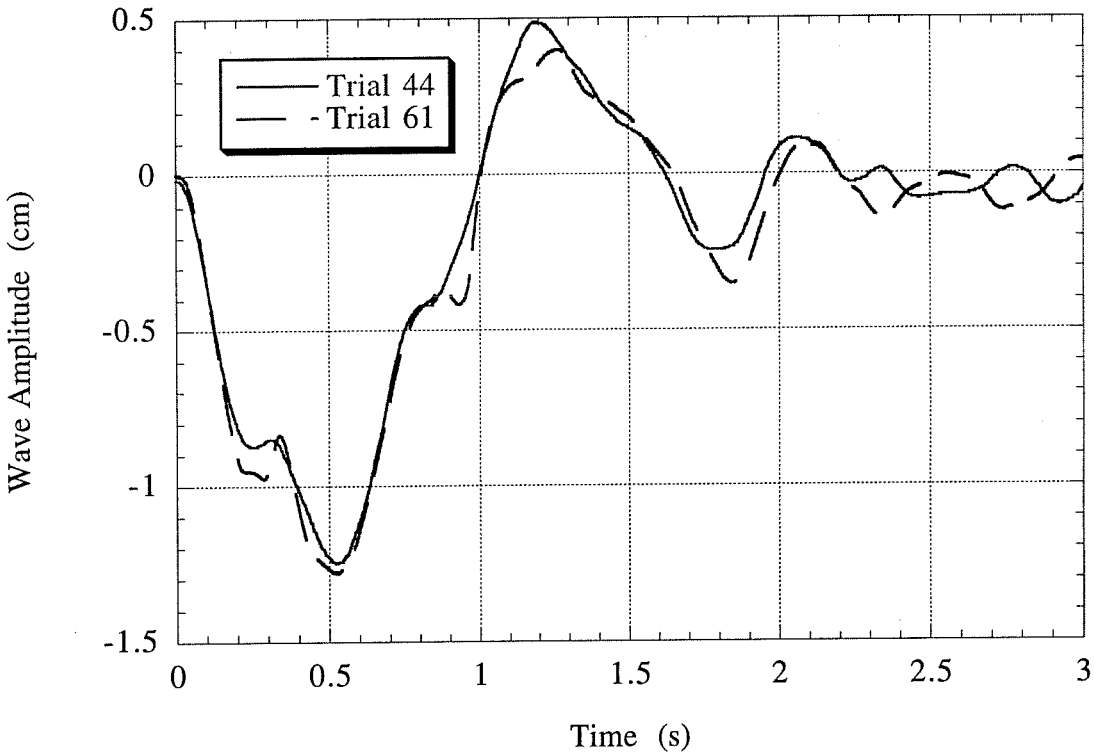

Figure A.1: Comparison of measured near-field wave amplitudes above the middle of the initial solid block position for Trials 44 and 61. Block 1_n was released from rest with an initial submergence of d=45.0 mm. The agreement between the two wave profiles is exceptional.

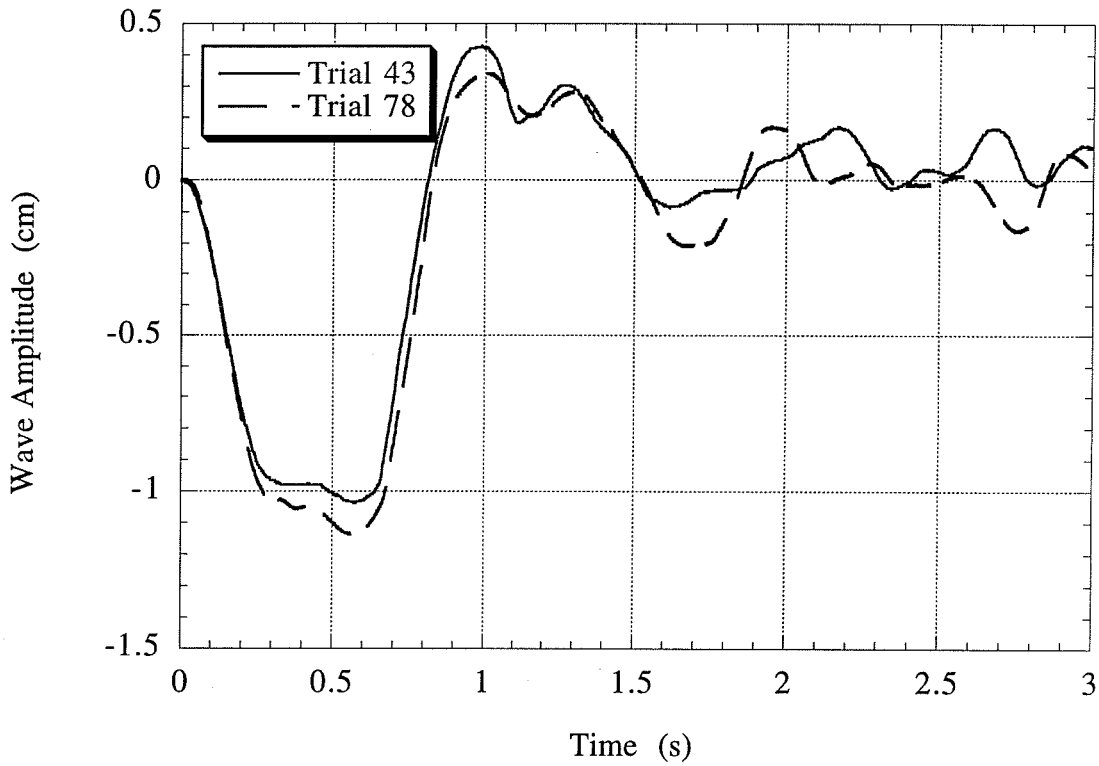

Figure A.2: Comparison of measured near-field wave amplitudes above the middle of the initial solid block position for Trials 43 and 78. Block 1_n was released from rest with an initial submergence of d=73.5 mm. The agreement between the two wave profiles is exceptional.

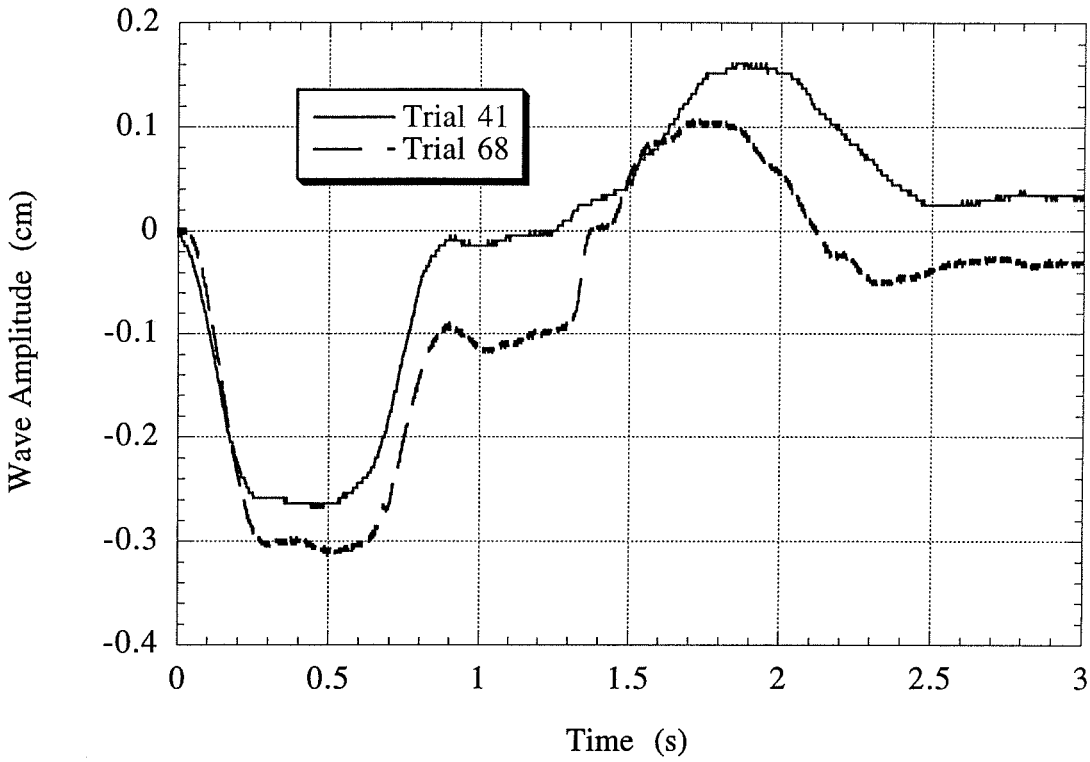

Figure A.3: Comparison of measured near-field wave amplitudes above the middle of the initial solid block position for Trials 41 and 68. Block 2_o was released from rest with an initial submergence of d=74.5 mm. The agreement between the two wave profiles is within standard error bounds.

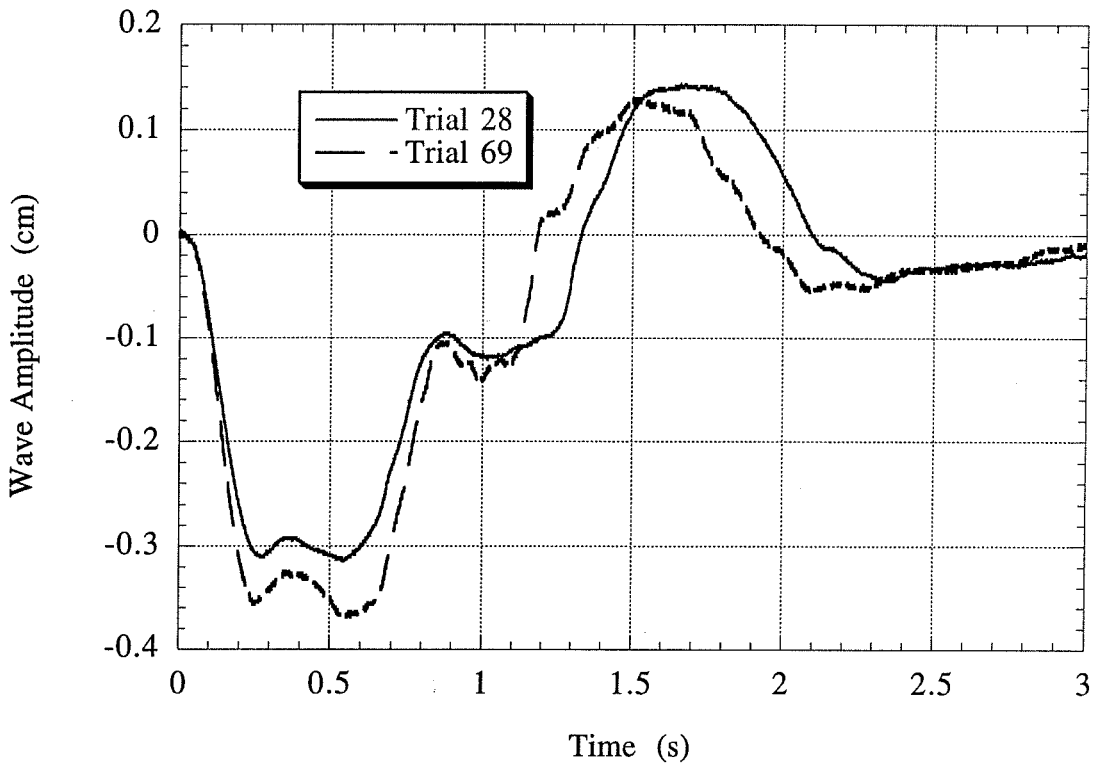

Figure A.4: Comparison of measured near-field wave amplitudes above the middle of the initial solid block position for Trials 28 and 69. Block 2_a was released from rest with an initial submergence of d=74.5 mm. The agreement between the two wave profiles is exceptional.

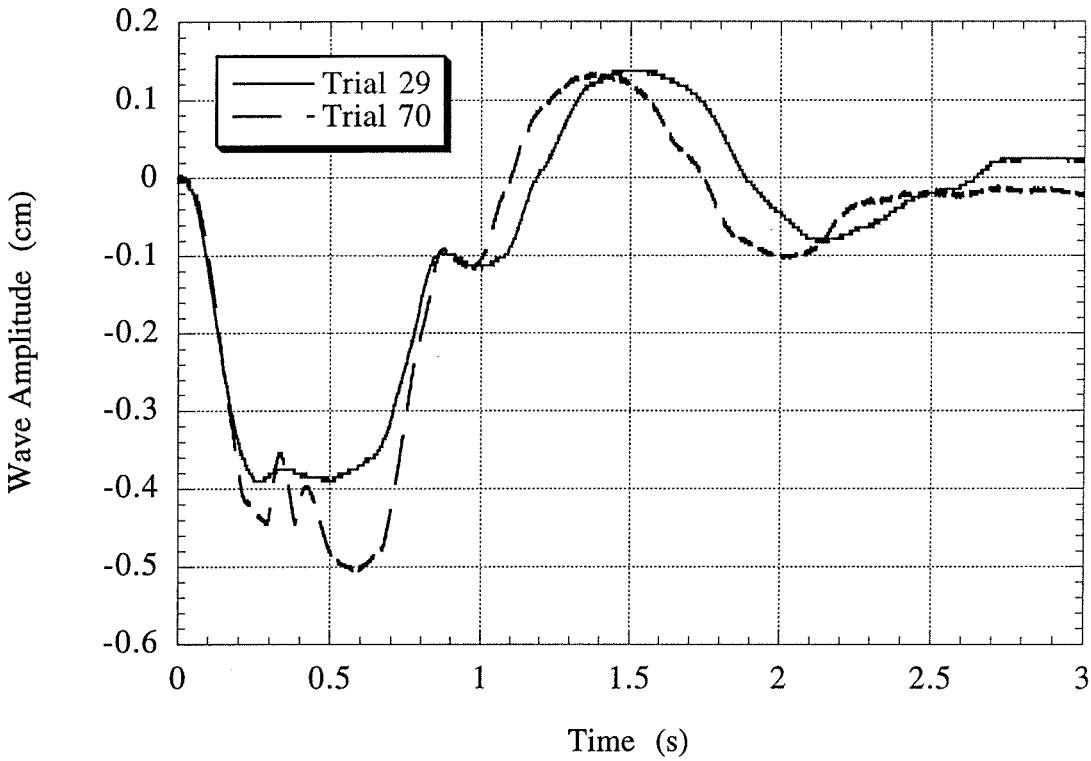

Figure A.5: Comparison of measured near-field wave amplitudes above the middle of the initial solid block position for Trials 29 and 70. Block 2_b was released from rest with an initial submergence of d=74.5 mm. The agreement between the two wave profiles is within standard error bounds despite the noise in Trial 70.

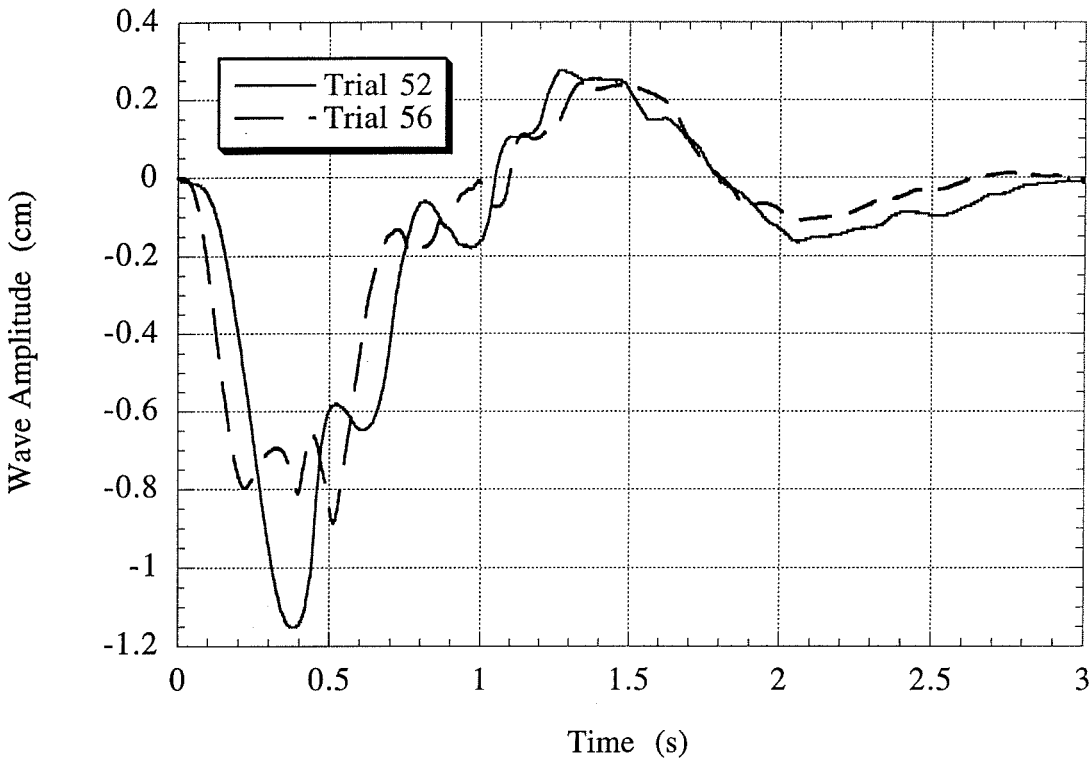

Figure A.6: Comparison of measured near-field wave amplitudes above the middle of the initial solid block position for Trials 52 and 56. Block 2_n was released from rest with an initial submergence of d=40.0 mm. The agreement between the two wave profiles is poor.

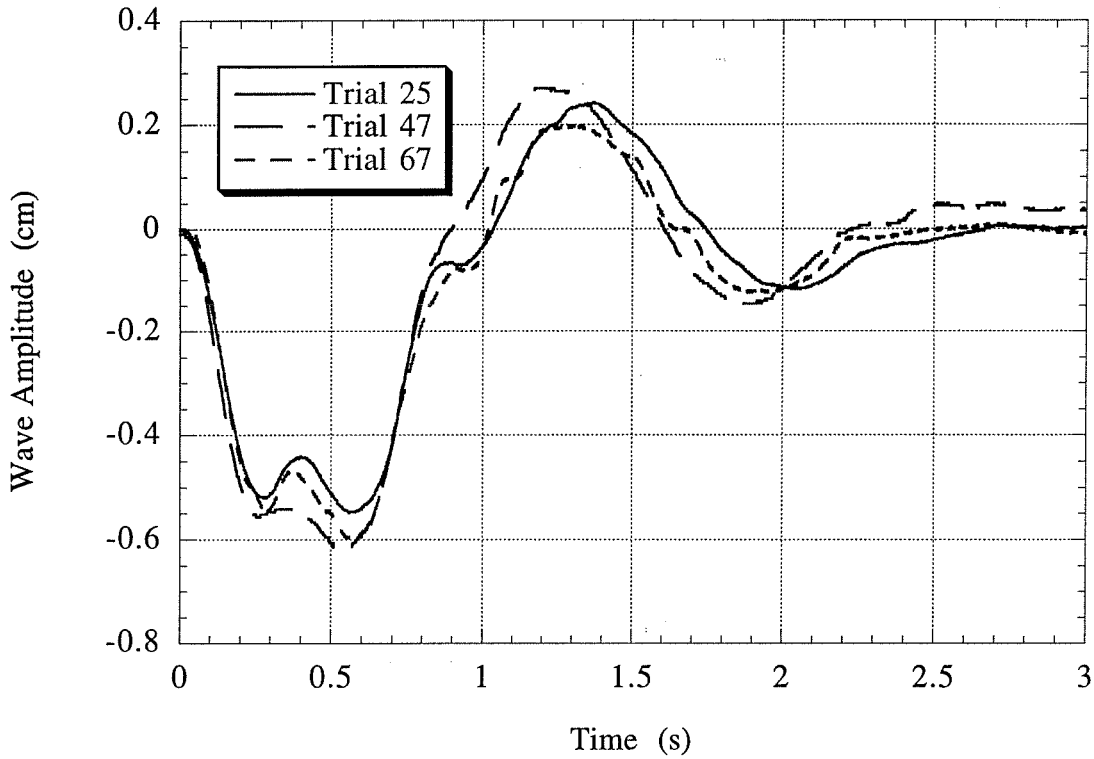

Figure A.7: Comparison of measured near-field wave amplitudes above the middle of the initial solid block position for Trials 25, 47 and 67. Block 2_n was released from rest with an initial submergence of d=74.5 mm. The agreement between the three wave profiles is exceptional.

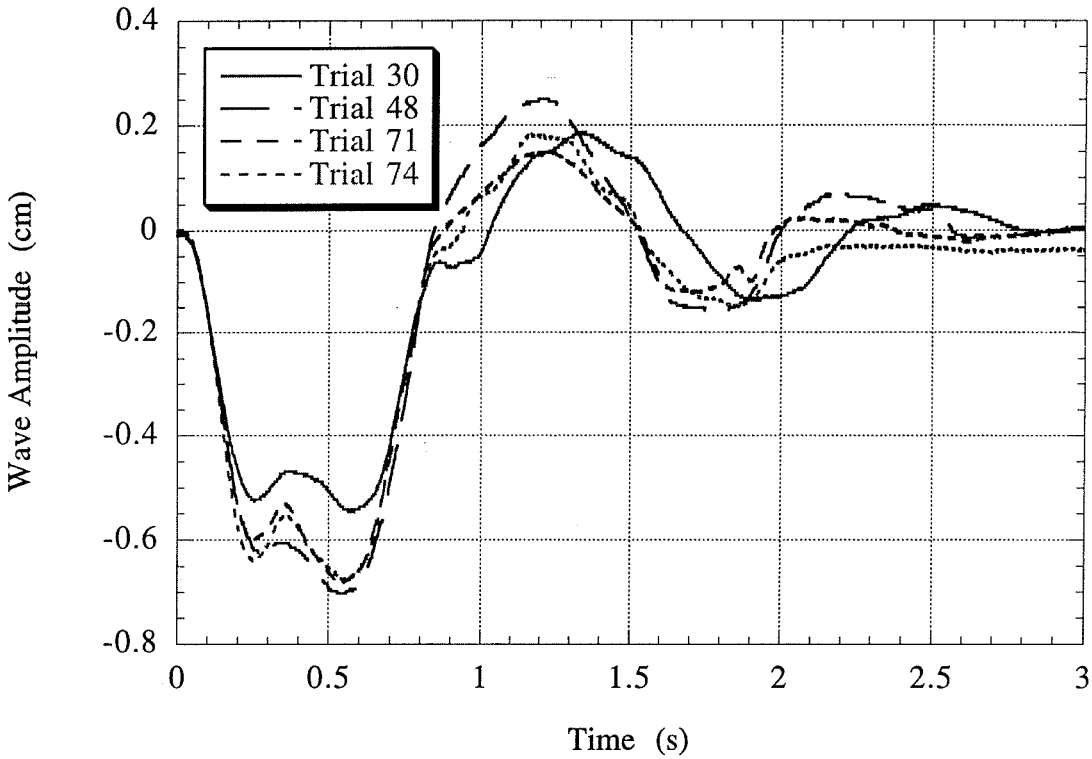

Figure A.8: Comparison of measured near-field wave amplitudes above the middle of the initial solid block position for Trials 30, 48, 71 and 74. Block 2_d was released from rest with an initial submergence of d=74.5 mm. The agreement between the four wave profiles is within standard error bounds.

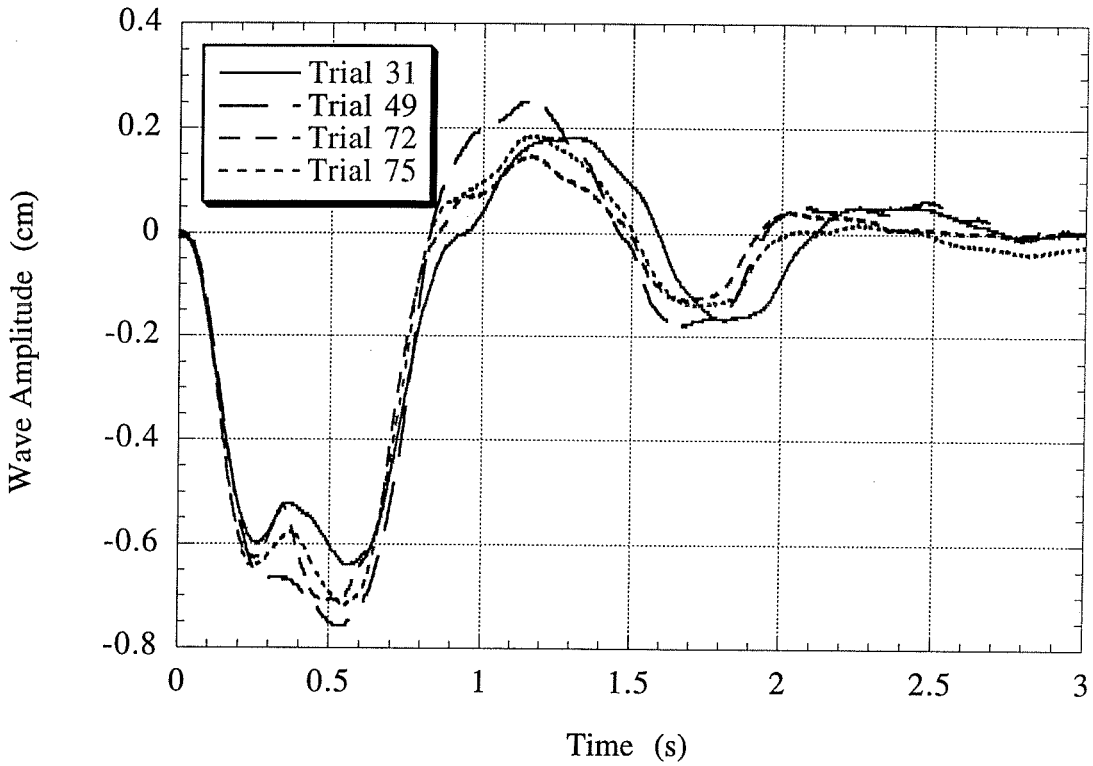

Figure A.9: Comparison of measured near-field wave amplitudes above the middle of the initial solid block position for Trials 31, 49, 72 and 75. Block 2_e was released from rest with an initial submergence of d=74.5 mm. The agreement between the four wave profiles is within standard error bounds.

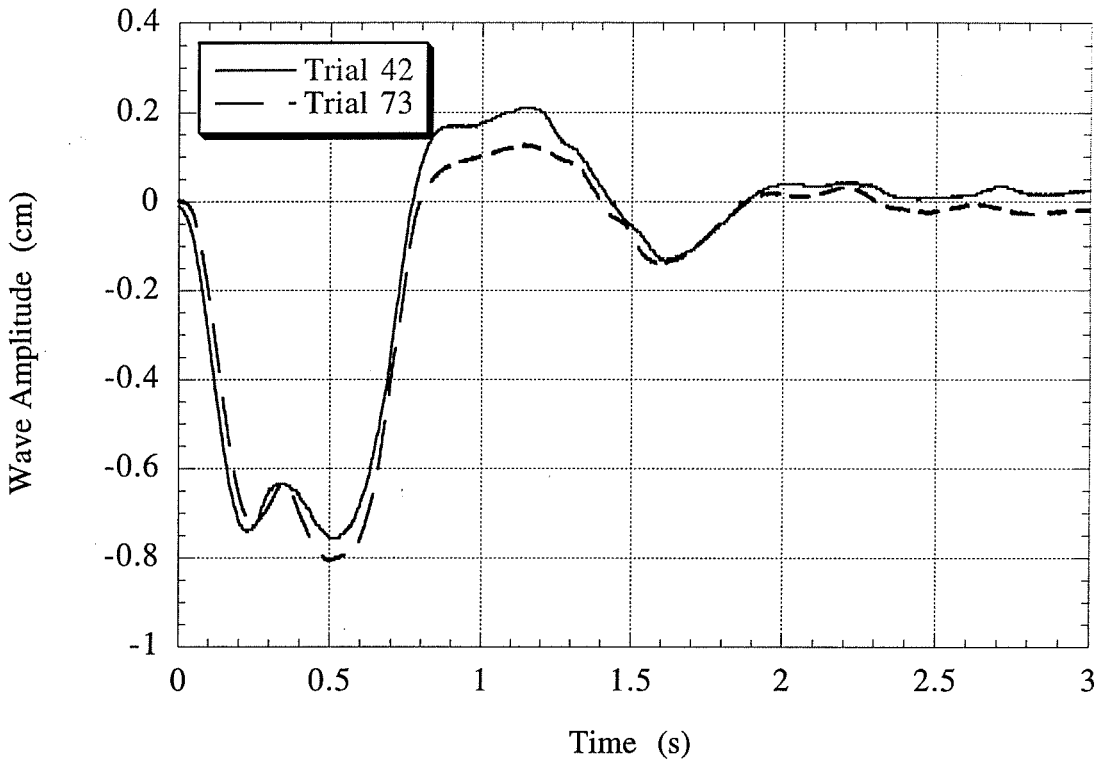

Figure A.10: Comparison of measured near-field wave amplitudes above the middle of the initial solid block position for Trials 42 and 73. Block 2_1 was released from rest with an initial submergence of d=74.5 mm. The agreement between the two wave profiles is exceptional.

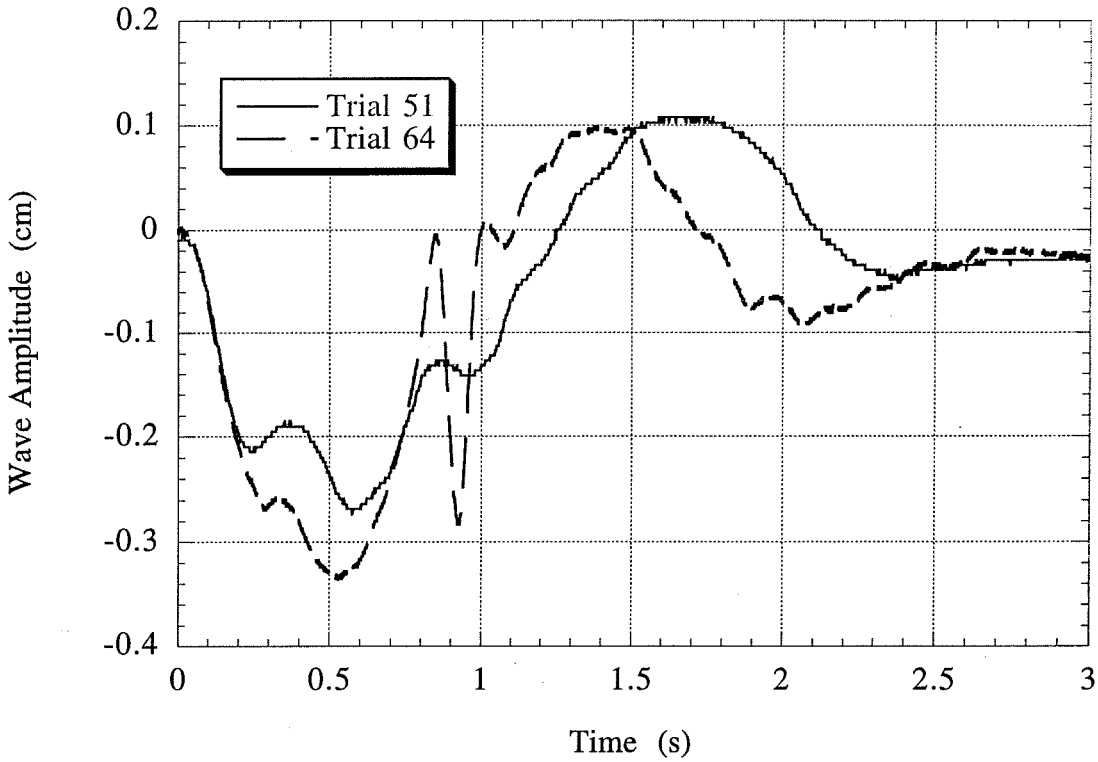

Figure A.11: Comparison of measured near-field wave amplitudes above the middle of the initial solid block position for Trials 51 and 64. Block 3_n was released from rest with an initial submergence of d=81.5 mm. The agreement between the two wave profiles is within standard error bounds despite the apparent wave spike at t=1 s.

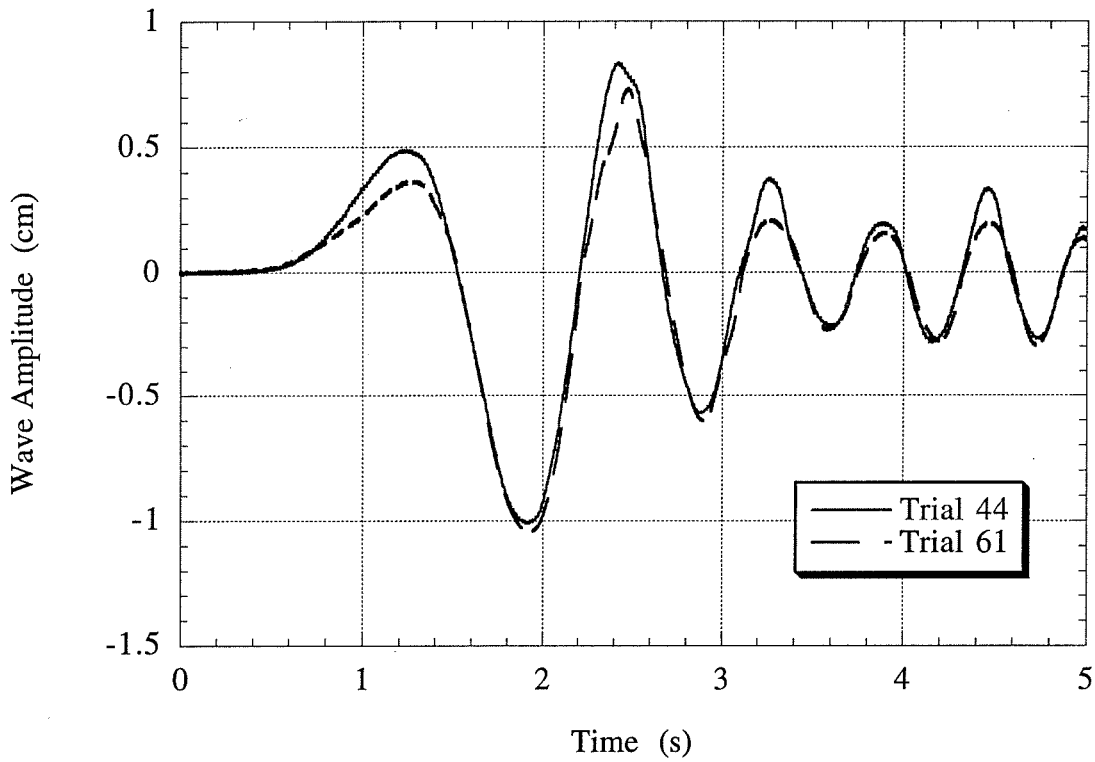

Figure A.12: Comparison of measured far-field wave amplitudes above the middle of the initial solid block position for Trials 44 and 61. Block 1_n was released from rest with an initial submergence of d=45.0 mm. The agreement between the two wave profiles is exceptional.

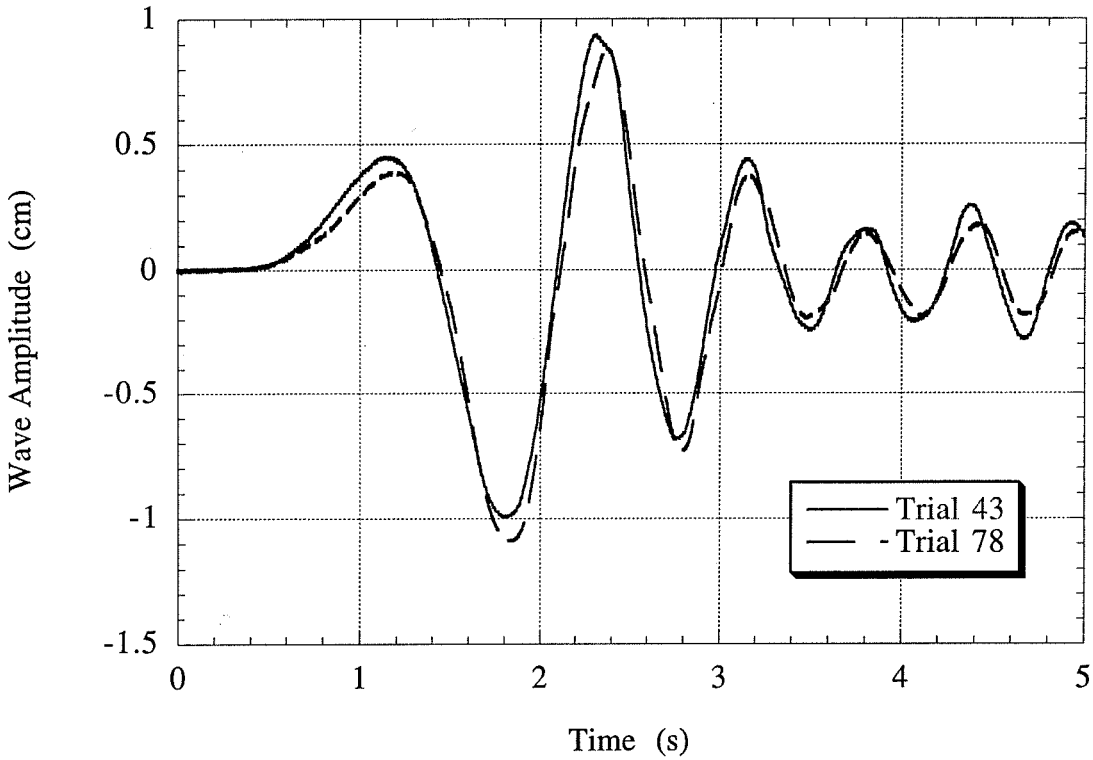

Figure A.13: Comparison of measured far-field wave amplitudes above the middle of the initial solid block position for Trials 43 and 78. Block 1_n was released from rest with an initial submergence of d=73.5 mm. The agreement between the two wave profiles is exceptional.

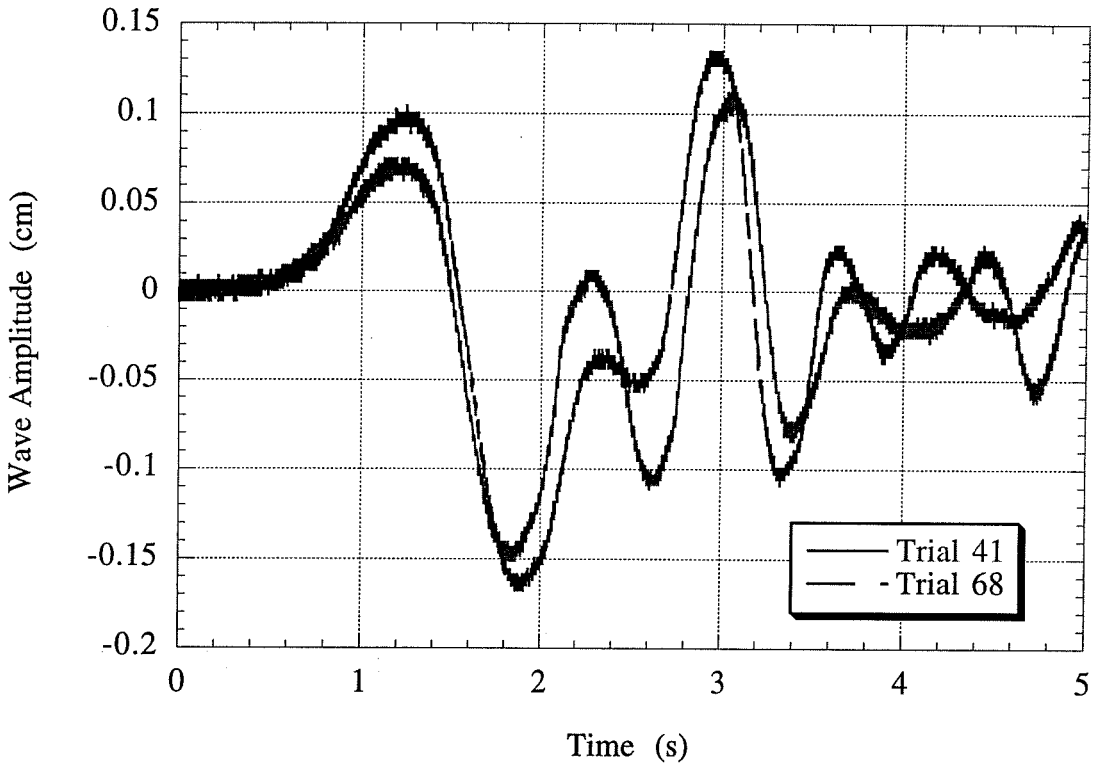

Figure A.14: Comparison of measured far-field wave amplitudes above the middle of the initial solid block position for Trials 41 and 68. Block 2_o was released from rest with an initial submergence of d=74.5 mm. The agreement between the two wave profiles is within standard error bounds.

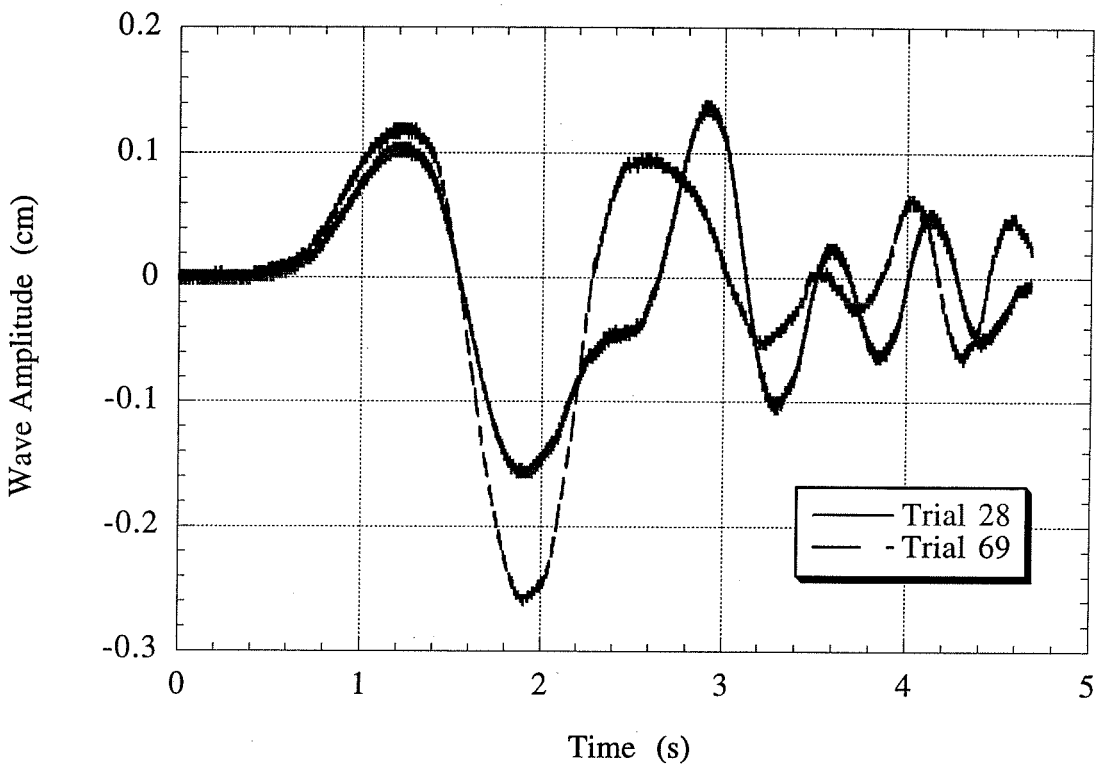

Figure A.15: Comparison of measured far-field wave amplitudes above the middle of the initial solid block position for Trials 28 and 69. Block 2_a was released from rest with an initial submergence of d=74.5 mm. The agreement between the two wave profiles is poor.

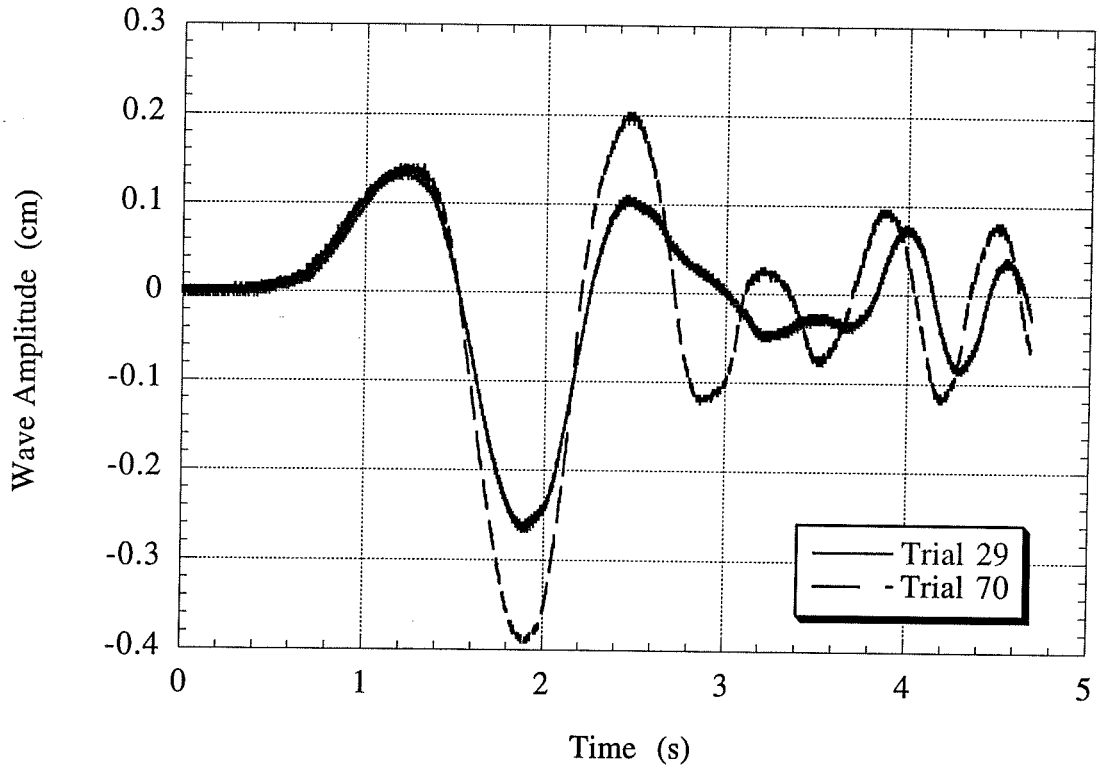

Figure A.16: Comparison of measured far-field wave amplitudes above the middle of the initial solid block position for Trials 29 and 70. Block 2_b was released from rest with an initial submergence of d=74.5 mm. The agreement between the two wave profiles is poor.

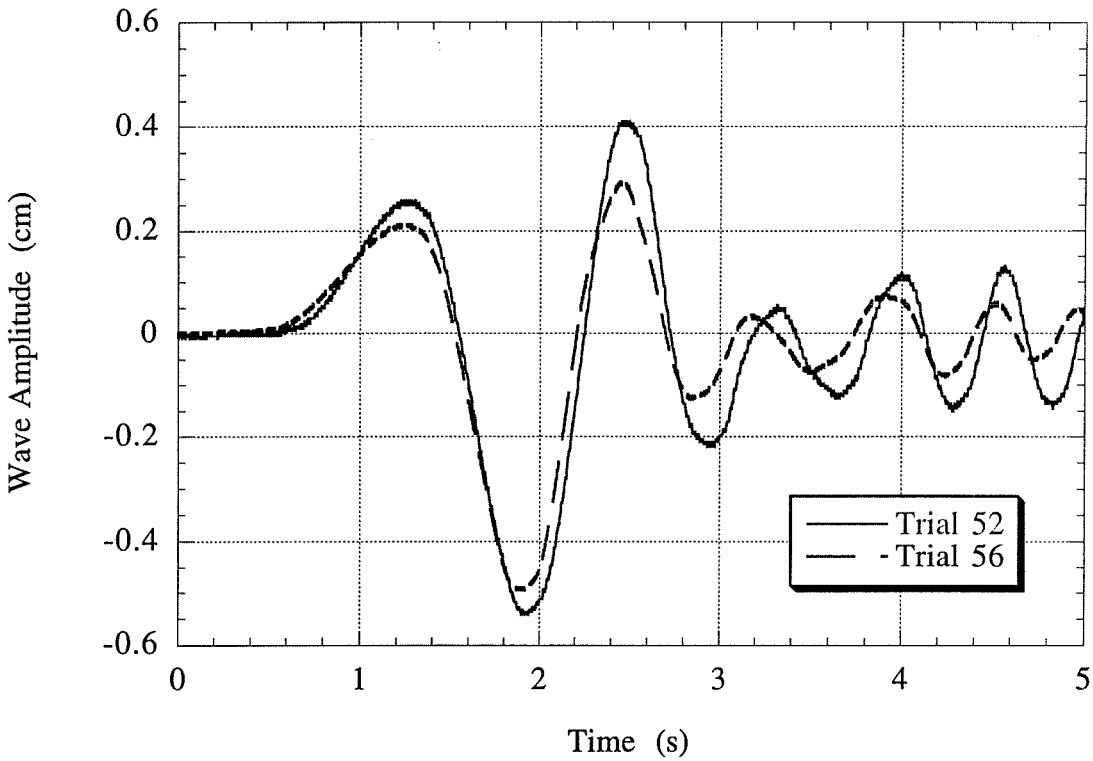

Figure A.17: Comparison of measured far-field wave amplitudes above the middle of the initial solid block position for Trials 52 and 56. Block 2_n was released from rest with an initial submergence of d=40.0 mm. The agreement between the two wave profiles is exceptional.

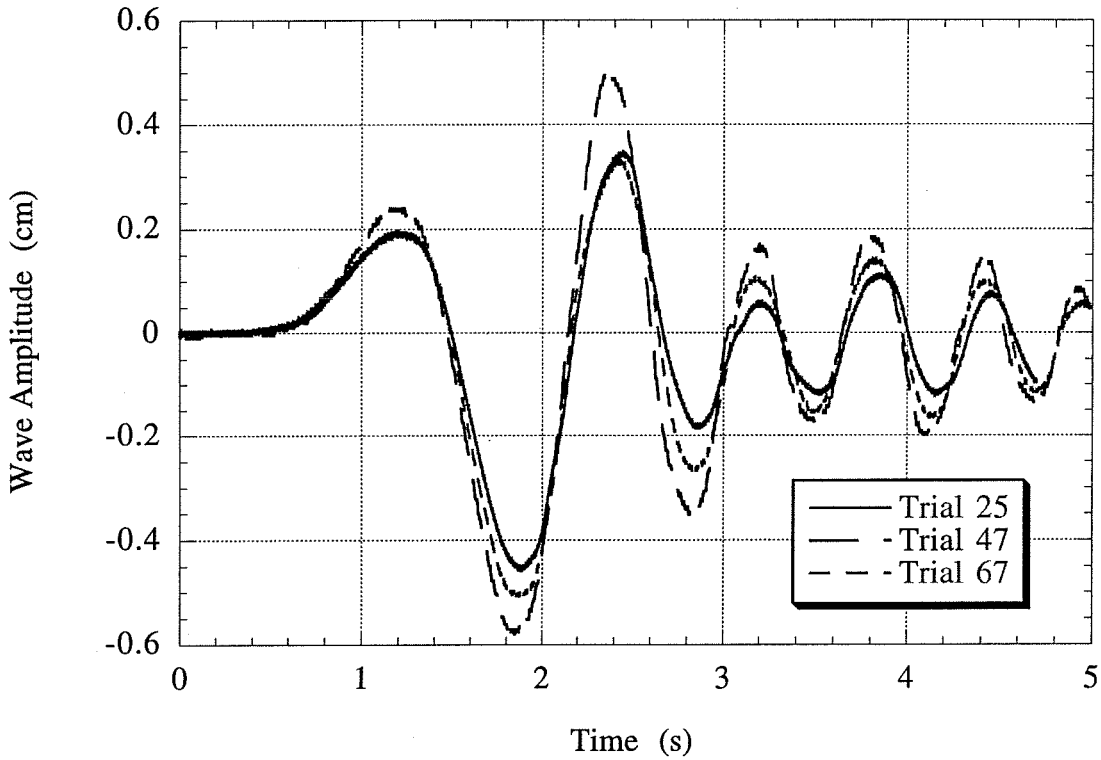

Figure A.18: Comparison of measured far-field wave amplitudes above the middle of the initial solid block position for Trials 25, 47 and 67. Block 2_n was released from rest with an initial submergence of d=74.5 mm. The agreement between the three wave profiles is within standard error bounds.

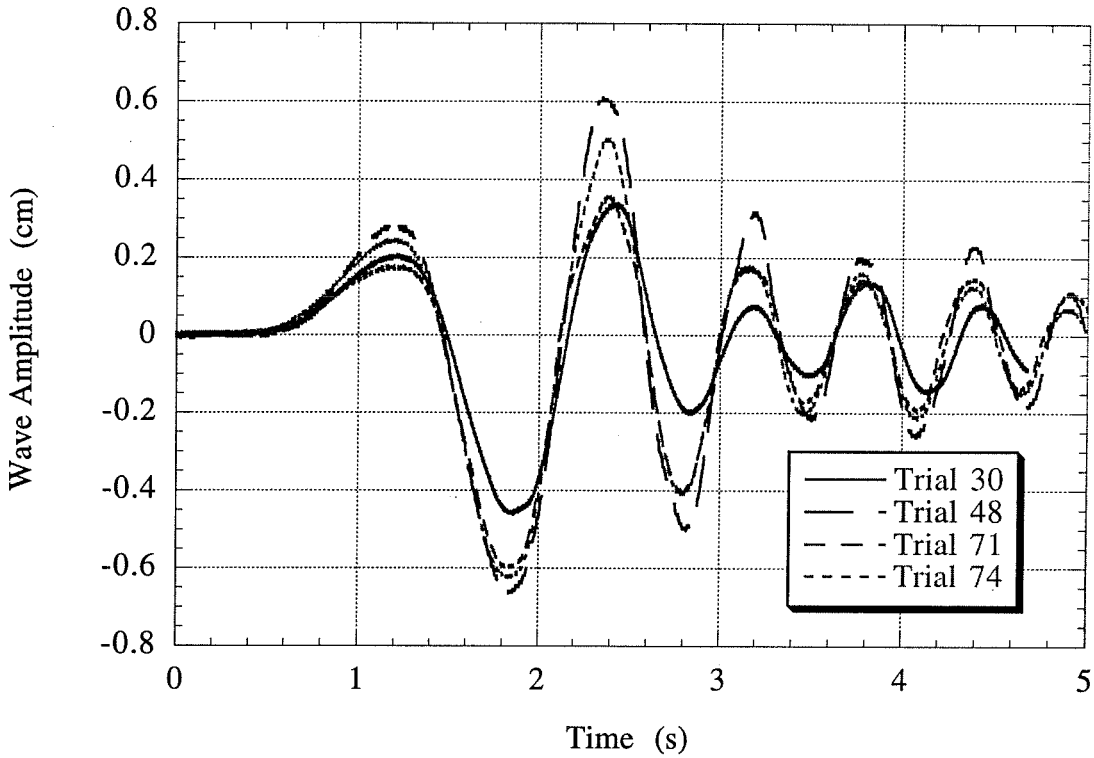

Figure A.19: Comparison of measured far-field wave amplitudes above the middle of the initial solid block position for Trials 30, 48, 71 and 74. Block 2_d was released from rest with an initial submergence of d=74.5 mm. The agreement between the four wave profiles is within standard error bounds.

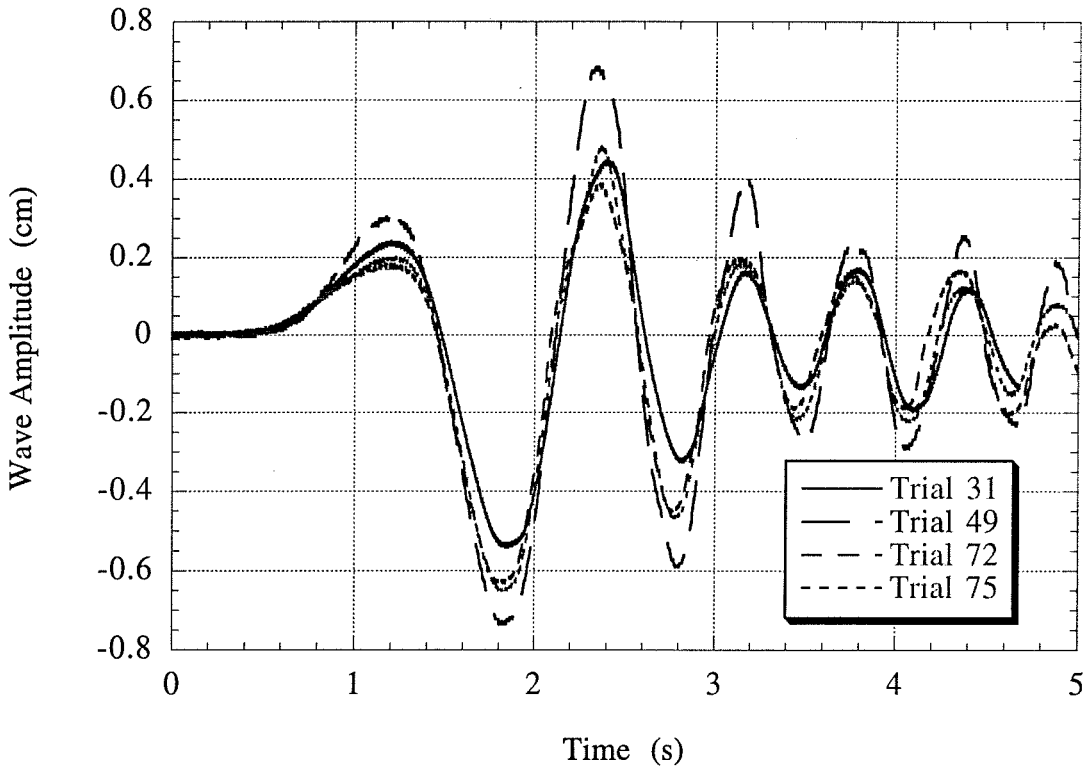

Figure A.20: Comparison of measured far-field wave amplitudes above the middle of the initial solid block position for Trials 31, 49, 72 and 75. Block 2_e was released from rest with an initial submergence of d=74.5 mm. The agreement between the four wave profiles is within standard error bounds.

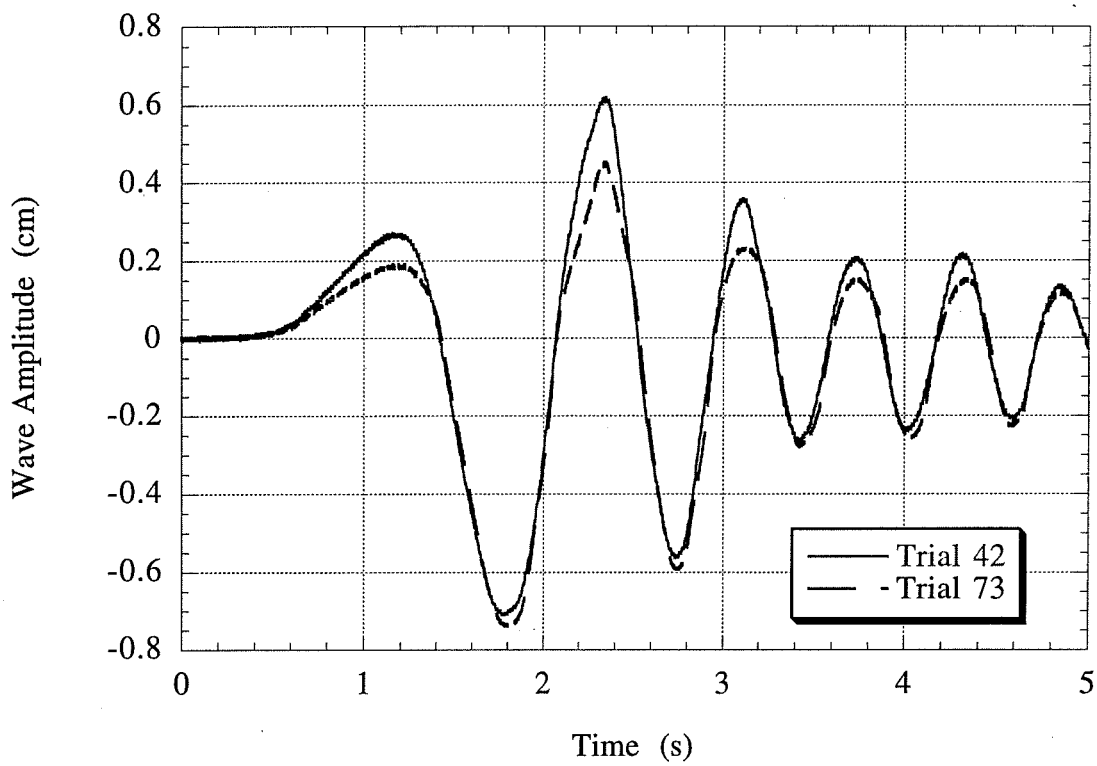

Figure A.21: Comparison of measured far-field wave amplitudes above the middle of the initial solid block position for Trials 42 and 73. Block 2_l was released from rest with an initial submergence of d=74.5 mm. The agreement between the two wave profiles is exceptional.

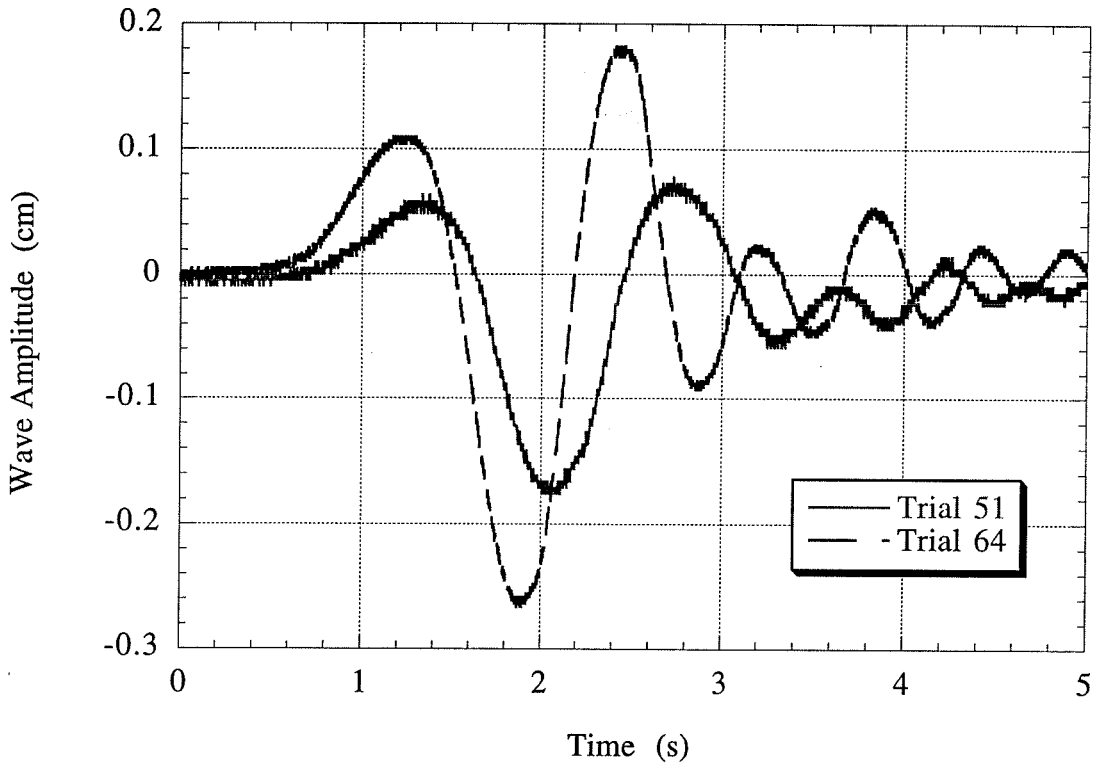

Figure A.22: Comparison of measured far-field wave amplitudes above the middle of the initial solid block position for Trials 51 and 64. Block 3_n was released from rest with an initial submergence of d=81.5 mm. The agreement between the two wave profiles is very poor.

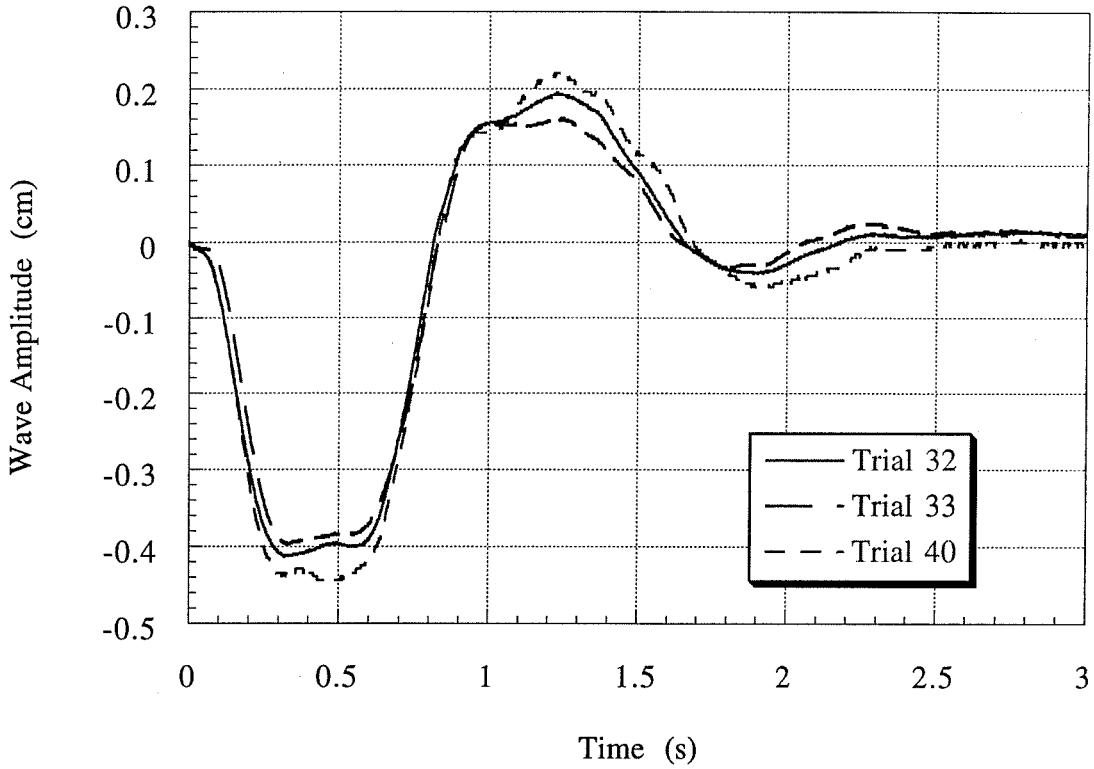

Figure A.23: Comparison of measured near-field wave amplitudes above the middle of the initial material position for Trials 32, 33 and 40. Crushed calcite was released from rest with an initial submergence of d≈74 mm. The agreement between the three wave profiles is exceptional.

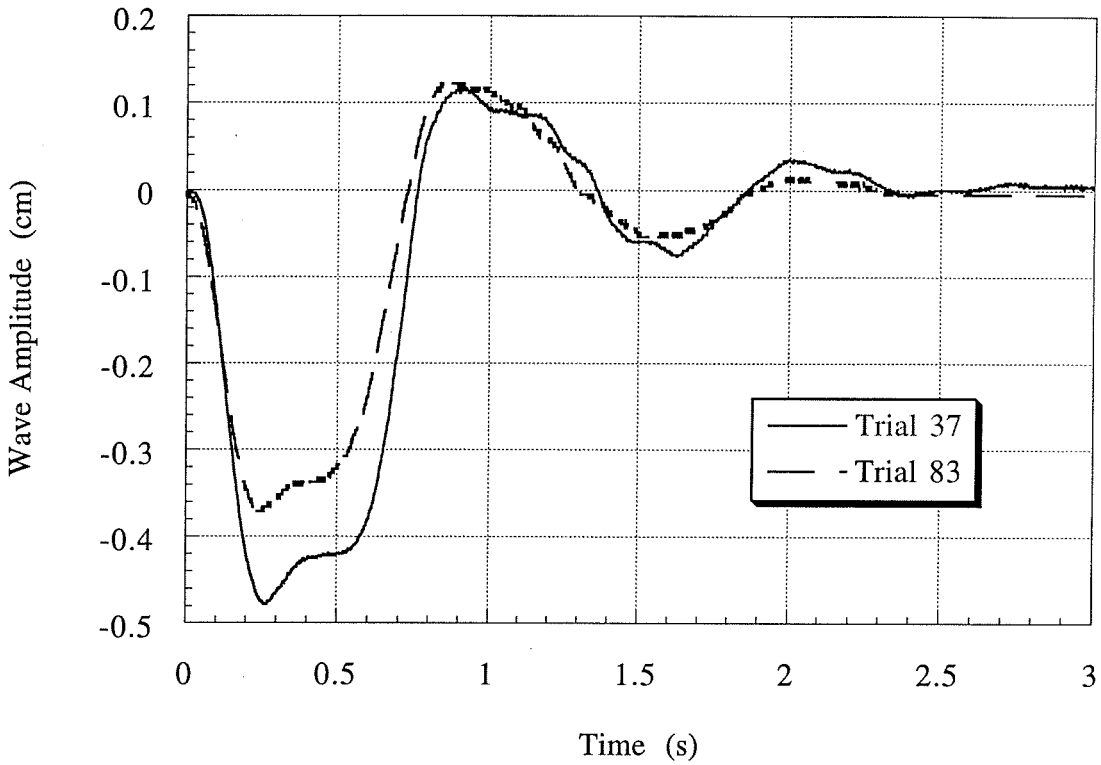

Figure A.24: Comparison of measured near-field wave amplitudes above the middle of the initial material position for Trials 37 and 83. Glass marbles were released from rest with an initial submergence of d≈74 mm. The agreement between the two wave profiles is poor.

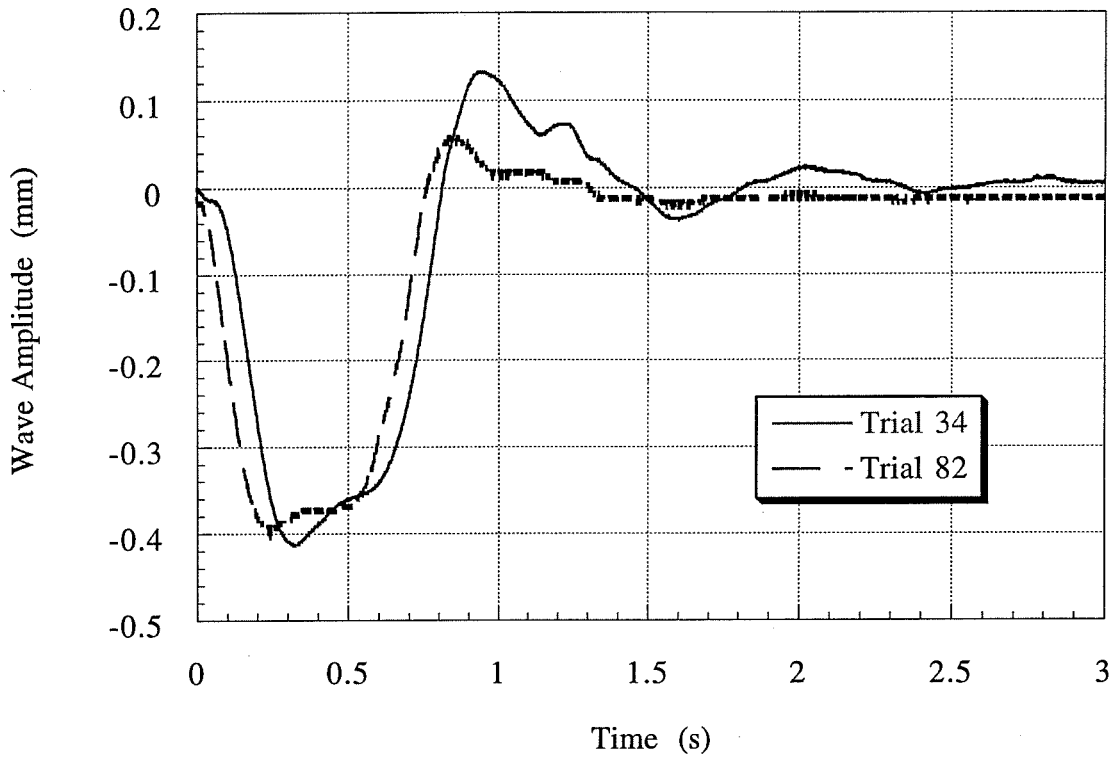

Figure A.25: Comparison of measured near-field wave amplitudes above the middle of the initial material position for Trials 34 and 82. Three millimeter glass beads were released from rest with an initial submergence of d≈74 mm. The agreement between the two wave profiles is exceptional.

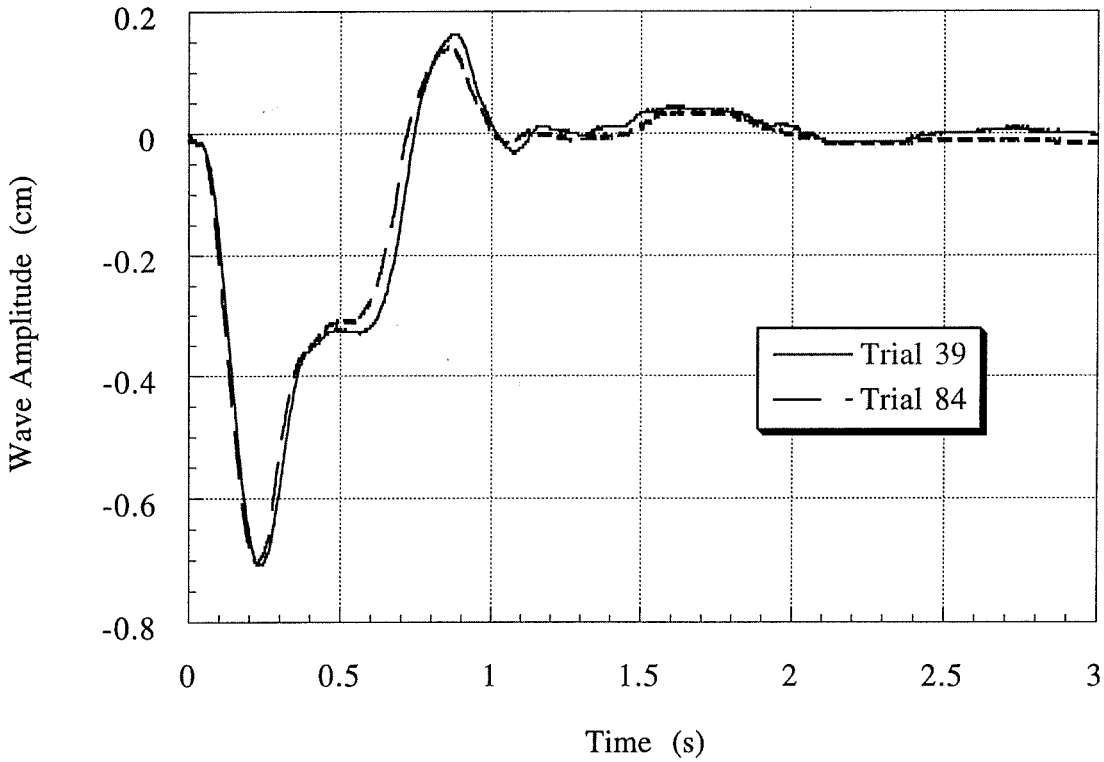

Figure A.26: Comparison of measured near-field wave amplitudes above the middle of the initial material position for Trials 39 and 84. Two millimeter lead shot was released from rest with an initial submergence of d≈77 mm. The agreement between the two wave profiles is exceptional.

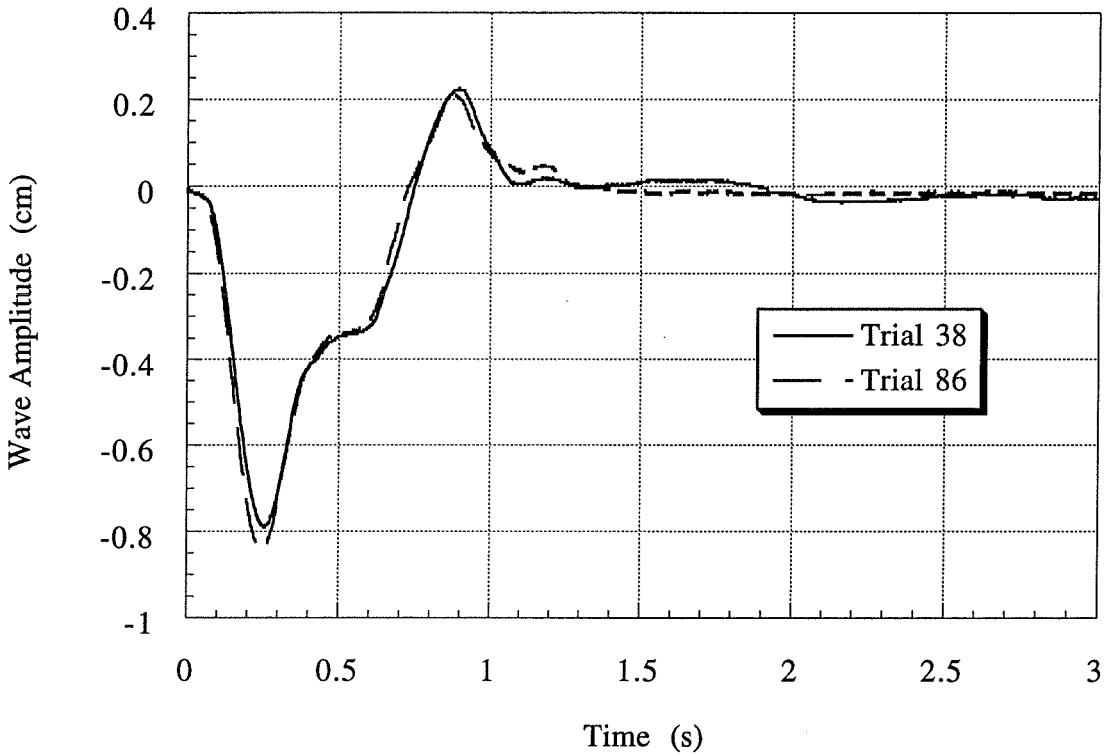

Figure A.27: Comparison of measured near-field wave amplitudes above the middle of the initial material position for Trials 38 and 86. Three millimeter lead shot was released from rest with an initial submergence of d≈74 mm. The agreement between the two wave profiles is exceptional.

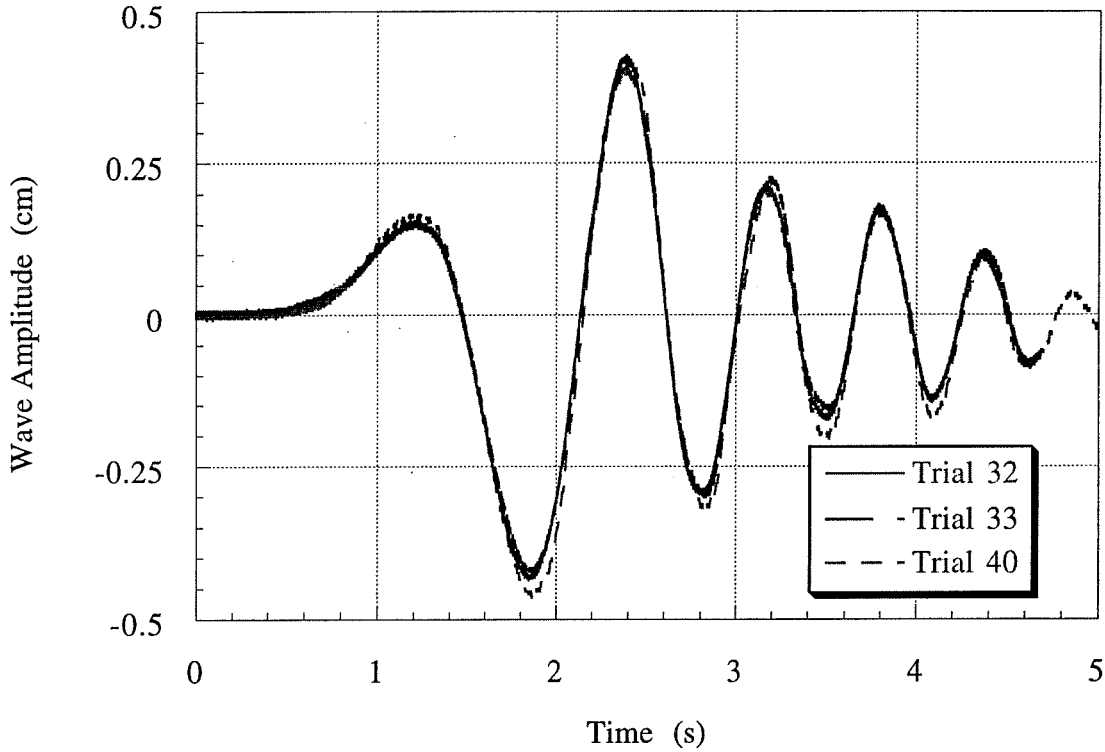

Figure A.28: Comparison of measured far-field wave amplitudes above the middle of the initial material position for Trials 32, 33 and 40. Crushed calcite was released from rest with an initial submergence of d≈74 mm. The agreement between the three wave profiles is exceptional.

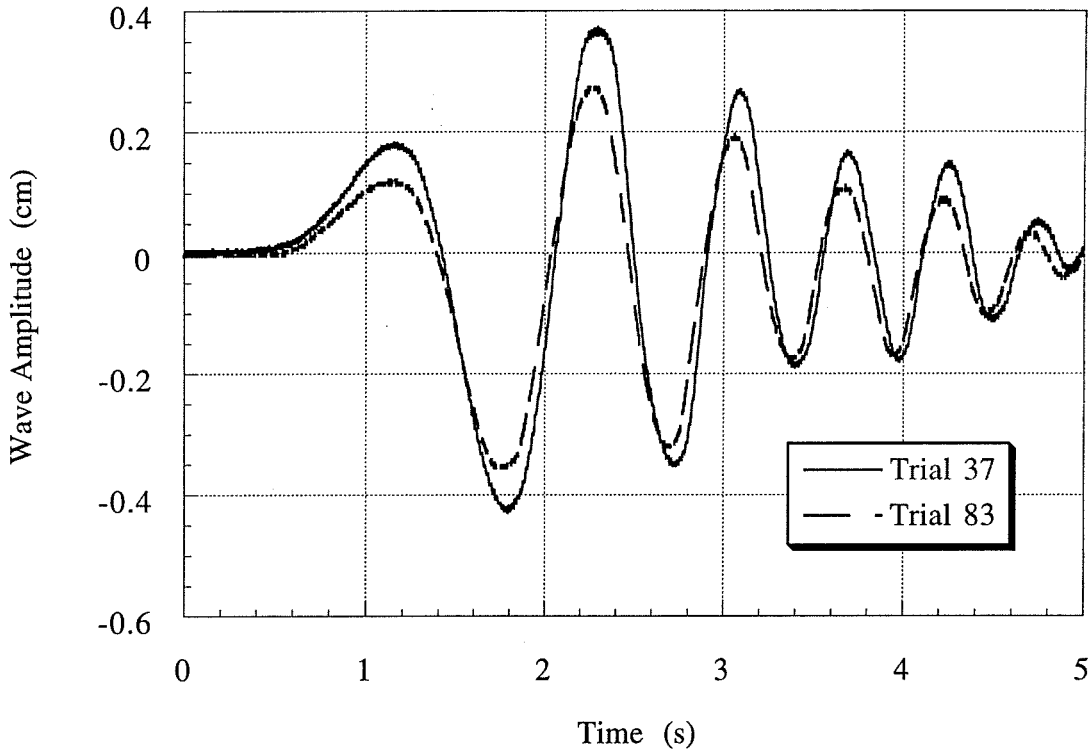

Figure A.29: Comparison of measured far-field wave amplitudes above the middle of the initial material position for Trials 37 and 83. Glass marbles were released from rest with an initial submergence of d≈74 mm. The agreement between the two wave profiles is poor.

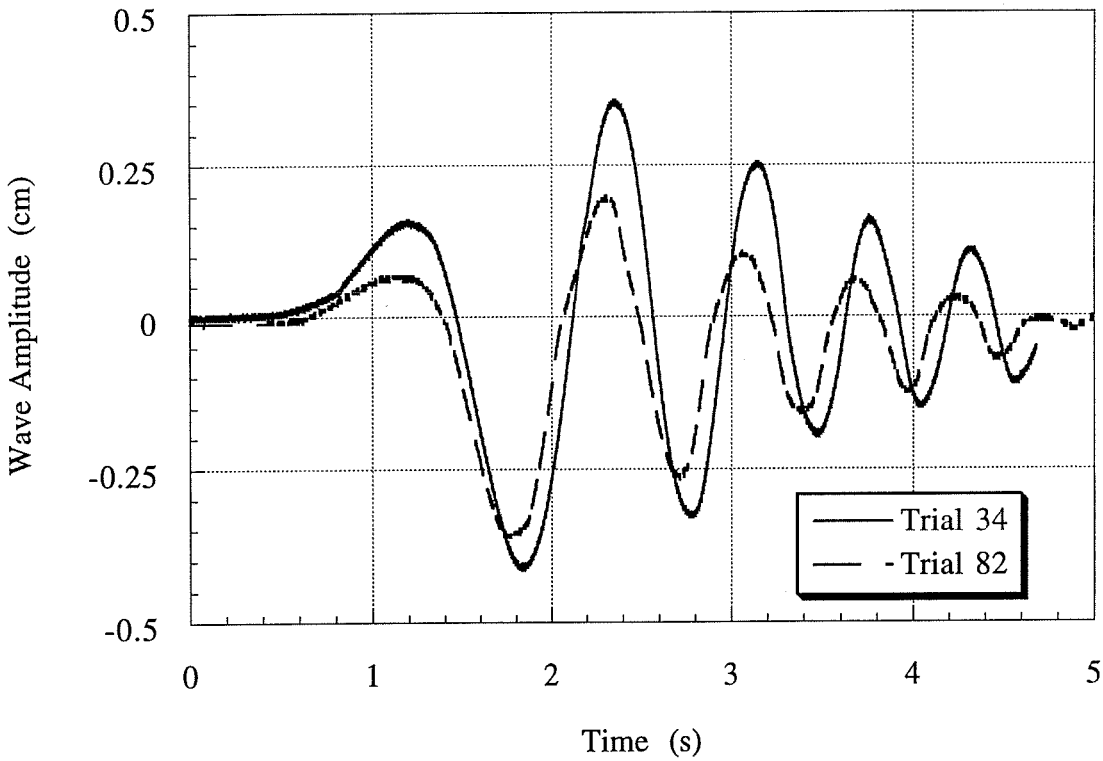

Figure A.30: Comparison of measured far-field wave amplitudes above the middle of the initial material position for Trials 34 and 82. Three millimeter glass beads were released from rest with an initial submergence of d≈74 mm. The agreement between the two wave profiles is poor.

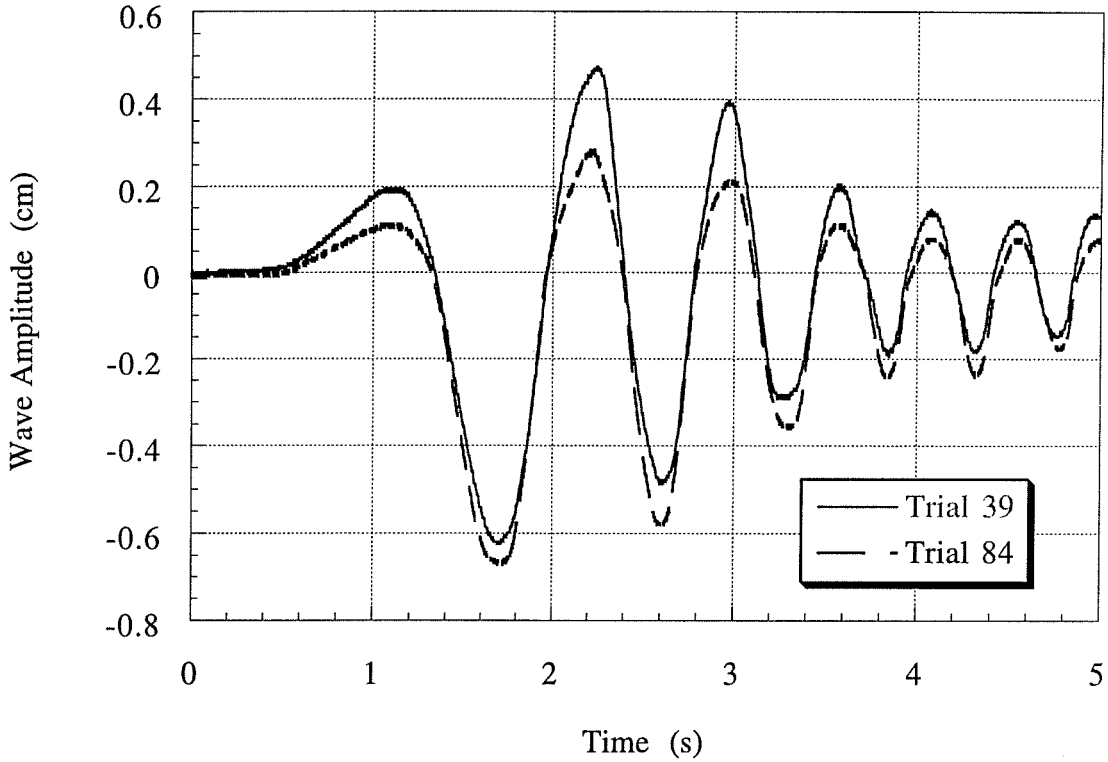

Figure A.31: Comparison of measured far-field wave amplitudes above the middle of the initial material position for Trials 39 and 84. Two millimeter lead shot was released from rest with an initial submergence of d≈77 mm. The agreement between the two wave profiles is poor.

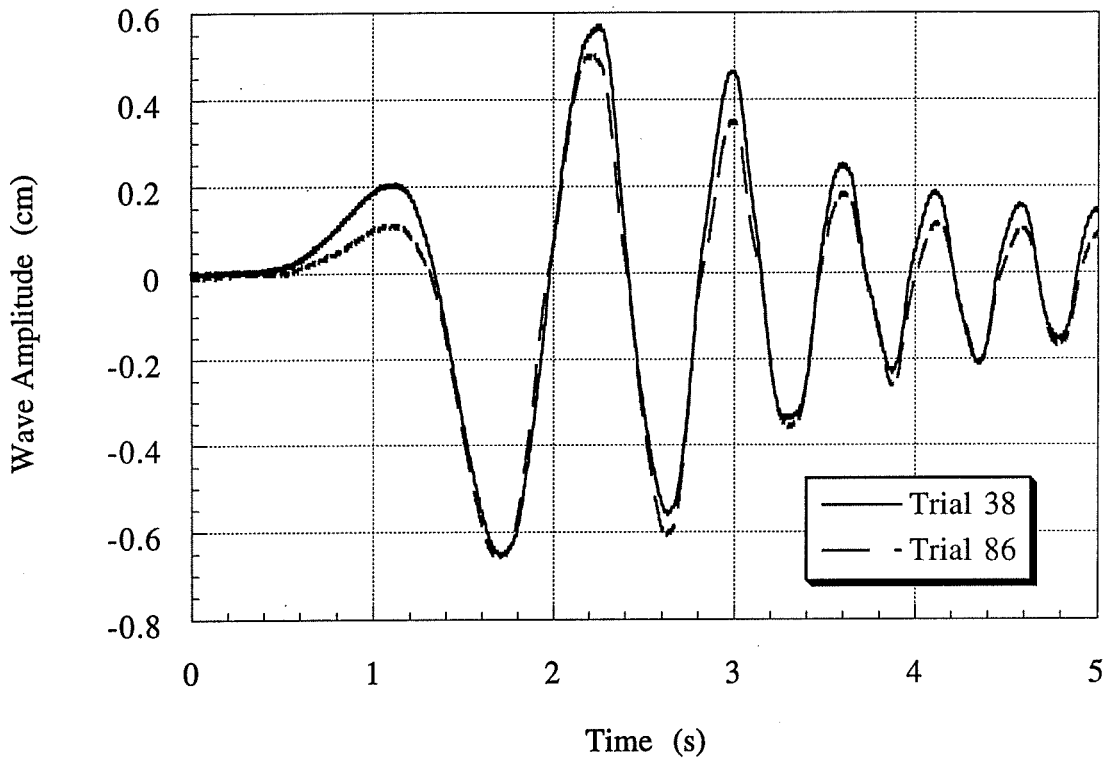

Figure A.32: Comparison of measured far-field wave amplitudes above the middle of the initial material position for Trials 38 and 86. Three millimeter lead shot was released from rest with an initial submergence of d≈74 mm. The agreement between the two wave profiles is within standard errors.

Appendix B

B. Error Analyses

Every plot of experimental or simulation data in this thesis shows standard errors if those errors are greater than the symbol used to denote the data. This appendix derives these error estimates. Significant effort has been made to ensure that error estimates are independent from the actual data being shown. Therefore, agreement of data to within the error bars shown represents an affirmation of the error estimates in this appendix as well as a general understanding of the accuracy and repeatability of the experimental methods employed for this work.

B.1 Landslide Motion and Deformation Analyses

It was found early on in this research that inaccurate landslide kinematics could conceal trends in the nondimensional wavemaker formulation. Therefore, much of the work presented in this section evolved from the need to reduce the errors derived from landslide kinematics as much as possible. Hence, the purpose of this section is to estimate the accuracy of the landslide motion data.

B.1.1 Solid Block Coulombic Friction

The error in the critical friction angle ψ was taken as half of the 1° precision available from the protractor used to measure the incline angle. The resulting error in the Coulombic friction coefficient C_n is nearly ±3% for all solid blocks, a fact that follows either from the nearly linear behavior of the tangent function for such a small argument or from direct substitution of $\psi_c+\Delta\psi$ in equation (4.7). The effective gravitational forcing when $\theta=45° \pm 0.5°$ is given by the fourth column of Table 5.1 with an error found by substituting the smaller bound for θ and the larger bound for ψ or *vice versa*. The error is once again around ±3%.

B.1.2 Solid Block Initial Acceleration

Based on the static accelerometer calibration shown in Figure 4.9, the accuracy of accelerometer measurements is typically much less than 1% of actual acceleration values. Therefore, almost all of the error in the initial acceleration measurements was derived from some lack of repeatability. Sources of error include spurious vibrations of the wave tank, drift in the zero level of the accelerometer, unintentional differences in the way the Nylon fishing line holding the solid block was released, small differences in the initial block position and incline surface, or even differences in block-incline friction induced by different contact (or block settling) times. The curve fits of the initial accelerations of blocks 1_n-3_n shown on Figures 5.1-5.3 are sufficiently rich to capture the inflection points present in the data and appear to be good predictors of mean initial accelerations. Assuming that there is a single variance σ^2 that describes the distribution of data about one of the curve fits over all initial submergences d, then the Central Limit Theorem from statistics dictates that the observed mean of the results tends towards a Gaussian distribution about the actual mean as the number of experimental points goes to infinity. That is, any suitable curve fit approaches the expected initial acceleration as the number of experimental points goes to infinity over some small range of initial submergences. Since the range of initial submergences is arbitrary for a relatively flat function $a_o \approx k$, the least-squares curve fit is used to represent the observed mean even if the number of samples for any given initial submergence is small. In practice, all that is desired is an estimate of the repeatability of the initial acceleration about the curve fit so

$$\% \text{ Error} \approx 100\% \frac{a_o - a_o(d)}{a_o(d)} \tag{B.1}$$

suffices to provide a reasonable estimate of the standard deviation σ, where a_o is the observed initial acceleration and $a_o(d)$ is the curve fit mean result. The repeatability of the initial acceleration gives rise to a $\pm 5\%$ error at one standard deviation about the curve fit for all three solid blocks and over all initial submergences tested. Since most initial accelerations are around 1.7 m/s^2, there exists an almost constant standard deviation of $\sigma = 0.09$ m/s^2 for solid blocks 1_n-3_n and the original assumption is now justified *a posteriori*.

For solid blocks 2_o-2_l listed in Table 5.2, the five or six measured initial accelerations provide errors of between ±2-13% with the standard deviation for each block given in the table.

The two independent techniques used for estimating the error in the initial acceleration obtained from high speed movies of solid block landslides are now described. The first technique examined the inherent sensitivity of the parabolic curve fits to the number of position measurements available. Since it not clear for exactly how long the parabolic curve fit remains valid in time, the last two measurements were systematically removed from the plot of position *versus* time for Trial 54 with the curve fit recalculated each time. The five distinct initial accelerations for this one trial had a standard error of ±5%. The second technique examined the error incurred by not knowing the start of a solid block trial to within better than one movie frame. Position *versus* time data from Trials 44 and 50 were displaced both right and left by 0.01 s and then curve fit by a parabola. The mean error incurred in the initial acceleration by a one movie frame uncertainty in the start of a trial was ±16%. This mean error can be considered a standard error since the starting time of a trial was known to better than 1 frame in about 63% of the solid block trials studied -- those trials for which a proper calibration of the timing LED on the film was available. Given that both of these errors are independent and that variances are additive, the expected error for an initial acceleration obtained from a high speed movie is ±17% at one standard deviation. This error estimate is shown in Figure 5.4.

B.1.3 Solid Block Added Mass Coefficient

Errors in the gravitational forcing g_{eff} also contribute to the error in the added mass coefficient. Taking the logarithm of both sides of equation (5.5) and differentiating yields

$$\frac{dC_m}{C_m} = \frac{(m_b + C_m m_o)}{C_m m_o} \left[\frac{da_o}{a_o} + \frac{dg_{eff}}{g_{eff}} \right] \qquad \text{(B.2)}$$

where the solid block mass m_b and displaced water mass m_o are considered known quantities with little to no error as shown in Section 4.2.1. Given a ±5% error in the initial acceleration from Section B.1.2, a ±3% error in the effective gravitational forcing from Section B.1.1 as well as $m_b/m_o \approx 2$ and $C_m \approx 0.8$, the added mass coefficient C_m can only be known to within ±28% at one standard deviation for the initial acceleration

measurements shown in Figures 5.1-5.3. The cumulative ±8% error of the two inputs is amplified around 3.5 times by the fraction in front of the square brackets of equation (B.2). The standard errors are not shown on Figure 5.5 because they would obscure the data. However, the spread of the data gives an accurate impression of the per cent error just derived.

For solid blocks 2_o-2_l listed in Table 5.2, the mean of all six added mass coefficients is $C_m \approx 0.8$ while the standard deviation $\sigma=0.07$ of the six blocks indicates a standard error of ±9%. This error in the added mass coefficient of these six blocks is based on the mean values in the table rather than on the raw data used to construct Table 5.2.

B.1.4 Solid Block Terminal Velocity and Drag Coefficient

The mean drag coefficient of $C_d=1.7 \pm 0.17$ varied by ±10% at one standard deviation. Using the mean value of the drag coefficient $C_d=1.7$ in equation (3.74) yielded theoretical terminal velocities accurate to within ±3% at one standard deviation from the maximum measured velocities. According to equation (3.78), the measured velocities should theoretically be very close to the actual terminal velocities. Hence, terminal velocities are known to within ±3% at one standard deviation. The ±3% error in the terminal velocity can be used to calculate another estimate of the error in the drag coefficient by taking the logarithm of both sides of equation (5.10) and differentiating

$$\frac{dC_d}{C_d} = \frac{2\,du_t}{u_t} + \frac{dg_{eff}}{g_{eff}} + \frac{dA}{A} \qquad \text{(B.3)}$$

where the error in the projected area is expected to be around ±2% from measurement accuracy and solid block clearances with the side walls. Given the error in the effective gravity from Section B.1.1, it follows that the drag coefficient is known to within ±11% at one standard deviation. This is almost exactly the same error in the drag coefficient as found in Table 5.3. While the two methods of estimating the error are not completely independent, the agreement is reassuring and was certainly not a foregone conclusion. The relatively large error in the drag coefficient is due in part to the square root in equation (3.74) for the terminal velocity which ends up doubling the error of the terminal velocity. Hence, the solid block terminal velocity is not overly sensitive to the drag coefficient given the inverse power of $C_d>1$ within the square root.

B.1.5 Solid Block Motion Characteristics

Given the ±5% error in the initial acceleration from Section B.1.2 and the ±3% error in the terminal velocity from Section B.1.4, the standard errors in s_o and t_o follow from

$$\frac{ds_o}{s_o} = \frac{2\,du_t}{u_t} + \frac{da_o}{a_o} \tag{B.4}$$

$$\frac{dt_o}{t_o} = \frac{du_t}{u_t} + \frac{da_o}{a_o} \tag{B.5}$$

where s_o is known to within ±11% while t_o is known to within ±8%. These error estimates are needed in Section 5.2.3 when constructing wavemaker plots and in Section B.2.5 when estimating the errors of the wavemaker plots.

B.1.6 Material Motion Characteristics

In order to convert landslide traces from pixel coordinates to real space coordinates, a conversion factor had to be determined for each movie frame. Registry marks were evenly spaced 101.6 mm (four inches) along the front of the wave tank parallel to (yet below) the incline. Each landslide trace had two black dots drawn on the piece of paper at the location of different registry marks. The distance in real space along the incline between the two black dots was either 101.6 mm (four inches) or 203.2 mm (eight inches) depending on the movie magnification and the instantaneous landslide position. The black dots were placed 25.4 mm (one inch) below the surface of the incline as measured on the piece of paper. The conversion factor F from pixel distance to real distance was found by dividing the real spacing between the registry marks by the distance in pixels between the registry marks. The distance in pixels between the two registry marks was calculated from the centroid (x_i,z_i) position of each black dot given by NIH Image

$$d_{1,2} = \sqrt{(x_1 - x_2)^2 + (z_1 - z_2)^2} \tag{B.6}$$

where the coordinate system is established for each scan by the scanner and has no bearing on the development given here. The absolute error in locating the black dots on each sheet of paper was ±0.5 mm over an absolute separation distance of between 24.6 mm and 37.9 mm depending on the magnification of each movie. Using a typical separation distance of 305 mm applicable to most movies, the accuracy error in the

conversion factor F is about ±0.2%. Over a typical sample size of 16 conversion factors per movie, the conversion factor had an error of ±0.25% at one standard deviation. Considering the mean conversion factor of F≈0.03437 cm/pixel for all material landslide movies as a typical value, an error of ±0.32% or $\pm 1.1 \times 10^{-4}$ cm/pixel is found at one standard deviation.

The registry marks allowed the absolute position of the landslide centroid along the incline to be calculated in real space for each landslide trace. The first step was to locate the intersection of the straight line joining the two black dots with the perpendicular line going through the landslide centroid. The straight line connecting the two black dots formed an axis parallel to the incline with a slope

$$m = \frac{z_1 - z_2}{x_1 - x_2} \tag{B.7}$$

in the coordinate system of the scanned image, where the black dot centroid with coordinates (x_2,z_2) is further down the incline. If the landslide centroid given by NIH Image is denoted by the point (x_C,z_C), then the closest point on the straight line to the point (x_C,z_C) defined an intersection point

$$x_I = \frac{z_C - z_1 + m\,x_1 - \frac{x_C}{m}}{m - \frac{1}{m}} \tag{B.8}$$

$$z_I = m\,x_I + y_1 - m\,x_1 \tag{B.9}$$

where (x_1,z_1) are the coordinates of the black dot centroid further up the incline. The straight line connecting the intersection point to the landslide centroid was perpendicular to the straight line connecting the two black dots. The intersection point was calculated for each landslide trace.

The second step involved calculating the distance in pixels between the intersection point (x_I,z_I) and the black dot centroid (x_2,z_2) further down the incline. The distance in pixels

$$d_{C.2} = \sqrt{(x_C - x_2)^2 + (z_C - z_2)^2} \tag{B.10}$$

gave the converted distance $Fd_{C.2}$ in real space. The landslide centroid could now be assigned an absolute position along the incline for each landslide trace merely by knowing which registry mark corresponded to the point (x_2,z_2). The third step required identifying the registry mark corresponding to the point (x_2,z_2) in the first landslide trace of a given material landslide trial. As subsequent frames were traced, the point (x_2,z_2) would occasionally jump to the next registry mark. For each jump to a successive registry mark down the incline, an additional 101.6 mm (four inches) was added to the centroid position along the incline. Therefore, each landslide trace in a given material landslide movie had the correct relative centroid position along the incline in real space. The last step was to subtract off the centroid position of the first landslide trace in the movie from all centroid positions in the movie so that s=0 at t=0 without changing the relative centroid positions. Repeated tracings of a single movie frame in Trials 33, 38, and 89 indicate a repeatability of about ±1 mm in the centroid positions.

The method used to calculate the framing rate to within ±0.01% is given in Section 4.2.2. The method used to determine the beginning of a material landslide trial to within ±1 ms was given in section 4.3.2. Neither of these errors is significant and the time associated with each high speed movie frame can be considered exact to within ±1 ms. The data for material landslide centroid position along the incline as a function of time was curve fit by equation (3.78) using the KaleidaGraph general curve fitting algorithm. The result of the curve fits was a characteristic distance s_o and characteristic time t_o for each material landslide trial. Three such curve fits are shown in Figures 5.11 to 5.13.

The normal errors in the characteristic distance and time scales were established directly by the KaleidaGraph general curve fitting algorithm for each least-squares curve fit of equation (3.78). These normal errors were based on the reliability of the fit to the data and are an important feature of the KaleidaGraph software. The curve fitting algorithm in KaleidaGraph utilizes the Levenberg-Marquardt algorithm to minimize the χ^2 merit function. Press *et al.* (1992) describe the application and programming of the fully nonlinear and recursive Levenberg-Marquardt algorithm for minimization problems. The normal errors in the curve fit parameters are a direct result of evaluating the second partial derivatives of the χ^2 merit function with respect to the curve fitting parameters near the minimum of the χ^2 merit function. Moreover, the normal errors given by KaleidaGraph software are the correct statistical measures of the standard errors in the curve fitting parameters based on the sample data.

The curve fitting algorithm within KaleidaGraph had trouble converging for certain position *versus* time records of centroid motion down the incline. For the lead shot landslides of Trials 38 and 84, all of the data appeared to be within the domain of the first term of the Taylor series given in equation (3.87). The result was that data being curve fit with two parameters s_o and t_o only contained information for the initial acceleration $a_o \equiv s_o/t_o^2$. Fitting a single parameter curve with two parameters often results in an infinite number of combinations of the characteristics of motion that would fit the data. One could watch the curve fit of the data diverge with each subsequent iteration. Trials 85 and 93 each had poor data that rendered convergence of the curve fit very slow and the values of the fitted parameters highly inaccurate. Errors on the order of 100% were found in the curve fit parameters with the value of the errors dependent on the desired accuracy of the curve fit. For all other curve fits, values of the parameters converged after a few iterations and were independent of the accuracy sought. For all material landslides listed in Table 5.4, the mean error in the characteristic distance s_o was ±14.5% while that of the characteristic time t_o was ±7.9% both at one standard deviation. These errors are not significantly different from those found for solid block characteristics of motion in Section B.1.5 above. However, if one calculates an initial acceleration $a_o \approx s_o/t_o^2$ from equation (5.8), then one can expect a standard error in the initial acceleration of ±30.3%. Likewise, a terminal velocity $u_t \approx s_o/t_o$ calculated from equation (5.10) has an error of ±22.4% at one standard deviation. These errors are shown in Figures 5.15 and 5.17.

As the gravity currents approached the bottom of the incline in glass bead Trials 87, 89 and 91, one trace was made of the entire gravity current profile while another trace was made of the dense core of the landslide excluding the landslide wake. The distinction between gravity current core and wake was easily perceived as a rather sharp gradient in the brightness of the landslide profile -- see Figures 5.8 and 5.10 for examples. The mean difference in landslide centroid position along the incline for the three trials was 9.8%. In all cases studied, the entire gravity current centroid had not progressed as far along the incline as the dense core because of the presence of a wake. By arbitrarily assigning a relative density of one half to the landslide wake, errors in the centroid position along the incline of 4.9% can be expected. These errors were neglected for all landslides not composed of glass beads or garnet sand since landslide wakes were either accurately reproduced during tracing or non-existent. Figures 5.11, 5.13 and 5.23 indicate the expected standard error in the centroid position along the incline.

B.1.7 Material Landslide Center of Mass Height

The centroid height above the incline was found by first calculating the distance in pixels between the intersection point (x_I,z_I) and the material landslide centroid (x_C,z_C) in the scanned coordinates. The distance between these points in pixels

$$d_{C,I} = \sqrt{(x_C - x_I)^2 + (z_C - z_I)^2} \tag{B.11}$$

provided the converted distance $Fd_{C,I}$ in real space. The landslide centroid could now be assigned an absolute height perpendicular to the incline for each landslide trace. However, the distance in real space between the straight line connecting (x_1,z_1) to (x_2,z_2) and surface of the incline needed to be subtracted from $Fd_{C,I}$. This distance is known to be 25.4 mm (one inch) on the sheet of paper with the landslide trace. Therefore, a conversion factor was needed to convert distance on the sheet of paper to real space distance. For each material landslide movie, the landslide trace with the conversion factor F closest to the mean conversion factor for all landslide traces was found. The distance between the black dots on the sheet of paper was then accurately measured. The real distance between the black dots (either 101.6 mm or 203.2 mm) divided by their separation on the sheet of paper provided this specific conversion factor. The distance 25.4 mm was multiplied by this conversion factor and subtracted from all distances $Fd_{C,I}$ for that material landslide movie. The result was the landslide centroid height perpendicular to the incline z_c described in Section 5.1. Repeated tracings of a single movie frame in Trials 33, 38, and 89 indicate a repeatability of about ±0.5 mm in the centroid heights. Three plots of centroid height above the incline in time can be found in Figures 5.24 to 5.26.

The error in the centroid height above the incline due to formation of a landslide wake was calculated from the same three trials described in Section B.1.6. The mean difference in landslide height above the incline for the three trials was 6.5%. In all cases studied, the entire gravity current centroid was situated higher above the incline than the centroid of the dense core. By arbitrarily assigning a relative density of one half to the landslide wake, errors in the centroid height above the incline of 3.3% were found. These errors were neglected for all landslides not composed of glass beads or garnet sand since landslide wakes were either accurately reproduced during tracing or non-existent. Figures 5.24 to 5.26 show the resulting error bars at one standard deviation.

The initial normal rate of strain was found from a linear curve fit of the data near t=0. Since it was not clear how far the linear curve fit should extend in time, two or more curve fits were attempted around what appeared to be the limit of linear behavior judged by eye. Since a rate of change was being extracted from the data, reasonably small changes in the temporal extent of the curve fit could result in appreciable changes in the slope of the linear curve fit -- i.e., differentiation exacerbates errors in data. Therefore, an error in the repeatability of the initial normal rates of strain for each trial was sought. A mean standard error of ±23% was found for the initial normal rate of strain of all trials. Only Trials 83 and 90 had errors significantly higher than the mean at ±45% and ±43%, respectively. The initial normal rates of strain and their corresponding errors can be found in Table 5.5.

B.1.8 Material Landslide Area

The cross-sectional area of a material landslide was analyzed over the duration of landslide deformation during a trial. Every third or fourth movie frame was traced for a typical material landslide giving on average 16 landslide profiles per trial. The area was measured by NIH Image and converted from square pixels to square centimeters using

$$A = N F^2 \tag{B.12}$$

where N is the number of square pixels and F is the conversion factor from pixels to centimeters derived in Section B.1.6. The perimeter of a landslide trace was also provided by NIH Image and converted to centimeters by

$$p = N F \tag{B.13}$$

where N is the number of perimeter pixels on the edge of the black and white image. With the maximum scanning density of 600 dpi, the size of each pixel on the sheet being scanned was 42 μm. The ability of a 42 μm grid to resolve surface length depends on the size of the surface roughness and the fractal dimension of the surface rendition in pixels. No error analysis on the perimeter is attempted. Instead, the perimeter is used as an error estimate of the area repeatability below.

Repeated analysis of the same image revealed a scanning error of up to 0.4% in the pixel count of the traced area. This error is probably associated with the orientation of the

image relative to the quantized pixel grid. The error estimate in the area calculation is therefore given by

$$\frac{dA}{A} = \frac{dN}{N} + 2\frac{dF}{F} \tag{B.14}$$

which amounts to an accuracy error of at most ±1% at one standard deviation. The repeatability of landslide area traces was estimated from the equation

$$\frac{dA}{A} = \frac{0.05\,p}{A} \tag{B.15}$$

where p is the perimeter of the cross-sectional profile and a tracing error of ±0.05 cm was assumed over the entire perimeter in real space. The values found from equation (5.19) were typically consistent over an entire landslide and were even similar between landslide experiments. This is not surprising given that most material landslides had similar surface to volume ratios. The mean error in repeatability was 4.6% for all traces over all trials with a maximum mean error of 6.2% for the traces of the 2 mm lead shot landslides. This error estimate agrees with the worst observed repeatability of landslide area found when the same movie frame was traced several times. Combining the mean repeatability error and the accuracy error provides a standard error in landslide area of about 4.7%. This method of arriving at landslide area appears to be remarkably robust. This standard error is shown in Figures 5.21 to 5.23.

However, two other sources of error need to be considered in addition to the customary analyses provided above: i) perspective changes and ii) blurring of the front face of the landslide. In particular, the insidious effects of perspective were measurable despite attempts to reduce the effect with careful lighting. Even for the best backlit experiments performed with dark particles, the easily delineated front face of the landslide blurred once surface shearing began to mobilize particles. For many material landslides, the center of mass motion had already carried the front face past the movie camera before the perspective of the front face of the landslide became blurred by particle motion. Calcite landslides formed a notable exception in part because the irregular shape of the material particles apparently made them easy to loft in the surface shearing flow. However, almost half of the material landslides were performed with clear glass beads for which perspective of the front face of the landslide became a shady region of subtle grays. The response to this dilemma was to calibrate the experimenter's eye to the rate of

disappearance of the front face of the landslide with distance down the incline provided the said experimenter acknowledge the deficiency during the first few (usually four or five) landslide traces (out of 15-20 total traces). It is difficult to gauge reliable error estimates for the corrected landslide area during the first few traces. However, deliberate attempts to completely include the entire visible front face of the landslide amounted to around 15% errors in the landslide area at early times (close to $t=0^{+}$). Science is clearly inept without the occasional assistance of skillful artisans.

Examples of area change with either time or position can be seen in Figures 5.21 to 5.23. All but two material landslides (involving 0.5 mm glass beads and garnet sand) had linear variations of cross-sectional area in time. Therefore, linear curve fits were made over all area data for these material landslides. There was no estimate of accuracy available for these curve fits. Instead, a measure of repeatability was sought for the rate of change of area in time for all trials repeated more than once. A mean standard error of ±13% was found for the initial rate of area change in time. No trials had errors significantly different from the mean. The initial rate of change of area in time and the corresponding errors can be found in Table 5.5.

B.1.9 Landslide Rate of Deformation

Equation (3.86) is sufficiently accurate to serve as the source of an error analysis of the initial landslide rate of deformation. A typical value of the initial normal rate of strain is $-1\ s^{-1}$ with a standard error of ±23%. A typical value of the initial rate of area change in time is $1.5\ s^{-1}$ with a standard error of ±13%. The typical value of the initial landslide rate of deformation 2.5 rad/s has expected bounds of 2.08 rad/s and 2.93 rad/s based on the standard errors in the initial normal rate of strain and the initial rate of area change in time. The initial landslide rate of deformation therefore has an error of ±17% at one standard deviation. This per cent error was used to calculate the standard errors given in Table 5.5.

The error in the nondimensional landslide deformation Γt_o given in Table 5.6 was calculated from the chain rule of calculus

$$d(\Gamma t_o) = d\Gamma\, t_o + \Gamma\, dt_o \tag{B.16}$$

where t_o and dt_o are found in Table 5.4 while Γ and $d\Gamma$ are found in Table 5.5. Therefore, each error shown is calculated from standard errors for that particular trial. An estimate of the expected error for all trials is found from

$$\frac{d(\Gamma t_o)}{\Gamma t_o} = \frac{d\Gamma}{\Gamma} + \frac{dt_o}{t_o} \tag{B.17}$$

which has typical values of ±25% at about one standard deviation. The errors calculated from equation (B.16) and shown in Table 5.6 agree quite well with mean errors calculated from equation (B.17). The error in the nondimensional landslide deformation applies to Figure 5.44 although there is no clear way to indicate errors in Γt_o on the graph.

B.2 Solid Block Landslide Analyses

The computerized wave data acquisition used for this work allowed for a quantitative error analysis of every step of water wave measurement and processing. Therefore, reliable error bounds at one standard deviation are derived for measured and calculated characteristic waves quantities. Some references are made to wave measurements not included in this work. More than seventy near-field wave measurements were made with a laser rangefinder immersed in the water immediately above the solid blocks. The data were never used because the laser rangefinder failed to provide accurate solid block motion. However, the wave records are reliable and many experiments were repeated five times. In many instances, this is the only data set able to provide repeatability errors for wave measurements. Reliable error estimates for landslide kinematics and wave measurements have allowed reliable error bounds to be calculated for the nondimensional parameters in the wavemaker formalism.

B.2.1 Near-field Wave Measurements

The mean slope of the near-field wave gauge calibration curve in the region of zero displacement for the twenty Trials 25-44 was 3.7 mm/V. The A/D board had a 12 bit resolution of ±5 mV over the range ±10 V which for a typical near-field wave gauge gives an error of ±19 μm at one standard deviation. Likewise, the mean peak to peak noise for the twenty Trials 25-44 provided a typical error of ±54 μm at one standard deviation. The stepper motors had an accuracy of one step or ±33 μm. There were also accuracy errors incurred when curve fitting the calibration points with a polynomial. A

typical measure of these errors is the displacement of the curve fit at zero voltage difference which in theory should be zero. The near-field polynomial curve fits of the 12 solid block trials from Trial 25 to Trial 44 were offset from the origin by ±101 μm at one standard deviation. A comparison of the maximum near-field wave amplitudes for 25 trials (not reported herein) using a calibration curve before the trials were performed and another immediately after the trials were performed gives an excellent measure of the wave amplitude accuracy. The two calibration curves were used to convert each voltage signal into two maximum near-field wave amplitudes for each trial. The expected accuracy of the maximum near-field wave amplitude was the larger of ±210 μm or ±4.1% of the wave amplitude at one standard deviation. This error, found by comparing different calibration curves, is almost equal to the ±207 μm sum of the aforementioned accuracy errors and is therefore used below. The error expressed in length applies to smaller wave amplitudes while the error expressed in percentage applies to larger wave amplitudes. The error in the maximum near-field wave amplitude due to repeatability was found from 12 distinct solid block experiments (not reported herein) with each experiment repeated five times. The repeatability of the maximum near-field wave amplitude was the larger of ±96 μm or ±1.8% of the wave amplitude at one standard deviation. Given that accuracy and repeatability errors are independent, the total error in the near-field wave gauge measurement can be taken as the square root of the sum of the two variances. A typical error in near-field wave amplitude would therefore be the larger of ±231 μm or ±4.5% of the wave amplitude. This error estimate is shown on Figures 5.29 and 5.33.

Based on the repeated 2_a, 2_b, 2_n, 2_d, 2_e trials shown in Appendix A, the pointwise repeatability of the near-field wave record was ±229 μm at one standard deviation. The pointwise error in repeatability is greater than that of the maximum near-field wave amplitude due to the increasing signal drift at larger times when the water level is supposed to settle back to zero. The mean drift rate in the zero level voltage was 1.8×10^{-4} V/s with a typical variability of $\pm 3.6 \times 10^{-4}$ V/s at one standard deviation. The voltage drift rate was measured from the changes in zero level voltage at the beginning and end of the 12 wave gauge calibrations for solid block trials from Trial 25 to Trial 44 lasting between 250-350 s. After four seconds, the error in wave amplitude due to voltage drift alone could be in the range of ±20 μm at one standard deviation. Another source of drift is residual wetting of the wave gauge wires after a wave has passed. This form of drift is harder to quantify. The wave gauge calibration procedure is supposed to correct for this effect but the rates of water rise and fall differed between the gauge calibration and the

actual experiment waves. The maximum near-field wave amplitude is close enough to the beginning of the trial to not be subjected to significant amounts of drift and is therefore more repeatable. The pointwise error in near-field wave measurements just derived applies to Figures 5.27, 5.28, 5.42, and half of the figures in Appendix A.

B.2.2 Amplitude Integral

The error in $t_o\eta_{max}$ was calculated in the usual fashion and resulted in an error of ±12.5% at one standard deviation given error analyses from Sections B.1.5 and B.2.1. A comparison of the amplitude integrals for 25 trials (not reported herein) using a calibration curve before the trials were performed and another immediately after the trials were performed provided an error of ±146 μm·s or ±5.2% at one standard deviation. The repeatability of the amplitude integral for all 2_n, 2_d, 2_e trials was ±200 μm·s or ±5.3% at one standard deviation. The resulting error in the amplitude integral is therefore ±248 μm·s or ±7.4% at one standard deviation. This is approximately the same error found by integrating the near-field errors discussed in Section B.2.1 from t=0 s until about $t_x \approx 1$ s. Both error estimates made here are employed in Figure 5.30. The nondimensional ratio $I(0)/t_o\eta_{max}$ in Figure 5.30 has an error of ±19.9% at one standard deviation.

B.2.3 Energy Integral

The error in $t_o\eta_{max}^2$ was calculated in the usual fashion and resulted in a standard error of ±17% given error analyses from Sections B.1.5 and B.2.1. A comparison of the near-field energy integrals for 25 trials (not reported herein) using a calibration curve before the trials were performed and another immediately after the trials were performed yielded an approximate accuracy error of ±1.4 mm^2·s or ±11.0% at one standard deviation. The repeatability of the near-field energy integral for all 2_n, 2_d, 2_e trials was ±3 mm^2·s or ±13.7% at one standard deviation. The resulting error in the near-field energy integral is ±3.3 mm^2·s or ±17.6% at one standard deviation. The close agreement between the two errors given here is fortuitous, although they must be similar in magnitude. The energy integral error given here is more than double that of the amplitude integral because the energy integral extended until about t=4 s which increases the error associated with drift. These errors are shown on Figure 5.31. The nondimensional ratio $E_p(0)/t_o\eta_{max}^2$ in Figure 5.31 has an error of ±34.6% at one standard deviation.

A measure of the accuracy of the far-field energy integral was obtained by applying before and after calibration curves to Trials 26, 29 and 30. An accuracy of ±0.3 $mm^2 \cdot s$ or 3.6% at one standard deviation was found. The accuracy is not exceptional: the far-field calibration curves had relatively small curvatures converting relatively small waves amplitudes when compared to the near-field. The repeatability of the far-field energy integral for all 2_n, 2_d, 2_e trials was ±8.7 $mm^2 \cdot s$ or ±33.5% at one standard deviation. The far-field energy integral is seen to be quite sensitive to the highly variable rates of drift. The resulting error in the far-field energy integral is ±8.7 $mm^2 \cdot s$ or ±33.7% at one standard deviation. Figure 5.40 shows error bars for the nondimensional ratio $E_p(4.25)/E_p(0)$ with values of ±51.3% at one standard deviation.

Since the error associated with the energy integral depends on the wave gauge used to measure the wave record, no single error estimate would be appropriate for Figure 5.39. It was decided to set vertical error bars for the data at ±25% to provided an approximate indication of the expected error in the energy integral.

B.2.4 Far-field Wave Measurements

The mean slope of the far-field wave gauge calibration curve in the region of zero displacement was 5.4 mm/V. Therefore, the A/D board wave resolution was typically ±27 μm at one standard deviation for the far-field wave gauge. Likewise, the mean peak to peak noise provided a typical error of ±144 μm at one standard deviation. The far-field wave gauge was consistently noisier than the near-field wave gauge. The stepper motor once again had an accuracy of ±33 μm. The polynomial curve fit usually missed the origin by ±46 μm at one standard deviation. Summing the accuracy errors yields an expected accuracy of a far-field wave amplitude of ±250 μm at one standard deviation. Another measure of the accuracy was obtained by applying before and after calibration curves to Trials 26, 29 and 30 and comparing maximum Airy wave amplitudes. An estimate of the accuracy error of the maximum Airy wave amplitude was ±30 μm or 1.9% at one standard deviation. The larger estimate of the accuracy error ±250 μm is used below, especially given the noise in the far-field signal. The repeatability of the maximum Airy wave amplitude for all 2_n, 2_d, 2_e trials was ±330 μm or ±14.8% at one standard deviation. There is much less repeatability in far-field wave records. Summing the variances yields an error in maximum Airy wave amplitude of ±414 μm or ±18.6% at one standard deviation. The per cent error given here was inferred from the repeatability error. Figure 5.33 shows the standard error in the maximum Airy wave amplitude.

Based on all repeated 2_a, 2_b, 2_n, 2_d, 2_e trials, the pointwise repeatability of the far-field wave record was ±326 μm at one standard deviation. The pointwise error in repeatability is greater than the error of the maximum Airy wave amplitude due to the increasing signal drift at larger times when the water level is supposed to settle back to zero. The mean drift rate in the zero level voltage was 1.3×10^{-4} V/s with a typical variability of $\pm 0.9 \times 10^{-4}$ V/s at one standard deviation. After four seconds, the error in wave amplitude due to voltage drift alone could be in the range of ±8 μm. The pointwise error in far-field wave measurements given here applies to Figures 5.32, 5.43, and half of the figures in Appendix A.

B.2.5 Wavemaker Curve

The error bars on Figures 5.34 and 5.35 represent one standard deviation and are the culmination of many separate error analyses. To begin with, the error in the characteristic distance s_o is given by equation (B.4) as ±11% error at one standard deviation. Likewise, the error in the characteristic time t_o is given by equation (B.5) as a standard error of ±8%. For a perfectly well known gravitational acceleration, the Hammack number has an error given by

$$\frac{dHa_o}{Ha_o} = \frac{dt_o}{t_o} + \frac{dd}{2\,d} + \frac{db}{b} \tag{B.18}$$

which results in a ±9.5% standard error since the error in each distance measurement is approximately ±1%. The error in the initial block submergence results from the 0.5 mm accuracy of the submergence measurement while the error in the block size results from the 0.5 mm precision of solid block construction. The error in the nondimensional wave amplitude η_{max}/s_o is clearly ±15.5% at one standard deviation given results from Section B.2.1. These error estimates also appear in Figures 5.37 and 5.48.

The existence of a wavemaker curve theoretically relates the maximum near-field wave amplitude error to errors in the landslide geometry and kinematics. If the theoretical wavemaker curve equation (5.40) with n=2 is exact, then there is an intrinsic error in the maximum near-field wave amplitude of ±8% at one standard deviation. On the other hand, if equation (5.41) with the exponent n=1 is exact, then one finds an intrinsic standard error of ±4.5% in the maximum near-field wave amplitude.

B.2.6 Linear Theory Predictions

If the solid block motion used to calculate theoretical wave amplitudes of corresponding solid block trials were exact, then there would be no horizontal error bars in Figure 5.37. However, errors in Ha_o found in Section B.2.5 above become part of the theoretical error when comparing experimental and theoretical nondimensional wave amplitudes. The correct way to take the error in Ha_o into account is to use equation (5.35). Taking the natural logarithm of each side of equation (5.35) and differentiating yields the error in the Hammack number multiplied by the factor n=1.625. There results an error in η_{max}/s_o of ±15.4%.

B.2.7 Energy Conversion

The vertical error bars in Figure 5.41 were calculated from

$$\frac{de}{e} = \frac{2\,d\eta_{max}}{\eta_{max}} + \frac{dd}{2\,d} + \frac{da_o}{a_o} + \frac{du_t}{u_t} + \frac{2\,db}{b} \qquad \text{(B.19)}$$

which provides a standard error of ±19.5%.

B.3 Material Landslide Analyses

Standard errors in the characteristics of material landslide motion are given in Section B.1.6. The error in the maximum near-field wave amplitude from Section B.2.1 was used as well. The error analyses of material landslide wavemaker plots was carried out in the same manner as described in Section B.2.5 for solid block landslides. The standard error in the Hammack number Ha_o is found to be ±9.5% while that of the nondimensional wave amplitude is ±19% at one standard deviation. These errors are indicated on Figure 5.44. However, Figure 5.44 does not indicate the ±25% error in the nondimensional landslide deformation calculated in Section B.1.9 above.

B.4 Numerical Simulation Analyses

Laplace's partial differential equation arises from conservation of volume in an inviscid fluid flow. Therefore, an accurate ideal fluid simulation that uses Laplace's equation

should do an excellent job conserving mass. In the very least, any loss of mass should be minimized as discussed in Section 5.4.1. The relative volume change per unit width $\Delta V/V_o$ was calculated at each time step by the simulation. Since most of the volume change can be attributed to the landslide vertex, the characteristic wave height calculation made in Section 3.1.3 can be used to evaluate the expected error in the numerical simulations. Replacing $bs_o\sin\theta$ in equation (3.14) with $\Delta V(t_o)$ gives the error estimate

$$\frac{\Delta H}{2} \approx \frac{\Delta V(t_o)}{t_o \sqrt{g\, d}} \tag{B.20}$$

in the maximum near-field wave amplitude. The numerical simulations have a typical error in the maximum near-field wave amplitude of 5.6% due to errors in the conservation of volume. This error appears in Figures 5.48 and 5.50.

Appendix C

C. Raw Data

The data used to construct figures in Chapter 5 are provided in this appendix. Experimental data are identified by the type of landslide and ordered by increasing trial number. Numerical simulations are ordered by increasing run number. The notation in the tables is consistent for a given type of landslide: solid block, material, or simulated. The entry "NA" in the tables means either "not applicable" or "not available." The numbers appear as they did in the KaleidaGraph spreadsheets; they were not truncated to the significant decimal place. All trials were performed with an incline angle 45° from horizontal. Equation numbers in parentheses sometimes describe a column to avoid notational ambiguity. The solid block characteristics of motion in Table C.2 were calculated from equations (3.75). Equation (3.97) in Table C.4 yielded the linear theory prediction of the nondimensional maximum near-field wave amplitude. Equation (5.26) in Table C.7 provided the channel depth corresponding to deep water waves propagating in the far-field. Equations (5.8) and (5.10) estimated the experimental initial acceleration and terminal velocity of material landslides, respectively. The initial acceleration a_o in Table C.10 and the terminal velocity u_t in Table C.11 are theoretical values calculated from equations (3.73) and (3.74), respectively. The particle velocities in Table C.14 were taken from Table 4.3. The computer simulations employed a Coulombic friction coefficient C_n=0.344 and a nondimensional solid block size b=1.

Table C.1: Solid Block Landslide Initial Geometry and Long Wave Celerity

Block #	Trial	b (m)	d (m)	$\sqrt{g\,d}$ (m/s)	d / b
2_n	25	0.086	0.0745	0.85489	0.86628
2_n	26	0.086	0.1160	1.06680	1.34880
2_n	27	0.086	0.0970	0.97548	1.12790
2_a	28	0.086	0.0745	0.85489	0.86628
2_b	29	0.086	0.0745	0.85489	0.86628
2_d	30	0.086	0.0745	0.85489	0.86628
2_e	31	0.086	0.0745	0.85489	0.86628
2_o	41	0.086	0.0740	0.85202	0.86047
2_l	42	0.086	0.0740	0.85202	0.86047
1_n	43	0.124	0.0740	0.85202	0.59677
1_n	44	0.124	0.0450	0.66442	0.36290
2_n	47	0.086	0.0730	0.84624	0.84884
2_d	48	0.086	0.0730	0.84624	0.84884
2_e	49	0.086	0.0730	0.84624	0.84884
4_n	50	0.040	0.0850	0.91315	2.12500
3_n	51	0.061	0.0820	0.89689	1.34430
2_n	52	0.086	0.0400	0.62642	0.46512
3_n	55	0.061	0.0520	0.71423	0.85246
2_n	56	0.086	0.0400	0.62642	0.46512
2_n	57	0.086	0.0500	0.70036	0.58140
3_n	58	0.061	0.0620	0.77988	1.01640
3_n	59	0.061	0.0715	0.83751	1.17210
2_n	60	0.086	0.0595	0.76400	0.69186
1_n	61	0.124	0.0450	0.66442	0.36290
2_n	62	0.086	0.0640	0.79236	0.74419
3_n	63	0.061	0.0760	0.86346	1.24590
3_n	64	0.061	0.0810	0.89141	1.32790
1_n	65	0.124	0.0500	0.70036	0.40323
2_n	66	0.086	0.0690	0.82273	0.80233
2_n	67	0.086	0.0745	0.85489	0.86628
2_o	68	0.086	0.0745	0.85489	0.86628
2_a	69	0.086	0.0745	0.85489	0.86628
2_b	70	0.086	0.0745	0.85489	0.86628
2_d	71	0.086	0.0745	0.85489	0.86628
2_e	72	0.086	0.0745	0.85489	0.86628
2_l	73	0.086	0.0745	0.85489	0.86628
2_d	74	0.086	0.0745	0.85489	0.86628
2_e	75	0.086	0.0745	0.85489	0.86628
3_n	76	0.061	0.0865	0.92118	1.41800
1_n	77	0.124	0.0555	0.73787	0.44758
1_n	78	0.124	0.0735	0.84914	0.59274
2_n	79	0.086	0.0925	0.95259	1.07560
3_n	80	0.061	0.1045	1.01250	1.71310

Table C.2: Solid Block Landslide Characteristics of Motion

Block #	Trial	a_o (m/s^2)	u_t (m/s)	t_o (s)	s_o (m)
2_n	25	1.6321	0.5585	0.34220	0.19112
2_n	26	1.6112	0.5585	0.34664	0.19360
2_n	27	1.6314	0.5585	0.34234	0.19120
2_a	28	1.1972	0.4415	0.36878	0.16282
2_b	29	1.4490	0.5369	0.37053	0.19894
2_d	30	1.9478	0.6484	0.33289	0.21584
2_e	31	2.2201	0.7095	0.31958	0.22674
2_o	41	0.8256	0.3691	0.44706	0.16501
2_l	42	2.4142	0.8036	0.33286	0.26749
1_n	43	1.5590	0.6517	0.41802	0.27243
1_n	44	1.6082	0.6517	0.40524	0.26409
2_n	47	1.6321	0.5585	0.34220	0.19112
2_d	48	1.9478	0.6484	0.33289	0.21584
2_e	49	2.2201	0.7095	0.31958	0.22674
4_n	50	1.5625	0.4198	0.26867	0.11279
3_n	51	1.6473	0.4271	0.25927	0.11074
2_n	52	1.6505	0.5585	0.33838	0.18899
3_n	55	1.6088	0.4271	0.26548	0.11339
2_n	56	1.6505	0.5585	0.33838	0.18899
2_n	57	1.6543	0.5585	0.33761	0.18855
3_n	58	1.6577	0.4271	0.25765	0.11004
3_n	59	1.6094	0.4271	0.26538	0.11334
2_n	60	1.5318	0.5585	0.36460	0.20363
1_n	61	1.6200	0.6517	0.40228	0.26217
2_n	62	1.7132	0.5585	0.32600	0.18207
3_n	63	1.5650	0.4271	0.27291	0.11656
3_n	64	1.5608	0.4271	0.27364	0.11687
1_n	65	1.5795	0.6517	0.41260	0.26889
2_n	66	1.6289	0.5585	0.34287	0.19149
2_n	67	1.6786	0.5585	0.33272	0.18582
2_o	68	0.8200	0.3691	0.45012	0.16614
2_a	69	1.1617	0.4415	0.38005	0.16779
2_b	70	1.3880	0.5369	0.38682	0.20768
2_d	71	1.8855	0.6484	0.34389	0.22298
2_e	72	2.1885	0.7095	0.32419	0.23002
2_l	73	2.4171	0.8036	0.33246	0.26717
2_d	74	1.9174	0.6484	0.33817	0.21927
2_e	75	2.0908	0.7095	0.33934	0.24076
3_n	76	1.5067	0.4271	0.28347	0.12107
1_n	77	1.6126	0.6517	0.40413	0.26337
1_n	78	1.5326	0.6517	0.42523	0.27712
2_n	79	1.6458	0.5585	0.33935	0.18953
3_n	80	1.8001	0.4271	0.23726	0.10134

Table C.3: Solid Block Landslide Ha_o, Sg and Maximum Near-Field Wave Amplitudes

Block #	Trial	Ha_o	Sg	η_{max} (cm)	η_{max} / s_o
2_n	25	3.4017	1.8140	0.549	0.028726
2_n	26	4.2997	1.1801	0.417	0.021540
2_n	27	3.8832	1.3938	0.514	0.026883
2_a	28	3.6659	1.5453	0.315	0.019347
2_b	29	3.6833	1.8882	0.391	0.019654
2_d	30	3.3091	2.0487	0.547	0.025342
2_e	31	3.1768	2.1521	0.640	0.028226
2_o	41	4.4291	1.5767	0.269	0.016302
2_l	42	3.2978	2.5560	0.757	0.028300
1_n	43	2.8723	2.6032	1.040	0.038175
1_n	44	2.1713	4.1498	1.250	0.047332
2_n	47	3.3672	1.8512	0.620	0.032441
2_d	48	3.2756	2.0908	0.703	0.032570
2_e	49	3.1447	2.1963	0.757	0.033386
4_n	50	6.1335	0.9383	0.176	0.015604
3_n	51	3.8121	0.9549	0.273	0.024653
2_n	52	2.4648	3.3408	1.152	0.060957
3_n	55	3.1084	1.5418	0.448	0.039511
2_n	56	2.4648	3.3408	0.889	0.047040
2_n	57	2.7493	2.6665	0.674	0.035746
3_n	58	3.2940	1.2550	0.394	0.035805
3_n	59	3.6435	1.1209	0.399	0.035203
2_n	60	3.2390	2.4200	0.629	0.030889
1_n	61	2.1555	4.1196	1.282	0.048900
2_n	62	3.0036	2.0116	0.673	0.036964
3_n	63	3.8630	1.0845	0.379	0.032516
3_n	64	3.9988	1.0203	0.337	0.028835
1_n	65	2.3304	3.8027	1.299	0.048310
2_n	66	3.2801	1.9624	0.657	0.034309
2_n	67	3.3074	1.7637	0.598	0.032181
2_o	68	4.4745	1.5769	0.314	0.018900
2_a	69	3.7779	1.5926	0.372	0.022171
2_b	70	3.8452	1.9712	0.508	0.024461
2_d	71	3.4185	2.1164	0.682	0.030586
2_e	72	3.2227	2.1832	0.709	0.030824
2_l	73	3.3049	2.5358	0.808	0.030243
2_d	74	3.3616	2.0811	0.679	0.030967
2_e	75	3.3733	2.2852	0.719	0.029863
3_n	76	4.2807	0.9897	0.293	0.024201
1_n	77	2.4048	3.3555	1.227	0.046588
1_n	78	2.9119	2.6660	1.139	0.041101
2_n	79	3.7588	1.4488	0.565	0.029811
3_n	80	3.9382	0.6857	0.314	0.030986

Table C.4: Solid Block Landslide Linear Theory and Amplitude Integral

Block #	Trial	(3.97)	η_{airy} (cm)	$t_o\eta_{max}$ (cm·s)	I(0) (cm·s)
2_n	25	0.10600	0.197	0.18787	0.323
2_n	26	0.09532	0.159	0.14455	0.261
2_n	27	0.10130	0.163	0.17596	0.300
2_a	28	0.09378	0.108	0.11616	0.238
2_b	29	0.09305	0.141	0.14488	0.275
2_d	30	0.11080	0.208	0.18209	0.330
2_e	31	0.11830	0.241	0.20453	0.368
2_o	41	0.06789	0.074	0.12026	0.163
2_l	42	0.11090	0.273	0.25198	0.410
1_n	43	0.10850	0.449	0.43475	0.577
1_n	44	0.12260	0.488	0.50654	0.685
2_n	47	0.10630	0.239	0.21216	0.352
2_d	48	0.11110	0.283	0.23402	0.392
2_e	49	0.11860	0.303	0.24192	0.415
4_n	50	0.07037	0.039	0.04729	0.097
3_n	51	0.11410	0.063	0.07078	0.191
2_n	52	0.11930	0.259	0.38982	0.457
3_n	55	0.12120	0.137	0.11893	0.247
2_n	56	0.11930	0.213	0.30082	0.418
2_n	57	0.11470	0.211	0.22755	0.392
3_n	58	0.12320	0.117	0.10151	0.224
3_n	59	0.11390	0.115	0.10589	0.228
2_n	60	0.09832	0.188	0.22934	0.388
1_n	61	0.12420	0.368	0.51573	0.729
2_n	62	0.11720	0.167	0.21940	0.379
3_n	63	0.10760	0.103	0.10343	0.203
3_n	64	0.10560	0.112	0.09222	0.201
1_n	65	0.11780	0.292	0.53597	0.715
2_n	66	0.10680	0.156	0.22527	0.373
2_n	67	0.11090	0.196	0.19897	0.347
2_o	68	0.06707	0.104	0.14134	0.242
2_a	69	0.08924	0.123	0.14138	0.262
2_b	70	0.08666	0.142	0.19650	0.309
2_d	71	0.10510	0.179	0.23453	0.372
2_e	72	0.11560	0.182	0.22985	0.379
2_l	73	0.11100	0.192	0.26863	0.420
2_d	74	0.10800	0.246	0.22961	0.381
2_e	75	0.10740	0.200	0.24399	0.384
3_n	76	0.09851	0.078	0.08306	0.173
1_n	77	0.12080	0.245	0.49587	0.671
1_n	78	0.10550	0.390	0.48433	0.635
2_n	79	0.10380	0.155	0.19173	0.329
3_n	80	0.12090	0.091	0.07450	0.179

Table C.5: Solid Block Landslide Energy Integrals

Block #	Trial	$t_o\eta_{max}^2$ ($cm^2 \cdot s$)	$E_p(0)$ ($cm^2 \cdot s$)	$E_p(4.25)$ ($cm^2 \cdot s$)
2_n	25	0.10314	0.166	0.128
2_n	26	0.06028	0.108	0.092
2_n	27	0.09045	0.134	0.099
2_a	28	0.03659	0.066	0.023
2_b	29	0.05665	0.096	0.039
2_d	30	0.09960	0.164	0.134
2_e	31	0.13090	0.213	0.206
2_o	41	0.03235	0.051	0.017
2_l	42	0.19075	0.283	0.400
1_n	43	0.45214	0.580	0.781
1_n	44	0.63318	0.683	0.745
2_n	47	0.13154	0.212	0.244
2_d	48	0.16452	0.256	0.365
2_e	49	0.18314	0.290	0.467
4_n	50	0.00832	0.015	0.008
3_n	51	0.01932	0.043	0.017
2_n	52	0.44907	0.375	0.197
3_n	55	0.05328	0.093	0.046
2_n	56	0.26743	0.283	0.131
2_n	57	0.15337	0.227	0.126
3_n	58	0.04000	0.073	0.035
3_n	59	0.04225	0.074	0.037
2_n	60	0.14425	0.217	0.142
1_n	61	0.66116	0.745	0.661
2_n	62	0.14765	0.231	0.202
3_n	63	0.03920	0.058	0.033
3_n	64	0.03108	0.059	0.040
1_n	65	0.69622	0.761	0.554
2_n	66	0.14800	0.216	0.153
2_n	67	0.11898	0.176	0.163
2_o	68	0.04438	0.059	0.023
2_a	69	0.05259	0.078	0.038
2_b	70	0.09982	0.127	0.083
2_d	71	0.15995	0.215	0.225
2_e	72	0.16297	0.229	0.250
2_l	73	0.21705	0.288	0.348
2_d	74	0.15591	0.229	0.272
2_e	75	0.17543	0.239	0.271
3_n	76	0.02434	0.042	0.026
1_n	77	0.60843	0.693	0.537
1_n	78	0.55165	0.667	0.753
2_n	79	0.10833	0.159	0.115
3_n	80	0.02339	0.046	0.023

Table C.6: Solid Block Landslide Nondimensional Wave Characteristics

Block #	Trial	$I(0) / t_o \eta_{max}$	$E_p(0) / t_o \eta_{max}^2$	$E_p(4.25) / E_p(0)$
2_n	25	1.7193	1.6095	0.7711
2_n	26	1.8056	1.7918	0.8519
2_n	27	1.7049	1.4815	0.7388
2_a	28	2.0488	1.8037	0.3485
2_b	29	1.8982	1.6947	0.4063
2_d	30	1.8123	1.6465	0.8171
2_e	31	1.7992	1.6272	0.9671
2_o	41	1.3554	1.5765	0.3333
2_l	42	1.6271	1.4836	1.4134
1_n	43	1.3272	1.2828	1.3466
1_n	44	1.3523	1.0787	1.0908
2_n	47	1.6591	1.6117	1.1509
2_d	48	1.6751	1.5561	1.4258
2_e	49	1.7154	1.5835	1.6103
4_n	50	2.0513	1.8024	0.5553
3_n	51	2.6984	2.2253	0.3954
2_n	52	1.1723	0.8351	0.5253
3_n	55	2.0768	1.7454	0.4946
2_n	56	1.3895	1.0582	0.4629
2_n	57	1.7227	1.4801	0.5551
3_n	58	2.2066	1.8252	0.4795
3_n	59	2.1533	1.7515	0.5000
2_n	60	1.6918	1.5043	0.6544
1_n	61	1.4135	1.1268	0.8873
2_n	62	1.7275	1.5645	0.8745
3_n	63	1.9626	1.4796	0.5690
3_n	64	2.1796	1.8985	0.6780
1_n	65	1.3340	1.0930	0.7280
2_n	66	1.6558	1.4595	0.7083
2_n	67	1.7440	1.4792	0.9261
2_o	68	1.7122	1.3294	0.3898
2_a	69	1.8532	1.4831	0.4872
2_b	70	1.5725	1.2722	0.6535
2_d	71	1.5861	1.3442	1.0465
2_e	72	1.6489	1.4052	1.0917
2_l	73	1.5635	1.3269	1.2083
2_d	74	1.6593	1.4688	1.1878
2_e	75	1.5738	1.3624	1.1339
3_n	76	2.0829	1.7259	0.6191
1_n	77	1.3532	1.1390	0.7749
1_n	78	1.3111	1.2091	1.1289
2_n	79	1.7159	1.4678	0.7233
3_n	80	2.4026	1.9664	0.5000

Table C.7: Solid Block Landslide Energy Conversion and Channel Depth

Block #	Trial	ρ_b (kg/m^3)	e (%)	h (m)	(5.26) (m)
2_n	25	1 870	3.9940	0.3730	0.293
2_n	26	1 870	2.9126	0.3730	0.370
2_n	27	1 870	3.9965	0.3730	0.334
2_a	28	1 460	2.9043	0.3730	0.315
2_b	29	1 710	2.5958	0.3730	0.317
2_d	30	2 180	2.4547	0.3730	0.285
2_e	31	2 465	2.3828	0.3730	0.273
2_o	41	1 225	4.3637	0.3730	0.381
2_l	42	2 745	2.4224	0.3730	0.284
1_n	43	1 890	6.0992	0.3678	0.356
1_n	44	1 890	6.6608	0.3678	0.269
2_n	47	1 870	5.0423	0.3730	0.290
2_d	48	2 180	4.0135	0.3730	0.282
2_e	49	2 465	3.2999	0.3730	0.270
4_n	50	1 835	2.8702	0.4155	0.245
3_n	51	1 835	2.7191	0.4060	0.233
2_n	52	1 870	12.742	0.3730	0.212
3_n	55	1 835	5.9707	0.3730	0.190
2_n	56	1 870	7.5884	0.3730	0.212
2_n	57	1 870	4.8654	0.3730	0.236
3_n	58	1 835	4.8938	0.3730	0.201
3_n	59	1 835	5.5514	0.3730	0.222
2_n	60	1 870	4.9922	0.3731	0.279
1_n	61	1 890	6.9552	0.3730	0.267
2_n	62	1 870	5.2996	0.3730	0.258
3_n	63	1 835	5.3105	0.3730	0.236
3_n	64	1 835	4.3463	0.3730	0.244
1_n	65	1 890	7.7201	0.3731	0.289
2_n	66	1 870	5.5156	0.3730	0.282
2_n	67	1 870	4.6075	0.3730	0.284
2_o	68	1 225	6.0067	0.3730	0.385
2_a	69	1 460	4.1743	0.3730	0.325
2_b	70	1 710	4.5743	0.3730	0.331
2_d	71	2 180	3.9420	0.3730	0.294
2_e	72	2 465	2.9665	0.3730	0.277
2_l	73	2 745	2.7658	0.3730	0.284
2_d	74	2 180	3.8424	0.3730	0.289
2_e	75	2 465	3.1934	0.3730	0.290
3_n	76	1 835	3.5171	0.3730	0.261
1_n	77	1 890	7.1080	0.3730	0.298
1_n	78	1 890	7.4166	0.3730	0.361
2_n	79	1 870	4.6744	0.3730	0.323
3_n	80	1 835	3.7161	0.3730	0.240

Table C.8: Material Landslide Initial Geometry and Long Wave Celerity

Material	Trial	b (m)	d (m)	$\sqrt{g\,d}$ (m/s)	d / b
Crushed Calcite	32	0.084	0.073	0.84624	0.86905
Crushed Calcite	33	0.085	0.073	0.84624	0.85882
3 mm Glass Beads	34	0.085	0.073	0.84624	0.85882
1 mm Glass Beads	35	0.084	0.075	0.85776	0.89286
12 mm Marbles	37	0.084	0.076	0.86346	0.90476
3 mm Lead Shot	38	0.090	0.076	0.86346	0.84444
2 mm Lead Shot	39	0.085	0.080	0.88589	0.94118
Crushed Calcite	40	0.082	0.076	0.86346	0.92683
3 mm Steel Shot	81	0.085	0.074	0.85202	0.87059
3 mm Glass Beads	82	0.083	0.074	0.85202	0.89157
12 mm Marbles	83	0.084	0.072	0.84043	0.85714
2 mm Lead Shot	84	0.087	0.075	0.85776	0.86207
Garnet Sand	85	0.087	0.075	0.85776	0.86207
3 mm Lead Shot	86	0.085	0.072	0.84043	0.84706
0.5 mm Glass Beads	87	0.085	0.075	0.85776	0.88235
1 mm Glass Beads	89	0.085	0.049	0.69332	0.57647
1 mm Glass Beads	90	0.085	0.100	0.99045	1.17650
3 mm Glass Beads	91	0.112	0.097	0.97548	0.86607
1 mm Glass Beads	92	0.068	0.059	0.76078	0.86765
1 mm Glass Beads	93	0.057	0.050	0.70036	0.87719

Table C.9: Material Landslide Physical Properties

Material	Trial	D (mm)	C_n	ρ_s (kg/m^3)	D / b
Crushed Calcite	32	3.328	0.36397	1 950	0.03962
Crushed Calcite	33	3.328	0.36397	1 950	0.03915
3 mm Glass Beads	34	2.959	0.10510	1 935	0.03481
1 mm Glass Beads	35	1.257	0.08749	1 910	0.01496
12 mm Marbles	37	12.16	0.09629	1 899	0.14476
3 mm Lead Shot	38	3.114	0.21256	7 321	0.03460
2 mm Lead Shot	39	2.059	0.08749	7 114	0.02422
Crushed Calcite	40	3.328	0.36397	1 965	0.04059
3 mm Steel Shot	81	3.311	0.10510	5 102	0.03895
3 mm Glass Beads	82	2.959	0.10510	1 935	0.03565
12 mm Marbles	83	12.16	0.09629	1 899	0.14476
2 mm Lead Shot	84	2.059	0.08749	7 114	0.02367
Garnet Sand	85	0.400	0.70021	2 640	0.00460
3 mm Lead Shot	86	3.114	0.21256	7 321	0.03664
0.5 mm Glass Beads	87	0.500	0.09629	1 882	0.00588
1 mm Glass Beads	89	1.257	0.08749	1 910	0.01479
1 mm Glass Beads	90	1.257	0.08749	1 910	0.01479
3 mm Glass Beads	91	2.959	0.10510	1 935	0.02642
1 mm Glass Beads	92	1.257	0.08749	1 910	0.01849
1 mm Glass Beads	93	1.257	0.08749	1 910	0.02205

Table C.10: Material Landslide Characteristics of Motion

Material	Trial	t_o (s)	s_o (m)	(5.8) (m/s^2)	a_o (m/s^2)
Crushed Calcite	32	0.28960	0.13520	1.6120	1.5282
Crushed Calcite	33	0.27215	0.12425	1.6775	1.5282
3 mm Glass Beads	34	0.31909	0.18132	1.7808	2.1280
1 mm Glass Beads	35	0.34165	0.17895	1.5331	2.1314
12 mm Marbles	37	0.35338	0.25982	2.0806	2.0940
3 mm Lead Shot	38	NA	NA	NA	4.2538
2 mm Lead Shot	39	0.25233	0.30367	4.7695	4.8927
Crushed Calcite	40	0.27051	0.11579	1.5823	1.5439
3 mm Steel Shot	81	0.27086	0.29477	4.0178	4.3177
3 mm Glass Beads	82	0.32403	0.17086	1.6273	2.1280
12 mm Marbles	83	0.36429	0.27977	2.1082	2.0940
2 mm Lead Shot	84	NA	NA	NA	4.8927
Garnet Sand	85	NA	NA	NA	0.9931
3 mm Lead Shot	86	0.29484	0.38447	4.4228	4.2538
0.5 mm Glass Beads	87	0.53112	0.26339	0.9337	NA
1 mm Glass Beads	89	0.37949	0.20729	1.4394	2.1314
1 mm Glass Beads	90	0.39005	0.21365	1.4043	2.1314
3 mm Glass Beads	91	0.31714	0.19216	1.9106	2.1280
1 mm Glass Beads	92	0.31164	0.14843	1.5283	2.1314
1 mm Glass Beads	93	NA	NA	NA	2.1314

Table C.11: Material Landslide Characteristics of Motion and Initial Shape

Material	Trial	(5.10) (m/s)	u_t (m/s)	A_o (cm^2)	$z_{c.o}$ (cm)
Crushed Calcite	32	0.4669	0.5423	41.812	2.2771
Crushed Calcite	33	0.4565	0.5455	40.713	2.1861
3 mm Glass Beads	34	0.5682	0.6419	39.441	2.1615
1 mm Glass Beads	35	0.5238	0.6358	36.579	2.1029
12 mm Marbles	37	0.7352	0.6227	42.181	2.4141
3 mm Lead Shot	38	NA	1.6096	43.010	2.3730
2 mm Lead Shot	39	1.2035	1.6561	40.894	2.3354
Crushed Calcite	40	0.4280	0.5400	37.155	2.1688
3 mm Steel Shot	81	1.0883	1.3435	37.644	2.2769
3 mm Glass Beads	82	0.5273	0.6344	36.675	2.1562
12 mm Marbles	83	0.7680	0.6227	36.146	2.1302
2 mm Lead Shot	84	NA	1.6755	36.602	2.2150
Garnet Sand	85	NA	0.4976	36.624	2.1630
3 mm Lead Shot	86	1.3040	1.5643	42.462	2.2652
0.5 mm Glass Beads	87	0.4959	NA	34.665	2.0135
1 mm Glass Beads	89	0.5462	0.6395	34.864	2.0100
1 mm Glass Beads	90	0.5478	0.6395	35.441	2.0795
3 mm Glass Beads	91	0.6059	0.7369	62.889	2.8488
1 mm Glass Beads	92	0.4763	0.5720	23.531	1.6753
1 mm Glass Beads	93	NA	0.5237	15.504	1.3225

Table C.12: Material Landslide Initial Rates of Strain

Material	Trial	$1/A_o\ dA/dt\ (s^{-1})$	$1/z_{c.o}\ dz_c/dt\ (s^{-1})$	$A_o / 9\ z_{c.o}^2$
Crushed Calcite	32	1.55	-0.4025	0.89597
Crushed Calcite	33	1.92	-0.4560	0.94657
3 mm Glass Beads	34	2.41	-0.9805	0.93798
1 mm Glass Beads	35	2.35	-0.6006	0.91908
12 mm Marbles	37	1.17	-0.5934	0.80420
3 mm Lead Shot	38	1.92	-1.4806	0.84866
2 mm Lead Shot	39	2.16	-1.4968	0.83309
Crushed Calcite	40	1.83	-0.5195	0.87768
3 mm Steel Shot	81	1.53	-1.7123	0.80680
3 mm Glass Beads	82	1.75	-0.8886	0.87650
12 mm Marbles	83	1.44	-0.5510	0.88507
2 mm Lead Shot	84	1.57	-1.6700	0.82892
Garnet Sand	85	0.52	-0.8242	0.86978
3 mm Lead Shot	86	0.83	-1.5860	0.91949
0.5 mm Glass Beads	87	0.83	-0.5201	0.95005
1 mm Glass Beads	89	2.33	-0.3305	0.95883
1 mm Glass Beads	90	2.62	-0.4904	0.91064
3 mm Glass Beads	91	1.61	-0.5474	0.86101
1 mm Glass Beads	92	2.26	-0.7035	0.93156
1 mm Glass Beads	93	2.82	-0.5516	0.98494

Table C.13: Material Landslide Initial Rates of Deformation, Ha_o and Sg

Material	Trial	$\Gamma\ (s^{-1})$	$\Gamma\ t_o$	Ha_o	Sg
Crushed Calcite	32	-1.1704	-0.3390	2.9176	1.3096
Crushed Calcite	33	-1.4139	-0.3848	2.7095	1.2035
3 mm Glass Beads	34	-2.1810	-0.6956	3.1768	1.7563
1 mm Glass Beads	35	-1.7693	-0.6045	3.4887	1.6872
12 mm Marbles	37	-1.1510	-0.4067	3.6325	2.4174
3 mm Lead Shot	38	-2.4081	NA	NA	NA
2 mm Lead Shot	39	-2.5344	-0.6395	2.6298	2.6841
Crushed Calcite	40	-1.4224	-0.3848	2.8485	1.0773
3 mm Steel Shot	81	-2.4213	-0.6558	2.7151	2.8167
3 mm Glass Beads	82	-1.7484	-0.5665	3.3263	1.6327
12 mm Marbles	83	-1.2616	-0.4596	3.6447	2.7476
2 mm Lead Shot	84	-2.4124	NA	NA	NA
Garnet Sand	85	-1.0737	NA	NA	NA
3 mm Lead Shot	86	-1.9940	-0.5879	2.9152	3.7759
0.5 mm Glass Beads	87	-0.9339	-0.4960	5.3597	2.4833
1 mm Glass Beads	89	-1.4942	-0.5670	3.0954	2.9914
1 mm Glass Beads	90	-1.7925	-0.6992	4.5450	1.5107
3 mm Glass Beads	91	-1.3374	-0.4241	2.7622	1.4008
1 mm Glass Beads	92	-1.8289	-0.5700	3.4867	1.7789
1 mm Glass Beads	93	-1.9614	NA	NA	NA

Table C.14: Material Landslide Maximum Near-Field Wave Amplitudes

Material	Trial	(5.8) / a_o	(5.10) / u_p	η_{max} (cm)	η_{max} / s_o
Crushed Calcite	32	1.0548	1.8674	0.420	0.031065
Crushed Calcite	33	1.0977	1.8262	0.400	0.032193
3 mm Glass Beads	34	0.8369	1.5358	0.420	0.023163
1 mm Glass Beads	35	0.7193	2.9099	0.327	0.018273
12 mm Marbles	37	0.9936	1.5005	0.488	0.018782
3 mm Lead Shot	38	NA	NA	0.791	NA
2 mm Lead Shot	39	0.9748	1.4677	0.713	0.023479
Crushed Calcite	40	1.0249	1.7122	0.449	0.038777
3 mm Steel Shot	81	0.9305	1.4319	0.654	0.022187
3 mm Glass Beads	82	0.7647	1.4251	0.405	0.023704
12 mm Marbles	83	1.0068	1.5673	0.371	0.013261
2 mm Lead Shot	84	NA	NA	0.708	NA
Garnet Sand	85	NA	NA	0.308	NA
3 mm Lead Shot	86	1.0397	1.3040	0.840	0.021848
0.5 mm Glass Beads	87	NA	7.0844	0.273	0.010365
1 mm Glass Beads	89	0.6753	3.0346	0.523	0.025230
1 mm Glass Beads	90	0.6589	3.0431	0.288	0.013480
3 mm Glass Beads	91	0.8979	1.6376	0.566	0.029455
1 mm Glass Beads	92	0.7170	2.6460	0.327	0.022031
1 mm Glass Beads	93	NA	NA	0.269	NA

Table C.15: Simulation Initial Geometry, Characteristics of Motion and Ha_o

Run	d / b	$t_o\sqrt{g/b}$	s_o / b	$t_{max}\sqrt{g/b}$	Ha_o
1	0.87	3.8306	2.2243	2.606	3.5729
2	0.87	5.6930	1.6866	3.511	5.3101
3	0.87	3.5937	2.9536	2.394	3.3520
4	2.13	3.8306	2.2243	3.285	5.5906
5	1.35	3.8306	2.2243	2.918	4.4507
6	1.08	3.8306	2.2243	2.752	3.9809
7	0.58	3.8306	2.2243	2.398	2.9173
8	2.13	5.6930	1.6866	3.959	8.3087
9	2.13	3.5937	2.9536	3.072	5.2449
20	0.87	7.9682	1.5824	5.942	7.4323
21	0.87	4.2372	1.9575	2.812	3.9522
22	2.13	7.9682	1.5824	4.588	11.629
23	2.13	4.2372	1.9575	3.480	6.1839

Table C.16: Simulation Maximum Near-Field Wave Amplitude and Error Analysis

Run	η_{max} / b	$\Delta V \cdot 10^4$ / V_o	V_o / $1 \cdot b^2$	ΔV / $1 \cdot b^2$	ΔH / 2 b
1	0.04847	1.635	43.833	0.007168	0.0020062
2	0.02146	0.653	50.634	0.003306	0.0006227
3	0.06532	2.185	52.856	0.011549	0.0034454
4	0.02083	2.176	66.035	0.014369	0.0025703
5	0.03327	1.974	51.864	0.010238	0.0023003
6	0.04061	1.805	47.281	0.008534	0.0021438
7	0.06493	1.363	39.242	0.005349	0.0018334
8	0.00912	0.622	78.897	0.004910	0.0005909
9	0.02821	3.254	75.936	0.024709	0.0047112
20	0.01434	-0.698	66.002	-0.004610	-0.0006201
21	0.03791	1.217	43.340	0.005274	0.0013346
22	0.00495	0.255	103.01	0.002630	0.0002262
23	0.01626	1.512	66.502	0.010055	0.0016260

Table C.17: Simulation Maximum Near-Field Wave Amplitude and Solid Block Trial

Run	η_{max} / s_o	Trial
1	0.021791	67
2	0.012724	68
3	0.022115	73
4	0.009365	50
5	0.014958	51
6	0.018257	79
7	0.029191	57
8	0.005406	NA
9	0.009551	NA
20	0.009062	NA
21	0.019367	NA
22	0.003128	NA
23	0.008307	NA